

Encapsulation of Functional Magnetic-Oxides inside Carbon Nanotubes

A thesis
submitted in partial fulfillment of the requirements
of the degree of
Doctor of Philosophy

by

Aakanksha Kapoor

ID No. 20143349



Indian Institute of Science Education and Research Pune

June 2020

To
my parents,
for getting me started;
‡
my sister Gunjan,
for getting through...

Declaration

I declare that this written submission represents my ideas in my own words and where others' ideas have been included, I have adequately cited and referenced the original sources. I also declare that I have adhered to all principles of academic honesty and integrity and have not misrepresented or fabricated or falsified any idea/-data/fact/source in my submission. I understand that violation of the above will be cause for disciplinary action by the Institute and can also evoke penal action from the sources which have thus not been properly cited or from whom proper permission has not been taken when needed.

Pune

Date 17.12.19


Aakanksha
Aakanksha Kapoor
ID:20143349

Certificate

Certified that the work incorporated in the thesis entitled "**Encapsulation of Functional Magnetic-Oxides inside Carbon Nanotubes**" submitted by **Aakanksha Kapoor** was carried out by the candidate, under my supervision. The work presented here or any part of it has not been included in any other thesis submitted previously for the award of any degree or diploma from any other University or institution.

Pune

Date: 17.12.19


Dr. Ashita Bajpai
Thesis Supervisor

Acknowledgments

I would like to express my sincere gratitude to my thesis supervisor Dr. Ashna Bajpai for the continuous support of my Ph.D. study and related research, for her patience, constant motivation, and immense knowledge. Her guidance taught me to be motivated during difficult days, weeks or months; and be grounded during the good days. It was a great learning experience for me to be a part of the research journey. Her guidance has helped me build research attitude and skills pertinent in science as well as other aspects of life.

I would like to thank my Research and Advisory Committee (RAC) members, Dr. Mukul Kabir and Dr. Atikur Rahman for their constant support and guidance. Their feedbacks and insightful comments, during the annual meetings, helped me improve my research work and widen my research from various perspectives. I would also like to express my gratitude towards Dr. Surjeet Singh for helping me during the coursework. I have learnt a lot about the field through his impressive teaching skills.

I would like to sincerely thank Prof. A.K. Nigam for providing me the opportunity to conduct TEM and SQUID measurements in TIFR, Mumbai. I would also like to thank Dr. Sunil Nair for providing SQUID slots and Dr. G.V. Pavan Kumar for Raman spectroscopy measurements. I also thank Prof. Satishchandra Ogale and Prof. Ruediger Klingeler (Heidelberg University, Germany) for energy-related measurements. Without their precious support it would not be possible to conduct this research. I would also like to thank my collaborators – Vikram Bakaraju, Arka Bikash Dey, Apurva Patrike, Charu Garg, and Shruti Chakravarty.

I thank my fellow labmates – Namrata Pattanayak, Nitesh Singh, Suvidya Kumar, and Bharat for stimulating discussions which were not just limited to work related things. In particular, I am grateful to my senior labmate Namrata Pattanayak for helping me learn the working of the lab and other technical stuff during the initial

years of my Ph.D. I always rejoiced and looked forward to work discussions over coffee.

I would like to acknowledge IISER Pune for the research fellowship throughout my Ph.D. I would also like to acknowledge the Infosys foundation funds for supporting my travels towards attending international school.

I am grateful to our technical staff members Nilesh Dumbre, Anil Prathamshetti, Parveen Nasa, Prashant Kale, Sudhir Lone, Yathis T Shakarappa and Santosh Khilare for their technical assistance in various stages during PhD. I am also thankful to all the administrative staff members – Prabhakar sir, Kalpesh, Dhanashree ma'am, Tushar, Nayana, Sayalee, Priyadarshini and Prabhas for their support throughout this journey. I am extremely grateful to the supporting staff – security, housekeeping, librarian, and electrician at IISER Pune for their kind help.

My heartfelt gratitude to all the teachers who have taught me from my school days to post-graduate education. I Kohli sir, Meenakshi ma'am, Dr. Phookun, Dr. Vyas, Dr. Sanjay Jain. Without their blessings, support, motivation and encouragement, it would have been impossible for me to reach this stage.

I would like to express my deepest and sincere gratitude towards my parents, and sister, Gunjan, for their unflinching belief in my capabilities. I thank them for their constant moral support, unconditional and immense love, encouragement and most importantly their enormous faith in me. I cannot thank my sister enough for always being there and understanding my unspoken words. I am also thankful to her for sparing her time and helping me out with the creative work throughout this journey. I thank my paternal and maternal grandparents for their incessant love and affection. I also express my gratitude towards my aunt, Neeta, for being my pillar of support in good as well as bad times. I also thank Yash and Mehak for their love and encouragement. I take this opportunity to thank my friends – Angelina, Sucheta, Anu, Ekta, and Aaron who have always been a major source of support. I specially thank Angelina for pestering me to attend the interview at IISER Pune five years back, and Sucheta for always being there.

Contents

List of Figures	xvi
List of Tables	xx
1 Introduction	1
1.1 A Brief History of Carbon Nanotubes	1
1.2 Structure of Carbon Nanotubes	2
1.3 Properties of Carbon Nanotubes	4
1.3.1 Electronic Properties	4
1.3.2 Mechanical Properties	5
1.3.3 Thermal Properties	6
1.4 Synthesis of Carbon Nanotubes	6
1.4.1 Arc Discharge	7
1.4.2 Laser Ablation	7
1.4.3 Chemical Vapor Deposition	8
1.4.3.1 <i>Aerosol Assisted CVD</i>	9
1.4.3.2 <i>Solid State CVD</i>	9
1.4.3.3 Synthesis of Filled Carbon Nanotubes : Challenges .	10
1.5 Raman Spectroscopy of Carbon Nanotubes	11
1.6 Magnetism and Exchange Interactions	13
1.6.1 Indirect Exchange	14
1.6.1.1 Superexchange Interactions	14
1.6.1.2 Double Exchange Interaction	15
1.7 Weak Ferromagnetism	18
1.8 The Concept of Remanence	19

1.9	Filling of Carbon Nanotubes with Functional Magnetic Materials : The Fundamental Aspect	20
1.9.1	A General Overview	20
1.9.2	Weak Ferromagnetism in Hematite	22
1.9.2.1	Time-stable Remanence in Hematite (α -Fe ₂ O ₃)	24
1.9.3	Temperature-dependent Raman Spectroscopy	25
1.10	Filling of Carbon Nanotubes with Transition Metal Oxides : The Applications	26
1.11	Scope and Outline of the Thesis	29
2	Experimental Methods	31
2.1	Characterization Techniques	31
2.1.1	Field-Emission Scanning Electron Microscope	31
2.1.2	Transmission Electron Microscope	34
2.1.3	X-Ray Diffraction	36
2.1.4	Synchrotron X-Ray Diffraction	37
2.1.5	Rietveld Refinement	39
2.1.5.1	Principle of Rietveld Refinement	39
2.1.5.2	Criteria of fit	42
2.1.5.3	Refinement Procedure	42
2.1.6	Raman Spectroscopy	43
2.1.7	Thermal Gravimetric Analysis	45
2.2	Magnetic Characterization	46
2.3	Electrochemical Characterization	48
2.3.1	Cell Fabrication	48
2.3.1.1	Coin Cell	48
2.3.1.2	Swagelok-type Cell	49
2.3.2	Electrochemical Measurements	50
2.3.2.1	Galvanostatic Cycling	50
2.3.2.2	Cyclic Voltammetry	52
2.3.2.3	Electrochemical Impedance Spectroscopy	53
3	Synthesis of 3d Transition Metals and Oxides filled Carbon Nanotubes	56
3.1	Solid State CVD for Metal-filled CNT	56

3.2	Single-Zone Furnace for Powder CVD of Metallocene : Mechanical Assembly	58
3.2.1	Synthesis Chamber and Sample Insertion Arrangements	59
3.2.2	Experimental Procedure	60
3.2.3	Role of Synthesis Parameters	61
3.2.3.1	Sublimation Temperature (T_{sub})	61
3.2.3.2	Rate of Argon-flow	62
3.2.3.3	Pyrolysis Temperature (T_{pyro})	62
3.2.3.4	Camphor as a Co-precursor with Metallocene	63
3.3	Iron-filled Carbon Nanotubes (Fe@CNT)	63
3.3.1	Morphology and Structural Characterization	63
3.3.2	Estimation of Filling Efficiency	66
3.3.2.1	Thermo-Gravimetric Analysis TGA	67
3.3.2.2	Bulk Magnetization	67
3.3.3	Influence of Synthesis Parameters	68
3.3.3.1	Role of Pyrolysis Temperature (T_{pyro})	68
3.3.3.2	Role of Sublimation Temperature (T_{sub})	71
3.3.3.3	Role of Precursor	72
3.4	Nickel-filled Carbon Nanotubes (Ni@CNT)	74
3.4.1	Optimization of Synthesis Parameters	74
3.4.1.1	Significance of Camphor as a Co-precursor	74
3.4.1.2	Pyrolysis Temperature T_{pyro} and Sublimation Temperature T_{sub}	75
3.4.2	Characterization of Ni@CNT	76
3.4.3	Variations in Morphologies for Ni@CNT : Role of Camphor	81
3.5	Oxides-filled Carbon Nanotubes (Oxides@CNT)	83
3.6	Summary	87
4	Magnetism at the Interface of Hematite & Carbon Nanotubes	89
4.1	Introduction	89
4.2	The Concept of FC and ZFC	91
4.2.1	Magnetization Measurement Protocol : FC and ZFC	92
4.2.2	Remanence Measurement Protocol	92
4.3	Results and Discussion	93

4.3.1	α -Fe ₂ O ₃ @CNT	93
4.3.2	α -Fe ₂ O ₃ -template	95
4.3.3	Comparison of Magnetization in α -Fe ₂ O ₃ @CNT and α -Fe ₂ O ₃ - template	96
4.3.4	Remanence in α -Fe ₂ O ₃ @CNT and α -Fe ₂ O ₃ -template	99
4.3.5	Weak Ferromagnetism and <i>Time-Stable</i> Remanence	102
4.3.6	Structural Correlation : <i>Interface</i> Effects	104
4.3.7	Magnitude of Time-Stable Remanence at Room Temperature : Practical Implications	109
4.3.8	Magnetization and Remanence for <i>FeO_x@CNT</i>	111
4.4	Summary	112
5	Interface-Effects in FeO_x@CNT using Raman Spectroscopy	114
5.1	Introduction	114
5.2	Results and Discussion	115
5.2.1	Characterization	115
5.2.2	Temperature Evolution of Raman Spectra of FeO _x @CNT . . .	117
5.2.2.1	Temperature Evolution of Raman Spectra of Hematite	117
5.2.2.2	Temperature Evolution of Raman Spectra of Carbon Nanotubes	123
5.2.2.3	Influence of Magnetic System's (Hematite) Environ- ment on Carbon Nanotubes : <i>Interface</i> Effects	126
5.3	Summary	127
6	Oxides-filled CNT as Anode Materials in Lithium-ion Batteries	128
6.1	Introduction	128
6.2	Iron-Oxide filled Carbon Nanotubes	130
6.2.1	Structural Characterization	130
6.2.2	Electrochemical Performance	132
6.3	Nickel-Oxide filled Carbon Nanotubes	136
6.3.1	Structural Characterization	136
6.3.2	Electrochemical Performance	137
6.4	Cobalt-Oxide filled Carbon Nanotubes	140
6.4.1	Structural Characterization	140
6.4.2	Electrochemical Performance	141

6.5	Role of Morphology of CNT for LIB	143
6.6	Significance of Carbon Nanotubes	145
6.7	Summary	147
7	Conclusions and Future Outlook	148
A	Glossary of Battery-related Terms	152
B	Cobalt- and Cobalt Oxide- filled Carbon Nanotubes	153
B.1	Cobalt-filled Carbon Nanotubes	153
B.1.1	Synthesis and Characterization	153
B.1.2	Variations in morphology with the change of synthesis parameters	155
B.2	Cobalt-Oxide filled Carbon Nanotubes	156
C	Magnetoresistance on Iron-Oxide filled Carbon Nanotubes	158
	Bibliography	160

List of Figures

1.1	Schematic of a graphene sheet to define the unit cell of single-wall CNT.	3
1.2	Schematic of Solid State CVD method.	10
1.3	Typical Raman spectrum of Multi-wall Carbon Nanotubes in the range 1200-3000 cm^{-1}	12
1.4	Schematic of Superexchange paths.	15
1.5	<i>Illustration of (a) double-exchange and (b) superexchange interactions in Fe_3O_4.</i>	16
1.6	Schematic of a collinear antiferromagnet and a canted antiferromagnet.	17
1.7	Schematic of spin configuration of hematite ($\alpha\text{-Fe}_2\text{O}_3$).	23
1.8	Remanence as a function of time and cooling magnetic field.	24
1.9	Schematic of a typical Li-ion battery.	27
2.1	Schematic of a typical scanning electron microscope.	32
2.2	Schematic representation of a typical transmission electron microscope	34
2.3	Schematic of principle of X-ray diffraction.	36
2.4	A typical layout of synchrotron radiation facility	38
2.5	Energy level diagram depicting Rayleigh scattering and Raman scat- tering – stokes and anti-stokes.	44
2.6	Schematic of a typical Raman spectrometer.	45
2.7	Schematic of Superconducting Quantum Interface Device (SQUID). .	46
2.8	Schematic of a typical coin cell assembly of the electrode half-cells. .	49
2.9	Schematic of a Swagelog-type cell.	50
2.10	Energy level diagram depicting Rayleigh scattering and Raman scat- tering – stokes and anti-stokes.	51
2.11	A typical cyclic voltammetry curve.	52
2.12	A typical Nyquist plot.	54

3.1	Representation of ferrocene molecule.	57
3.2	Schematic of the single-zone furnace depicting the modified synthesis chamber and temperature profile of the furnace.	58
3.3	FESEM images of iron-filled CNT at different magnifications.	64
3.4	Characterization of iron-filled CNT : Representative Powder XRD pattern and Raman spectrum.	65
3.5	TEM micrographs for iron-filled CNT depicting the filling efficiency.	66
3.6	TGA and bulk magnetization for iron-filled CNT : estimation of filling efficiency.	67
3.7	FESEM micrographs of iron-filled CNT with variation in pyrolysis temperature T_{pyro}	69
3.8	Real-time image of inner quartz tube depicting the variation in morphology of the sample obtained from different regions.	70
3.9	FESEM micrographs of iron-filled CNT with variation in pyrolysis temperature T_{sub}	71
3.10	FESEM micrographs of iron-filled CNT using camphor as a co-precursor.	72
3.11	FESEM micrographs of nickel-filled CNT at different sublimation temperature T_{sub} indicating higher T_{sub} is more conducive for obtaining well-formed nickel-filled CNT.	76
3.12	Characterization of nickel-filled CNT : Morphology and Structure.	77
3.13	TEM micrographs for nickel-filled CNT depicting the filling efficiency.	78
3.14	TGA and bulk magnetization of nickel-filled CNT.	79
3.15	FESEM micrographs of nickel-filled CNT obtained by varying the ratio of amount of camphor to amount of nickelocene.	82
3.16	Characterization of Iron-Oxide filled CNT : Morphology and Structure.	86
4.1	Schematic of spin configuration in hematite for antiferromagnetic and weak ferromagnetic states.	90
4.2	Characterization of α -Fe ₂ O ₃ @CNT : Morphology and Structure.	93
4.3	Magnetization as a function of temperature for α -Fe ₂ O ₃ @CNT.	94
4.4	Characterization for α -Fe ₂ O ₃ -template : Morphology and Structure.	95
4.5	Comparison of magnetization in α -Fe ₂ O ₃ @CNT and α -Fe ₂ O ₃ -template.	97
4.6	Magnetization as a function of temperature for α -Fe ₂ O ₃ @CNT and α -Fe ₂ O ₃ -template at different fields.	98
4.7	Remanence as a function of time for α -Fe ₂ O ₃ @CNT at room temperature.	100

4.8	Remanence as a function of time for α -Fe ₂ O ₃ @CNT and α -Fe ₂ O ₃ - template at room temperature and low temperatures.	101
4.9	Temperature variation of lattice parameters for α -Fe ₂ O ₃ @CNT and α -Fe ₂ O ₃ -template.	106
4.10	Magnetization and Remanence for <i>Oxide@CNT</i>	111
5.1	Characterization of FeO _x @CNT : Morphology and Structure.	115
5.2	Raman spectrum for FeO _x @CNT at room temperature showing the Lorentzian fitting.	116
5.3	Raman spectra of FeO _x @CNT in the range 100 - 1500 cm ⁻¹	118
5.4	Temperature evolution for A _{1g} mode and E _g mode across the Morin transition.	119
5.5	Normalized intensity and phonon frequencies as a function of temper- ature for A _{1g} mode and E _g mode.	121
5.6	Typical Raman spectrum of Multi-wall Carbon Nanotubes in the range 1200-3000 cm ⁻¹	123
5.7	Temperature evolution of Raman bands pertaining to CNT.	124
5.8	Phonon frequencies and normalized intensity as a function of temper- ature for D-, G-, and 2D-band.	125
5.9	Comparison of temperature evolution of phonon frequency for G-band (CNT) as a function of temperature with magnetic transition of the hematite encapsulate.	126
6.1	Characerization of Iron-Oxide filled CNT : Morphology and Structure.	131
6.2	CV curve and discharge/charge profiled for Iron-Oxide filled CNT.	133
6.3	Electrochemical performance of Iron-Oxide filled CNT.	134
6.4	Electrochemical impedance spectroscopy (EIS) spectra of Iron-Oxide filled CNT.	135
6.5	Characterization of Nickel-Oxide filled CNT : Morphology and Structure.	137
6.6	Electrochemical performance of Nickel-Oxide filled CNT.	138
6.7	Characterization of Cobalt-Oxide filled CNT : Morphology and Struc- ture.	140
6.8	Electrochemical performance of Cobalt-Oxide filled CNT.	142

6.9	Cycling performance of different morphologies of Iron-Oxide@CNT signifying the importance of morphology of CNT in electrochemical performance.	144
6.10	Comparison of cyclic performance of Oxide@CNT with bare oxide template.	145
B.1	FESEM micrographs of cobalt-filled CNT.	153
B.2	TEM micrographs of cobalt-filled CNT.	154
B.3	Characterization of cobalt-filled CNT.	155
B.4	FESEM micrographs of cobalt-filled CNT by varying synthesis conditions.	156
B.5	Characterization of cobalt-oxide filled CNT.	157
C.1	Transport measurements on iron-oxide filled CNT.	158

List of Tables

3.1	Optimized synthesis parameters for Fe@CNT.	64
3.2	Saturation Magnetization values for bulk transition metal and when they are encapsulated inside CNT at room temperature. For metal@CNT, the M_S is further compared with literature for each sample.	80
3.3	Summary of the synthesis parameters for Ni@CNT listing various morphologies obtained when the ratio of amount of camphor to nickelocene is varied. A tendency to form aligned morphology is observed at lower T_{pyro}	83
3.4	Annealing conditions for oxidization for a fixed amount of Fe@CNT sample (10 mg). Different phases of metal-oxide are formed depending on the annealing temperatures.	84
4.1	Numerical values of M and Remanence (μ) for the sample α -Fe ₂ O ₃ @CNT at room temperature to depict the magnetization retention. Both the values are quoted for three different magnetic fields.	110

List of Abbreviations

TMOs	Transition Metal Oxides
CNT	Carbon Nanotubes
AFM	Antiferromagnet
CVD	Chemical Vapor Deposition
MFH	Magnetic Fluid Hyperthermia
SEM	Scanning Electron Microscope
FESEM	Field Emission Scanning Electron Microscope
TEM	Transmission Electron Microscope
XRD	X-Ray Diffraction
ICDD	International Center for Diffraction Data
TGA	Thermal Gravimetric Analysis
SQUID	Superconducting Quantum Interface Device
CV	Cyclic Voltammetry
EIS	Electrochemical Impedance Spectroscopy
Fe@CNT	Iron-filled Carbon Nanotubes
Ni@CNT	Nickel-filled Carbon Nanotubes
Co@CNT	Cobalt-filled Carbon Nanotubes
Oxides@CNT	Oxides-filled Carbon Nanotubes
DMI	Dzyaloshinskii-Moriya Interaction
WFM	Weak Ferromagnet
LRO	Long Range Order
ZFC	Zero Field Cooled
FC	Field Cooled
FM	Ferromagnet
LIB	Li-Ion Batteries

Abstract

Transition Metal Oxides (TMOs) are well-known to host a diverse range of exotic electronic and magnetic ground states. Carbon Nanotubes (CNT), on the other hand, possess exceptional electrical, thermal and mechanical properties. This thesis presents a novel approach of encapsulating and preserving functional TMOs inside CNT, thereby, bringing into fore new possibilities in the arenas of nanoscience and nanotechnology, and providing an opportunity for direct patterning of nano-electronic devices. With special focus on TMOs relevant to antiferromagnet (AFM) spintronics, we have explored the fundamental as well as application based aspects of TMOs encapsulated inside CNT.

The transition metals and oxides, when confined and protected within CNT, can provide huge tunability in their functional properties as well as give rise to new emergent phenomena at the interface. In this context, we find that although Fe@CNT have been extensively investigated, encapsulation of other transition metals like Ni or Co, and their respective oxides, is rarely explored. Even though magnetic oxides exhibit a remarkably wide range of properties, oxide-based electronics applications are still scarce.

In the first part of the thesis, we demonstrate the use of a *single-zone* furnace with a modified synthesis chamber design to obtain metal (Fe, Ni) as well as their respective oxides-filled carbon nanotubes with high filling efficiency and controlled morphology. We employ pyrolysis of metallocene, a technique which is well-known to successfully yield Fe-filled CNT, but does not result in well-formed Ni or Co-filled CNT. This is achieved by innovative use of a green compound *camphor* as a co-precursor with metallocene. Here the key result is an order of magnitude enhancement in the filling efficiency and controlled morphology in case of Ni@CNT.

For AFM spintronics, our attention has been on the encapsulation of a multi-functional oxide, α -Fe₂O₃ (hematite), inside CNT. Bulk α -Fe₂O₃ is a well-known

Dzyaloshinskii-Moriya Interaction driven canted AFM and a piezomagnet. Previous studies have shown that these canted systems exhibit an unusually slow magnetization relaxation phenomenon, which leads to the observation of a *time-stable* remanence. The magnitude of this unique remanence scales up with the extent of spin canting, and bears an inverse correlation with the Néel temperature. Bulk α -Fe₂O₃ is a room temperature canted AFM which can be advantageous for technological applications. However, the extent of spin canting in α -Fe₂O₃ is small, owing to its high Néel temperature ~ 950 K, which limits its use in various applications. Through rigorous magnetization and remanence measurements using SQUID magnetometry, we show that the encapsulation of α -Fe₂O₃ inside CNT leads to a significant enhancement in the magnitude of this *time-stable* remanence, and therefore, in the extent of spin canting. More importantly, these effects exist at the room temperature which can have profound technological implications. Further still, the encapsulation of α -Fe₂O₃ gives rise to novel *interface* effects, which are evident from the temperature variation of lattice parameters derived using Synchrotron X-ray diffraction. Investigation of these oxide/CNT hybrids through temperature variation of Raman Spectroscopy further confirms the presence of novel *interface* effects in these systems.

For energy related applications, different TMOs@CNT (including α -Fe₂O₃, Fe₃O₄, NiO, and Co₃O₄) in various morphologies are scaled up, and tested as an anode material in Li-ion batteries for cyclic stability and electrochemical performance. Here the key result is that encapsulation inside CNT results in superior cyclic stability, irrespective of the type of the oxide-encapsulate. The oxides filled CNT maintain outstanding cyclic stability and high-reversible capacity, even at higher current densities. In addition, the electrochemical studies of various oxides-filled CNT also shed light on the role of the morphology well as filling efficiency of oxide@CNT. The facile environment-friendly synthesis approach and unique nano-structure design of oxide/CNT hybrids presented in this work can serve as potential materials for high-performance Li-ion batteries.

This thesis comprises of seven chapters, which are organized as follows.

Chapter *one* is divided into three sections. In the first section, the evolution of carbon nanotubes along with a brief overview on its structure, electronic, mechanical and thermal properties is discussed. This is followed by a discussion about the various synthesis techniques, emphasizing on the chemical vapor deposition, which is routinely employed to obtain the pristine and the filled CNT. The major chal-

Challenges faced in encapsulating 3d transition metals, especially Ni and Co within the core cavity of the CNT are also discussed. In the second section, the phenomena of magnetism and exchange interactions is briefly discussed. The concepts of *weak ferromagnetism* and *remanence* are outlined. In the last section, we discuss the motivation to fill functional magnetic oxides inside CNT. The prime objective to encapsulate Dzyaloshinskii-Moriya Interaction driven canted AFM α -Fe₂O₃ is presented. Further to this, the importance of Raman spectroscopy to explore the Oxide/CNT interface is highlighted. In addition, the motivation behind the usage of TMOs@CNT as potential anode materials is introduced.

Chapter *two* discusses the details of various experimental techniques used to investigate the sample studied in this thesis. This includes the structural characterization by Scanning and Transmission Electron Microscopy, X-ray diffraction using lab and synchrotron sources. This is followed by a brief introduction to Rietveld Profile Refinement technique, which is used to refine lattice parameters using temperature variation of synchrotron X ray diffraction in case of α -Fe₂O₃@CNT. The metal and oxide filled CNT are also extensively characterized using SQUID magnetometry and Raman spectroscopy, and both these techniques are discussed. The equipment used for electrochemical characterization of oxide@CNT are also discussed in this chapter.

In chapter *three*, synthesis details for encapsulation of transition metals (iron and nickel), as well as their respective oxides are presented. The mechanical assembly arrangement used in *single-zone* furnace, along with synthesis chamber, sample insertion arrangements, and the role of individual synthesis parameters are shown in the first part of this chapter. The synthesis conditions and their optimization for Fe-filled and Ni-filled CNT are then discussed individually. For both the samples, a systematic variation of synthesis parameters and its effect on the morphology of the final product is presented. In the last section, experimental protocol for the conversion of metal@CNT into oxide@CNT is discussed.

Chapter *four* presents the magnetization and remanence studies for α -Fe₂O₃@CNT, which is a DMI driven weak ferromagnet. A key result here is that α -Fe₂O₃@CNT sample exhibits a significant enhancement in the magnitude of magnetization, as compared to bare α -Fe₂O₃ formed in the same morphology. Previous studies have shown that such symmetry allowed weak ferromagnets exhibit the phenomenon of *time-stable* remanence. We show that encapsulation of α -Fe₂O₃ inside CNT leads to substantial enhancements in magnitude of this *time-stable* remanence. The results

elucidate that encapsulation of $\alpha\text{-Fe}_2\text{O}_3$ @CNT inside CNT is an efficient way to manipulate the spin canting and the associated weak ferromagnetism. To gain insights into the underlying reasons for enhancement in magnetization and *time-stable* remanence, temperature dependent synchrotron diffraction studies were performed. The temperature variation of the lattice parameters of CNT exhibits a clear anomaly in the vicinity of the magnetic transition of the encapsulate, suggesting the presence of novel *interface* effects. In the last section, magnetization and remanence studies are also performed on a hybrid FeO_x @CNT. Here the encapsulate FeO_x contains $\alpha\text{-Fe}_2\text{O}_3$ as well as ferromagnetic Fe_3O_4 .

The *interface* effects in oxide/CNT hybrid are further probed using temperature-dependent Raman spectroscopy on a representative sample of FeO_x @CNT. The temperature variation of phonon modes corresponding to the CNT as well as $\alpha\text{-Fe}_2\text{O}_3$ reveal significantly large Raman shifts $\sim 15\text{ cm}^{-1}$. Raman modes also exhibit anomalies near the Morin transition temperature, which is intrinsic to the magnetic encapsulate. More importantly, these anomalies occur in the vicinity of Morin transition are also observed in Raman modes corresponding to CNT, confirming the novel *interface* effects.

Chapter *six* is devoted to the testing of TMOs@CNT for battery applications. The electrochemical performance of various oxides – $\alpha\text{-Fe}_2\text{O}_3$, Fe_3O_4 , NiO, Co_3O_4 encapsulated inside CNT for anode materials in Li-ion batteries is presented. In addition, a comparative study of different morphologies of CNT is discussed for $\alpha\text{-Fe}_2\text{O}_3$ @CNT, which brings out the role of morphology in the overall electrochemical performance. The oxides@CNT also deliver significant improvement in cyclic stability in comparison with bare oxide. The improved electrochemical performance is attributed to the unique oxide/CNT hybrids, which is rendered as potential anode materials for future lithium-ion batteries.

Chapter *seven* provides a summary of the results presented in this thesis and the conclusions drawn from the results, and a future plan is proposed at the end this chapter.

List of Publications

1. *3d transition metals and oxides within carbon nanotubes by co-pyrolysis of metallocene & camphor: High filling efficiency and self-organized structures*; **Aakanksha Kapoor**, Nitesh Singh, Arka Bikash Dey, A.K. Nigam, and Ashna Bajpai; Carbon, Volume 132, 2018, 733-745.
2. *Enhanced magnetism and time-stable remanence at the interface of hematite and carbon nanotubes*; **Aakanksha Kapoor**, Arka Bikash Dey, Charu Garg, and Ashna Bajpai; Nanotechnology, Volume 30, 2019, 385706.
3. *Applications of Oxides@CNT for Lithium-ion Battery Anodes : An Environment-friendly Approach*; **Aakanksha Kapoor**, Apurva L.Patrike, Nitesh Singh, Rudiger Klingeler, Satishchandra Ogale, and Ashna Bajpai; to be submitted.
4. *Exploring Interface-effects in Fe₂O₃@CNT using Raman Spectroscopy*; **Aakanksha Kapoor**, Vikram Bakaraju, G.V. Pavan Kumar, and Ashna Bajpai; to be submitted.

Chapter 1

Introduction

This thesis is primarily based on filling of magnetic materials inside the carbon nanotubes. The encapsulate includes ferromagnetic metals as well as antiferromagnetic insulators based on the 3d transition metal ions. In this chapter, carbon nanotubes and their physical properties are discussed followed by a brief discussion on the basics of magnetism and the underlying interactions. A special emphasis is placed on the phenomenon of weak ferromagnetism and Dzyaloshinskii-Moriya interaction (DMI) driven spin canting mechanism. In the last section of this chapter, the motivation to fill functional magnetic materials inside Carbon Nanotubes along with the outline of this thesis is discussed.

1.1 A Brief History of Carbon Nanotubes

The birth of Carbon Nanotubes (CNT) can be traced back to 1886 when the first scientific report of synthesizing carbon filaments using thermal decomposition of hydrocarbons was reported in a patent filed by T.V. Hughes and C.R. Chambers. [1] In 1950s, studies showed that carbon filaments can be produced by decomposition of hydrocarbons in the atmosphere of transition metals such as iron, cobalt, and nickel. However, these reports could not establish the presence of CNT due to the resolution limitations of the available microscopic tools.

In 1952, first electron micrographs of carbon filaments with 50 nm diameter were reported by L.V. Radushkevich and V.M. Lukyanovich in the Soviet *Journal of Physical Chemistry*. [2] In 1970s, the research into the catalytic formation of carbon fibers flourished with a concrete objective to study the growth mechanisms. The pioneer-

ing study by A. Oberlin, M. Endo, and T. Koyama in 1976 reported the growth of nano-meter scale carbon fibers, which was later termed as single-wall carbon nanotubes. [3, 4]

In 1985, while attempting an investigation in formation of long chained carbon molecules in interstellar space, Harold W. Kroto and Richard Smalley discovered a new allotrope of carbon by vaporizing graphite via laser ablation. [5] The mass spectra studies revealed the presence of interesting stable clusters with a truncated icosahedron structure consisting of sixty carbon atoms. [5] It was named Buckminsterfullerene or C_{60} , a zero-dimensional allotrope of carbon. [5]

After years of Kroto's discovery, in 1991, Sumio Iijima observed long hollow fibers in the soot generated on the graphite cathode while studying various carbon materials using Krätschmer–Huffman method. [6, 7] The carbon nanotubes detected consisted of more than one layer of graphene with inner diameters ~ 4 nm. In 1993, single-wall CNT were discovered by two independent groups led by Donald Bethune and Sumio Iijima. [8] Fine single-wall nanotubes were formed when the electrodes in the arc-evaporation chamber were impregnated with transition metals like iron, cobalt or nickel.

The unique structure of single-wall CNT can be conceptualized by rolling up of a graphene layer in the form of a cylinder. [9] Multi-wall CNT can be described as stack of single-wall CNTs forming a concentric geometry. [6] In the present time, almost after three decades of proclamation of CNT on the scientific stage, it continues to attract considerable attention in the area of nanoscience. CNT have become a subject of worldwide research focus and rendered as promising building blocks for future nanoscience and nanotechnology.

1.2 Structure of Carbon Nanotubes

The element carbon consists of several allotropes in different dimensions – fullerene (0-D), carbon nanotube (1-D), graphene (2-D), graphite and diamond (3-D). The carbon atoms in diamond consists of sp^3 -hybridized orbitals, and the three dimensional network, thus formed, possess extreme rigidity which is responsible for its hardness. CNT consists of sp^2 -hybridized orbitals with each atom connected evenly to other three carbons (120°) in the xy plane. In addition, a weak π bond is present along the z axis.

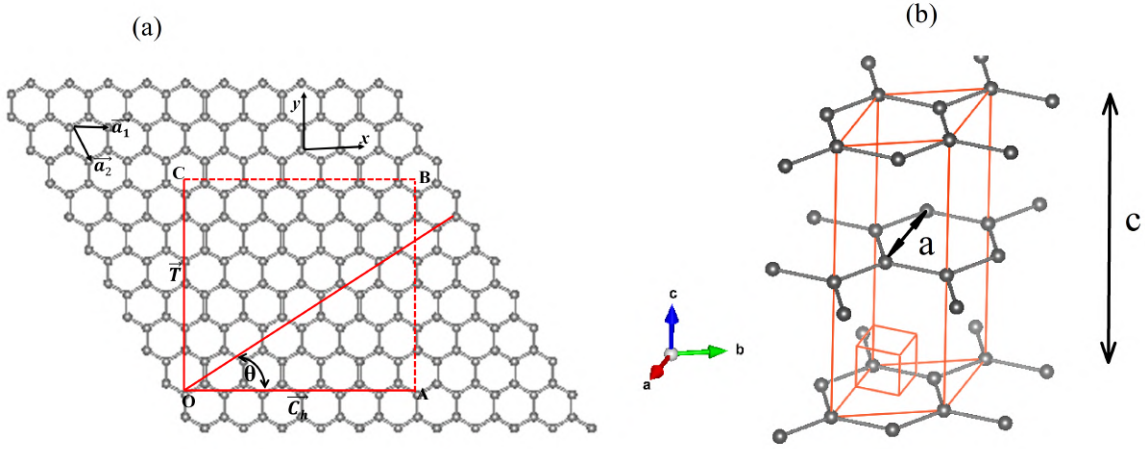


Figure 1.1: (a) Schematic of a graphene sheet to define the unit cell of single-wall CNT. (b) Crystal structure of graphite depicting its unit cell (in red). The figure is adapted from [11].

Carbon Nanotubes can be broadly classified into two types – Single-wall CNT and Multi-wall CNT. The structure of single-wall CNT can be envisioned as a rolled-up graphene sheet consisting of hexagonal rings of carbon atoms. Typical diameter of single-wall CNT is $\sim 0.4 - 1$ nm and is one-atom thick. Multi-wall CNT is stack of graphene sheets rolled in the form of a cylinder and the outer diameter can vary up to ~ 100 nm. [10] The interlayer distance is ~ 0.34 nm.

Graphene is the simplest structure of all the allotropes of carbon. It consists of a honeycomb lattice made up of single layer of atoms. The structure and properties of CNT can be better visualized by considering the theory of graphene with modulations to consider the special features of curved surface of CNT. It is easy to focus on the structural properties of CNT using graphene as a base model and extending the concept to CNT. Thus, the case of a single-wall CNT can be considered as rolling of a graphene sheet in the form of cylinder. This results in an one dimensional tube exhibiting axial symmetry. [11] The structure of single-wall CNT can be represented with different vectors. Figure 1.1 (a-b) shows a 2-D graphene sheet depicting the relevant parameters, and the unit cell of graphite, respectively. [11]

A single-wall CNT can be formed by rolling up a graphene sheet around a vector denoted by \vec{OC} in the schematic shown in Figure 1.1(a). The circumference of the CNT is defined by vector \vec{OA} , and \vec{T} is the translational vector which is the long axis

of the CNT. \vec{OA} is known as the chiral vector \vec{C}_h of the CNT. The Bravais lattice vectors \vec{a}_1 and \vec{a}_2 define the chiral vector \vec{C}_h as: [11]

$$\vec{C}_h = n\vec{a}_1 + m\vec{a}_2, \quad (1.1)$$

where, n and m are integers. [11]

\vec{T} is a vector parallel to the axis of the CNT, and the chiral angle θ is the angle between \vec{a}_1 and \vec{C}_h . Different nanotube structures are formed depending on the values of n and m. [11] Each pair of n and m defines a particular way of rolling up of the graphene sheet to configure CNT with certain chirality. The limiting cases can be defined as: [11]

- Zigzag tubes : $n \neq 0, m = 0, \theta = 0$.
- Armchair tubes : $n = m \neq 0, \theta = \pi/6$.

The diameter d_t and chiral angle θ of the tube, for a particular value of n and m are presented by equation 1.2 and 1.3.

$$d_t = |C_h/\pi, |C_h = a\sqrt{m^2 + n^2 + mn}. \quad (1.2)$$

$$\theta = \arctan\left(\frac{-\sqrt{3}}{2n + m}\right). \quad (1.3)$$

where, $a = 2.46 \text{ \AA}$ is the lattice constant of 2-D graphene.

1.3 Properties of Carbon Nanotubes

1.3.1 Electronic Properties

The electronic properties of CNT are intimately related to that of graphene. As a result of the 2-D structure with sp^2 -hybridized orbitals of the carbon atoms, a sheet of graphene is a zero band-gap semiconductor. [11] The valence and the conduction bands are degenerate at six K points, which define the corners of the first Brillouin zone. [11]

The electronic properties of carbon nanotubes are strongly influenced by the sp^2 -hybridized orbitals of carbon atoms. In addition, the geometric structure of the CNT,

especially the diameter and chirality, shows a significant influence on the electronic properties of the CNT. The band gap of the CNT depends on the diameter and the chirality of the CNT. [11] The high aspect-ratio of CNT imparts electrical conductivity at lower weight ratios compared to traditional additive materials such as carbon black, carbon fiber, etc. This acts as a great advantage in integrating nano-electronic devices.

Many properties of the CNT are similar to that of graphene. Modulations to the properties arise due to the fact that only preferred k-states are allowed. The nanotubes can behave electrically either as a semiconductor or metal depending on the direction of the axis and the unit vectors describing the graphene 1-D lattice. If the allowed sub-bands pass through the K-points, CNT will be metallic, and will be otherwise semiconducting. For semiconducting nanotubes, the band gap bears an inverse correlation with diameter. [11] In case of multi-wall CNT, the conductivity mechanism is rather complex, and the inter-wall interactions also play an important role apart from the diameter and chirality of CNT. Nevertheless, multi-wall CNT have known to exhibit exceptional electronic properties and a number of devices based on multi-wall CNT have been extensively studied. [11]

Metallic carbon nanotubes have known to possess electric current densities of $\sim 10^9$ A cm⁻², which is about 1000 times higher than that of copper. [11] They exhibit remarkable electrical conductivity which have been theoretically and experimentally investigated. [12] For example, the metallic CNT can be efficiently used as interconnects in integrated circuits. [13–18] Further, the electronic properties can be tuned by addition of functionalized materials. For instance, it is reported that encapsulating an insulator within the core cavity of the CNT increases the current carrying capacity of the CNT, and can find applications as heat sink in nano-electronic devices. [19] CNT are potential candidates for designing nano-electronic devices. There are various arenas of technology where CNT have been employed, such as, panel displays, scanning probe microscopes, sensing devices, energy science, and other areas of technology. [13–18]

1.3.2 Mechanical Properties

The carbon atoms in a sheet of graphene form a planar honeycomb lattice. [11] Each atom in the honeycomb lattice is connected via a strong sp² bond to the neighboring carbon atoms. The elastic modulus of graphite is the largest due to the

presence of these strong sp^2 bonds. CNT are the strongest known nano-materials in terms of elastic modulus and tensile strength. [20]

There are three major forces due to which CNT inherent exceptional mechanical properties. The primary forces involved in CNT are the strong in-plane σ bonds. Owing to their remarkable flexibility, they can be bent around sharp edges without any breakage. The Young's modulus ~ 1.8 TPa has been reported for single-wall CNT. [20,21] In case of multi-wall CNT, a weak inter-layer interaction exists between adjacent layers which reduces their effective strength to a few GPa. [20,21] They are regarded as materials with exceptional mechanical strength. CNT possess fascinating elastic properties, and can withstand non-linear deformations.

1.3.3 Thermal Properties

CNT are known to be exceptionally good thermal conductors along the tube axis and good insulators lateral to the axis of the tube. [22,23] CNT possess almost zero in-plane thermal expansion due to strong in-plane C-C bonds and large inter-plane expansion. This implies the presence of a strong in-plane coupling, and high adaptability against strains in the non-axial directions. The thermal conductivity of CNT depends on a number of factors such as the number of graphitic shells, its diameter, length and defects. [22,23] Measurements have shown that an individual single-wall CNT possess thermal conductivity of $3500 \text{ W m}^{-1} \text{ K}^{-1}$ at room temperature along its axis. This is significantly large as compared to a well-known thermal conductor, copper, which transmits $385 \text{ W m}^{-1} \text{ K}^{-1}$. [22,23] A variety of applications exploiting the exceptional thermal properties such as nanoscale electronics, sensing devices, etc., have been studied in detail. [16,23] There also have been reports on CNT-polymer composites suggesting enhancement thermal conductivities of CNT-embedded matrix in comparison to the bare polymer matrix. [24,25] The CNT reinforcements in polymer materials have significantly improved the thermal properties of the hybrid composites. [24,25]

1.4 Synthesis of Carbon Nanotubes

High-temperature techniques such as arc discharge or laser ablation were first used to synthesize CNT. These techniques have now been replaced by a more conve-

nient technique – Chemical Vapor Deposition (CVD). [10] The growth parameters of CNT – nanotubes length, diameter, density, alignment, etc. can be better controlled with CVD method. [26–28] In the work presented in this thesis, we have extensively used the CVD approach to synthesize multi-wall CNT filled with magnetic materials. Following a brief overview of arc discharge and laser ablation, a detailed approach of CVD method is discussed below.

1.4.1 Arc Discharge

The arc-vaporization of carbon rods was originally employed to synthesize CNT. The carbon rods are situated end-to-end in an inert gas filled chamber maintained at low pressure. The discharge evaporates from the surface of one of the carbon electrodes which creates rod-shaped deposit on the opposing electrode. The production of CNT in high yield using this method depends on the synthesis conditions such as uniformness of the plasma arc and the temperature maintained at the deposit. [29,30]

Earlier, arc discharge method had been utilized to form C_{60} fullerenes. It was one of the most general and convenient way to obtain CNT owing to its simple procedure. However, this technique yields a complex mixture of different components. Additionally, purification is required to isolate CNT from the soot and the residual catalyst particles. This method produces both single-wall and multi-wall CNT with few structural defects and lengths up to $50\ \mu\text{m}$. [29,30] This method also uses higher temperatures (above $1700\ ^\circ\text{C}$) for synthesis of CNT which results in fewer structural defects, in comparison to the other synthesis techniques.

1.4.2 Laser Ablation

In 1996, CNT were first synthesized in with the help of a dual-pulsed laser. This yielded CNT of more than 70% in weight purity. [31,32] In this method, a pulse laser vaporizes the graphite target in a high-temperature reactor. This is done in the presence of an inert gas which is fed into the chamber. The CNT, thus formed, deposit on the cooler surfaces of the reactor.

Due to the utilization of two consecutive laser pulses, the amount of soot carbon is significantly reduced. The bigger particles ablated by the initial laser pulse are removed by the second laser pulse. The CNT synthesized by this process is a mat of "ropes," $\sim 100\ \mu\text{m}$ in length and up to 10 to 20 nm in diameter. Each rope consists

of a bundle of single-wall CNT. The quality and properties of CNT prepared by this method are dependent on the synthesis conditions – laser power, chamber pressure, the distance between the target and the substrates. [31,32]

1.4.3 Chemical Vapor Deposition

Arc-discharge and laser ablation were the primary methods for obtaining tiny quantities of high quality CNT. However, these two methods have major limitations. The CNT grown by these methods consists of twisted forms of carbon along with undesirable carbon soot and metal particles, which requires further purification. These are the major bottlenecks for developing CNT-based device architecture for practical implications. Laser ablation produces high-quality CNT, but the use of lasers make it an expensive technique.

The most popular and convenient choice to synthesize different types of CNT ranging from single-wall to multi-wall to filled CNT is Chemical Vapor Deposition. This method is widely employed to obtain well-formed CNT in large quantities, and allows one to synthesize CNT with defined diameter, length, and filling fraction to a reasonable extent. [10, 26–28] The methods to obtain filled and empty CNT are similar. Both the processes require a hydrocarbon precursor for the formation of the CNT walls, and a catalyst, usually metallic nano-particles. The catalyst can either be on a suitable substrate, or be used in gaseous form. Organometallic compounds are routinely used as a precursor for the catalytic synthesis of filled CNT, whereas for empty CNT an additional hydrocarbon in the form of liquid or gas is used. [10, 28]

The organometallic family of metallocenes is the most suitable precursor used to obtain CNT with filling of metals its core cavity. [10, 33, 34] Metallocenes with formula $M(C_5H_5)_2$, where M can be iron, cobalt or nickel, accommodates both the carbon atoms and the metallic catalyst particles to facilitate the growth of the CNT. The family of metallocenes consists of metal atom in the centre with the two cyclopentadiene rings forming a sandwich-like structure. [35] The relatively low sublimation temperature (150 - 300 °C) and suitable thermal decomposition temperature (600 - 900 °C) make metallocenes the most popular choice as a precursor. [36] The use of metallocene as a precursor for the formation of CNT is an *in-situ* process which allows the formation and filling of the CNT to be a simultaneous process.

The two widely employed synthesis procedures for utilizing metallocenes to form CNT are – *Solid State CVD* and *Aerosol Assisted CVD*. In *Solid State CVD*, the

metallocene precursor is used in powder form. In *Aerosol Assisted CVD*, the precursor is in the form of solution, consisting of metallocene and a suitable solvent such as benzene, heptane, acetylene, etc.

1.4.3.1 *Aerosol Assisted CVD*

Aerosol Assisted CVD employ liquid precursors for the synthesis of CNT. This method is widely used to obtain pristine CNT without any filling. [37–45] Here the liquid precursor acts as a source of carbon or a solvent for organometallic compounds. For synthesis of CNT, the commonly used liquid precursors are hydrocarbon, for example, benzene, acetonitrile, heptane, etc. The organometallic compounds (metallocene in this case) are dissolved in the liquid solvent and are then used as precursors.

In case of *Aerosol Assisted CVD*, the liquid precursor consisting of hydrocarbon and metallocene are introduced into the reactor zone simultaneously. Due to the presence of excessive amount of carbon source in gaseous phase, hollow empty carbon nanotubes are obtained. In this case, filled CNT with encapsulation in the form of long nano-wires are not obtained. *Aerosol Assisted CVD* is primarily employed for the catalytic growth of the pristine CNT and can be achieved by using any of the three metallocenes. [37, 39–41, 44]

1.4.3.2 *Solid State CVD*

In *Solid State CVD*, a two-zone horizontal furnace is typically used for the synthesis of CNT. Figure 1.2 shows a typical setup for *Solid State CVD*. The furnace consists of two temperature zones. In the first temperature zone known as the *sublimation zone* (marked as 'A' at temperature T_{sub} in Figure 1.2). The precursor is positioned in a quartz boat. The sublimed plumes are then transferred into the second temperature zone known as *pyrolysis zone* (marked 'B') set at a relatively higher temperature T_{pyro} , via a controlled transport gas which can be argon, nitrogen or hydrogen. The deposition of the CNT takes place in region 'B' at temperature T_{pyro} .

The deposition of the CNT takes place on the inner wall of the quartz reactor as well as suitable substrates placed in the pyrolysis zone of the reactor. Commonly used substrates are thin oxide layer coated silicon wafers with an additional layer of metal (iron, cobalt or nickel). The thin metal layer acts as a secondary catalyst to improve the filling efficiency and obtain aligned morphology. *Solid-State CVD* method is employed to obtain filled with high filling efficiency. [10, 33, 34, 46–49] The metal catalyst

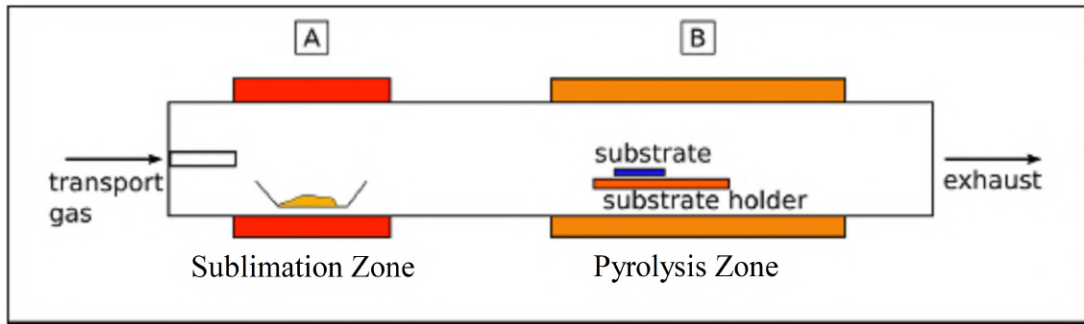


Figure 1.2: *Schematic of Solid State CVD method. The precursor is sublimated in the solid form placed in the pre-heated zone A at temperature. [10]*

particles, which aid in facilitating the growth of CNT, are trapped within its core cavity and also adhere outside the CNT. Due to the inherent ferromagnetic nature of these catalyst particles, the CNT, thus formed, exhibit ferromagnetic hysteresis in bulk magnetization measurements. [50] The saturation magnetization (M_S) acts as a yardstick to assess such magnetic contributions.

Solid State CVD using sublimation of metallocene in powder form is the best suited method for formation of CNT along with deliberate and efficient filling of ferromagnetic metal within its core cavity [10, 46, 47] In this case the metal particles not only facilitate the growth of CNT growth, but also assembles in the form of long nano-wires well within the core of the CNT, giving rise to significantly higher filling factor and consequently substantially larger M_S . For instance, $M_S \sim 20 - 60$ emu/g has been reported in the case of Fe@CNT. [48, 51] It is also noteworthy that using *Solid State CVD*, iron-filled CNT with significant filling efficiency are easily formed. [10, 46, 47, 51] There have been reports in which the filling efficiency (and consequently M_S) has been tuned by variations in synthesis parameters. [46–48]

1.4.3.3 Synthesis of Filled Carbon Nanotubes : Challenges

Hitherto, the most popular magnetic encapsulate has been iron, which is a ferromagnetic (FM) metal in bulk. When encapsulated within the CNT, the iron-filled CNT hybrids find applications in various areas such as medical science, energy sector and nano-electronic devices. [52–56] One important parameter deciding the utility of these hybrid materials in various applications is the filling fraction of the mag-

netic encapsulate inside the CNT. Although there are various reports on iron-filled CNT, achieving high filling fraction of the encapsulate within the core cavity of the CNT still remains a big challenge. [52–56] In addition, we find that most reports are on iron-filled CNT, whereas, encapsulation of other 3d transition metals – cobalt and nickel and their respective oxides, with significant filling efficiency are rarely explored. [10, 33, 34, 46–48] Even though the sublimation temperature of the metallocenes – cobaltocene and nickelocene are in close vicinity, there are no reports on synthesis of cobalt or nickel-filled CNT employing powder metallocene.

There have been reports using nickel-filled and cobalt-filled CNT using *Aerosol Assisted CVD* where the metallocene is used primarily for the providing the catalyst particles. [38, 45, 57] The fraction of the residual catalyst particles is typically small in *Aerosol Assisted CVD*. In case of iron-filled CNT, observed $M_S \sim 2 - 10$ emu/g, whereas $M_S \sim 0.1 - 0.8$ emu/g in case of cobalt or nickel filled CNT. [46–48] There are also reports of nickel and cobalt filled by using nanoparticles grown on suitable substrates, however, the filling efficiency is not on par with iron-filled CNT. [38, 45, 57]

Thus, following the CVD of metallocenes (nickelocene and cobaltocene) using *Solid State CVD* to obtain good quality filled-CNT, the major challenges involved are: [58]

- (i) Magnetic nano-material protected well within the core cavity of the CNT.
- (ii) Minimum residue particles outside the CNT.
- (iii) Narrow length / diameter distribution of filled CNT.
- (iv) Reproducibility and cost-effectiveness of the synthesis procedure.

To overcome the above-mentioned challenges, we have used an innovative and environment friendly approach to synthesize nickel- and cobalt-filled CNT by employing the use of camphor as a co-precursor with respective metallocenes. [58] This approach enabled us to obtain CNT filled with 3d transition metals – nickel and cobalt, and consequently, their respective oxides with significant filling efficiency, control over morphology, and fairly identical filled CNT in terms of its length and diameter. [58] The results have been presented in chapter *three*.

1.5 Raman Spectroscopy of Carbon Nanotubes

Raman spectroscopy is a powerful tool to characterize CNT as well as transition metal oxides. [59, 60] A typical Raman spectra of multi-wall CNT consist of three

prominent bands. Figure 1.3 shows the Raman spectra of multi-wall CNT in the region $1200 - 3000 \text{ cm}^{-1}$ recorded at room temperature. A strong band at 1575 cm^{-1} is the most dominant band in CNT, and is referred as G-band. The G-band is due to the degenerate phonon mode with E_{2g} symmetry. This band is characteristic feature of graphitic layers corresponding to tangential or in-plane vibration of carbon atoms. [59, 60]

The graphitic shells of the CNT, due to finite size, edges, stacking of layers, etc. induces disorder in the graphitic shells. The band around 1340 cm^{-1} , known as the D-band, is assigned to the presence of disorder in the graphitic materials. [60] A band present around 2690 cm^{-1} is an overtone or second harmonic of the D-mode. This band is referred to as G' or 2D band. This band belongs to A_{1g} symmetry and involves in-plane vibrational motion of carbon atoms towards and away from the centre of the hexagon ring. [60] This band is indicative of long-range order in the sample, and reflects the interlayer interactions between the graphitic layers. [59, 60]

The ratio of the peak intensities of the D- and G- bands, I_D/I_G , is used as an indicator to determine the level of disorder and the quality of the graphitic shells. A lower value of I_D/I_G signifies the good quality of the graphitic shells and less number of defects present in the sample.

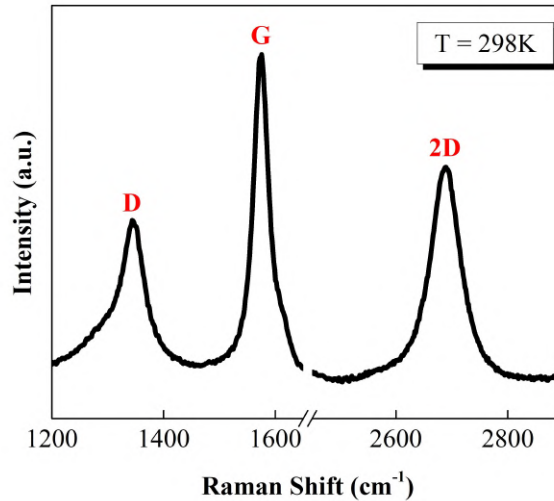


Figure 1.3: (a) Raman spectrum for typical multi-wall CNT in the range $1200-3000 \text{ cm}^{-1}$ recorded at room temperature. The Spectra shows the typical bands pertaining to CNT in the hybrid.

Since Raman spectroscopy is an effective tool to study the sensitive changes in the CNT based systems, we have performed temperature-dependent Raman spectroscopy of a magnetic oxide (α -Fe₂O₃) filled inside CNT. The motive of this measurement to gain insights about the interactions occurring at the interface of the magnetic oxide and the graphitic shells of the CNT. This is discussed further in detail in the following sections.

1.6 Magnetism and Exchange Interactions

The magnetic behaviour of materials can be primarily categorized as – diamagnetism, paramagnetism, ferromagnetism, antiferromagnetism. [61] The work presented in this thesis lays its foundations on ferromagnetic 3d transition metals and antiferromagnetic transition metal oxides. The magnetic behaviour of these materials can be understood by considering the interactions which either give rise to either ferromagnetic or antiferromagnetic state in a material. In order to study these interaction, certain effects which are quantum mechanical in nature have to taken into account. The inter-site correlations of the magnetic moments are determined by *exchange* interactions. [61, 62] The exchange interaction reflects the Coulomb repulsion between two neighbouring electrons in conjunction with the Pauli's exclusion principle which forbids the two electrons to exist in the same quantum state. [61, 62]

Exchange interaction is a quantum-mechanical effect that occurs between identical particles. The exchange interaction results from the competition between kinetic energy (leading to delocalization) and the Coulomb energy of the electrons. [61, 62] Considering the spins of the electrons in any system, no two electrons can be in the same place if they possess same spin in accordance with Pauli's exclusion principle. [62] Hence, the overall wavefunction of the system (spatial and spin) should be antisymmetric. Therefore, for symmetric spatial wavefunction, the spin wavefunction must be antisymmetric singlet state. Whereas, in case of antisymmetric spatial wavefunction, the spin wavefunction must be symmetric triplet state. [61] This leads to splitting of the energies of the symmetric and antisymmetric orbital states.

Hence, according to Heisenberg, the Hamiltonian for many electron systems with spin \vec{S}_i can be written as: [62]

$$H = -2 \sum_{i>j} J_{ij} \vec{S}_i \cdot \vec{S}_j, \quad (1.4)$$

where, J_{ij} is the effective exchange constant between the spins \vec{S}_i and \vec{S}_j . The exchange constant J_{ij} can be positive or negative, and decides the magnetic ordering in any system. This gives rise to two cases.

Case (i) $J > 0$ – Ferromagnetic interaction (parallel orientation).

Case (ii) $J < 0$ – Antiferromagnetic interaction (anti-parallel orientation).

In case of a ferromagnet, the exchange interaction forces the individual spins to align parallel to each other, whereas in case of an antiferromagnet, the spins are aligned in an anti-parallel fashion.

Direct exchange interaction arises between the neighbouring atoms due to a direct overlap of neighbouring magnetic orbitals. This type of interaction exists when the magnetic ions are close enough to allow sufficient overlap of the wavefunctions. Direct exchange is a strong interaction, albeit short ranged, and decreases in strength rapidly when the ions are separated. The exchange integral J_{ij} falls off rapidly with the increase of distance between the two spins, and is generally present in ferromagnetic metals such as iron, cobalt, nickel, etc. [62] In cases where direct overlapping is not sufficient, the direct exchange mechanism cannot explain the long range ferromagnetic or antiferromagnetic ordering.

We shall discuss different types of indirect exchange, including super and double exchange, briefly in the next section.

1.6.1 Indirect Exchange

In alloys and compounds, the ions which carry magnetic ions are separated by other atoms. This allows various types of indirect exchange mechanisms to become effective.

1.6.1.1 Superexchange Interactions

In ionic solids, the magnetic ions are separated by anions which are non-magnetic. In such cases, the direct exchange interaction cannot explain the long-range ordering. Oxides of 3d transition metal are a good example of superexchange interaction. The essential component of superexchange interaction in oxides is that the spin moments of the metal ions must interact with each other through the p-orbital of the oxygen ion. [61]

A classic example of a system involving superexchange interaction is MnO. [62]

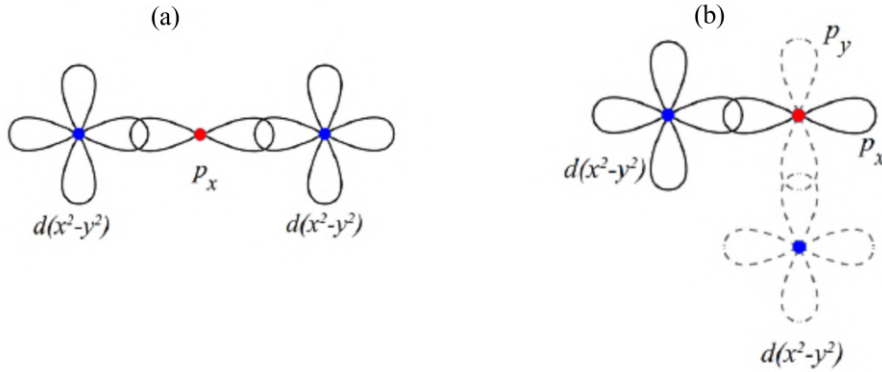


Figure 1.4: *Schematic of (a) weak ferromagnetic and (b) ferromagnetic superexchange paths.* [63]

The exchange interaction in such cases occur through hopping of electrons from one magnetic cation to another via an intermediary anion. The magnetic ground state in such systems is determined by two factors – hopping energy of the same spin electron between different atomic sites, and the Coulomb energy of the opposite spin electrons present at the same site. [61, 62]

A certain set of rules have been detailed after extensive calculations which determine the strength and the sign of the superexchange. These rules determine whether the superexchange interaction will lead to an anti-ferromagnetic or ferromagnetic state. These are known as Goodenough-Kanamori rules. [62] The rules can be stated as follows. [62]

1. A strong antiferromagnetic exchange interaction exists when the angle between M-O-M orbital is close to 180° as depicted in Figure 1.4(a).
2. A weak ferromagnetic exchange interaction exists when the angle between M-O-M orbital is close to 90° as shown in Figure 1.4(b)

On a general note, superexchange interaction is usually antiferromagnetic than ferromagnetic. A few examples with superexchange interaction are α - Fe_2O_3 , MnO_2 , CuO , etc.

1.6.1.2 Double Exchange Interaction

This kind of interaction arises between the 3d ions possessing both localized and delocalized electrons. When the magnetic cations possess mixed valence configura-

tion, double exchange interaction comes into play. In order to explain ferromagnetism in systems consisting of ions with two different ionic states, the idea of a double exchange interaction was introduced.

Double exchange interaction is encountered in systems consisting of mixed valence compounds. This type of interaction results from a combination of Coulomb and kinetic exchange. In case of a mixed valence system, the number of electrons per site is non-integer. Thus, even for a very large Coulomb energy, some sites will have more electrons than the others. This leads to hopping of electrons between such sites without incurring the cost of Coulomb repulsion.

To gain a better understanding, let us consider the example of Fe_3O_4 . One-third of Fe ions in Fe_3O_4 are tetrahedrally coordinated with four oxygen ions and the remaining two-third of Fe ions are octahedrally coordinated with six oxygen ions. Fe ions in Fe_3O_4 are distinguished into FeA and FeB ions. The FeA ions are Fe^{3+} cations which occupy one-eighth of tetrahedral sites (A sites) in the unit cell, while FeB ions are a 1:1 mixture of Fe^{2+} and Fe^{3+} cations filling half of the octahedral sites (B sites) in the unit cell. [61, 64, 65]

Fe^{3+} ion has five electrons in d-subshell, whose spins are parallel to one another as dictated by Hund's rule. Whereas, Fe^{2+} ion has an additional spin-down electron occupying d-subshell. At B sites, electron transport between Fe^{2+} and Fe^{3+} ions occur via an oxygen ion, which is known as double-exchange interaction. Figure 1.5(a) illustrates the mechanism of double-exchange in Fe_3O_4 . In this interaction, the extra electron at Fe^{2+} site can hop into Fe^{3+} site only if those ion spins are parallel to each other as shown in Figure 1.5(a). This process causes the extra electron to delocalize,

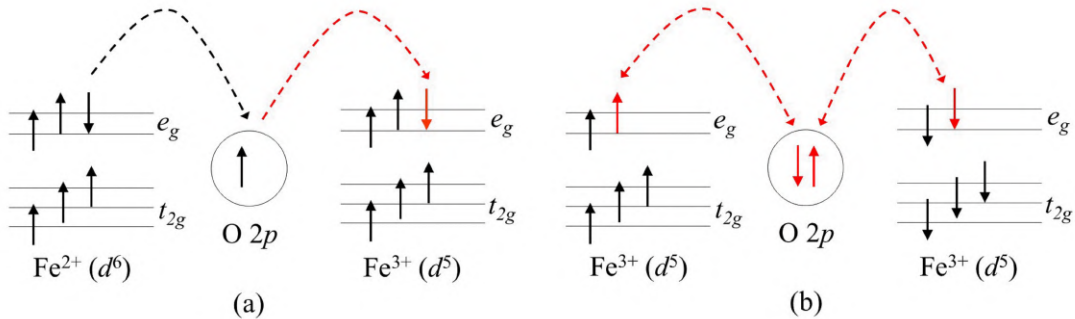


Figure 1.5: Illustration of (a) double-exchange and (b) superexchange interactions in Fe_3O_4 .

hence increases its band width, which then minimizes its kinetic energy. Thus, this interaction tends to couple the ions ferromagnetically. On the other hand, Fe^{3+} ion at B sites can also interact with another Fe^{3+} ion at A sites through oxygen ion with a mechanism called superexchange interaction (Figure 1.5(b)). This interaction causes Fe^{3+} ion spin at A and B sites to be anti-parallel, resulting in antiferromagnetic alignment of their spins. The magnetic interaction among iron ions at octahedral and tetrahedral sites is antiferromagnetic in nature, and that among the octahedral ions is ferromagnetic. Overall, a ferrimagnetic arrangement exists for Fe_3O_4 . [61, 62, 65]

It is noteworthy to mention that Fe_3O_4 , interestingly, is also known to be a half-metal. [61, 65] A half-metal acts as a conductor to electrons of one spin orientation, but as an insulator or semiconductor to those of the opposite orientation. In half-metals, the valence band for one spin orientation is partially filled, whereas for the other spin orientation, there exists an energy gap in the density of the states. [65] Fe_3O_4 , thus, acts as a metal for one spin orientation, and insulator for the other spin orientation. [65] Fe_3O_4 due to its half metallicity and high Curie temperature ($T_C \sim 860$ K) has attracted a lot of attention in spintronic devices. [65] At ~ 120 K (T_V), it undergoes a first metal-insulator transition which is known as the Verwey transition. Upon warming through T_V , Fe_3O_4 lattice changes from a (monoclinic structure) insulator to the metallic (cubic inverse spinel) which persists at room temperature, and is known as half metal ferromagnet. [65] Fe_3O_4 , thus, being a half-metal ferromagnet with high Curie temperature ($T_C \sim 860$ K), has attracted a lot of attention in spintronic devices. [65]

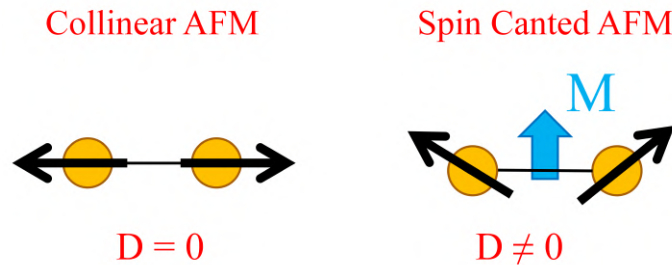


Figure 1.6: *Schematic of a collinear antiferromagnet and a canted antiferromagnet.*

1.7 Weak Ferromagnetism

In some antiferromagnetic crystals, such as α -Fe₂O₃, MnCO₃, spontaneous magnetization is observed. The magnitude of this magnetization is extremely little, and varies between 10^{-2} to 10^{-4} of the nominal value. [66] Various reasons were postulated to explain the presence of net spontaneous magnetization, like, antiferromagnetic domains with magnetized boundaries, presence of ferromagnetic impurity, etc. [67, 68] However, this was possible only when some structural or chemical defects are present in the system and, the non-zero net magnetization did not disappear for pure crystals. Hence, these propositions could not explain the presence of ferromagnetic-like magnetization in certain classes of antiferromagnetic crystals.

In 1957, the phenomenon of 'weak ferromagnetism' was theoretically explained by Dzyaloshinskii. [66] The phenomenon of weak ferromagnetism is associated with the presence of a spontaneous magnetic moment in certain classes of antiferromagnetic crystals. [66] The crystal's symmetry dictates the existence of weak ferromagnetism in selective antiferromagnetic compounds. [66] Dzyaloshinskii explained that weak ferromagnetism exists in uniaxial crystals when the sub-lattice magnetization is perpendicular to the principal symmetry axis of the crystal, and absent in case the sub-lattice magnetization is parallel to the axis. [66]

A net magnetization arises in a few classes of antiferromagnetic compounds when the spins are canted away from the antiferromagnetic axis, as opposed to the case of a collinear antiferromagnet (AFM), when the spins are exactly anti-parallel and the net magnetization is zero. Figure 1.6 shows the schematic of a collinear AFM with spins aligned exactly in anti-parallel fashion resulting in net zero magnetization, and a canted AFM which results in a net magnetization.

Moriya provided the underlying microscopic reason for the phenomenon of weak ferromagnetism and its connection with spin-orbit coupling. [69] He considered the anti-symmetric part of the anisotropic superexchange interaction, and provided detailed calculations to show the existence of weak ferromagnetic moment in AFM with uniaxial crystal structure. [66, 69] This is now well-known as Dzyaloshinskii-Moriya interaction (DMI), and can be represented as: [66, 69]

$$H = \vec{D} \cdot (\vec{S}_i \times \vec{S}_j), \quad (1.5)$$

where, \vec{D} is the Dzyaloshinskii-Moriya vector which is proportional spin-orbit cou-

pling constant. \vec{D} depends on the position of the oxygen ion between the two transition metal ions. This is a higher order effect that occurs between the ions coupled by superexchange. In case of collinear AFM, \vec{D} is zero, resulting in no net magnetization (Figure 1.6). On the other hand, when the spins are canted, \vec{D} is not zero which results in a net ferromagnetic moment as shown in (Figure 1.6). Moriya also showed that in magnetic oxides, the DMI is proportional to the symmetric superexchange 'J', and $\vec{D} \sim \Delta g/g$. [69] Here g is the spectroscopic splitting factor, and Δg is deviation of g from the free electron value. [69] Further Δg is proportional to the orbital momentum 'l' and spin 's' of the electron. [69] A few classic examples exhibiting the phenomenon of weak ferromagnetism include α -Fe₂O₃, FeBO₃, CoCO₃, MnCO₃, etc.

In addition to DMI, there are other possible mechanism responsible for the phenomenon of weak ferromagnetism, which include single-ion anisotropy. NiF₂ belongs to this category, where the origin of weak ferromagnetism is single-ion anisotropy. We shall not delve into details for this mechanism. The work presented in this thesis is based on weak ferromagnetism due to DMI, as we are primarily exploring hematite which is a DMI driven weak ferromagnet. The details are discussed in the following sections.

1.8 The Concept of Remanence

Remanence is the residual magnetization obtained in a ferromagnetic material after removing the external magnetic field. [70] When a ferromagnetic material is exposed to external magnetic field, the magnetic domains orient themselves in the direction of the magnetizing field. When the external magnetic field is removed, the domain walls do not return to their original position, which results in remanent magnetization or remanence. Remanence of magnetic materials is used as magnetic memory in magnetic storage devices. [71] The remanent magnetization or remanence is an important tool engineering applications and spintronic devices. [72]

The magnetization dynamics of complex systems including nanoscale antiferromagnets can be studied using remanence measurements. These measurements allow to unravel the systems and discover subtle magnetic features which are not reflected in routine *in-field* magnetization measurements. [73] These measurements represent the magnetization relaxation dynamics of a system which carries rich information about the magnetic phase associated with the system.

The utilization of magnetic material in a variety of practical applications uses remanence as an important parameter to judge its properties related to permanent magnets, soft or hard. [61, 74] In addition, it is also an important tool for probing fundamental magnetic interactions in conventional long range order (LRO) as well as complex magnetic systems, spin glasses, superparamagnets, nano- and core shell magnets. [73, 75, 76] Remanence measurements carry a wealth of information about the underlying magnetic interaction associated with each of these distinct phases.

In the present thesis, we have extensively explored remanence in the samples α -Fe₂O₃, wherein α -Fe₂O₃ is a well known weak ferromagnet. Filling functional magnets such as α -Fe₂O₃ inside carbon nanotubes can provide new avenues that cover both fundamental and application based aspects, as discussed in the next section.

1.9 Filling of Carbon Nanotubes with Functional Magnetic Materials : The Fundamental Aspect

1.9.1 A General Overview

The unprecedented electrical and mechanical properties due to sp²-hybridized nano-structures render CNT as promising building blocks for future nanoscience and nanotechnology. Their exceptional properties such as small size, high aspect ratio, excellent tensile strength, electronic properties open new avenues of research for CNT applications in nano-electronics, nano-mechanics, and various other applications. [11]

The filling of CNT structures with multi-functional materials opens up new avenues in areas ranging from medical science, energy science, spintronic, etc. [10, 19, 55, 56] The encapsulation of CNT with magnetic materials adds another dimension to exploit the extraordinary properties of CNT. Nanoscale magnetic materials, when encapsulated within the CNT are multi-functional hybrids, important from both fundamental and application points of view. While CNT are well known to possess exceptional electrical, thermal and mechanical properties, [11] the magnetic encapsulate can give rise to a broad diversity in both magnetic and electrical properties, depending on its type, size and morphology. [58, 77, 78] Encapsulation of ferromagnetic materials can bring into fore new possibilities arising at the interface of the two mate-

rials holding promising applications in spintronic, nano-electronic, etc. [10, 19, 55, 56]

The filling of CNT with application-specific materials realizes nano-scaled containers in which the active material is confined and protected by graphitic shells. For example, in case of iron, encapsulation inside CNT finds applications in bio-medicine sector. One medical application of a ferromagnetic material is the "magnetic fluid hyperthermia" (MFH). [56] The use of bare nano-particles is hindered due to the fact that metal nano-particles are oxidized under ambient conditions, and encapsulation inside CNT can be an effective method to avoid degradation of the filling.

In view of the above-mentioned advantages of encapsulation of magnetic materials inside CNT, it is pertinent to mention that extensive studies have been performed focusing on iron-filled CNT. [10, 46, 56, 79, 80] Significant amount of work has been reported on iron-filled CNT studying the magnetization mechanisms, transport measurements, utility as a nano-pipette, etc. [79–81] However, encapsulation of other ferromagnetic transition metals as well as transition metal-oxides (TMOs) is rarely explored. The TMOs belong to a unique class of materials, and are well-known for a host of novel electronic and magnetic ground states. [77] The richness of TMOs stems from the incomplete 3d orbitals of the transition metal, and have grown to be associated with a wide variety of applications, and nanoscaling these materials opens up a wider range of properties to be exploited. In particular, magnetic TMOs nanoparticles find interesting applications in magnetic fluids, data storage, catalysis, and bio-medicine, energy storage, [77, 82–86] and exhibit remarkable emergent properties upon nanoscaling.

An important class of TMOs belong to the antiferromagnets. On a general note, nanoscale antiferromagnets hold significant importance in the field of fundamental science and technological applications. [87] Antiferromagnets possess interesting properties such as robustness against perturbation due to magnetic fields, capability of producing large magneto-transport effects, etc., which make them a promising representative for next generation spintronic devices. [87] The phenomenon of exchange coupling between ferro- and antiferromagnets results in unique pinning of magnetization in the ferromagnet. This phenomenon is known as exchange-bias, and finds applications in various magnetic devices, has the potential to be utilized in the emerging field of spintronics. [87]

A very interesting example is the case of Cr_2O_3 which is a well known antiferromagnetic insulator and symmetry allowed magneto-electric compound. Cr_2O_3

appears to develop piezomagnetic traits (stress induced magnetism) on nanoscaling in ultra thin form. [88] Further, when this thermal insulating oxide is encapsulated inside CNT, the current carrying capacity of the CNT is enhanced as compared to the pristine CNT. [19] The magnetization measurements in Cr_2O_3 encapsulated CNT reveal an interesting pinning mechanism, which hints towards the possibility of stress induced moments, and hence, results in slow magnetization dynamics. [19] Thus, investigation of multi-functional oxides encapsulated inside CNT can provide insights of paramount importance. Multi-functional oxides encapsulated can be next-generation candidates for device applications. In the present work, we have encapsulated another antiferromagnetic insulator $\alpha\text{-Fe}_2\text{O}_3$ inside CNT and explored its magnetic properties. As previously mentioned, $\alpha\text{-Fe}_2\text{O}_3$ is also a symmetry allowed weak ferromagnet at the room temperature.

1.9.2 Weak Ferromagnetism in Hematite

With focus on TMOs relevant to AFM spintronics, we have studied encapsulation of DMI driven canted AFM – hematite ($\alpha\text{-Fe}_2\text{O}_3$) inside CNT. Hematite is a classic example of an antiferromagnet exhibiting the phenomenon of weak ferromagnetism, and has been explained in detail by Dzyaloshinskii. [66] It belongs to the family of rhombohedral antiferromagnets, and possesses interesting structure and magnetic properties. [66] The crystal structure of bulk hematite is rhombohedral with the space group $R\bar{3}c$ with lattice parameters of $a = 5.038 \text{ \AA}$ and $c = 13.772 \text{ \AA}$. [66] The iron ions are ordered in alternating planes along the [111] direction, and coupled antiferromagnetically via superexchange interaction. The magnetic moments in hematite is associated with the Fe^{3+} ions. Fe^{3+} with configuration $3d^5$ is almost always in the high-spin state ($S = 5/2$), and the electronic configuration can be written as $(t_g)^3(e_g)^2$. The effective magnetic moment of Fe^{3+} is $5.9 \mu_B$.

The generation of weak ferromagnetism in hematite ($\alpha\text{-Fe}_2\text{O}_3$) is due to a slight canting of its inherent AFM sub-lattice which persists from its Néel temperature (T_N) 950K down to 265K, well-known Morin transition temperature (T_M). [66, 69] Figure 1.7 shows the schematic of the spin configuration of $\alpha\text{-Fe}_2\text{O}_3$ in antiferromagnetic (AFM) and weak ferromagnetic (WFM) states. Below T_M , the spins lie along the c -axis of the rhombohedral lattice as shown in Figure 1.7(a) resulting in zero net magnetic moment. Above the Morin transition temperature (T_M), the spins turn from "c" axis to "a" axis (rhombohedral unit cell in hex setting) within which they

are slightly canted as shown in Figure 1.7 (b) and (c). This canting produces a net ferromagnetic moment in the lattice, thus, exhibiting weak ferromagnetic traits. The Morin transition is clearly seen in magnetization (M_{FC}) as a function of temperature for α - Fe_2O_3 single crystal at magnetic field $H = 1$ kOe as shown in Figure 1.7(d). [89] The Morin transition (T_M) $\sim 260\text{K}$ demarcates the pure AFM and WFM regions. It is to be noted that the magnitude of magnetization is ~ 0.35 emu/g in the WFM region and ~ 0.015 emu/g in the pure AFM region below 260K.

Dzyaloshinskii also pointed that the strength of the weak ferromagnetism in antiferromagnets bears an inverse correlation its Néel temperature. [66] Thus, weak ferromagnets with lower Néel temperature (T_N) will exhibit stronger weak ferromagnetic traits as compared to the weak ferromagnets with higher T_N . For instance, the weak ferromagnetism effect is weaker in hematite with its $T_N \sim 950\text{K}$ as compared to MnCO_3 with $T_N \sim 30\text{K}$.

α - Fe_2O_3 exhibits remarkably wide range of functional properties and possess galore advantages such as low cost, non-toxicity, environmentally friendly characteristics and high resistance to corrosion. α - Fe_2O_3 can exist in both AFM and WFM states, more importantly, exhibits weak ferromagnetism at room temperature. These properties make α - Fe_2O_3 advantageous for variety of practical applications.

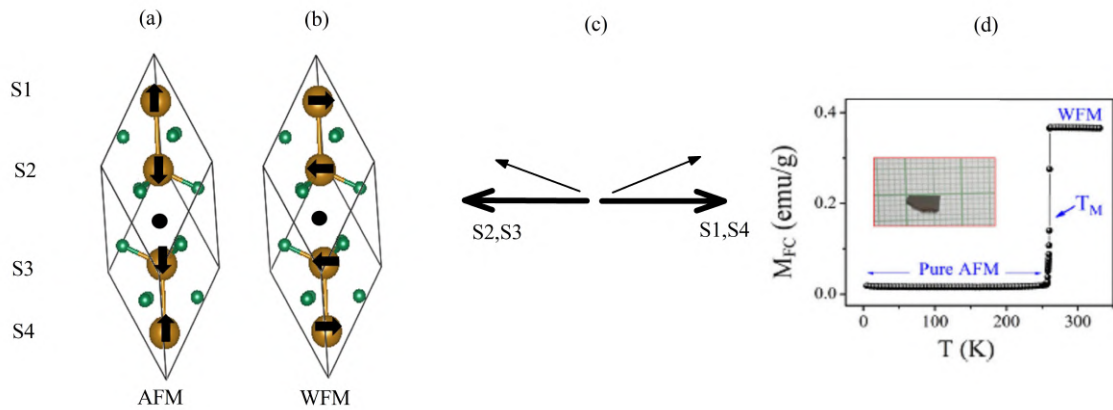


Figure 1.7: Schematic of spin configuration in (a) pure AFM and (b) WFM state for rhombohedral unit cell of hematite (α - Fe_2O_3). The yellow and green spheres are the Fe and O ions respectively. The black dot is the inversion centre. (c) Depicts the spin canting for WFM state which leads to a net weak ferromagnetic moment. (d) Magnetization (M_{FC}) as a function of temperature at 1 kOe for α - Fe_2O_3 single crystal depicting the pure AFM and WFM states [89].

1.9.2.1 Time-stable Remanence in Hematite ($\alpha\text{-Fe}_2\text{O}_3$)

A systematic remanent magnetization study conducted on a number of DMI driven canted AFM or WFM including $\alpha\text{-Fe}_2\text{O}_3$ reveals some unique features. It is consistently observed that these weak ferromagnets exhibit an unusually slow magnetization relaxation phenomenon. [89] This ultra-slow magnetization relaxation phenomenon leads to the observation of *time-stable* remanence which appears to be exclusive to many WFM. Figure 1.8(a) shows the remanence (μ_{FC}) as a function of time for rhombohedral weak ferromagnets. As shown in Figure 1.8(a), a part of remanence exhibited no decay in a time period of 1.5 hours, thus, exhibiting *time-stable* character. The remanent state for Figure 1.8(a) was obtained by cooling each sample from room temperature down to 5K in the presence of a magnetic field (1 kOe), and recording remanent magnetization as a function of time after switching off the field at 5K.

In addition to the ultra-slow magnetization dynamics, an unusual magnetic field dependence was also observed in these canted AFM. [89] An example is shown in Figure 1.8(b) depicting the counter-intuitive magnetic field dependence in $\alpha\text{-Fe}_2\text{O}_3$. As evident from Figure 1.8(b), the values of magnetization (M_{FC}) are observed to increase with increasing magnetic field (H) at a constant temperature 5K, which is expected for a regular AFM. However, the values of remanence (μ_{FC}) in red, increases initially with increasing magnetic field (H), and thereafter drops sharply. This type of magnetic field dependence is not expected for a regular ferromagnet or

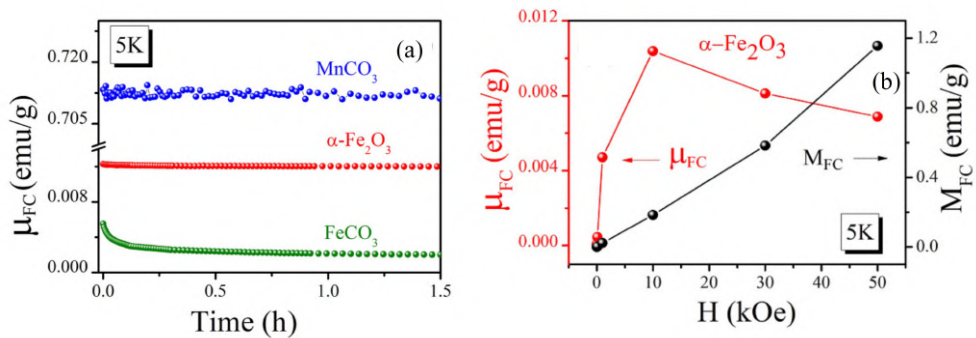


Figure 1.8: (a) Remanence (μ_{FC}) as a function of time for rhombohedral weak ferromagnets depicting its time-stable nature. (b) Magnetization (M_{FC}) and remanence (μ_{FC}) as a function of cooling field (H) indicating the unusual magnetic field dependence of remanence. [89]

antiferromagnet. [89] Thus, the remanence measurements bring into fore a unique functional form which is not observed in routine M-H isotherms or magnetization data recorded as a function of temperature. The reasons for the unusual magnetic field dependence are covered in detail in chapter *four*.

Interestingly, these unusual features – ultra-slow magnetization relaxation and counter-intuitive magnetic field dependence were also observed in the case of α -Fe₂O₃ single crystal devoid of any impurity or size effects. Therefore, it was concluded that these features were intrinsic to weak ferromagnetism arising from spin canting, and not due to other phenomena such as, glassy phase, magnetocrystalline anisotropy, or routine exchange bias. [89]

Furthermore, this feature has also been explored in detail in α -Fe₂O₃ in various sizes and morphologies. [90] It was observed that the magnitude of remanence in the sample consisting of ultra-small nano-particles was substantially enhanced as compared to the samples in regular morphology (hexagonal plates or cuboids), suggesting that the magnitude of remanence can be tuned with size, and/or interface-effects. [90] These data also established a correlation of magnitude of remanence with the extent of spin canting. As discussed in the previous section, the magnitude of weak ferromagnetism (and also remanence) is indirectly proportional to its T_N . [66, 89, 90] Therefore, the weak ferromagnetic moment, and, hence, the magnitude of remanence is observed to be weak due to its high T_N . Nevertheless, α -Fe₂O₃ being a room temperature weak ferromagnet holds promising implications in the field of spintronic applications.

We would like to recall, remanence is an important parameter for any magnetic material, when deciding the utility of these materials for practical applications. The presence of unusual magnetization relaxation phenomena, leading to the observation of *time-stable* remanence in α -Fe₂O₃ nanoparticles, motivated us to encapsulate this multi-functional hybrid inside CNT. Here we find that the magnitude of this *time-stable* remanence, which is exclusive to the weak ferromagnetic trait of hematite is significantly enhanced upon the encapsulation of hematite inside carbon nanotubes. These results are discussed in chapter *four*.

1.9.3 Temperature-dependent Raman Spectroscopy

In addition to probing the multi-functional oxides encapsulated inside CNT through magnetization and remanence studies, Raman spectroscopy is an effective technique

to study the CNT systems. The temperature dependent behaviour of the Raman bands for the multi-functional hybrid allows for a detailed investigation of underlying interactions involved in the system. The temperature-dependent Raman spectra carry a wealth of information on thermal properties, anharmonicity, phonon-phonon and electron-phonon coupling. In case of magnetic materials, the phonon-phonon interactions originating from the coupling of the lattice vibrations to the spin degrees of freedom. This coupling between the lattice and the spin-degrees of freedom is known as spin-phonon coupling. The spin-phonon coupling is reflected in the phonon frequency shifts around the magnetic transition. [91] This can be utilized to investigate the magnetic phase transitions and further study the influence of spin-phonon coupling on phonon scattering.

It is important to understand the interaction between the magnetic encapsulate and the CNT in order to exploit magnetic-oxides encapsulated carbon nanotubes in CNT-based spintronic devices. Raman spectroscopy studies on multi-functional oxides encapsulated inside CNT can shed some light on the interactions occurring at the interface of the encapsulate and the CNT.

1.10 Filling of Carbon Nanotubes with Transition Metal Oxides : The Applications

In addition to the unprecedented magnetic properties, TMOs are promising candidates for energy-related applications. We have tested a number of TMOs including Fe, Co and Ni oxides for battery applications. In this section we present a brief introduction to lithium-ion batteries followed by discussion about the limitations of currently employed electrode materials and the advantages of TMOs as anode materials.

Before discussing the applications of TMOs in Lithium-ion batteries (LIBs), and further to this, the encapsulation of TMOs inside CNT, we introduce some battery related terms and terminology. The performance of any battery is decided by the properties of its components – anode, cathode, and electrolyte. The electrode materials should be able to withstand the large amounts of lithium (in case of LIB) without any structural variations which can rupture the cell and affect the performance of the battery. The electrode materials should be electrically conductive, ionically diffusive, and inexpensive. The glossary of terms such as specific capacity, C-rate and

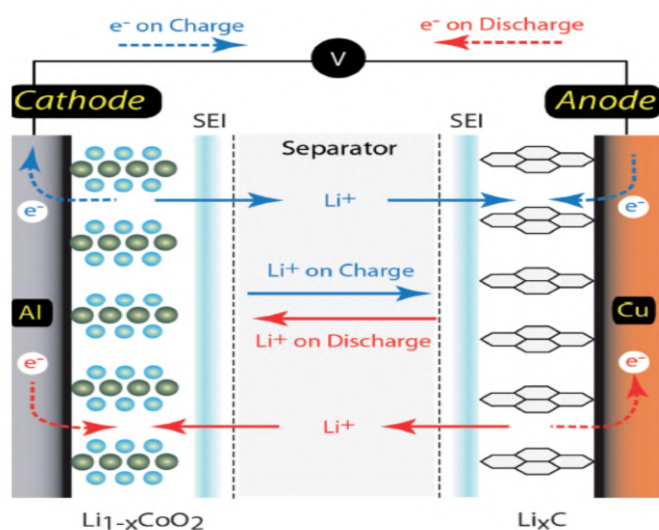


Figure 1.9: Schematic of a typical Li-ion battery with lithium cobalt oxide as the cathode and graphite as anode. [96]

cyclability, relevant to batteries have been discussed in Appendix A.

A lithium-ion battery is rechargeable battery and most commonly used for portable electronics. [92] The technology of LIB was developed by John Goodenough, Stanley Whittingham, and Akira Yoshino during 1970s. [92] In 1991, LIBs have commercialized and have become a pivotal part of the modern era in the field of energy storage devices and have emerged as the most promising candidate for rechargeable energy technologies. [92–95] Figure 1.9 shows a schematic of a typical lithium-ion battery. The three primary components of a lithium-ion battery consists of the positive and the negative electrode and electrolyte. In conventional Li-ion batteries, the positive electrode is a layered metal oxide which is generally lithium cobalt oxide, or a spinel (like lithium manganese oxide). The negative electrode primarily employed in commercial batteries is graphite. [92] The electrolyte is typically a mixture of organic carbonates such as ethylene carbonate, or diethyl carbonate containing complexes of lithium ions. [92]

When the battery is fully charged, the lithium ions move towards the negative electrode from the positive electrode and are stored between the graphitic layers. This is known as intercalation. In this state, the battery can be thought as a multi-layer sandwich: graphitic layers alternating with layers of lithium ion. In the discharge cycle, the intercalated lithium ions move to the positive electrode (lithium cobalt

oxide) from the negative electrode. This process is known as de-intercalation of lithium ions. The overall reaction can be written as: [92]



The commercial LIB employ graphite as the anode material which has a theoretical capacity of 372 mA h g^{-1} , which limits the applications of LIB for practical purposes with the increasing demand of LIB. [97] In this regard, efforts have been made to explore the alternatives to achieve higher capacity with better stability to meet the increasing demand of LIB. Transition metal oxides (TMOs), such as iron oxides, cobalt oxides, nickel oxides, copper oxides, etc., have attracted considerable attention as promising anode materials due to their higher theoretical capacities compared to graphite, low cost, abundant resources and low toxicity. [98–101]

However, the practical applications of oxides are hampered due to the large volume changes – expansion and contraction of the active material during the conversion reaction during the cyclic process which eventually causes rapid capacity fading during long term cycling and destruction of the electrode during electrochemical cycling. [97] The low electrical conductivity of TMOs also demotes the performance of LIB, hence, limiting the practical realization of TMOs in commercial batteries.

To circumvent the problem of volumetric variation during charging/discharging processes, one effective strategy is to introduce carbonaceous materials to improve the structural stability and electrical conductivity. [97, 102–106] Among various carbon materials, CNT possess excellent conductivity, chemical stability and structural flexibility, which have been widely explored for hybrid electrode materials. [55, 107–113] The CNT network acts as scaffold structures to host a variety of nano-sized electrode materials. Their exceptional mechanical properties are utilized to buffer the volumetric strain in the electrode materials during charging/discharging processes. [55, 107–113] The high electrical conductivity of CNT also mark them as a superior choice for anode materials for LIB.

In this regard, we find that there have been a few reports on the encapsulation of $\alpha\text{-Fe}_2\text{O}_3$ inside CNT, however, there is no detailed study of the effect of filling fraction or morphology of the encapsulate in $\alpha\text{-Fe}_2\text{O}_3$. [55] In addition, encapsulation of various other oxides, such as nickel oxide, cobalt oxide, magnetite (Fe_3O_4) has not been studied. These oxides are also potential anode materials with high theoretical

capacity, and encapsulation of these oxides CNT can be an efficient approach to achieve high capacity hybrid materials.

In light of the afore-mentioned advantages of filling CNT with functional magnetic oxides, this thesis addresses the challenges concerning the filling of CNT of functional magnetic materials (metals and metal-oxides). The structure and the scope of the thesis is outlined in the following section which bridges the missing gap in literature in the areas of synthesis, fundamental studies, and applications of functional magnetic materials encapsulated inside CNT.

1.11 Scope and Outline of the Thesis

This thesis presents a novel approach of encapsulating and preserving functional TMOs inside CNT, thereby providing an opportunity for direct patterning of nano-electronic devices. With focus on the TMOs relevant to antiferromagnet spintronics, we have explored both fundamental and application related aspects of Oxide/CNT hybrids. This thesis unravels three major areas related to filling of CNT with multi-functional hybrids – synthesis of CNT filled with 3d transition metals and oxides, fundamental aspect of multi-functional oxides encapsulated inside CNT, application-related studies of oxides inside CNT.

The first part of the thesis deals with the challenges involved in synthesizing CNT encapsulated with functional magnetic materials – 3d transition metals and metal oxides. A facile technique with innovative use of green compound 'camphor' to synthesize ferromagnetic metals (Fe, Ni or Co), and their corresponding oxides within CNT with precise control over morphology and filling efficiency is demonstrated. Pyrolysis of metallocene is employed, a technique which is well-known to successfully yield iron-filled CNT, but does not yield well-formed nickel- or cobalt-filled CNT. The details of the synthesis procedure and a systematic variation of synthesis parameters are discussed in chapter *three*.

In the second part of the thesis, fundamental studies of encapsulation of DMI driven canted antiferromagnet – hematite is presented. Through rigorous magnetization and remanence measurements using SQUID magnetometry, we show that the encapsulation of hematite inside CNT leads to a significant enhancement in the magnetic functionalities of the encapsulate. Further still, encapsulation leads to some novel interface effects, which evidently manifest in the lattice parameters of CNT

derived using Synchrotron X-Ray diffraction. The temperature variation of Raman Spectroscopy of the hybrid system is investigated in detail and the results suggest the presence of novel interface-effects. The results are presented in chapter *four* and *five*.

The third major section of the thesis is devoted to for energy related applications of these multi-functional oxides encapsulated inside CNT. Different oxides encapsulated inside CNT (Fe_2O_3 , Fe_3O_4 , NiO , Co_3O_4) are tested as an anode material in Li-ion batteries. The encapsulation of these oxides inside CNT leads to a significant improvement on cyclic stability, irrespective of the type of the oxide. Further to this, the results shed light on the importance of morphology of the CNT for its electrochemical performance as anode materials in Li-ion batteries. The results are presented in chapter *six*.

Chapter 2

Experimental Methods

Accurate measurements of physical properties are crucial for advances in science. The aim of this chapter is to introduce the experimental methods and techniques used to synthesize and characterize the samples studied in this thesis. In the first section, the characterization techniques: X-ray diffraction, Synchrotron X-Ray diffraction, Transmission Electron Microscopy, Scanning Electron Microscopy, Thermal Gravitimetric Analysis, Raman spectroscopy, are introduced. For analyzing the synchrotron X-ray data, Rietveld refinement method has been employed. Bulk magnetic properties have been studied by dc magnetization as a function of temperature and magnetic field using Superconducting Quantum Interference Device magnetometry.

The second section of this chapter covers the experimental protocols of the methods to fabricate the cell for testing which includes coin cell and Swagelok-type cell. The electrochemical measurement techniques for testing the *as-prepared* samples as anode materials for lithium-ion batteries are then discussed in detail.

2.1 Characterization Techniques

2.1.1 Field-Emission Scanning Electron Microscope

The morphology of the metal and metal-oxide encapsulated inside carbon nanotubes were studied using the Field-Emission Scanning Electron Microscope (FESEM). FESEM produces high-resolution images of the sample in the electron imaging mode. The characteristic X-rays are also used to determine the elemental composition with the help of a technique known as Energy Dispersive X-Ray (EDX). EDX

can provide qualitative and quantitative information of the selected area on the surface of the sample, since the energy of the scattered X-rays is characteristic for each chemical element. The instrument used to acquire images for the samples studied in this thesis is *ZEISS ULTRA plus*.

The working principle of SEM can be described as follows. When a high-energy electron beam is incident on a sample, secondary electrons are emitted with relatively low energy. [114] These secondary electrons carry information about the topography of the sample. Some electrons from the incident electron beam are bounced back by the atomic electron cloud of the sample. These electrons are known as the back scattered electrons (BSE). The scattering cross section of the back scattered electrons are dependent on the atomic density of the sample. [114] A sample with large atomic density will produce more BSE, and hence, a brighter image with high contrast resolution is obtained.

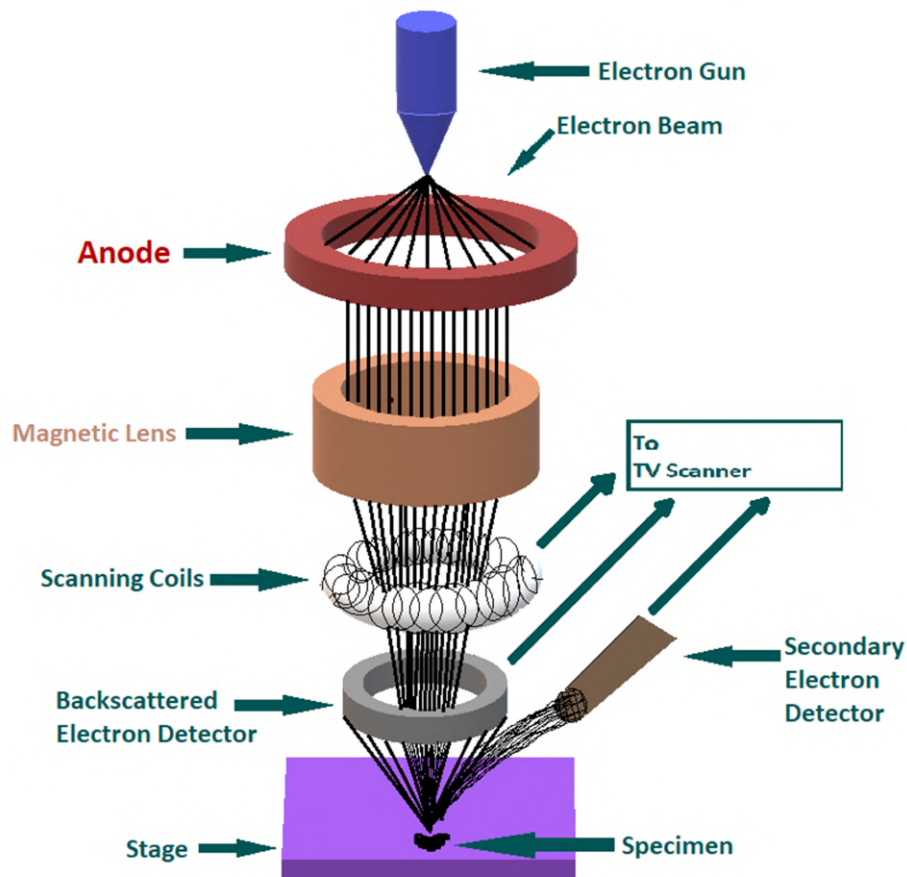


Figure 2.1: *Schematic representation of a typical SEM.*

When the secondary electrons are emitted from the inner shells of the atoms, the electrons from the outer shells fill the empty inner shells. This transition emits x-ray photons with an energy equal to the difference between the energy levels. The wavelength of these emitted x-ray photons are characteristic of the atom, and, therefore, the analysis of these energy can determine the elemental composition of the sample. [114]

Figure 2.1 shows the schematic of a typical SEM setup. When the high-energy focused beam of electrons strikes the surface of the sample, it interacts with the atoms of the sample. The emitted electrons are then collected by the detector to generate an image and composition of the sample. In a typical SEM, the electron beam is passed through scanning coils and deflector plates as shown in Figure 2.1. The final lens of the column deflects the beam horizontally and vertically, thus scanning the sample in a raster fashion. Detectors and amplifiers are used to display the image. The image, thus displayed, is a resultant of the intensity distribution map of the emitted electrons from the sample. The primary condition when using SEM technique is that the sample should be preferably conducting to allow the beam to scan the sample's surface for conventional imaging. The non-conducting samples can be coated with a layer of conducting material using sputter coating or high vacuum evaporation.

FESEM works on the same principle as conventional SEM, but with a higher resolution and greater energy range of the electron beam. The FESEM differs from SEM in terms of the system in which electron is generated. FESEM uses a field emission gun as a source of electron. The extremely focused electron beams greatly improves the resolution of the image, and enables imaging at very low potentials (0.02 – 5 kV). The charging effect on non-conductive samples is also reduced. In addition, the in-lens detectors employed in FESEM provide high-resolution images at low accelerating potential.

The energy of the incident electron beam plays a crucial role in this technique. The low energy beams (5 - 10 keV) are used to determine the surface topography, whereas, for EDS analysis higher energies are preferred. [114] EDS measurement is carried out at 15 - 20 keV. The higher energies can, however, damage the sample. Even when the samples being images are resilient to high energies, the emergent beam is likely to be absorbed by the sample before reaching the detector. An empirical rule while choosing the excitation energy is that it should be higher than the highest excitation energy of the concerned sample. [114]

For FESEM imaging of the samples studied in this thesis, carbon tape with the powder sample was placed on the sample holder mounts. FESEM images of CNT encapsulated with functional materials are shown in subsequent chapters.

2.1.2 Transmission Electron Microscope

Transmission Electron Microscopy (TEM) is an imaging tool in which an electron beam is transmitted through a specimen. The interaction of the electrons with the sample produces a magnified image and reveals finest details about the structures of the samples with atomic resolution. [115] The TEM micrographs presented in this thesis have been recorded on *FEI-TECNAI* microscope at an operating voltage of 200 kV.

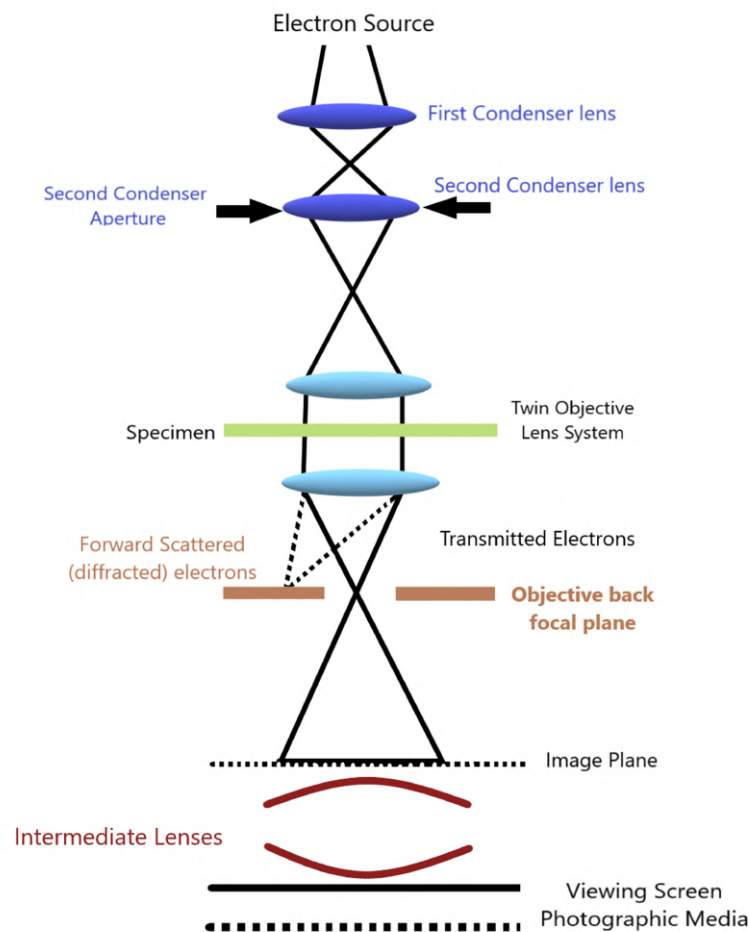


Figure 2.2: Schematic representation of a typical TEM.

The wavelike behaviour of electrons allows a beam of electrons to be focused and diffracted. The wavelength of the electrons after taking into account the relativistic effects can be written as: [115]

$$\lambda_e \approx \frac{h}{\sqrt{2m_0E\left(1+\frac{E}{2m_0c^2}\right)}}, \quad (2.1)$$

where, h is the Planck's constant, m_0 is the rest mass of an electron, and E is the energy of the accelerated electron. In an electron microscope, the electrons are generated by thermionic emission from a filament or through field electron emission. [115] An electric potential then accelerates the electrons, and the accelerated electrons are focused by electrostatic and electromagnetic lenses onto the specimen. The transmitted beam which consists of information about the specimen's electron density is used to form an image.

Figure 2.2 shows a schematic of a typical TEM setup. The electron gun consists of an emission source (tungsten or LaB₆ single crystal) which is connected to a high voltage source (100 - 300 kV). When sufficient current is provided, the gun emits electrons by thermionic or field emission. When the electron beam leaves the gun, it is accelerated by the electrostatic plates to achieve the final voltage. The electron beam is manipulated with the help of electromagnets. The magnetic fields form a magnetic lens of variable focusing power and the lens shape originates due to the magnetic flux distribution. [115] The electrostatic plates allow the electrons to be deflected by a constant angle. The electron beam then enters the next stage, i.e., the condenser lens system. The lenses are used to focus the beam on the location of the specimen. [115]

The electron beam can be manipulated by the solenoid or the electromagnet. The focusing power of the magnetic lens can be altered by changing the current passing through the coils of the solenoid. This is known as the condenser lens system which produces a focused beam on the specimen. [115] In addition, intermediate lens system is also used which is placed after the sample. This lens system can be adjusted to form diffraction pattern or image of the specimen with magnification up to 1,000,000x. The screen consists of a phosphorescent plate which glows when being hit by electrons and the image formed in a way similar to photography.

The specimen preparation is a complex procedure for TEM imaging. The specimen's thickness should be, typically less than 100 nm for conventional TEM. A TEM

specimen to be imaged must be thin enough for electrons to penetrate and produce an image. In case of CNT (powder) studied in this thesis, the sample solution in ethanol was ultra-sonicated for 30 minutes prior to imaging, to disperse the CNT forest on the TEM grid. The ultra-sonication of the solution was required to disperse the sample and produce high-quality images.

2.1.3 X-Ray Diffraction

X-ray powder diffraction (XRD) is a characterization technique which is primarily used for identification of phases and obtaining information about the structure of the crystalline materials. The samples presented in this thesis have been characterized by *Bruker D8 Advance*. The setup consists of an X-ray source tube, sample platform, and a detector to collect for the diffracted rays from the sample; with a monochromatic source with Cu $K\alpha$ radiation ($\lambda = 1.54056 \text{ \AA}$).

Crystalline materials can be considered as 3-D diffraction gratings for X-ray whose wavelengths are similar to the lattice spacing of planes in a crystal. All crystalline materials comprise of regular array of atoms. When a beam of monochromatic X-rays is bombarded at the target material, the X-rays are scattered from atoms within the target material. The periodic structure in materials allow the scattered X-rays to undergo constructive and destructive interference obeyed by Bragg's law. This is

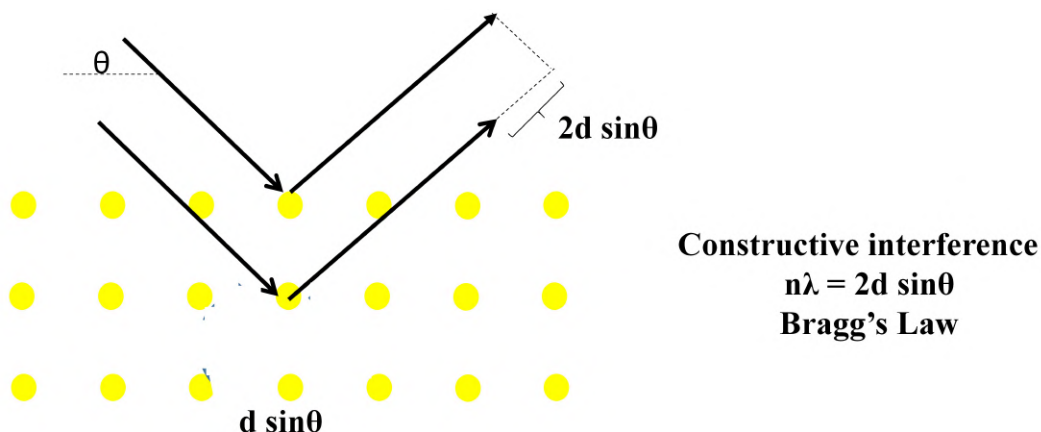


Figure 2.3: *Schematic representation of XRD depicting Bragg's law. [116]*

known as diffraction. The equation describing the Bragg's law is given by: [117]

$$n\lambda = 2d \sin(\theta). \quad (2.2)$$

Here d is the lattice spacing, θ is the incident angle, n is any integer, and λ is the wavelength of the incident beam. Figure 2.3 shows a schematic representation depicting Bragg's law.

The wavelength of the X-rays is typically of the same order of magnitude (1 – 10 Å) as the lattice spacing d . These X-rays are directed at the sample, and the diffracted rays are collected at the detector. The intensities of the XRD pattern provide information about the arrangement of atoms in the crystal structure. Polycrystalline samples are comprised of tiny crystallites which are oriented in all possible directions. When a powder sample is exposed to the X-ray beam, the XRD pattern will consist of all possible planes. Thus, the sample is scanned through a range of 2θ angles, attaining all possible diffraction directions of the lattice. Further, the conversion of the diffraction angles to corresponding d -spacings aids in identifying the material. Typically, this is achieved by comparison of d -spacings with the standard reference patterns.

The diffraction pattern were recorded in the Bragg-Brentano geometry. [117] This geometry offers the advantages of high resolution and high beam intensity analysis at the cost of very carefully prepared samples. The acquired X-ray pattern. For phase confirmation the acquired X-ray pattern was matched with the standard data available with the International Centre for Diffraction Data (ICDD).

2.1.4 Synchrotron X-Ray Diffraction

The electrons or other charged particles moving at relativistic speeds are forced to follow curved trajectories when subjected to magnetic fields. In this process, they emit electromagnetic radiation which is known as Synchrotron radiation. [118, 119] The synchrotron radiation is now used to probe the structure of matter at atomic and molecular level, ranging from the surface of the solids to the structure of protein molecules.

X-Ray diffraction experiments can be conducted with lab sources and synchrotron sources. Standard laboratory XRD instruments generate X-rays by hitting a pure element with a beam of electrons which is accelerated with energies ~ 30 keV. However,

diffraction data using laboratory sources have several practical limitations. Laboratory XRD sources require sample sizes which are sometimes not achievable due to limited synthesis conditions. This affects the intensity of the acquired data and produces data with limited resolution. The limited minimum wavelength restricts the accessible Q range which, in turn, limits the number of reflections that can be collected from the laboratory XRD sources.

On the other hand, synchrotron sources can produce high intensity data even with small amount of samples (powder or single crystal). The signal-to-noise ratio is high, and thus, the data acquired is of high quality which reflects the presence of weak features such as impurities, below the resolution of laboratory XRD data. The data acquired from synchrotron source is of high resolution with fine peak splitting and the strain effects, particle size, complex structures can easily be extracted and studied. The major applications of synchrotron light lie in the areas of condensed matter physics and biology. In a large fraction of experiments, synchrotron light is used to the structure of matter at different scales ranging from the sub-nanometer to the micrometer and millimeter level.

Specially designed storage rings with high energy electron or positron accelerators are the sources of synchrotron radiation. [118, 119] The energy of the electrons is a few gigaelectron volts which causes the electrons to move with almost the speed of light. The storage ring has insertion devices at well defined positions which force the electrons to radiate. In the absence of any external force, the electrons tend to travel in a straight line. Therefore, magnetic fields are used to constrain the

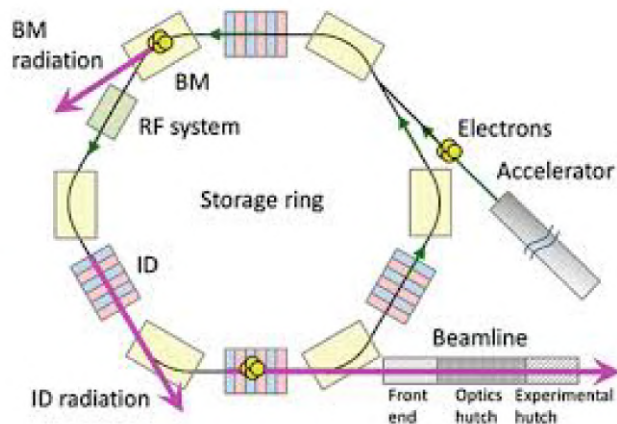


Figure 2.4: A typical layout of synchrotron radiation facility. [118]

electrons in the storage ring. To serve this purpose, bending magnets are installed every few meters along the storage ring. The electrons experience a Lorentz force at the the locations of the bending magnets, which force them to follow the curvature of the storage ring. [118, 119] This Lorentz force is responsible for acceleration of the electrons, and, the accelerated electrons emit electromagnetic radiation. This is the how a synchrotron light is produced. Each bending magnet becomes the source of the synchrotron radiation. The emitted light is then collected by a beamline, and sent to experimental chamber after optical processing. Figure 2.4 shows the schematic of a typical synchrotron facility.

The samples presented in this thesis deals with small quantities of ferromagnetic metals and magnetic oxides encapsulated within the core cavity of the CNT, synchrotron XRD was required to detect the phases of the oxides formed in the sample, which are typically not detected in laboratory XRD setup. The temperature variation of synchrotron XRD from 20 K to 300 K for the samples discussed in this thesis has been conducted in BL-18 beamline, Photon Factory, Japan. The data have been fitted using Rietveld Profile Refinement discussed in the next section.

2.1.5 Rietveld Refinement

Rietveld refinement is a technique devised by Hugo Rietveld for crystalline materials. [120] The Rietveld method refines user-selected parameters to minimize the difference between an experimental pattern (observed data) and a model based on the hypothesized crystal structure and instrumental parameters (calculated pattern). [120] A least squares approach is used in the Rietveld method to refine a theoretical line profile with the the observed pattern. [120] The observed diffraction pattern is refined with theoretical models considering the factors – crystal structure, diffraction optic effects, instrumental factors, lattice parameters, etc. simultaneously.

2.1.5.1 Principle of Rietveld Refinement

The powder diffraction pattern is recorded as numerical intensity value y_i in the incremental steps i . The increments can be in either scattering angle 2θ , or an energy parameter, depending on the source and the application. The 'best fit' is the best least squares fitting to accommodate all the y_i 's simultaneously. The quantity to be

minimized is the residual function S_y given by: [120]

$$S_y = \sum_i w_i (y_i - y_{ci})^2, \quad (2.3)$$

where,

$$w_i = 1/y_i,$$

y_i = observed intensity at the i^{th} step,

y_{ci} = calculated intensity at the i^{th} step.

A typical powder diffraction pattern is a collection of individual reflections where each reflection profile possess peak height, peak width, peak position and an integrated area proportional to the Bragg intensity I_K . Here K stands for Miller indices $-h, k, l$; and I_K is proportional to the square of the absolute value of structure factor (F_K). Typically, the observed intensity y_i consists of contributions from many Bragg reflections. The calculated intensity y_{ci} is determined from $|F_K|^2$ calculated from the structural model. The calculated intensity y_{ci} is given by:

$$y_{ci} = s \sum_K L_K |F_K|^2 \phi(2\theta_i - 2\theta_k) P_K A + y_{bi}, \quad (2.4)$$

where,

s is the scale factor,

K represents the Miller indices h,k,l for a particular Bragg reflection,

L_K is the Lorentz–Polarization factor,

F_K is the structure factor for the K^{th} Bragg reflection,

ϕ is the reflection profile function,

P_K is the preferred orientation factor,

A is the volume absorption factor,

y_{bi} is the background intensity at the i^{th} step.

The background intensity y_{bi} at the i^{th} step can be obtained from either an user supplied file, or linear interpolation of the user selected points, or a specific background function. Background function is generally a fifth-order polynomial function and can also be an input from the user in the form of user generated .bg file with refinable heights.

The reflection profile function ϕ approximates the effects of instrumental features as well as sample's features. The reflection profiles available in most of the programs

include two different pseudo-Voigt functions, Gaussian, Pearson VII, Lorentzian and modified Lorentzian functions. [120] We have used pseudo-Voigt function in refining the data presented in this thesis. The dependence of the the breadth H in the reflection profile is described by Caglioti's formula written as:

$$H^2 = U \tan^2\theta + V \tan\theta + W, \quad (2.5)$$

where U , V , W are refine-able parameters. These parameters define the peak width and the peak shape of the reflection profile.

It is assumed in the default calculation model that there are an equal number of crystallites for every diffraction peak. However, the crystallites are randomly oriented, and a tendency exists for the crystallites to orient in one particular way. The preferred orientation can create distortions in the peak intensities and can be corrected with March distribution function given by : [120]

$$P_K = (G_1 \cos^2\alpha_K + (1/G_1) \sin^2\alpha_K)^{-3/2}, \quad (2.6)$$

where G_1 is refinable parameter and α_K is the angle between the preferred orientation vector and the normal to the planes generating the diffracted peak.

The generalized structure factor F_K is given by: [120]

$$|F_K|^2 = m_K \left| \sum_{n=1}^N f_n e^{-B_n \frac{\sin^2\theta}{\lambda^2}} (e^{2\pi i(hx_n + ky_n + lz_n)}) \right|^2, \quad (2.7)$$

where, N is the number of atoms, x_n , y_n , z_n are the coordinates of the n^{th} atom, and f_n is the atomic structure factor. The structure factor F_K includes the multiplicity of the K^{th} reflection (with h , k , l Miller indices) given by m_K , the structure factor and the temperature factor B_n known as the Debye-Waller factor which is responsible for thermal displacement of the n^{th} atom.

The Lorentz-Polarization factor L_K takes care of the instrumental factors. The scattering of the light from the atom and diffracted light from the monochromator to remove unwanted wavelengths of radiation can polarize the X-ray beam. These factors are included in the Lorentz-Polarization factor L_K .

2.1.5.2 Criteria of fit

The Rietveld refinement process adjusts the refinable parameters until the residual function given by the equation 2.3 is minimized. The 'best fit' will depend on the model and on whether a global minimum is attained instead of a local minimum. The most straightforward discrepancy index i.e. the weighted profile R-factor R_{wp} is given by the square root of the quantity minimized which is S_y , scaled by the weighted intensities. This is represented as: [120]

$$R_{wp}^2 = \frac{\sum_i w_i (y_i - y_{ci})^2}{\sum_i w_i (y_i)^2} \quad (2.8)$$

The best possible value that can possibly be obtained for a particular set of data is expected R-factor R_{exp} which is the best possible R_{wp} . This is given by: [120]

$$R_{exp}^2 = \frac{1}{N \sum_i w_i (y_i)^2} \quad (2.9)$$

A related statistical concept is that of "Chi squared" or χ^2 given by: [120]

$$\chi^2 = (R_{wp}/R_{exp})^2 \quad (2.10)$$

The "goodness-of-fit" is the criterion of the fit and is given by equation 2.10.

The R_{wp} factor hold more value, and its absolute value does not depend on the absolute value of the intensities.

- $R_{wp} < 1$ acceptable refinement for a medium complex phase
- $R_{wp} < 0.15$ good for a complex phase
- $R_{wp} < 0.08$ acceptable for compounds with high symmetry
- R_{wp} (subtracted) to be referred in case of a high background data

The goodness of fit (χ^2) is the ratio between the R_{wp} and R_{exp} . This value cannot be lower than 1. A good refinement yields goodness of fit values which are lower than 2.

2.1.5.3 Refinement Procedure

The Rietveld refinement for the samples investigated in this thesis were done on *FullProf* software. The input files are the experimental data *.dat* file, and crystal-

lographic information *.cif* file which contains the crystallographic information about the crystal. After the input of the files, and manually adding/adjusting parameters such as wavelength of the X-ray source, background function/external background file, type of reflection profile function; the program is run for refinement.

The sequence followed for refinement for a crystal structure is as follows. [120]

1. Scale factor.
2. Scale factor, zero point of detector, background parameter and instrumental parameters. The background was fixed using linear interpolation with a set of pre-decided points provided by user.
3. Refine the lattice parameters – a,b,c.
4. Atomic positions.
5. Refine the peak shape (U, V, W) and asymmetry parameters (if necessary).
6. Add atomic occupancies (if required).
7. Add preferred orientation(if necessary).
8. Add the overall Debye-Waller factor.
9. Micro-structural parameters: size and strain effects.

2.1.6 Raman Spectroscopy

In condensed matter physics, Raman spectroscopy has been used to study the vibrational modes in a system – solid or liquid. This technique is based on inelastic scattering of monochromatic laser light. The photons of the laser light interact with the phonons of the systems resulting in change of incident energy of the photons. The information about the phonon modes in a system is carried by the energy shifts. Raman spectroscopy is a powerful tool which responds to sensitive changes in the system, and can reveal a considerable amount of information about the system. It is a widely used tool to study nano-materials, interface structures, strain and phonon properties in condensed matter science. [59, 121–125]

When the incident light is scattered from a molecule or crystal, most of the photons are elastically scattered. The energy of the scattered photons is same as that of the incident energy. This process is called Rayleigh scattering. A small fraction of light, however, is scattered at frequencies different from the frequency of the incident photons. This inelastic scattering of the incident light is known as Raman effect.

When the the sample is illuminated by monochromatic laser light, the spectrum

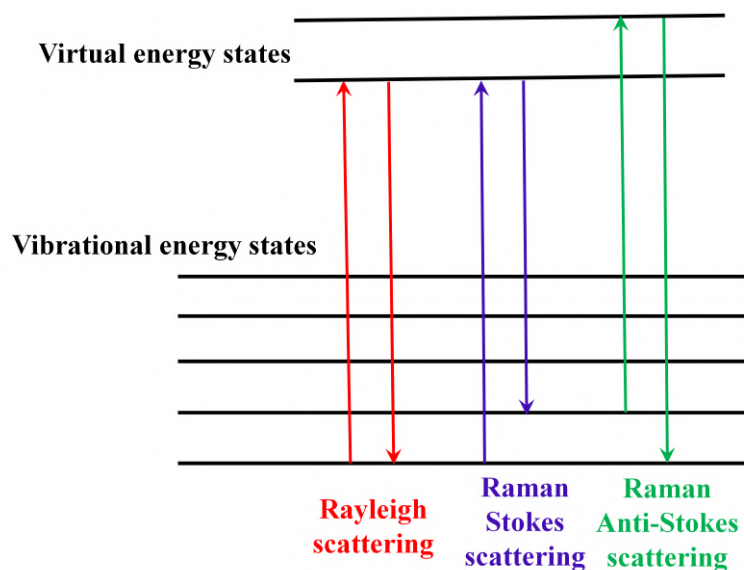


Figure 2.5: Energy level diagram depicting Rayleigh scattering and Raman scattering – stokes and anti-stokes.

of the scattered light consists of a strong line with frequency same as that of the incident monochromatic light. This results from Rayleigh scattering as shown in Figure 2.5. In addition to the Rayleigh line, weaker lines on either side of the strong line are also obtained as shown in Figure 2.5. The lines with frequency less than the incident frequency where the inelastically scattered photons lose energy by creating a phonon are known as Stokes lines. The lines with frequency higher than the incident frequency are called anti-Stokes lines. The probability of these processes depends on the excitation energy and the temperature.

The above discussion refers to the fundamental scattering process known as *first-order* processes. In a first-order process, the exchange of energy between the incident light and the sample excites a single phonon with very small momentum ($q \sim 0$). However, there is a finite probability of two or more phonons getting excited. These are known as *second-order* or higher-order processes. [11] The second-order processes are usually weaker in intensity than the first-order processes, but carry information about the overtones or combinations of bands.

Raman spectroscopy measurement system consists of four major components – (i) excitation source (laser), (ii) optical systems to collect light, (iii) filter, and (iv) detector. Figure 2.6 shows a schematic of a typical Raman measurement system.

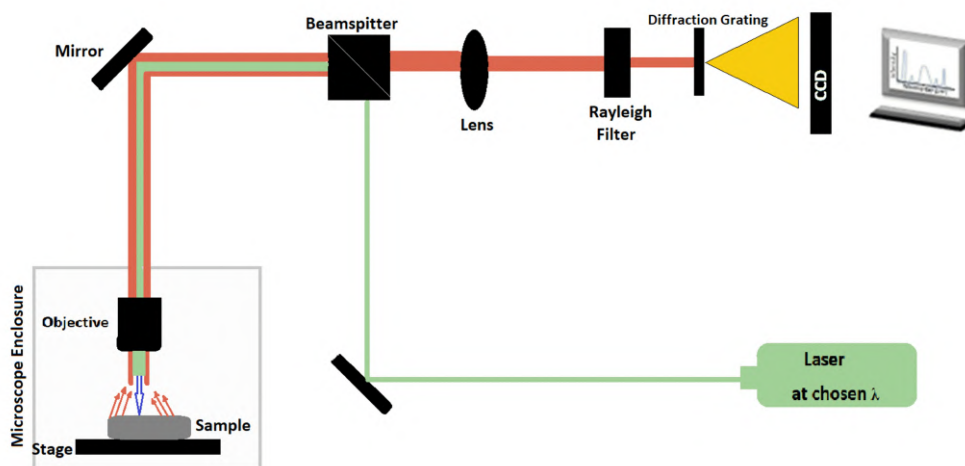


Figure 2.6: *Schematic of a typical Raman spectrometer.*

The sample is illuminated with a laser beam and the scattered light collected with the help of a lens is passed on to the interference filter to obtain Raman spectrum of the sample.

In case of CNT, the Raman spectrum carries a wealth of information about the structure. Raman spectra for samples involved in this thesis were acquired using *HORIBA JOBIN YVON LabRAM HR 800* with an excitation wavelength of 488 nm and 532 nm. The temperature variation of magnetic oxide encapsulated inside CNT sample was acquired with excitation wavelength 532 nm with the help of LINKAM stage from *LINKAM SCIENTIFIC*.

2.1.7 Thermal Gravimetric Analysis

Thermal Gravimetric Analysis (TGA) is a technique in which the mass of the sample is monitored. This is done either as a function of temperature, or (isothermally) as a function of time in a controlled temperature program and controlled atmosphere of nitrogen, helium, air, other gas, or vacuum. TGA is a technique in which weight of a material changes (increases or decreases) upon heating a material. This measurement provides information about several physical phenomena.

The sample pan is supported by a balance in a typical TGA measurement. The pan which sits in a furnace can be heated or cooled during the experiment. The mass of the sample is measured during the experiment. The environment is decided by the

purge gas. This gas may be inert or a reactive gas. The thermal analysis for the CNT samples was determined by a thermogravimetric analyzer, *PerkinElmer STA 6000*, under air at 20 mL/min, at a heating rate of $10\text{ }^{\circ}\text{C min}^{-1}$ from $30\text{ }^{\circ}\text{C}$ to $900\text{ }^{\circ}\text{C}$. This technique is used to characterize the CNT samples to yield information about the stability and purity of the sample as well provides an estimate of amount of carbon (CNT) / amount of residual particles present in the system.

2.2 Magnetic Characterization

In this section we explain the magnetic characterization technique. Bulk magnetization measurements were performed using Superconducting Quantum Interface Device (SQUID) magnetometer from *Quantum Design*. SQUID magnetometry is an effective and sensitive way of determining the magnetic properties of the sample. The system offers a sensitivity of $\sim 10^{-7}$ emu and the data can be recorded as magnetic moment as a function of temperature and magnetic field.

If a loop of superconducting wire is interrupted by a non-superconducting (resistive) region, it is expected that the wave function of the Cooper pairs exhibits a quick decay across the resistive barrier, which stops the flow of superconducting current. [62] In 1962, it was predicted by Josephson that the electrons can tunnel from one superconducting region to another when separated by an insulating barrier (weak link). For currents less than a critical value, the Cooper pairs can tunnel through the

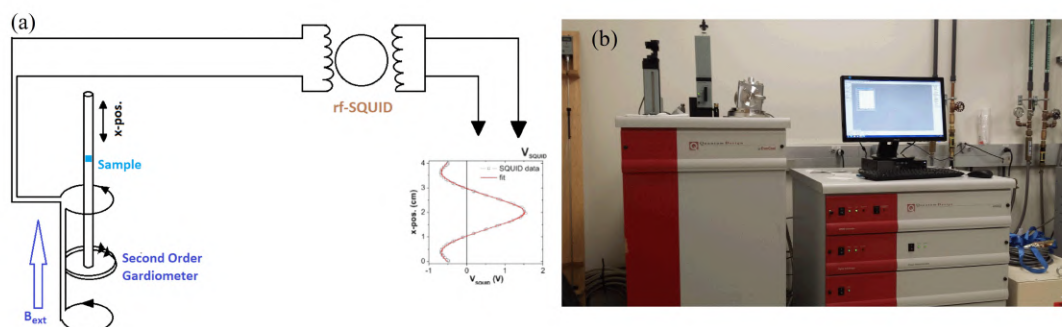


Figure 2.7: (a) Schematic of an SQUID magnetometer depicting configuration of superconducting detection coil. A typical response of the detection coil as a function of sample position is also shown. (b) Real-time picture of MPMS SQUID magnetometer from Quantum Design used for magnetic characterization of the samples.

weak link, and superconducting current can flow without any voltage applied. This is known as the Josephson effect. [62, 126]

SQUID utilizes the phenomenon of Josephson effect and magnetic flux quantization to measure the magnetic moment of a sample. [126] SQUID consists of a superconducting ring with superconductor-insulator-superconductor junctions. Each junction allows a small electric current flow through by Josephson effect which is highly sensitive to the magnetic field in the ring. The primary superconducting components in the system are – superconducting magnet and superconducting detection coil. The superconducting detection coil is a single wire wound as shown in Figure 2.7(a). This configuration is known as the second order gradiometer. The superconducting coils are positioned at centre of the superconducting magnet which allows the magnetic field from the sample to couple inductively with the superconducting coils. The gradiometer configuration ensures reduction in noise caused by the fluctuations in the large magnetic field of the superconducting magnet.

The sample space is made up of a tube maintained at a low pressure with helium gas. The top of the sample space is an airlock which can be evacuated and filled with helium from the liquid helium dewar. The powder sample is filled in a capsule and placed inside a plastic straw. It is then mounted on the sample holder attached to the end of a sample rod. The top of the sample rod is attached to a stepper motor system to move the sample through the detection coil in discrete steps. Figure 2.7(b) shows the real-time picture of the *MPMS SQUID magnetometer* from Quantum Design. [127] The detection coils sits outside the sample space dipped within the liquid helium bath. The superconducting detection coils are positioned at the centre of the superconducting magnet wound in solenoid configuration in such a manner that the magnetic field from the sample is inductively coupled to the detection coils.

When the sample is moved, flux changes within the detection coil. This change of flux changes the current flowing in the superconducting circuit. The current induced in the detection coil is associated with the movement of a magnetic dipole through a second order detection coil. The variations in the current flowing in the coils proportional are to the magnetic moment of the sample, and lead to corresponding variations in the SQUID output voltage.

2.3 Electrochemical Characterization

A variety of oxides (hematite, magnetite, cobalt oxide, nickel oxide) were encapsulated inside CNT which are presented in this thesis. To test the performance of these hybrids as anode materials for lithium-ion batteries, electrochemical measurements were performed. In this section, we discuss the two ways of cell fabrication – coin cell and Swagelok-type cell, which were used in this thesis for electrochemical characterization. This is followed by the discussion about the various electrochemical measurements to test the battery’s cycle life, performance at different rates, cyclic voltammetry to understand the cathodic and anodic reactions, and electrochemical impedance to gain information about the cell’s internal resistance and charge transfer resistance testing the conductivity of the material.

2.3.1 Cell Fabrication

2.3.1.1 Coin Cell

The electrodes prepared over the course of this thesis consisted of three components: the active material to be tested, a carbon additive used for increasing the conductivity of the electrode, and a binder to keep the electrode together on cycling. The working electrode was fabricated by making a slurry of the active material (Oxides filled CNT in powder form), conductive material (acetylene black), and binder (polyvinylidene fluoride) using N-Methyl-2-pyrrolidone (NMP) as the solvent. The weight ratio of active material: conductive carbon: binder = 8:1:1 was kept constant for preparing all the electrodes. The slurry was then spread onto the copper foil and kept for drying at 80 °C for 12 hours. Post drying the copper foil was hot pressed at a temperature of 50 °C, and thereafter, was cut into suitable shape and size according to the size of the coin cell.

The majority of the electrochemical data presented in this thesis were collected using coin cell assembly. Coin cells were assembled from CR2032 coin cell parts and the cell was assembled using a hydraulic argon press in an argon filled glove-box. Figure 2.8 shows a schematic of a typical coin cell using lithium foil as the counter electrode.

The electrochemical behaviour of the as-prepared Oxides@CNT as anode materials was studied using CR2032 coin type cells using lithium foil as the counter and reference electrode, Whatman membrane / Celgard as the separator with 1M LiPF₆

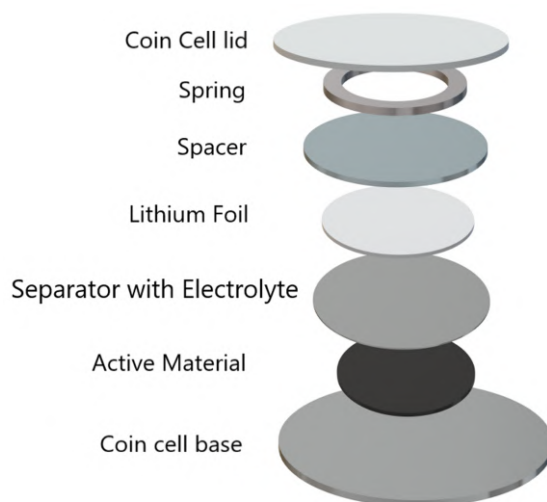


Figure 2.8: *Schematic of a typical coin cell assembly of the electrode half-cells.*

in ethylene carbonate and diethyl carbonate (EC:DEC = 1:1 v/v) as the electrolyte. When assembling a coin cell, spring is first placed in the negative case.

A spring was placed on end of the coin cell followed by a spacer on the top of the spring. The active material to be tested, which was casting of oxides encapsulated within the core cavity of the CNT was placed on the spacer. Three drops of electrolyte were placed with the help of a dropper on the active material (on copper foil) and then the separator was put on the top of the anode copper foil. The electrolyte helps to facilitate lithium-ion transfer between counter electrode and working electrode. Another three drops of electrolyte were placed on the separator, and then cathode was placed on the top of it. The other side of the coin cell was then put and the cell was pressed. After all elements were aligned, the coin cell was crimped using a compact hydraulic crimping machine.

2.3.1.2 Swagelok-type Cell

The active material, binder (PVDF), and carbon black were mixed in a pestle mortar with mass ratio 8:1:1. A few drops of NMP were added in order to produce a spreadable slurry. This was applied on a copper mesh (10mm diameter) with a spatula. The electrodes were then dried overnight in vacuum at 12 mbar and 65°C. The electrodes were then pressed at 10 MPa before putting them into the glovebox.

The Swagelok-type cells were prepared using copper mesh as the current collector.

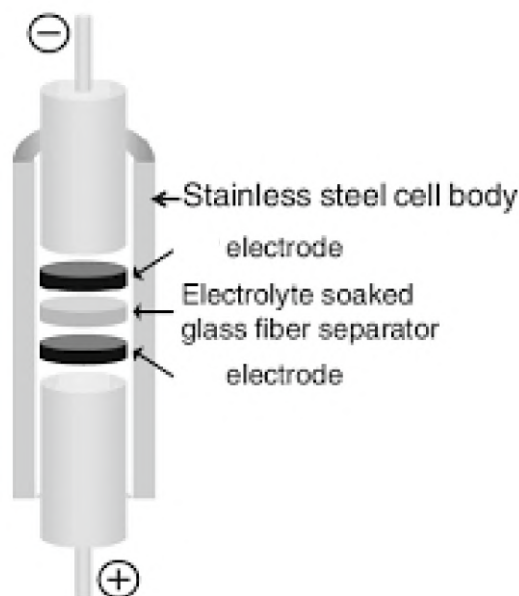


Figure 2.9: *Schematic of a Swagelok-type cell.* [128]

A schematic of Swagelok-type cell is shown in Figure 2.9. The counter electrode was lithium metal pressed on a nickel plate (12 mm diameter). Two layers of glass microfiber (Whatman) were used as a separator. The electrolyte was 200 μl of a 1M solution of LiPF_6 in 1:1 ethylene carbonate and dimethyl carbonate.

2.3.2 Electrochemical Measurements

2.3.2.1 Galvanostatic Cycling

Galvanostatic cycling is useful method for evaluating the electrochemical performance of an electrode and its active material. [96, 131] The amount of charge stored as a function of cycle numbers is measured under various experimental conditions. This method can be used to determine the specific capacity and the life expectancy of the electrode material (battery).

The dynamic performance of a battery is the speed at which current can be put into and extracted from storage during charging and discharging process respectively. Cyclic Charge-Discharge is the standard technique which is used to test the electrochemical performance and cycle-life of batteries. [96, 131] In galvanostatic cycling, the battery is charged and discharged between two specified voltage points at a constant

current.

During charging and discharging, the terminal voltage rises and falls as shown in Figure 2.10(a). The dynamics of charge and discharge of batteries can be characterized by measurements of voltage under constant charge and discharge current inputs. The charge and discharge measurements are performed at different current rates. Galvanostatic cycling is conducted over a range of current densities to gauge the rate capability of a battery. For example, the high rate discharge case indicates that the voltage falls quickly and only a part of capacity can be utilized at high discharge rates.

The charge behaviour for battery cell initiates at a constant current. The current is then held constant at a certain value. The specific charge current is expressed as mA g^{-1} . The mass mentioned is relative to the amount of the active material. The ratio between the charge put into and extracted during the intercalation and de-intercalation processes, respectively, is defined as the cycling Coulomb efficiency. [96, 131] This parameter indicates the reversibility of an electrochemical process.

There are several methods of galvanostatic cycling. The current can either be held at a constant current over several cycles to test the battery's life time and stability as shown in Figure 2.10(b). Here the specific capacity is plotted as a function of cycle number at a constant current density to examine the battery's cycle life. The initial capacity drop is due to the formation of solid electrolyte interface (SEI) film. [96] However, the curve shown in Figure 2.10(b) exhibits a good cyclic life over more

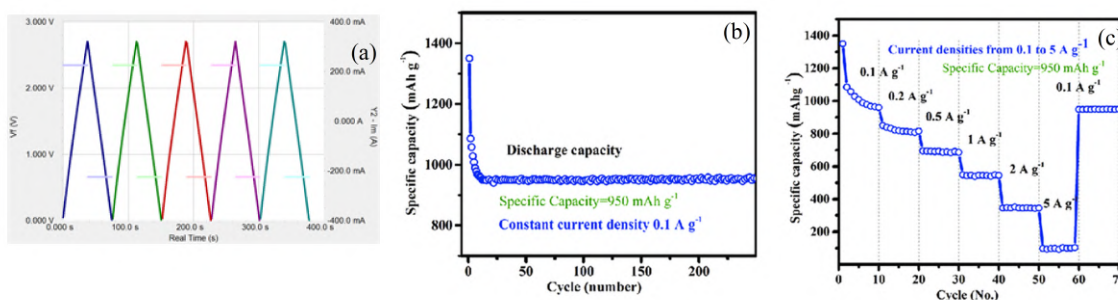


Figure 2.10: (a) Shows the voltage as a function of time for discharging and charging cycles. (b) Shows a typical specific capacity curve as a function of cycle number at constant current density to test the battery's cycle life. (c) Shows a typical rate capability curve performed at various rates to gauge a battery's performance at different current densities. [129, 130]

than 200 cycles. Or, the electrochemical performance can be measured at varying current rates (Figure 2.10(c)). This method would provide information about the load capability of the cell. The performance of the material typically decreases as higher current rates. This is due to the fact that at higher current rates, the time needed for Li-ion diffusion is often not sufficient, which affect the electrochemical performance. [96, 131]

The electrode materials discussed in this thesis were tested on *MTI corporation battery analyzer* for galvanostatic cycling.

2.3.2.2 Cyclic Voltammetry

Cyclic voltammetry (CV) is an electrochemical measurement technique which provides information about the electrochemical behaviour of a cell. [131] The primary event involved is the oxidation and reduction of the active material at the working electrode. Cyclic voltammetry is used to gain information about the thermodynamics of redox process occurring during the electrochemical measurements and also sheds light on the kinetics of the electron-transfer reactions taking place in the cell. [131] CV provides both qualitative and quantitative understanding of the electrode processes.

In a typical CV experiment, the voltage of a working electrode with respect to the reference electrode is ramped linearly as a function of time in cyclic phases. [131] After the potential is reached to a set value in a CV experiment, the working electrode's potential is ramped in the opposite direction to return to the initial value of the potential. A CV can be considered figuratively an electrochemical “fingerprint” for

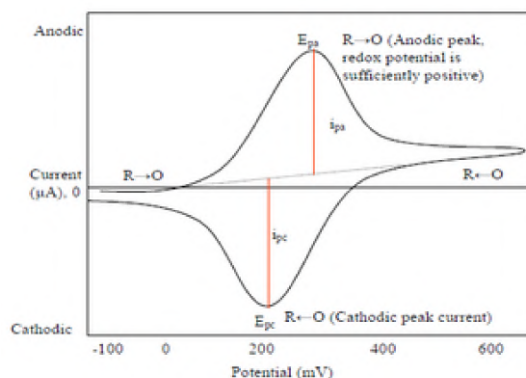


Figure 2.11: A typical cyclic voltammetry (CV) curve where i_{pc} is the cathodic current and i_{pa} is the anodic current. [132]

the redox processes taking place in the cell. The current response versus voltage data provide evidence which support the occurrence of a redox reactions in the cell.

The potential sweep rate is the rate of change of the potential with time and is known as the scan rate (V s^{-1}). The scan rate (dV/dt) changes sign at each reversal point. The scan rate (V s^{-1}) determines the timescale of the experiment. It is important to mention that the shape of the peak is dependent on the scan rate.

A typical CV curve is shown in Figure 2.11. During the initial forward scan, an increasing reduction potential is applied. The cathode current then start to increase denoted by i_{pc} , assuming there are reducible analytes in the system. When the reduction potential of the analyte has reached, the cathode current will start decreasing due to the the depletion of the reactants, which reduces the concentration of the analyte. In the reverse scan, the reduced species starts to re-oxidize. This gives rise to anodic current marked as i_{pa} in Figure 2.11. A symmetrical pair of current peaks indicate the presence of reversible and diffusion controlled reaction. The CV measurements presented in this thesis were performed on *Ametek potentiostat* at a scan-rate of 0.1 mV s^{-1} from 0.01 to 3 V.

2.3.2.3 Electrochemical Impedance Spectroscopy

Classical Ohm's law explains the simplistic definition of electrical resistance as the ratio between voltage V and current I for ideal resistors. [131] In case of real circuits consisting of resistors, capacitors, inductors, etc., impedance is a more relevant circuit parameter.

The fundamental approach of impedance lies in the application of a small amplitude sinusoidal signal (voltage or current) and investigate the response (current or voltage). Electrochemical Impedance Spectroscopy (EIS) involves application of sinusoidal potential signal of variable frequencies to the electrochemical cell and measure the resultant alternating current signal through the cell. The system response can provide information such as the interface, structure, and the reactions involved in the electrochemical cell. [131]

EIS is usually measured using a small sinusoidal AC voltage signal $V(t)$. The ac current response $I(t)$ will be a sinusoid of the same frequency but with a different phase. The excitation ac voltage has the form: [131]

$$V(t) = V_o \sin(\omega t), \quad (2.11)$$

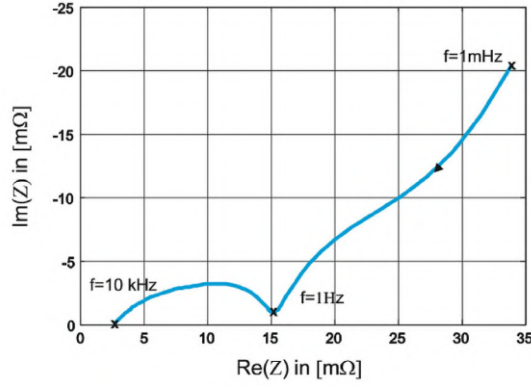


Figure 2.12: A typical Nyquist plot depicting the charge transfer resistance by the semi circle in the high frequency region and Warburg impedance by the tail in the low frequency region. [133]

where, V_o is the signal amplitude and ω is the radial frequency described as:

$$\omega = 2\pi f. \quad (2.12)$$

The current response signal can be written as: [131]

$$I(t) = I_o \sin(\omega t + \phi), \quad (2.13)$$

where, I_o is the amplitude of the response signal and ϕ is the phase shift. The impedance Z of the system can be written as: [131]

$$Z = Z_o (\cos(\phi) + i\sin(\phi)) = Z' + iZ'', \quad (2.14)$$

where, Z' and Z'' are the real and imaginary parts of the impedance respectively.

Data presentation of the EIS is done by plotting Z' versus Z'' at different frequencies in a complex plane. This is known as the Nyquist plot. Each point on this plot denotes impedance at that a particular frequency. [131] A typical Nyquist plot is shown in Figure 2.12. The Nyquist plot represents three different processes. The Ohmic resistance due to the Li-ion diffusion within the electrolyte is given by first point of the real component of the semi-circle. [92, 111, 131, 134] The semicircle represents the charge transfer between the electrode material and the electrolyte. [92, 111, 131, 134] This is known as the charge transfer resistance R_{ct} and consists of both capacitive and

resistive elements. [92, 111, 131, 134] Diffusion of the electro-active species creates an impedance known as Warburg impedance, and occurs as a tail in the low frequency range as shown in Figure 2.12. [92, 111, 131, 134] At lower frequencies, the impedance is capacitive in nature. [92, 111, 131, 134]

The EIS measurements for the samples examined in this thesis were performed on *Ametek potentiostat* instrument in the frequency range 10 mHz - 300 kHz.

Chapter 3

Synthesis of 3d Transition Metals and Oxides filled Carbon Nanotubes

This chapter demonstrates the use of a single-zone furnace to synthesize 3d transition metals and their respective oxides inside encapsulated CNT. We first outline the details of the experimental setup involving powder chemical vapor deposition (CVD) of metallocene. In the subsequent sections, synthesis and characterization details of metal-filled CNT are presented. A systematic variation of synthesis parameters and their effect on the morphology have been extensively explored for iron-filled and nickel-filled samples. This also sheds light on the underlying reasons that lead to the difficulties associated with the synthesis of nickel (and cobalt) filled CNT. In the last section, synthesis details for conversion of metal-filled CNT to metal-oxide filled CNT are discussed.

3.1 Solid State CVD for Metal-filled CNT

It is to be recalled that chemical vapor deposition (CVD) is an effective and convenient method to synthesize single-wall and multi-wall CNT, both pristine and filled. [10] This technique requires a hydrocarbon precursor compound and a catalyst which facilitates the growth of graphitic shells. Organometallic compounds are generally used for catalytic synthesis of filled CNT. Specifically, metallocenes ($M(C_5H_5)_2$), where M can be iron, nickel or cobalt, are the most commonly used precursors for

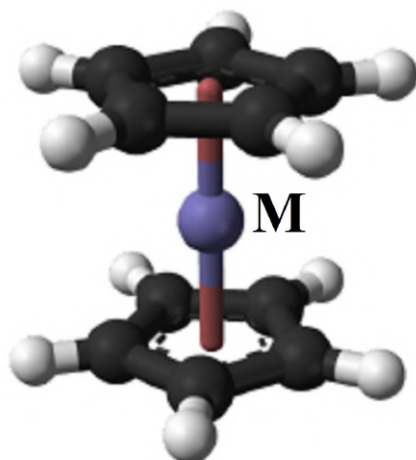


Figure 3.1: Representation of a ferrocene molecule as a model to depict the general structure of metallocene. It consists of two rings of organic molecules (ligands) which are bound to the central metal atom (M). The centre atom is iron (blue) marked as 'M' and the carbon atoms are marked black and hydrogen atoms are white respectively. [10]

filled carbon nanotubes synthesis. [10, 33, 34, 46–48, 51] The metallocene ($M(C_5H_5)_2$) consists of two cyclic organic molecules bound to a central metal atom. Figure 3.1 shows representation of a metallocene molecule depicting its general structure. These compounds provide both the carbon source and the metallic catalyst particles to facilitate the growth of the CNT. The metallocenes have relatively low sublimation temperature (150 - 300 °C) which make them the most common and convenient choice as a precursor. [10, 33, 34, 46–48, 51]

In the usual *Solid State CVD*, a dual-zone furnace is used for pyrolysis of *powder* metallocene. In the first temperature zone, known as the sublimation zone, the metallocene is directly sublimed at a specific temperature (sublimation temperature of the precursor) referred to as the sublimation temperature " T_{sub} ." The metallocene plumes are transferred by an inert gas to the second zone known as the pyrolysis zone which is maintained at a relatively higher temperature than the sublimation temperature referred to as the pyrolysis temperature " T_{pyro} ." The decomposition and growth of filled CNT occurs in the pyrolysis zone, and the morphology of the CNT formed depends crucially on T_{pyro} and T_{sub} . Therefore, one requires a dual-zone furnace with two independent temperature controllers to control sublimation or pyrolysis temperature.

The metal and metal-oxides filled Carbon Nanotubes (CNT) samples investigated

in this thesis have been synthesized using *Solid State* Chemical Vapor Deposition method. In the following section, we demonstrate the use of a *single-zone* furnace with a modified synthesis chamber design to obtain metal iron, nickel, and cobalt as well as metal-oxides filled CNT.

3.2 Single-Zone Furnace for Powder CVD of Metallocene : Mechanical Assembly

In this section, we present how a single-zone furnace can be modified efficiently to synthesize metal- and metal-oxides filled CNT which otherwise requires a dual-zone furnace. For this, a single-zone horizontal tube furnace *Nabertherm R 100/750/13* was used which can attain a maximum temperature of 1300 °C. The inner diameter of the ceramic tube furnace is 40 mm and the length of the ceramic tube is ~ 1.5 m.

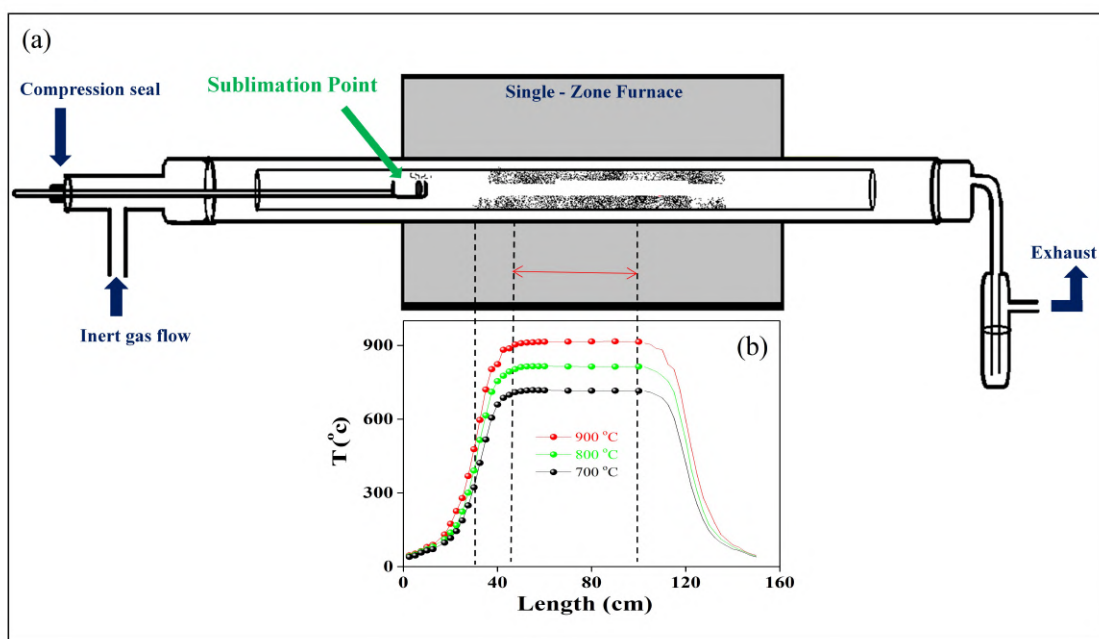


Figure 3.2: (a) shows a schematic of the single-zone furnace depicting the modified synthesis chamber. The synthesis chamber consists of two co-axial quartz tubes. The movement of the quartz rod attached to the quartz boat inside the synthesis chamber is enabled by the compression seal arrangement. The temperature profile of the furnace for three set temperatures, 900, 800, and 700 °C, is shown in (b).

Figure 3.2(a) shows the schematic of the single-zone furnace. The temperature profile of the furnace shown in Figure 3.2(b) was done using a 1.2 m K-type thermocouple. The temperature profiles for different set-temperatures; 700 °C (black), 800 °C (green), and 900 °C (red) are shown in Figure 3.2(b). The single-zone furnace consisted of a constant temperature zone in the middle extending up to ~ 60 cm in length with temperature stability of ± 2 °C, along with two variable temperature zones on either side. The constant region in the middle can be used as the pyrolysis region with T_{pyro} , and the variable temperature on either side of the constant zone can be then used as the sublimation zone at temperature T_{sub} .

3.2.1 Synthesis Chamber and Sample Insertion Arrangements

The synthesis chamber consists of two coaxial quartz tubes – outer tube and inner tube inserted within the single zone-furnace. The typical length of the outer quartz tube is ~ 170 cm with inner diameter is ~ 37 mm and wall thickness ~ 3 mm. The inner tube is ~ 1 m in length inner diameter with 25 mm and wall thickness ~ 3 mm. The inner tube serves as the main quartz reactor for the deposition of the CNT.

The outer quartz tube is connected to a standard compression seal arrangement at one side to allow the insertion of the precursor i.e. metallocene in powder form. The other end of the quartz tube is connected to the acetone trap as shown in Figure 3.2(a). A quartz boat (about 5 cm in length) is fused at one end of a quartz rod. The metallocene in powder (or pellet) form is placed in the quartz boat. This assembly can be moved to any predetermined spot within the inner quartz tube using the compression seal arrangement. The compression seal arrangement allows the quartz rod to move with precision inside the inner quartz reactor without disturbing the inert gas flow.

The compression seal arrangement along with the temperature profile allows one to extend the use of a single-zone furnace as a dual-zone furnace by suitable choice of T_{pyro} and T_{sub} . This removes the limitation of requirement of a dual-zone furnace for synthesis of filled CNT. The design of the synthesis chamber and modifications lead to a better control in length, diameter, filling efficiency and morphology.

A general experimental protocol followed for the synthesis of metal-filled CNT is discussed in the next section.

3.2.2 Experimental Procedure

The precursors – *Ferrocene*, *Nickelocene* and *Cobaltocene* 98% pure for synthesis of metal-filled CNT (metal@CNT) was procured from Sigma Aldrich. The setup described in section 3.2 is employed for the synthesis runs discussed throughout the thesis. The outer quartz tube (37 mm diameter and 170 cm length) were annealed at 800 °C for twelve hours prior to any synthesis run. Fresh and thoroughly cleaned dried inner quartz tubes (28 mm diameter and 100 cm length) were used for every synthesis run.

Appropriate amount of metallocene, typically 500 mg, was used in pellet or powder form. The metallocene was then placed at one of a quartz boat with one end fused to the quartz rod. The quartz boat containing the metallocene precursor was then connected to one end of the outer quartz tube. The quartz boat containing precursor is positioned such that it remains at room temperature, to avoid its sublimation while heating the furnace to a fixed set temperature.

Prior to heating of the furnace, the quartz chamber was flushed with argon gas for around ten minutes. The furnace was then switched on and programmed to heat from room temperature up to optimized T_{pyro} at a rate of 900 °C per hour while the quartz boat containing the metallocene is still held at room temperature. When the furnace attains the required fixed temperature (T_{pyro}), the quartz boat is pushed to a pre-determined sublimation point T_{sub} through the compression seal assembly. The sublimation point is the predetermined from the furnace temperature profile (Figure 3.2(b)). The sublimation enables the plumes to reach the the zone in the middle at T_{pyro} with the help of carrier gas, which is argon gas in our case.

The series of steps followed for the synthesis of metal-filled CNT are listed as follows.

- Place the precursor in powder or pellet form in the quartz boat and close the outer tubes from both the ends.
- Flush argon flow for ten minutes.
- Switch on the furnace and set it up to stabilize at a fixed T_{pyro} . The argon glow is maintained at 2000 sscm while the temperature is stabilized to $\pm 2^{\circ}\text{C}$ in the middle zone.

- After the furnace attains the set temperature, adjust the argon gas flow as per the synthesis conditions for a particular run.
- Push the quartz rod containing the precursor to the pre-determined spot i.e. sublimation point with the help of a compression seal-arrangement.
- Hold for the required reaction time (typically ten to fifteen minutes).
- Switch off the furnace and allow it to cool down to room temperature under argon gas flow atmosphere.
- The samples are scraped off from the walls of the inner quartz tube from its different regions – the variable temperature region and the constant pyrolysis region.

3.2.3 Role of Synthesis Parameters

In order to optimize the synthesis parameters, one needs to understand the role of individual synthesis parameter. Below we briefly discuss the four relevant synthesis parameters, and whether they are independent or inter correlated. For all the individual synthesis runs reported in this thesis, there are four important parameters that determine the morphology and the quality of the final product – the metal filled CNT. These parameters are T_{pyro} , T_{sub} , rate of argon flow, and the type and amount of precursor. For each type of filling we varied one of these four parameters while the remaining three were held constant during a particular synthesis run.

3.2.3.1 Sublimation Temperature (T_{sub})

The three metallocenes – ferrocene, nickelocene, and cobaltocene can sublime at any (fixed) temperature between 120 and 400 °C. For the present setup, the temperature accuracy of sublimation temperature is approximately ± 10 °C over a length of ~ 2 cm, when the precursor is used in the powder form. The temperature accuracy of the sublimation region can be further narrowed down to ± 5 °C by reducing the spread of the precursor, which can be achieved by using the precursor in the form of a pellet instead of powder. For each type of metallocene, the best sublimation temperature is optimized after many trials in which the T_{sub} was varied while other three parameters are kept fixed.

3.2.3.2 Rate of Argon-flow

The sublimed plumes are transferred to the pyrolysis zone which is ideally in the middle region of the furnace using an inert transport gas. The rate of argon-flow plays an important role in the synthesis of filled CNT. The rate of argon-flow has to be optimized so that the sublimed plumes are able to reach the pyrolysis temperature zone. In case of very high-flow rates, the plumes are carried to the other end of the quartz tube without any deposition in the pyrolysis region. Thus, optimization of rate of argon-flow is required, for a fixed set of other synthesis parameters.

3.2.3.3 Pyrolysis Temperature (T_{pyro})

For any given T_{pyro} , the constant temperature zone or the middle zone of this furnace extends up to ~ 60 cm in length (Figure 3.2(b)). The temperature accuracy of the pyrolysis region is $\sim \pm 2$ °C. For a fixed T_{pyro} , a larger yield of CNT with a fixed morphology is obtained due to a longer pyrolysis zone with better temperature accuracy.

For a fixed T_{pyro} , say 900 °C in the middle zone, CNT will not only deposit only in the middle constant zone, but also in the variable temperature zone on either side of the middle constant zone (pyrolysis zone). For $T_{pyro} : 900$ °C, the temperature in the variable region varies from 600 to 900 °C, a range which is known to be conducive to facilitate the growth of CNT. Therefore, scraping the CNT from the inner quartz tube reactor post the reaction can lead to unintentional mixing of CNT deposited in the variable temperature zone, along with the CNT deposited at the constant temperature region i.e in the pyrolysis region. It is also to be noted that the presence of a variable temperature region cannot be avoided either in a routine dual-zone furnace based CVD, or in the present single zone furnace.

However, to circumvent this problem, the portion of the inner quartz tube is marked w.r.t. a fixed point to separate the variable and constant temperature zones. The sample is then collected separately from both the regions. This prevents the mixing of the samples retrieved from the constant zone and the variable temperature region.

3.2.3.4 Camphor as a Co-precursor with Metallocene

There have been reports on the synthesis of CNT using only camphor as a precursor. [26, 122] However, in this work we have used camphor in combination with metallocene to form metal-filled CNT. Camphor can be used as a co-precursor with metallocene to yield metal-filled CNT. In cases where the carbon from the metallocene is insufficient to facilitate the growth of CNT, using camphor can provide the extra source of carbon. In addition, co-pyrolysis of camphor with metallocene can be used to achieve a variety of self-organized structures depending on the ratio of amount of camphor and metallocene. For these trials, additional parameter – the ratio of camphor : metallocene needs to be optimized along with T_{sub} , T_{pyro} , and rate of argon-flow.

Having discussed the significance of each synthesis parameter, in the following sections we present the results for each sample – iron-filled CNT and nickel-filled CNT in separately. For each sample, the each synthesis parameter is optimized for a fixed set of other parameters. In addition, a systematic variation of synthesis parameters is discussed for both the samples.

3.3 Iron-filled Carbon Nanotubes (Fe@CNT)

3.3.1 Morphology and Structural Characterization

Figure 3.3 depicts the outcome of a typical synthesis run for Fe@CNT. The synthesis parameters for this sample have been outlined in Table 3.1. These Fe@CNT carpets shown in Figure 3.3 are obtained from the T_{pyro} region. These carpets are up to a few 100 μm in length and consist of aligned forest of CNT with length $\sim 20 \mu\text{-m}$ and diameter $\sim 20 - 40 \text{ nm}$. The diameter distribution is significantly narrowed down as evident from Figure 3.3. Since, the sample is collected only from the pyrolysis region, fairly reproducible results are obtained in terms of morphology, length, diameter and filling efficiency. The narrow length and diameter distribution of the obtained Fe@CNT samples can be attributed to the temperature stability of the pyrolysis region. This circumvents one of the biggest challenges while investigating metal or metal-oxide encapsulated CNT for fundamental as well as the potential device applications.

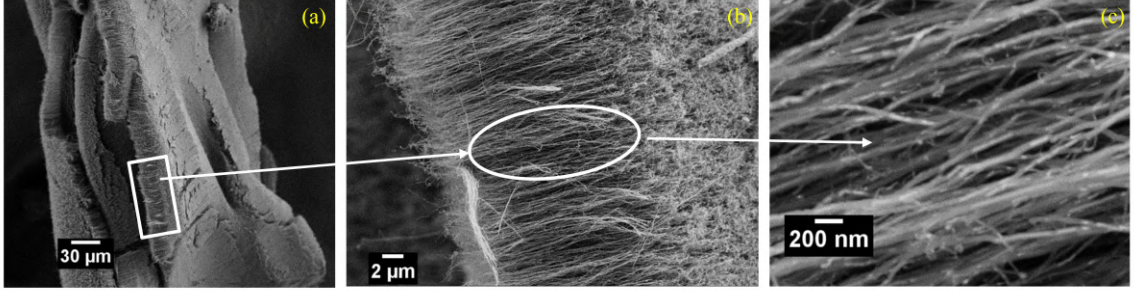


Figure 3.3: (a) - (c) Representative FESEM micrographs of Fe@CNT obtained using synthesis conditions given in Table 1. (a) depict aligned forests of Fe@CNT which are few μ -m in length. (b) - (c) display the as-prepared CNT at at higher magnifications clearly depicting narrow length and diameter distribution.

In order to access the crystallinity and phase of the Fe@CNT, XRD and Raman measurements were performed on the powder samples. Representative XRD pattern is shown in Figure 3.4(a). The diffraction peak observed at 26.0° corresponds to characteristic peak for graphitic shells of the CNT. In addition to the signature peak of CNT, peaks reflections from the encapsulate are also present. These diffraction peaks are attributed to body centered cubic (*bcc*) structure of iron. Minor contributions of oxides of iron are also present which are formed due to the oxidation of the outside residual particles.

Figure 3.4(b) shows the representative Raman spectra acquired at room temperature. The crystallinity of the graphitic shells and the defects in sp^2 -hybridized carbon structure are evaluated using Raman spectra. The Raman spectra show characteristic graphitic (G) band position 1575 cm^{-1} which is attributed to the tangential vibration of the carbon atoms. [11] Defect-induced D-band is also present at 1351 cm^{-1} which results from the presence of the defects. This mode is forbidden in perfect graphitic materials and is activated only in the presence of any kind of defects. A third peak, corresponding to 2D or G' at $\sim 2700\text{ cm}^{-1}$, is also observed and the

Table 3.1: Optimized synthesis parameters for Fe@CNT.

Amount of ferrocene	500 mg
T_{sub}	300 $^\circ\text{C}$
T_{pyro}	900 $^\circ\text{C}$
Rate of argon-flow	2500 sscm

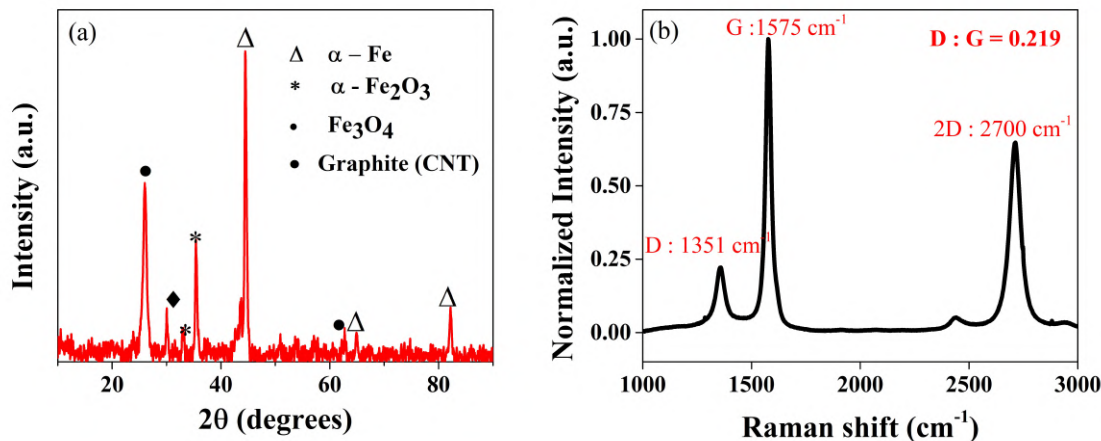


Figure 3.4: (a) Representative powder XRD pattern of as-prepared Fe@CNT at optimized conditions. (b) Representative Raman spectrum for Fe@CNT acquired at room temperature. The ratio of intensities of D-band and G-band is 0.219 signifying good crystallinity of the CNT.

data are consistent with earlier reports on Fe@CNT. [11] The ratio of the intensities of defect and graphitic band, I_D/I_G is 0.219 which indicates the good quality of the graphitic shells.

To confirm the nature of the encapsulate and examine the detailed structure of individual CNT, TEM micrographs were recorded and a few representative images are shown in Figure 3.5. The TEM images shown in Figure 3.5(a-c) were recorded for Fe@CNT at intermediate magnification range in order to examine a relatively broader area with multiple CNT. The TEM micrographs were also recorded at various different regions to gain statistical data. This confirms the uniformity of the filling as well as the length and diameter distribution.

The images presented in Figure 3.5(a-c) give a rough estimate of the filling efficiency of the *as-prepared* Fe@CNT samples. It is to be noted these images demonstrate good filling efficiency and reduced catalytic particle density for the *as-prepared* samples. These images also depict narrow diameter distribution of the nanotubes. The encapsulate is in the form of long nano-wires as evident from TEM images shown in Figure 3.5(a-c). The high-resolution TEM images in Figure 3.5(d) confirm the existence of crystalline metal (Fe) nano-wires encapsulated within the core cavity of the CNT. The well-formed graphitic shells are consistent with the Raman data. The

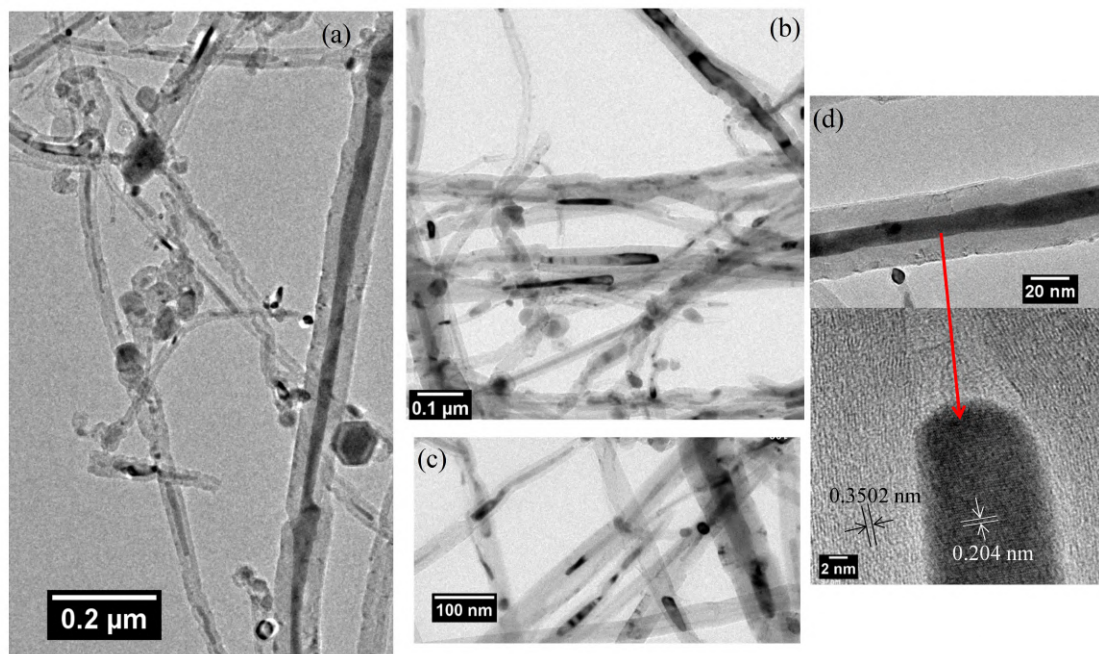


Figure 3.5: (a)-(c) are representative TEM micrographs for Fe@CNT. The images depict the metal nano-wires encapsulated inside CNT. (d) shows high-Resolution TEM micrograph of an individual CNT with well-formed graphitic shells. The crystalline nature of the encapsulate is evident from the TEM image. The black and white arrows mark the lattice spacing corresponding to the graphitic shells and Fe encapsulate.

metal encapsulate nano-wires are crystalline in nature which is confirmed by lattice periodicity. The lattice spacing obtained are in accordance with d-spacing value of (110) plane.

3.3.2 Estimation of Filling Efficiency

The filling efficiency of the samples can be estimated from the thermogravimetric analysis (TGA) and bulk magnetization measurements in conjunction with TEM and Raman data. However, the metal encapsulated within the core cavity and the catalytic metal particles which adhere outside CNT cannot be differentiated by either TGA, or magnetization measurements. In the following, we show TGA and bulk magnetization data to gauge the filling efficiency of the *as-prepared* Fe@CNT samples.

3.3.2.1 Thermo-Gravimetric Analysis TGA

The filling efficiency for Fe@CNT is estimated through thermogravimetric analysis measurements. The TGA measurement is performed in air from 30 °C to 900 °C at a heating rate of 10°C min⁻¹. The TGA profile shown in Figure 3.6(a) depicts the carbon weight to be ~ 52 % and residual weight to be ~ 48% which is oxidized iron. This gives an indication of the approximate filling efficiency. The residual percentage is the amount of oxidized iron which is left after heating the sample in air up to 900 °C. A high percentage of ~ 48% indicates high fraction of filling within the core cavity of the CNT; though it cannot rule out the contribution of the residual particles.

3.3.2.2 Bulk Magnetization

As mentioned in chapter *one*, in case of *Solid State* CVD, the metal nanoparticles help to facilitate the growth of CNT and assemble in the form of long nano-wires within the core cavity of the CNT (Figure 3.5). The metal nano-particles / nano-wires are inherently ferromagnetic in nature. When they are encapsulated inside CNT, they exhibit ferromagnetic behaviour which is reflected in bulk magnetization measurements. [50] The saturation magnetization (M_S) serve as a yardstick to evaluate the magnetic contributions from the metal encapsulated within the core cavity of the CNT. The metal nanoparticles which adhere outside the CNT also contribute

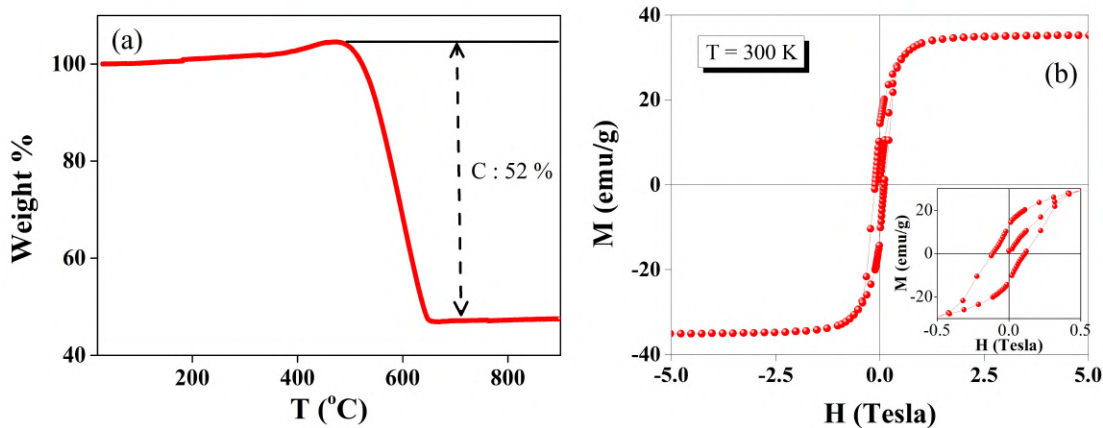


Figure 3.6: (a) displays the TGA curves of Fe@CNT sample obtained under air from 30 °C to 900 °C at a heating rate of 10 °C min⁻¹. The residue weight % was found to be 48%. (b) shows M-H isotherm of Fe@CNT depicting $M_S \sim 40$ emu/g.

to an overall magnetic signal. This contribution is often non-trivial to untangle from the metal encapsulate inside the CNT. Thus, the M_S values from bulk magnetization measurements are inclusive of magnetic contribution from the encapsulate as well as the residue particles adhering outside the CNT.

The high filling efficiency is gauged by experimentally observed M_S value. M-H isotherm recorded at room temperature for Fe@CNT is shown in Figure 3.6(b). The sample Fe@CNT in aligned forest morphology exhibits $M_S \sim 40$ emu/g. The inset of Figure 3.6(b) shows the M_S limited to low field scans for a clear depiction of coercivity, H_C . The H_C value are ~ 100 Oe. The coercivity can be tuned by variations in pyrolysis temperature and can be tailored depending on specifications of the application. [48]

It is to be noted that the morphology, as well as the filling efficiencies for Fe@CNT can be further controlled by variations in the synthesis parameters, including the ratio of camphor and metallocene. A few representatives are presented in the next section.

3.3.3 Influence of Synthesis Parameters

In this section, we discuss the role of individual synthesis parameter and how its variation affects the morphology and other characteristics of Fe@CNT samples.

3.3.3.1 Role of Pyrolysis Temperature (T_{pyro})

The pyrolysis temperature T_{pyro} exhibits a strong influence on the formation of Fe@CNT. This can be done studying the comparison of the morphology of the *as-prepared* samples synthesized at different pyrolysis temperature keeping all the other synthesis parameters and process conditions constant. The results reveal a very interesting pattern when the pyrolysis temperature is varied.

The representative FESEM images for Fe@CNT samples synthesized with varying T_{pyro} – 900, 800 and 700 °C, while T_{sub} and rate of argon-flow are held constant, are shown in Figure 3.7(a-c). We observe that as the pyrolysis temperature is reduced from 900 °C to 700 °C, the aligned forest structure starts to disrupt and entangled *spaghetti*-like CNT start to form. Figure 3.7(a) shows the CNT formed at 900 °C depicting aligned forest morphology of Fe@CNT samples. At 800 °C, the forests begin to deform and CNT with larger outside particle density are obtained (Figure

3.3. Iron-filled Carbon Nanotubes (Fe@CNT)

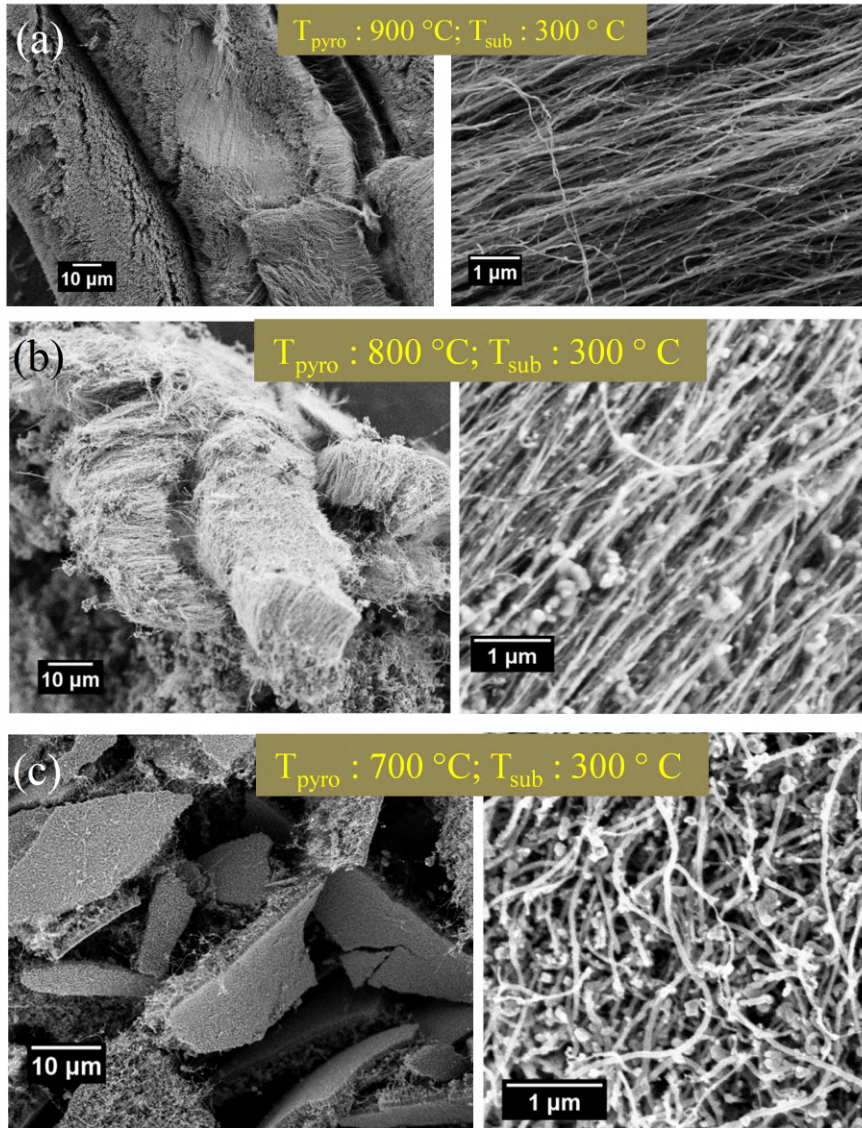


Figure 3.7: Representative FESEM micrographs for Fe@CNT for (a) the best-optimized parameters – $T_{\text{pyro}} : 900 \text{ }^\circ\text{C}$ and $T_{\text{sub}} : 300 \text{ }^\circ\text{C}$. (b) - (c) show representative FESEM images obtained at (b) $800 \text{ }^\circ\text{C}$ and (c) $700 \text{ }^\circ\text{C}$ at fixed T_{sub} and rate of argon flow.

3.7(b)). At low temperature $700 \text{ }^\circ\text{C}$, entangled CNT are formed as shown in Figure 3.7(c). It is also observed that on reducing the pyrolysis temperature, the outside residual particle density is larger. It is to be noted that for all the data shown in Figure 3.7, the sample for individual runs has been collected from the middle zone of the inner quartz tube. As evident from the temperature profile shown in Figure 3.2,

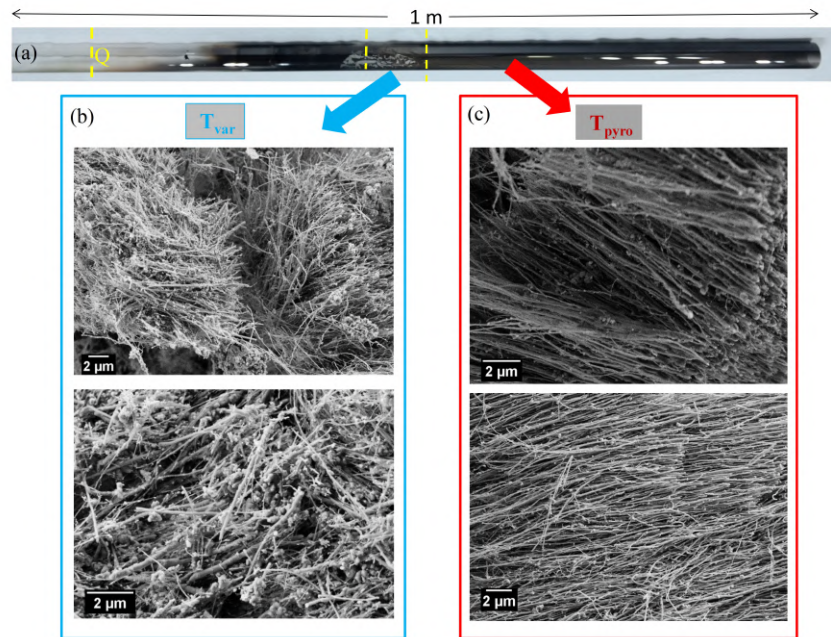


Figure 3.8: (a) shows a real-time image of typical inner quartz tube, post-synthesis. Q denotes the position of the quartz boat containing precursors. (b) and (c) show representative FESEM images of iron-filled CNT collected from a variable temperature region (T_{var}) and actual pyrolysis region (T_{pyro}).

the middle zone, also termed as T_{pyro} has temperature accuracy $\sim \pm 2^\circ\text{C}$.

The data presented in Figure 3.7, the sample is collected from the middle zone for individual runs. These data suggest the pyrolysis temperature decides the alignment of the formed Fe@CNT samples. A higher pyrolysis temperature is observed to be more suitable for aligned forest structures. By varying pyrolysis temperature T_{pyro} , the morphologies of the Fe@CNT samples can be varied and tailored to application specific needs. The entangled CNT structures are best suited for applications in energy sector, whereas the aligned forest structures with reduced catalytic particle density can be pertinent for nano-electronic devices based on these hybrids. Desired morphology with uniformity, narrow length and diameter distribution of the final product is enabled due to a longer pyrolysis region with better temperature accuracy.

It is to be recalled that for each run, the sample can be retrieved from the variable temperature (T_{var}) region as well as constant (pyrolysis) region (T_{pyro}) separately. Figure 3.8 shows a real-time picture of a typical inner quartz tube post the reaction. The images shown in Figure 3.8(b) and (c) are collected from the variable temperature

3.3. Iron-filled Carbon Nanotubes (Fe@CNT)

region (T_{var}) and pyrolysis region (T_{pyro}) respectively. The sample collected from the pyrolysis region contains aligned tubes with narrow length and diameter distribution. In case of the sample collected from the variable temperature zone, a mixture of entangled CNT as well as disrupted forest structures with a large number of catalytic particles residing outside the CNT is obtained. The M_S for both the morphologies – aligned forest as well as entangled CNT, was found to be $\sim 30 - 40$ emu/g.

3.3.3.2 Role of Sublimation Temperature (T_{sub})

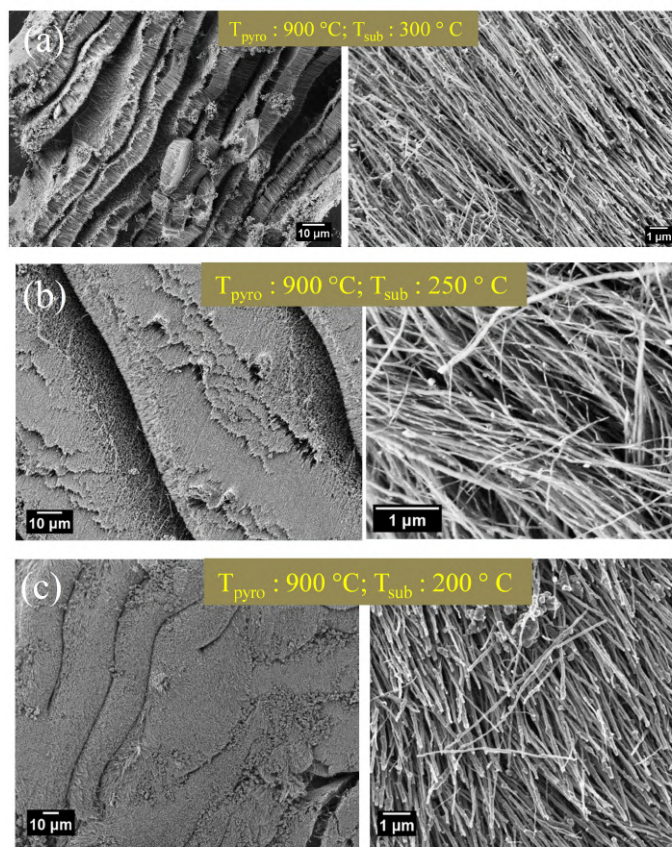


Figure 3.9: Images (a, b, c) show representative FESEM images of Fe@CNT sample with the variation in T_{sub} , keeping pyrolysis temperature constant. The forest structures are retained when the sublimation temperature is varied – (b) $250 \text{ }^\circ\text{C}$ and (c) $200 \text{ }^\circ\text{C}$.

In order to study the role of sublimation temperature T_{sub} on Fe@CNT samples, morphologies of samples prepared at different T_{sub} are compared keeping all the other

synthesis parameters fixed. Figure 3.9(a-c) shows representative FESEM micrographs obtained at different sublimation temperature $T_{sub} = 200, 250, 300$ °C, keeping T_{pyro} constant at 900 °C. The pyrolysis temperature is set to 900 °C which is the optimized T_{pyro} for best Fe@CNT samples (Table 3.1).

It is interesting to note that on varying the sublimation temperature T_{sub} , the morphology of the *as-prepared* CNT sample remains unchanged. The samples prepared at different sublimation temperature depict aligned forest morphology as evident from Figure 3.9. All the samples possess significantly narrow length and diameter distribution with very less residual nano-particles which adhere outside the CNT. Varying the sublimation temperature shows no / very little effect on the morphology of the samples. The aligned forest morphology is retained at different T_{sub} indicating that the sublimation temperature plays no major role in deciding the morphology while T_{pyro} is held constant. These data also hint towards that pyrolysis temperature primarily controls the morphology.

3.3.3.3 Role of Precursor

In this section, we investigate the influence and importance of the precursor employed for the synthesis of Fe@CNT. Here the important factors are – (i) amount of the precursor – ferrocene, and (ii) use of camphor as a co-precursor.

Owing to a long pyrolysis zone extending up to ~ 60 cm in length, the amount of precursor also becomes a crucial factor which affects the growth of CNT. We

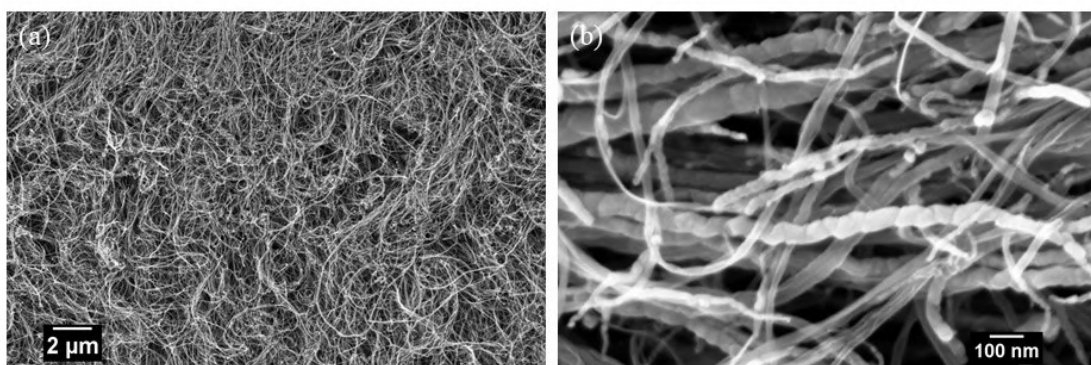


Figure 3.10: (a) - (b) Representative FESEM images of the sample Fe@CNT prepared using camphor as a co-precursor; with $T_{pyro} : 900$ °C and $T_{sub} : 300$ °C. The sample exhibits entangled morphology consisting of long curled entangled tubes.

find that on reducing the the amount of ferrocene (precursor) from 500 mg to 200 mg, keeping all the other parameters fixed as given in Table 3.1, the yield and the morphology of the *as-prepared* Fe@CNT samples is affected significantly. We find that no deposition of CNT was obtained in the pyrolysis region, and a mixture consisting of large quantities of carbon and iron composites along with disrupted CNT were formed in the variable region away from the middle constant pyrolysis zone. When the amount of ferrocene was further reduced to 100 mg, large chunks of nano-particles were observed in the variable temperature zone, with no traces of CNT in variable or pyrolysis region.

These data suggest that the amount of precursor holds an influential role on the formation of the CNT. The amount of the precursor shows a significant impact on the growth of the CNT due to a longer pyrolysis region. This factor is also dependent on the exact dimensions of the synthesis chamber. A bigger size of the chamber requires more amount of precursor. Therefore, it is necessary to optimize the amount of the precursor and the size of the inner quartz tube as these parameters appear to be strongly inter-linked.

We find that pyrolyzing ferrocene with camphor as a co-precursor adds another parameter to further tune the morphology, residual particle density as well as saturation magnetization. A variety of self-organized structures can be obtained employing the use of camphor as a co-precursor which can be tailored by modulating the ratio of amount of camphor and ferrocene.

Figure 3.10 shows representative FESEM images of an Fe@CNT sample obtained using camphor as a co-precursor. For this particular sample, the precursors – ferrocene (50 mg) and camphor (200 mg) are mixed in a pestle mortar in the ratio 1:4 respectively prior to the synthesis run. In this case *spaghetti*-like structures consisting of long entangled tubes are formed. These entangled structures can be promising materials for battery-related applications. An application of this sample as anode materials in lithium-ion batteries is presented in chapter *six*.

While Fe@CNT has been routinely synthesized by *Solid State* CVD method using powder precursor (ferrocene). [33, 34, 46–48] As mentioned in the previous section, filling efficiency, and consequently the saturation magnetization can be altered and tuned by varying the synthesis parameters. However, to the best of our knowledge, we find that there are no reports on nickel and cobalt-filled CNT formed using met-

allocene with high filling efficiency. In the next section, we discuss the reasons which lead to the difficulties in the formation of well-formed nickel-filled CNT, and an effective and innovative way to obtain good quality nickel-filled CNT using *Solid State* CVD.

3.4 Nickel-filled Carbon Nanotubes (Ni@CNT)

In this section we present synthesis and characterization details of nickel-filled CNT (Ni@CNT) using *Solid State* CVD method. A systematic variation of synthesis parameters is studied in detail providing insights for obtaining variations in morphology with significant filling efficiency and narrow length and diameter distribution.

3.4.1 Optimization of Synthesis Parameters

In order to achieve good quality and well-formed Ni@CNT, we had to optimize each synthesis parameter keeping other parameters fixed. We will now discuss each parameter and its optimization to yield Ni@CNT with good filling efficiency.

3.4.1.1 Significance of Camphor as a Co-precursor

Pyrolysis of nickelocene as a sole precursor in powder form has not been known to yield well-formed nickel-filled CNT. When nickelocene was sublimated as a sole precursor in the present setup, we find that no combination of synthesis parameters resulted in good quality filled CNT. This is also consistent with the previous reports. [26, 45] For a fixed T_{pyro} , and T_{sub} , lower rate of argon-flow yielded a large number of metal nanoparticles were accumulated near the sublimation point. When the rate of argon-flow was increased, most of the plumes come out of the inner quartz wall un-pyrolyzed, which resulted in a large number of metal nanoparticles formed in the pyrolysis region, and the soot contained little or no significant amount of CNT.

The overall data suggested that by the time plumes reach the temperatures conducive to CNT growth, the carbon content is not sufficient to facilitate the growth of CNT. This is unlike the case of Fe@CNT, where either entangled or forest structures are easily obtained over a wide range of experimental parameters. Camphor was employed as a co-precursor for the synthesis of Ni@CNT to provide the extra source of carbon. Employing camphor as a co-precursor indeed enabled the growth of

well-formed and clean samples of Ni@CNT. It is to be noted that camphor has been used earlier for the growth of pristine CNT by sublimation of camphor on suitable substrates. [122, 135] However, to the best of our knowledge, well-formed Ni@CNT with good filling efficiency has not been reported.

Thus, for the data presented in the following sections, the camphor is thoroughly mixed with metallocene and the mixture prior to any synthesis run. The precursor can be used either as a pellet, or in the form of powder. An additional parameter – ratio of camphor : metallocene is to be considered henceforth for these trials.

3.4.1.2 Pyrolysis Temperature T_{pyro} and Sublimation Temperature T_{sub}

In addition to the choice of having co-pyrolysis of camphor and nickelocene, another big challenge while synthesizing Ni@CNT still was optimization of synthesis parameters – pyrolysis temperature T_{pyro} and sublimation temperature T_{sub} . This section deals with the optimization of synthesis temperatures and the possible underlying reasons for difficulties and challenges faced while synthesizing Ni@CNT.

It was observed that for any fixed choice of T_{sub} and for a fixed ratio of camphor : metallocene, no CNT were formed at high pyrolysis temperature. Metal nanoparticles mixed with composites of nickel and carbon were obtained when pyrolysis temperature was set to 900 °C and 800 °. Increasing the amount of camphor at fixed pyrolysis temperatures (900 °C and 800 °) resulted in a variety of nano-structures like flower-like structures, spherical nano-particles, etc., but no evidence of CNT was obtained.

These data concluded that a high pyrolysis temperature is not conducive for the growth of Ni@CNT. It was observed that when the pyrolysis temperatures were set to lower temperatures, Ni@CNT with good quality of the graphitic shells and filling efficiency were obtained. We find that pyrolysis temperatures – 700 °C and 600 °C, were best suited for the formation of Ni@CNT.

After fixing the pyrolysis temperature to 700 °C, the sublimation temperature was optimized. We find that higher sublimation temperatures were found to be best suited for the formation of good quality Ni@CNT. Figure 3.11(a-c) shows the morphology of the *as-prepared* Ni@CNT at different sublimation temperatures – 250 °C, 300 °C, and 350 °C respectively keeping (i) pyrolysis temperature (700 °C), and (ii) camphor : metallocene ratio fixed. As evident from Figure 3.11, higher sublimation temperature 350 °C yields better quality of Ni@CNT as compared to lower sublimation temperatures.

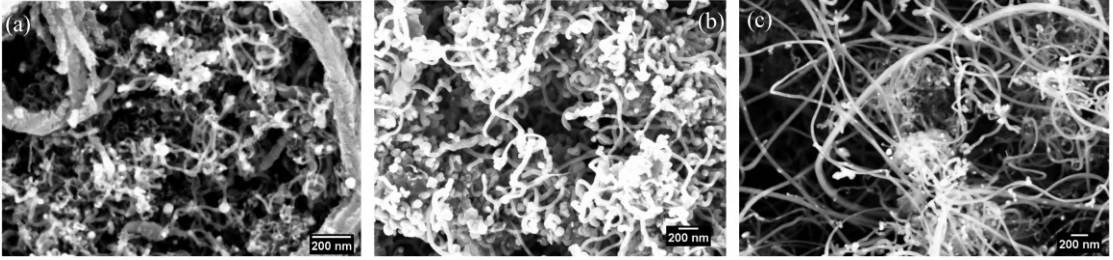
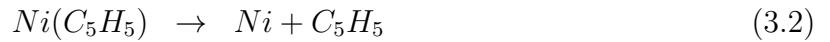
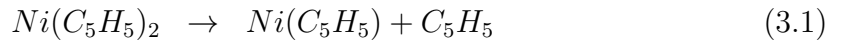


Figure 3.11: Representative FESEM images of Ni@CNT prepared at different T_{sub} – (a) 250 °C, (b) 300 °C, and (c) 350 °C for a fixed T_{pyro} as 700 °C.

The reactions involving decomposition of nickelocene are described as : [136]



The reason behind higher sublimation temperature being more conducive to the growth of Ni@CNT from nickelocene can be traced back from earlier reports on chemical vapor deposition of nickelocene. Nickelocene decomposes according to Equations 3.1 and 3.2. nickel cyclopentadienyl $Ni(C_5H_5)$ is the intermediate species obtained when nickelocene is decomposed. These reports conclude that when nickelocene is decomposed at lower sublimation temperatures i.e below 300 °C, the energy is not sufficient to completely dissociate the molecule and the dissociation of nickel with cyclopentadienyl bond is significantly low. [137] At higher temperatures, the dissociation of cyclopentadienyl ring becomes active which also increases the amount of carbon rapidly. [137] These factors crucially affect the growth of Ni@CNT when using nickelocene as a metal-organic precursor for the production of nickel-filled CNT.

Hence, it can be concluded that synthesis conditions – lower pyrolysis temperature and higher sublimation temperature are best suited to facilitate the growth of good quality nickel-filled CNT.

3.4.2 Characterization of Ni@CNT

In this section, we discuss the characterization of *as-prepared* Ni@CNT at optimized temperatures.

Figure 3.12(a-c) shows the representative images of Ni@CNT sample under dif-

3.4. Nickel-filled Carbon Nanotubes (Ni@CNT)

ferent magnifications. The corresponding sample is prepared at $T_{pyro} : 700\text{ }^{\circ}\text{C}$ and $T_{sub} : 350\text{ }^{\circ}\text{C}$ when the camphor (100 mg) : nickelocene (500 mg) ratio is 1:5. This sample consists of forests with short entangled CNT with *spaghetti-like* structures.

Representative XRD pattern obtained on the sample is shown in Figure 3.12(d). The diffraction data depict reflections from (002) plane of graphite (CNT). In addition, reflections corresponding to the metal encapsulate (Ni) are also present. Figure 3.12(e) shows the Raman spectrum acquired on the powder sample of Ni@CNT at room temperature. The spectrum consists of bands pertaining to CNT. The defect-induced D-band is obtained at $\sim 1350\text{ cm}^{-1}$. The band corresponding to tangential mode of vibration G-band is obtained at 1580 cm^{-1} . The ratio of intensities of D and G band is ~ 0.85 which can be tuned by varying the ratio of camphor : metallocene.

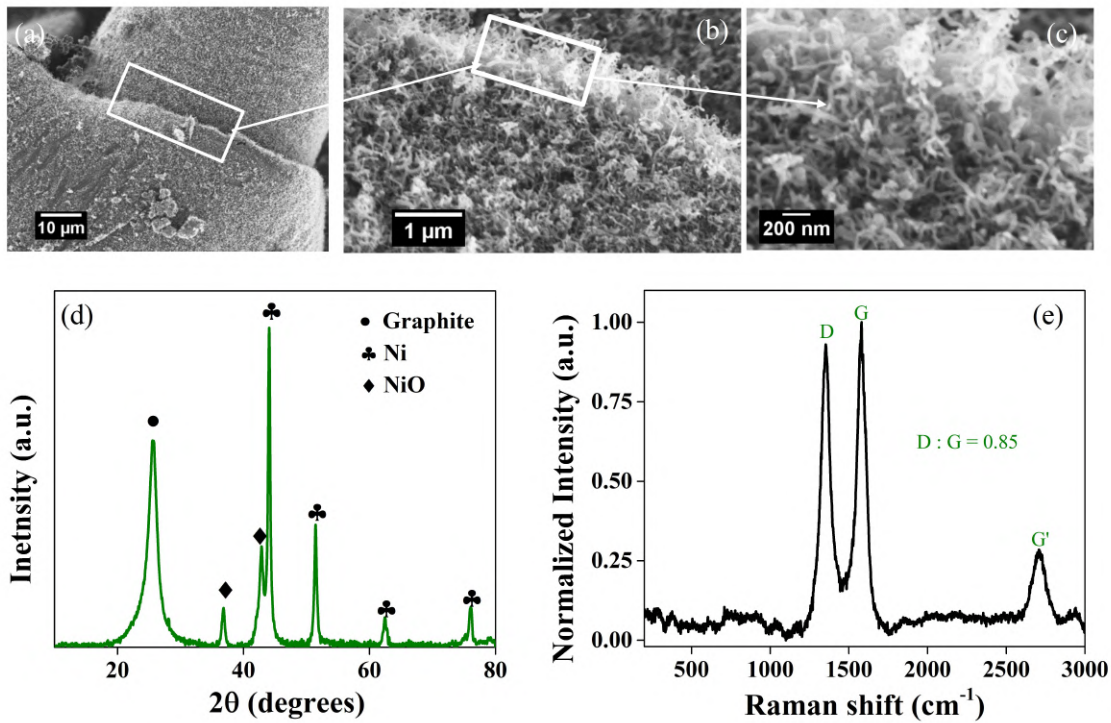


Figure 3.12: (a) - (c) Representative SEM images of the sample prepared at $T_{sub} : 350\text{ }^{\circ}\text{C}$ and $T_{pyro} : 700\text{ }^{\circ}\text{C}$ with camphor : metallocene ratio as 1:5. The sample consists of short entangled CNT with *spaghetti-like* morphology. (d) Representative powder XRD pattern for Ni@CNT with reflections corresponding to graphite (CNT) and nickel. (e) Representative Raman spectrum for Ni@CNT consisting of D-, G-, G'-bands corresponding to CNT.

TEM micrographs were recorded at different magnifications to access the nature of the encapsulate. A few representative images are shown in Figure 3.13. The images shown in Figure 3.13(a-d) indicate good filling ratio with metallic nanoparticles/nano-wires with very less residual particles outside the CNT. The encapsulate is in the form of short nano-wires and this pattern was observed on multiple CNT. The high-resolution TEM micrograph shown in Figure 3.13(e) confirms the existence of crystalline nickel nano-wires within the core cavity of the CNT. The well-formed graphitic shells indicate good quality of CNT. To the best of our knowledge, this is the first report of sublimation of nickelocene in powder form to obtain well-formed and good quality CNT with significant filling efficiency using *Solid State CVD*. [58]

To estimate the filling efficiencies of the *as-prepared* Ni@CNT, TGA and magne-

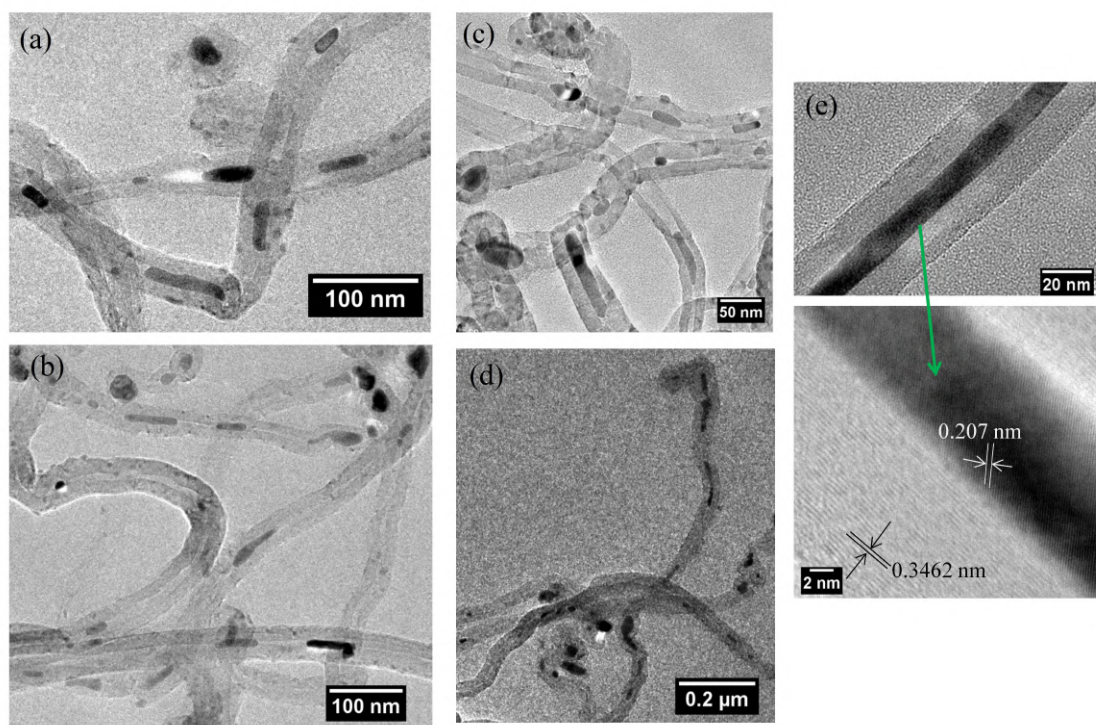


Figure 3.13: (a) - (d) display representative TEM micrographs recorded for Ni@CNT. The TEM micrographs depict the metal-filling inside CNT. The Ni nano-wires are of relatively shorter lengths, encapsulated within the core cavity of CNT. The residual catalytic particles which adhere outside the CNT are substantially reduced in these samples. (e) High-Resolution TEM micrograph of CNT depicting the filling of metallic Ni.

tization measurements were performed on the sample. Figure 3.14(a) shows the TGA curve obtained under air by heating the sample from 30°C to 900 °C at a heating rate of 10 °C min⁻¹. The TGA profile estimates the carbon weight to be ~ 75% and the residual weight (i.e. oxidized nickel) to be ~ 25%.

The filing efficiency is also reflected in high saturation magnetization values. Figure 3.14(b) shows the M-H isotherm at room temperature. The sample exhibits $M_S \sim 12$ emu/g and very low coercivity, mimicking a super-paramagnetic type of behaviour. The filling of metallic Ni within the core cavity of the CNT is primarily in the form of short nano-wires of the length 20 - 50 nm, as evident from the TEM images recorded on multiple CNT (Figure 3.13). This can lead to the formation of single domain states, which results in super-paramagnetic like traits, as observed in Figure 3.14(b).

As mentioned before, experimentally observed saturation magnetization is an indirect tool to gauge the filling efficiency for metal filled CNT. For bulk Ni the $M_S \sim 55$ emu/g. [64] The observed M_S for Ni@CNT sample is ~ 12 emu/g (Figure 3.14(b)). This indicates that the filling ratio for Ni@CNT is ~ 22%, neglecting the weight of the CNT. This also points out that at least one in five CNT should either be fully filled, or multiple CNT should be partially filled in a broad area TEM image. The TEM images shown in Figure 3.13(a-d) are in fair agreement with the TGA measure-

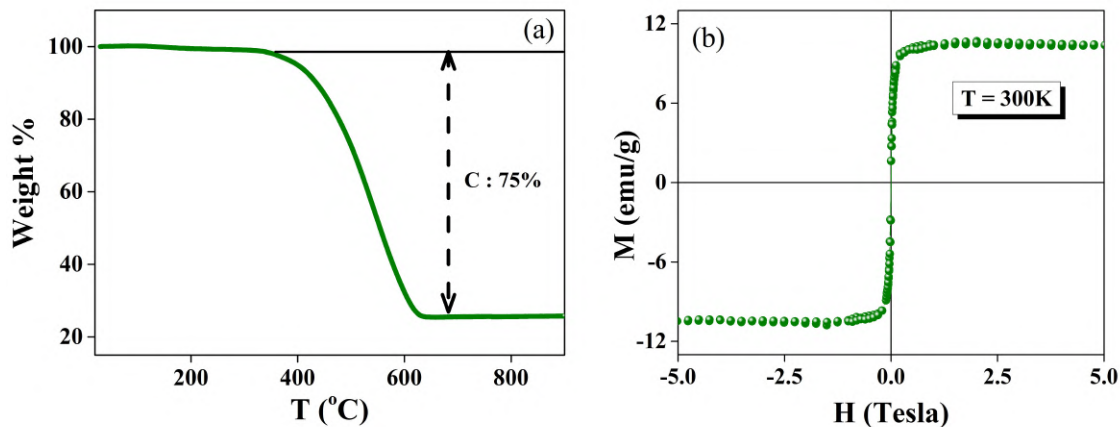


Figure 3.14: (a) displays the TGA curves of Ni@CNT sample obtained under air from 30 °C to 900 °C at a heating rate of 10 °C min⁻¹. The residue weight % was found to be 25%. (b) shows M-H isotherm of Fe@CNT depicting $M_S \sim 12$ emu/g signifying high filling efficiency of Ni@CNT.

Table 3.2: Saturation Magnetization values for bulk transition metal and when they are encapsulated inside CNT at room temperature. For metal@CNT, the M_S is further compared with literature for each sample.

Transition metals	Bulk M_S (emu/g)	Metal@CNT	M_S (emu/g) (literature)	M_S (emu/g) (this work)
Fe	~ 220 Ref. [64]	Fe@CNT	$\sim 8 - 60$ Ref. [48, 51]	$\sim \mathbf{40}$
Ni	~ 55 Ref. [64]	Ni@CNT	0.1 - 0.8 Ref. [39]	$\sim \mathbf{12}$

ment and the observed M_S value obtained from bulk hysteresis magnetization (Figure 3.14). Overall, the filling rate is estimated to be $\sim 20 - 25 \%$ as evident from FE-SEM, TEM, TGA, and M-H data (Figure (3.13-3.14)). The obtained filling efficiency with *spaghetti*-like morphology is the first report, to the best of our knowledge, on nickel-filled CNT by *Solid State* CVD using nickelocene as a precursor. [58]

Table 3.2 shows a comparison of the saturation magnetization for bulk transition metal and metal@CNT. As evident from Table 3.2, significantly high filling efficiency is achieved for Fe and Ni samples as compared to what has been reported earlier.

It is to be emphasized that the using camphor as a co-precursor enabled us to obtain well-formed nickel filled CNT with significantly improved M_S values (up to 12 emu/g), as compared to what one observed for *Aerosol assisted* (0.1 - 0.4 emu/g) reported earlier. [38, 39, 57] Further, co-pyrolysis of ferrocene and nickelocene yields nickel/iron-filled CNT. The magnetic signal from these samples contains contributions from both iron and nickel which makes the magnetization data ambiguous. [38] However, co-pyrolysis of camphor with nickelocene allows the formation of Ni@CNT with no such ambiguity in the magnetic measurements. The morphology as well as the filling efficiencies of Ni@CNT can be further controlled by tuning the synthesis parameters. The variations in morphologies of *as-prepared* Ni@CNT with change in amount of camphor is presented in the next section.

3.4.3 Variations in Morphologies for Ni@CNT : Role of Camphor

Nickel-filled is relatively the most challenging to obtain in the aligned forest morphology. Multiple attempts were made to obtain self-organized structures of Ni@CNT, similar to the case of Fe@CNT. These results concluded that aligned structures tend to form at lower pyrolysis temperature in case of Ni@CNT unlike the case of Fe@CNT where lower pyrolysis temperature disrupts the aligned forests. Further, we observed that by the ratio of the amount of camphor (C) to nickelocene (N), a variety of self-organized with different morphologies were obtained.

Figure 3.15 shows the results of these trials with variations in C : N. Figure 3.15(a) shows the representative FESEM image of the sample with C : N as 1 : 5 at T_{pyro} : 600 °C. A tendency to form aligned forest is observed in pyrolysis region as well as the variable temperature region as shown in Figure 3.15(a). However, no evidence of CNT was observed in this case.

We find that when the the amount of camphor is increased(C:N = 3:5), the sample obtained from the variable temperature region displays some interesting *sandwich*-type structure as shown Figure 3.15(b). Nano-particle beds of micron size are formed with CNT on either side of the bed, which gives rise to *sandwich*-type self-organized structures. The saturation magnetization value, in this case, is expected to be much larger owing to the presence of a large number of residual particles in the form of nano-carpet. However, these values will not indicate the true nickel filling encapsulated within the core cavity of the CNT.

When the amount of camphor is increased further(C: N ratio as 20:5), long curled tubes are formed, as shown in Figure 3.15(c). The outside particles in this case is found to be minimal. Magnetic characterization was conducted on samples prepared in different batches ranging from short to long entangled samples of Ni@CNT. The saturation magnetization values were observed to be in the range of 4 - 12 emu/g. The residue particle density was negligible in all the samples obtained in entangled morphology.

Table 3.3 summarizes the variety of morphologies obtained with the change of synthesis parameters especially the ratio of amount of camphor to nickelocene (C:N). The results obtained in the case of Ni@CNT indicate that the morphology of the sample is affected considerably with the slightest change in the synthesis parameters.

Thus, in case of Ni@CNT, it can be concluded that the synthesis parameters appear to be strongly correlated. In addition to these parameters, for a given size of synthesis chamber, the amount of nickelocene plays a significant and crucial role to decide the alignment. It can be concluded that for a fixed rate of Argon-flow, a lower pyrolysis temperature and a higher sublimation temperature are more conducive for the formation of well-formed Ni@CNT samples. Further to this, results suggest that a lower T_{pyro} is more suitable for the growth of aligned self-organized structures unlike the case of Fe@CNT.

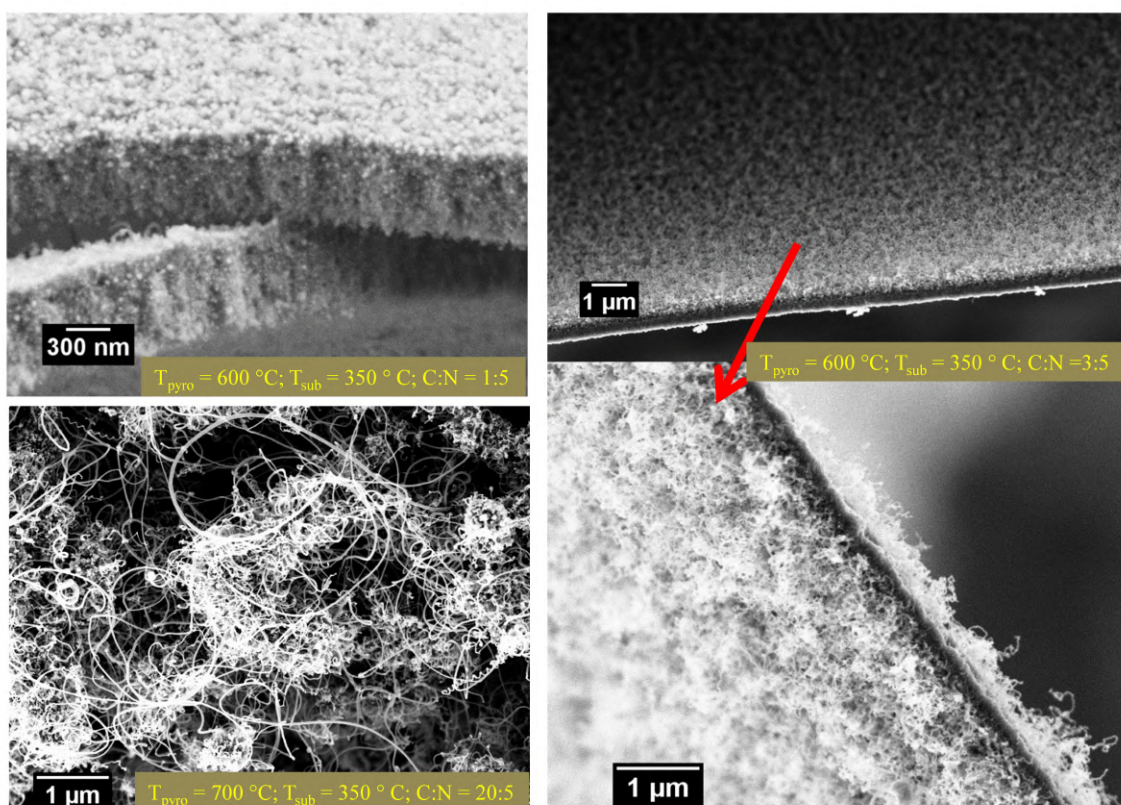


Figure 3.15: Representative FESEM micrographs of Ni@CNT formed varying the amount of camphor. (a) Aligned structures of metal nano-particles are formed in pyrolysis region when the ratio of camphor to nickelocene is 1:5. (b) For camphor to nickelocene as 3:5, a bed of nanoparticles spread over microns in length is obtained, with CNT formed on either side of the bed. The sample is obtained from variable temperature region. In this case, the pyrolysis region exhibits entangled CNT, similar to the ones shown in Figure 3.11(a-c). (c) Long entangled tubes are obtained by increasing the camphor to nickelocene ratio to 20:5 at $T_{pyro} : 700\text{ °C}$ and $T_{sub} : 350\text{ °C}$.

3.5. Oxides-filled Carbon Nanotubes (Oxides@CNT)

Table 3.3: Summary of the synthesis parameters for Ni@CNT listing various morphologies obtained when the ratio of amount of camphor to nickelocene is varied. A tendency to form aligned morphology is observed at lower T_{pyro} .

T_{sub} (°C)	T_{pyro} (°C)	C:N	Sample Collection region	Morphology
350	700	1:5	T_{var}	Spaghetti-like
350	600	1:5	T_{pyro}	Short (tendency to align)
350	600	3:5	T_{pyro}	Spaghetti-like
350	600	3:5	T_{var}	Sandwich-like
350	700	20:5	T_{pyro}	Long curled

However, the data presented underlines the reasons which lead to the difficulties and the challenges associated with the synthesis of Ni@CNT. This is due to a lot of inter correlation between the parameters. This is unlike the case of Fe@CNT, where the synthesis parameters are relatively independent of each other, and it is comparatively easier for optimization of synthesis conditions to obtain CNT with a higher filling fraction, narrow length/diameter distribution, and minimal residue particles adhering outside the CNT. Nevertheless, for a fixed set of experimental parameters, the reproducibility factor for the synthesis of Ni@CNT has been on par with Fe@CNT samples.

In addition to iron and nickel, cobalt-filled CNT samples were also synthesized in the lab. [58, 138] The synthesis details and characterization for cobalt-filled CNT are given in Appendix B.

3.5 Oxides-filled Carbon Nanotubes (Oxides@CNT)

After optimizing the parameters for metal@CNT (Fe@CNT and Ni@CNT), the next goal was to convert these metal@CNT into oxides@CNT in the same morphology and significant filling fraction. The nature of the application dictates the desired morphology of the filled CNT. For instance, α -Fe₂O₃ filled CNT is relevant for both battery-related and spintronic/nano-electronics applications, *spaghetti*-like morphol-

Table 3.4: Annealing conditions for oxidization for a fixed amount of Fe@CNT sample (10 mg). Different phases of metal-oxide are formed depending on the annealing temperatures.

T (°C)	Time (min)	Phases formed	Remarks
200-300	20	Fe + α -Fe ₂ O ₃ + Fe ₃ O ₄ + CNT	Mixed phases
300-450	20	α -Fe ₂ O ₃ + Fe ₃ O ₄ + CNT	Mixed phases
550-700	20	α -Fe ₂ O ₃ + CNT	CNT starts to burn (more nanoparticles)
>700	20	α -Fe ₂ O ₃	CNT burn completely
500	20	α -Fe ₂ O ₃ + CNT	Oxide@CNT (with significant filling)

ogy is more suitable for battery applications, whereas the aligned forest morphology can be more suitable for nano-electronics / spintronic applications. [55, 66, 89] In this section, we focus on the appropriate conditions to obtain oxides@CNT from metal@CNT.

The metal@CNT is converted into its respective oxide@CNT using suitable annealing treatments, using a typical 28 mm inner tube placed inside the main quartz reactor, under carbon dioxide atmosphere. The primary parameters involved while annealing metal@CNT samples are:

- (i) Temperature of annealing
- (ii) Duration for which the sample is annealed
- (iii) Amount of parent metal@CNT sample

Table 3.4 lists the annealing parameters and the results obtained when Fe@CNT was annealed at different temperatures to obtain α -Fe₂O₃, for a fixed amount (10 mg) of Fe@CNT parent sample.

As evident from Table 3.4, at low annealing temperatures (200 - 300 °C), CNT

with mixed phases of different oxides of iron was obtained. On increasing the annealing temperature (300 - 450 °C), for fixed amount of parent Fe@CNT sample and the time of annealing, it was observed that CNT starts to burn which reduces the yield of CNT. Annealing temperature was optimized to 500 °C for a fixed annealing time and amount of parent Fe@CNT sample. At this temperature, good quality sample with same morphology as of the parent sample Fe@CNT was obtained.

In a similar fashion, the annealing conditions to obtain NiO@CNT and Co₃O₄@CNT were optimized. The samples, thus obtained, are referred to as Oxide@CNT (α -Fe₂O₃@CNT; NiO@CNT; Co₃O₄@CNT) throughout the text hereafter. The optimized conditions for the formation of NiO@CNT were annealing 10 mg of the sample at 500 °C for 10 minutes. The annealing conditions for Co₃O₄@CNT have been discussed in Appendix B.

Another crucial factor affecting the morphology and the phases formed in oxidized metal filled CNT samples was the amount of the parent sample. For a fixed annealing temperature and its duration, multiple runs suggested that the amount of parent sample (metal@CNT) plays an important role deciding the phases obtained post annealing. For very less quantity of sample (less than 10 mg), the oxidized samples consisted of mostly nanoparticles with CNT almost burnt. For very large quantities of sample (more than 15 mg), the sample post annealing was found to be half-oxidized with a mixture of phases of oxides formed. Hence, it can be concluded that for a fixed annealing temperature and duration of annealing, the amount of parent sample (metal@CNT) to be oxidized needs to be optimized for successful annealing. It is to be noted that the measurements have been performed on various oxides@CNT presented in this thesis with optimized annealing conditions – annealing temperature, duration of annealing, and amount of parent sample (metal@CNT).

FESEM images of a representative sample α -Fe₂O₃@CNT obtained post annealing is shown in Figure 3.16. This sample is prepared by annealing the *as-prepared* Fe@CNT sample in aligned forest morphology (Figure 3.3). As evident from Figure 3.16, the morphology of the parent sample – Fe@CNT is retained post annealing. High-resolution TEM image confirm the presence of α -Fe₂O₃ within the core cavity of CNT shown in Figure 3.16(c). The TEM micrograph in Figure 3.16(c) depicts the well-formed graphitic shells of the CNT and α -Fe₂O₃ as encapsulate. The lattice spacings in Figure 3.16(c) corresponds to (002) plane of graphite (CNT) encircled in white and (202) and (006) planes of α -Fe₂O₃ encircled in yellow circles.

This sample was characterized by synchrotron XRD as shown in Figure 3.16(d). The observed XRD peaks shows reflections from the graphitic peak corresponding to the CNT (ICSD code: 015840) marked by black dot in Figure 3.16(d), and α -Fe₂O₃

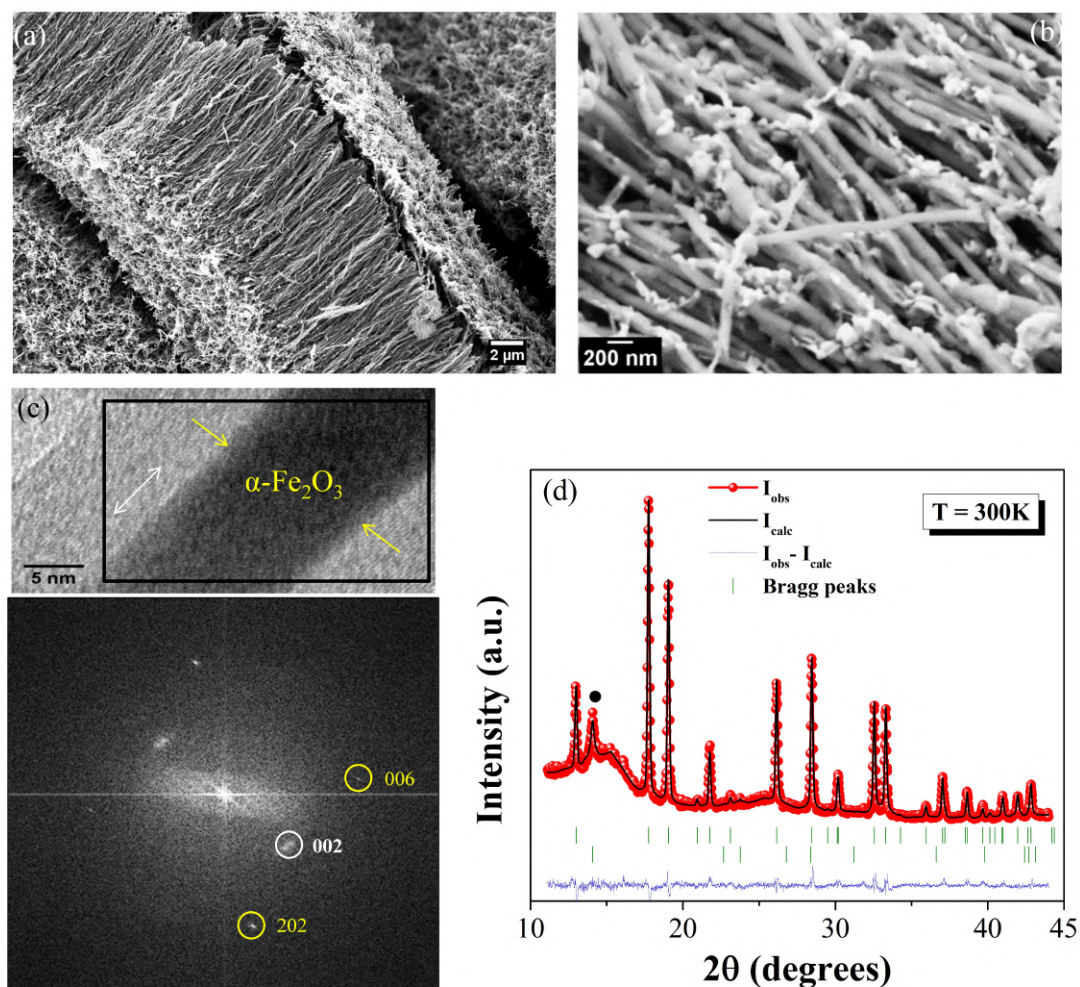


Figure 3.16: (a) - (b) Representative FESEM micrographs of α -Fe₂O₃@CNT depicting the morphology of the oxidized Fe@CNT sample. The oxidized sample retains the aligned forest morphology of the parent sample. (c) Representative TEM micrograph of α -Fe₂O₃@CNT with the corresponding Fast Fourier transform with yellow circles highlighting the reflections from the encapsulated α -Fe₂O₃@CNT and the graphitic (CNT) planes. (d) Synchrotron XRD data of α -Fe₂O₃@CNT along with Rietveld Profile Refinement. The goodness of fit obtained is 2.20. The red dots are the observed data, the black line is the best fit, and the blue line shows the difference in the observed and the calculated data.

(ICSD code: 031170). Two phases were identified – α -Fe₂O₃ and graphite (CNT), and the experimental data have been fitted with Rietveld Profile Refinement using a two-phase model. [120] The solid black line has been fitted to the experimental XRD data (red dots) Rietveld profile refinement – α -Fe₂O₃ with space group $R\bar{3}c$, and graphite with space group $P63mc$.

It is to be noted that no other phase (other oxides of iron) was detected in the synchrotron XRD data. The goodness-of-fit (χ^2), as discussed in chapter *two*, obtained was 2.20. The lattice parameters for the phase α -Fe₂O₃ were: $a = 5.02113 \pm 0.00025 \text{ \AA}$, $c = 13.7143 \pm 0.0009 \text{ \AA}$. The lattice parameters for the graphitic phase after Rietveld refinement were: $a = 2.4459 \pm 0.0003 \text{ \AA}$, $c = 6.77464 \pm 0.0004 \text{ \AA}$. The Rietveld refinement also reveals the percentage of α -Fe₂O₃ in the sample, which is $\sim 65\%$, which is inclusive of the metal oxide within the CNT as well as the particles outside CNT.

The utilization of oxides@CNT has been discussed in subsequent chapters. Chapters *four* and *five* show the fundamental : magnetization and Raman studies on oxide@CNT. Chapter *six* shows the application of these oxides in lithium-ion batteries as potential anode materials.

3.6 Summary

We conclude that any single-zone furnace, which is routinely available, can be utilized for the synthesis of CNT using pyrolysis of metallocene with careful temperature profiling, such as shown in Figure 3.2(b). Desired morphology of CNT with uniformity and narrow length/diameter distribution was achieved due to a longer pyrolysis zone with better temperature accuracy. In case of nickel (and cobalt [138]), the samples are difficult to obtain by sublimation of their respective metallocenes as a sole precursor. Only metallic particles were observed along the length of the inner quartz tube in these cases. These results indicated that the carbon source is not sufficient for growth of CNT. The addition of camphor, however, circumvents this problem by providing an extra source of carbon to facilitate the growth of metal filled CNT. This further another control parameter, the ratio of the amount of carbon and metallocene, to tune the morphology of filled CNT as well as the M_S . These factors are crucially dependent on the exact dimensions of the synthesis chamber. There also exists a systematic pattern for obtaining self-organized structures in all

the three cases.

We have presented synthesis of iron, nickel, [58] and cobalt [138], as well as their respective oxides filled CNT using metallocene as a powder precursor following *Solid State* CVD route. Utilizing camphor as a co-precursor enabled the formation Ni- (and Co@CNT) with significantly higher filling efficiency than what has been reported earlier using *Aerosol assisted* CVD of metallocene. We have also shown that a systematic study of the variation of synthesis parameters concluding a strong inter-correlation of synthesis parameters for Ni@CNT as compared to Fe@CNT samples. A systematic variation of synthesis parameters allowed to obtain self-organized structures of metal-filled CNT, with narrow diameter and length distribution, and reduced residual particle density. The co-pyrolysis of metallocene with camphor leads to a variety of self-organized structures which can be tailored by manipulating the ratio of metallocene to camphor according to the application. The metal@CNT samples can be obtained in desired morphology, and can be further used to obtain oxide filled CNT. These hybrids can have numerous applications in spintronic, magneto-optics and in the energy sector. For instance, these oxides-filled CNT have been tested for battery applications and the results are presented in chapter *six*.

For the fundamental studies, our focus has been on encapsulation of a functional magnetic oxide α -Fe₂O₃ inside CNT. α -Fe₂O₃ is a Dzyaloshinskii-Moriya Interaction driven canted antiferromagnet α -Fe₂O₃, and recent studies have shown that they exhibit an unusual magnetization relaxation phenomenon. In the next chapter, we present magnetization data of α -Fe₂O₃ encapsulated inside CNT; and the interesting phenomenon which arise at the interface of α -Fe₂O₃ and CNT.

Chapter 4

Magnetism at the Interface of Hematite & Carbon Nanotubes

4.1 Introduction

Hematite (or $\alpha\text{-Fe}_2\text{O}_3$) is an earth abundant and environment-friendly oxide, which is generally considered as a *menace* for its appearance as rust over elemental iron, but technologically, it is well-known for a diverse range of applications. [139] It belongs to the family of rhombohedral antiferromagnets and is a classic example of Dzyaloshinskii-Moriya Interaction (DMI) driven weak ferromagnet (WFM). [66] The observation of weak ferromagnetism [66] nearly six decades ago in hematite has had profound implications in the field of spintronics. A variety of non-trivial topological spin structures in chiral magnets stabilizing through DMI have prompted new research areas such as antiferromagnetic spintronics and spin orbitronics. [87, 140–144]

The generation of weak ferromagnetism in certain classes of antiferromagnetic materials has been associated with the experimental observation of a spontaneous moment in an otherwise antiferromagnetic material as discussed extensively in chapter *one*. The theoretical explanation for the presence of spontaneous moment in such antiferromagnets (AFM) was provided by Dzyaloshinskii. [66] The phenomenon of weak ferromagnetism has been attributed to a spin canting mechanism which leads to a net ferromagnetic moment. [66] The microscopic origin of the spin canting was discovered by Moriya who developed a theory of anisotropic superexchange interaction and revealed the connection of spin canting with spin orbit coupling [69] which is now the celebrated Dzyaloshinskii-Moriya Interaction (DMI). A few examples ex-

hibiting this phenomenon include $\alpha\text{-Fe}_2\text{O}_3$, MnCO_3 , CoCO_3 . Further, Dzyaloshinskii also showed that the compounds with smaller T_N possess larger spin canting. [66] Thus, weak ferromagnetism is expected to be the weakest in $\alpha\text{-Fe}_2\text{O}_3$ with $T_N \sim 950\text{K}$ as compared to MnCO_3 or NiCO_3 (T_N below 50K). [89]

As discussed in chapter *one*, the generation of weak ferromagnetism in $\alpha\text{-Fe}_2\text{O}_3$ is due to a slight canting of its inherent AFM sub-lattice which persists from its Néel temperature (T_N) 950K down to 265K, well-known Morin transition temperature (T_M). [66, 69] Below T_M , the spins lie along the c -axis of the rhombohedral lattice. Above the Morin transition temperature (T_M), the spins turn from " c " axis to " a " axis (rhombohedral unit cell in hex setting). In this configuration, the spins are slightly canted which produces a net ferromagnetic moment in an otherwise antiferromagnet. Figure 4.1 shows the spin configuration for (a) AFM and (b) WFM states; and the spin canting in (c), which results in a net ferromagnetic moment. $\alpha\text{-Fe}_2\text{O}_3$ can exist in both AFM and WFM states and exhibit weak ferromagnetism at room temperature.

Owing to the fact that $\alpha\text{-Fe}_2\text{O}_3$ exists in both WFM and AFM states, and exhibits weak ferromagnetic traits at room temperatures, make it advantageous for variety of practical applications. In spite of exhibiting these spectacular characteristics, device

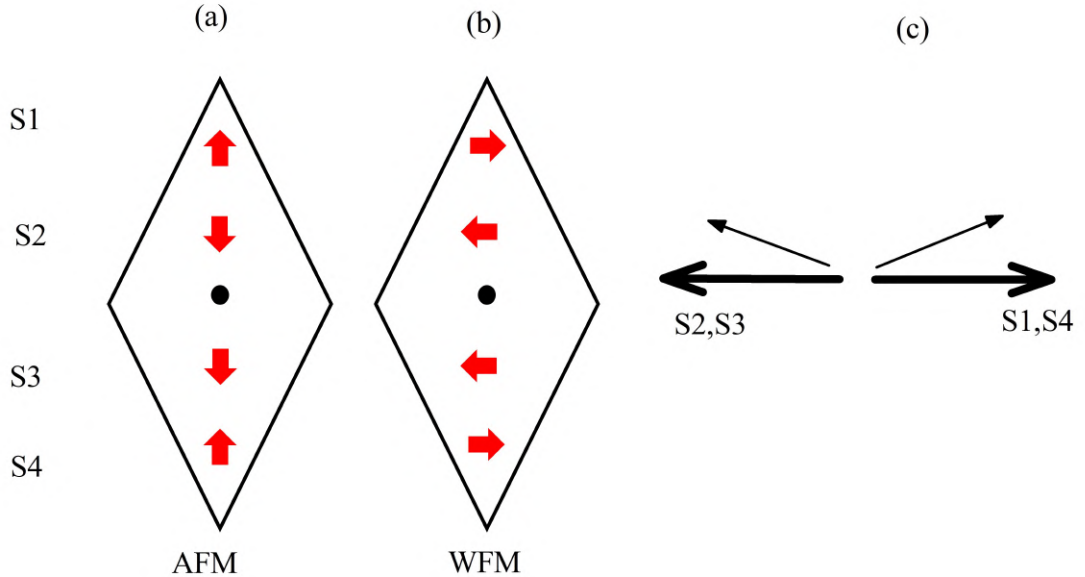


Figure 4.1: Schematic of spin configuration in hematite for (a) pure AFM and (b) WFM state for rhombohedral unit cell of hematite ($\alpha\text{-Fe}_2\text{O}_3$). (c) Depicts the spin canting for WFM state which leads to a net weak ferromagnetic moment.

fabrication utilizing α -Fe₂O₃ (and other magnetic oxides) still remains a challenge due to a number of practical issues. In addition, due to a higher $T_N \sim 950\text{K}$, the weak ferromagnetism effect (and magnitude of remanence) is found to be weaker in α -Fe₂O₃ [66, 89] which limits its use in practical applications.

Further, α -Fe₂O₃ exhibits the phenomenon of ultra-slow magnetization relaxation leading to *time-stable* remanence, and has been observed in various sizes and morphologies of α -Fe₂O₃. [89, 90] In this light, the encapsulation of this magnetic oxide inside CNT [11] can be potentially beneficial for a number of reasons. Carbon Nanotubes (CNT) possess unprecedented mechanical, electrical and thermal properties. [11] Magnetic oxides possessing exceptional electronic and magnetic ground states when encapsulated inside CNT can lead to novel *interface* effects. [19, 85, 145, 146] Thus, the primary motivation was to study the remanence when α -Fe₂O₃ is encapsulated within the core cavity of the CNT.

In this chapter, we present exciting magnetization and remanence results arising at the interface of two highly functional materials, namely the graphitic shells of CNT and DMI driven WFM α -Fe₂O₃. This chapter presents remanence results of two samples – α -Fe₂O₃@CNT and FeO_x@CNT. FeO_x@CNT contains both WFM α -Fe₂O₃ and ferromagnetic Fe₃O₄. In addition to remanence studies, magnetization studies and its correlation with structural parameters is presented for magnetic oxide α -Fe₂O₃ encapsulated inside CNT.

4.2 The Concept of FC and ZFC

The behaviour of any magnetic material is typically understood by the intrinsic response to external applied magnetic field. Further, the magnetic response of the material is highly dependent on the sequence of applying the external magnetic field. When the sample is cooled in the presence of a magnetic field above its ordering temperature, the spins tend to be locked in a particular direction dictated by the strength of the magnetic field. [147] This is known as Field Cooled (FC) measurement. However, the magnetization dynamics is different when the sample is cooled from above its ordering temperature down to low temperatures in the absence of any field. In such a case, the magnetization is recorded in the heating cycle, after switching on the field at low temperatures. This is known as the Zero Field Cooled (ZFC) measurement. The FC and ZFC magnetization measurements are im-

portant to identify and differentiate different magnetic phases. Therefore, it becomes important to specify the magnetization protocol to understand the system, and the sequence of the measurements crucially affect the magnetic behaviour of any material especially the nano-scale magnet. In this chapter, we have investigated the magnetization in FC and ZFC state as well as the corresponding remanence for the samples of α -Fe₂O₃@CNT. Our primary motivation is to investigate whether α -Fe₂O₃@CNT samples also exhibit a time-stable remanence, which is generally observed in a number of canted AFM including α -Fe₂O₃ in the form of single crystals [89] or in the form of nano-particles.

4.2.1 Magnetization Measurement Protocol : FC and ZFC

The magnetization (M) as a function of temperature (T) in the presence of a fix magnetic field (H) was recorded following routine Zero Field Cooled (ZFC) and Field Cooled (FC) cycles. The corresponding M has been referred as M_{ZFC} and M_{FC} respectively in the text.

In a typical FC measurement, the sample is cooled down to 5K in a fixed specified magnetic field (H) applied much above T_N (or T_M), and the magnetization is recorded as a function of temperature while cooling. In a typical ZFC protocol, the sample if first cooled from above T_N (or T_M) down to 5K in the presence of zero magnetic field. Thereafter, the magnetic field is applied at low temperature (5K) which is below T_N (or T_M) and the magnetization as a function of temperature is recorded in the warming cycle up to the room temperature.

4.2.2 Remanence Measurement Protocol

The remanent state has been prepared following either of the two protocols:

(i) The sample is cooled in the presence of H from 300 K up to 5K. The H is switched off at 5K. The corresponding remanence (μ) as a function of time is measured, while temperature is held constant at 5K. The remanent state in this case, is hence prepared using the FC protocol.

(ii) The sample is heated in presence of H from 5K up to 300 K. The H is switched off at 300K. Hereafter, the remanence as a function of time is measured while temperature is held constant at 300K. The remanent state in this case, is hence prepared using the ZFC protocol. It is to be emphasized that the remanence is strictly mea-

sured in $H = 0$ condition in either of the protocols. The H indicated in all the figures pertaining to remanence is to convey its magnitude while preparing a remanent state.

4.3 Results and Discussion

4.3.1 α - Fe_2O_3 @CNT

Figure 4.2(a) displays FESEM image of the sample α - Fe_2O_3 @CNT. The α - Fe_2O_3 @CNT consists of aligned forests of CNT as shown in the inset of Figure 4.2(a). The presence of α - Fe_2O_3 within the core cavity of CNT is confirmed from the high-resolution TEM image which is shown in Figure 4.2(b)). The high-resolution TEM image depicts the well-formed graphitic shells of the CNT and the oxide encapsulate.

The presence of α - Fe_2O_3 and the graphitic phase (CNT) is further confirmed by synchrotron XRD (blue dots) data fitted using Rietveld Profile Refinement [120] (black line) shown in Figure 4.2(c). The black dot indicates the reflections corresponding to the graphitic phase (CNT), and all the other peaks correspond to the reflections from the phase α - Fe_2O_3 . The synchrotron XRD data of α - Fe_2O_3 sample have been fitted using two phase model in Rietveld Profile Refinement, corresponding to rhombohedral α - Fe_2O_3 ($R\bar{3}c$; hex-setting) and the hexagonal graphitic phase (CNT) ($P63mc$). [49, 120] The goodness-of-fit obtained was 1.85. It is to be noted

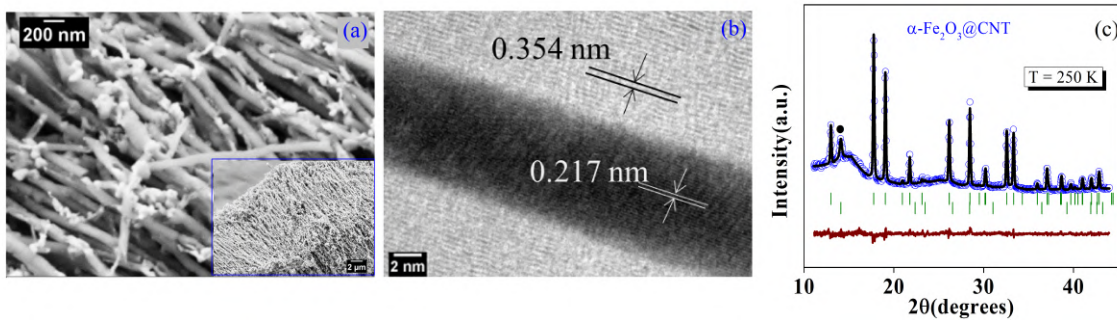


Figure 4.2: (a) FESEM micrograph of α - Fe_2O_3 @CNT. The inset of (a) shows the aligned forests of α - Fe_2O_3 @CNT. (b) Shows high-resolution TEM micrograph of α - Fe_2O_3 @CNT, depicting well-formed graphitic shells of CNT and α - Fe_2O_3 as encapsulate. (c) Synchrotron XRD of the sample α - Fe_2O_3 @CNT recorded at 250K. The black dot indicates the Bragg reflection from the graphitic phase (CNT). All the other peaks correspond to reflections from α - Fe_2O_3 . The XRD data have been fitted using two-phase model of Rietveld profile refinement.

that neither ferromagnetic iron, nor any other oxides of iron (such as magnetite, etc.) could be detected in synchrotron XRD for this sample.

We now discuss the magnetization data recorded for the sample $\alpha\text{-Fe}_2\text{O}_3\text{@CNT}$. Figure 4.3 shows magnetization as a function of temperature for $\alpha\text{-Fe}_2\text{O}_3\text{@CNT}$ in a typical FC (blue dots) and ZFC (black dots) cycles measured at magnetic field (H) = 1 kOe. The magnetization measurements have been recorded as per the magnetization protocol discussed in section 4.2. The sample exhibit well pronounced Morin transition at T_M marked by red arrow in Figure 4.3. The Morin transition is intrinsic to the bulk $\alpha\text{-Fe}_2\text{O}_3$. [148] We observe a shift in T_M towards lower temperatures as compared to the bulk $\alpha\text{-Fe}_2\text{O}_3$. This is because the Morin transition temperature T_M is dependent on various factors such as crystal defects, strains, and particle size, and exhibits a tendency to shift to lower temperatures the particle size of $\alpha\text{-Fe}_2\text{O}_3$ is reduced. [90, 148–150]

The functional form of magnetization as a function of temperature in $\alpha\text{-Fe}_2\text{O}_3\text{@CNT}$ is consistent with the previous reports in which $\alpha\text{-Fe}_2\text{O}_3$ is investigated in the form of nano-wires. [89, 148–150] A clear bifurcation in FC/ZFC curves along with other broad features of magnetization and history effects (i.e. bifurcation in FC/ZFC cycles) can be attributed to nano-scaling of the magnetic encapsulate. [148] These features are broadly consistent with previous reports on $\alpha\text{-Fe}_2\text{O}_3$ nano-particles. [90, 148]

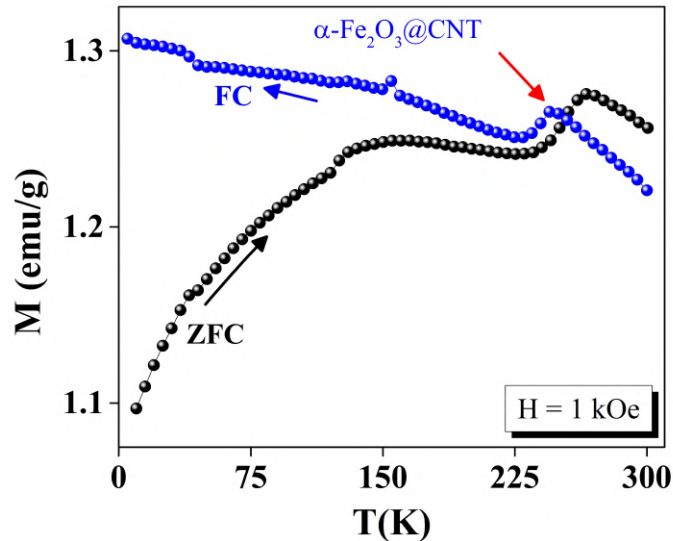


Figure 4.3: Magnetization as a function of temperature for $\alpha\text{-Fe}_2\text{O}_3\text{@CNT}$ in a typical FC (blue dots) and ZFC (black dots) measured at $H = 1$ kOe.

However, a prominent and an interesting observation is about an order of magnitude enhancement in magnitude of magnetization in $\alpha\text{-Fe}_2\text{O}_3\text{@CNT}$, as compared to what is observed for $\alpha\text{-Fe}_2\text{O}_3$ nano-particles/nano-wires. [89, 148] Assuming that the graphitic shells of CNT do not contribute magnetically in a conventional sense, the data presented in Figure 4.3 are intriguing and suggest that the encapsulation of $\alpha\text{-Fe}_2\text{O}_3$ inside CNT could be responsible for this enhanced magnetization.

4.3.2 $\alpha\text{-Fe}_2\text{O}_3$ -template

In order to gain a better understanding for the observation of enhanced magnetization in $\alpha\text{-Fe}_2\text{O}_3$, we anneal the sample $\alpha\text{-Fe}_2\text{O}_3\text{@CNT}$ at high temperature (900 °C) to intentionally remove the graphitic shells, and obtain bare $\alpha\text{-Fe}_2\text{O}_3$ nanoparticles without CNT. The sample obtained post burning $\alpha\text{-Fe}_2\text{O}_3\text{@CNT}$ retain the morphology of the encapsulate $\alpha\text{-Fe}_2\text{O}_3$, but with no CNT. This sample is referred as $\alpha\text{-Fe}_2\text{O}_3$ -template throughout the text.

Figure 4.4(a-b) depicts the morphology of the sample $\alpha\text{-Fe}_2\text{O}_3$ -template at different magnifications. The sample consists of long chains of $\alpha\text{-Fe}_2\text{O}_3$ aligned in the form of forests as evident from Figure 4.4(b). Figure 4.4(c) shows the synchrotron XRD data on the $\alpha\text{-Fe}_2\text{O}_3$ -template fitted using Rietveld Profile refinement. [120] The triangles in Figure 4.4(c) correspond to peak reflections from the copper sample

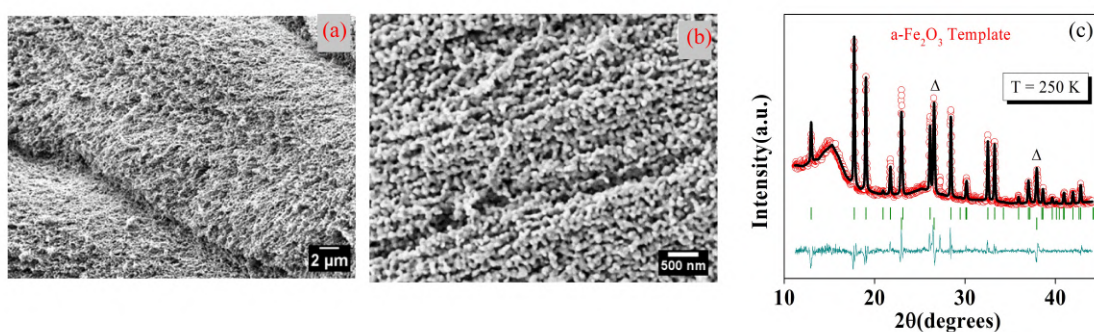


Figure 4.4: (a-b) FESEM micrographs of $\alpha\text{-Fe}_2\text{O}_3$ -template recorded at different magnifications. The sample retains the morphology of $\alpha\text{-Fe}_2\text{O}_3\text{@CNT}$. (c) Synchrotron XRD of the sample $\alpha\text{-Fe}_2\text{O}_3$ -template recorded at 250K. The triangles indicate the Bragg reflections from the copper sample holder. All the other peaks correspond to reflections from $\alpha\text{-Fe}_2\text{O}_3$. The XRD data have been fitted using Rietveld profile refinement.

holder. The synchrotron data on α -Fe₂O₃-template consists of reflections corresponding to α -Fe₂O₃, and no peak reflections corresponding to the graphitic phase could be detected in the template. The goodness-of-fit obtained was 2.83.

In the next section, we compare the magnetization results obtained on the samples α -Fe₂O₃@CNT and α -Fe₂O₃-template.

4.3.3 Comparison of Magnetization in α -Fe₂O₃@CNT and α -Fe₂O₃-template

In this section, we compare the magnetization results of α -Fe₂O₃@CNT and α -Fe₂O₃-template. Figure 4.5(a) compares the M-H isotherms of α -Fe₂O₃@CNT (blue dots) and α -Fe₂O₃-template (red dots) room temperature. For a given range of magnetic field, the magnitude of magnetization in α -Fe₂O₃-template (without CNT) is consistent with the previous reports. [89, 148, 150] However, a significant enhancement in magnitude of magnetization is observed in case of α -Fe₂O₃@CNT sample as evident from Figure 4.5(a). Figure 4.5(b) compares the magnetization as a function of temperature for α -Fe₂O₃@CNT (blue dots) and α -Fe₂O₃-template (red dots) in a typical FC measurement recorded at H = 1 k Oe. Both the samples exhibit well pronounced Morin transition intrinsic to bulk α -Fe₂O₃. However, the magnitude of magnetization is an order of magnitude enhanced in case of α -Fe₂O₃@CNT (blue dots) as compared to α -Fe₂O₃-template (red dots). For instance, M_{FC} ~ 1.3 emu/g (Figure 4.5(b)) for α -Fe₂O₃@CNT, whereas it is ~ 0.1 emu/g for the α -Fe₂O₃-template (Figure 4.5(e)) at 5K for H = 1 kOe. Since the graphitic shells of CNT do not contribute magnetically in a conventional sense, the data presented in Figure 4.5 are interesting. The magnitude of magnetization in α -Fe₂O₃-template is similar to what is usually observed in α -Fe₂O₃ nano-particles. [89, 90]

As evident from Figure 4.2(a) and 4.4(a-b), in both the samples α -Fe₂O₃@CNT and α -Fe₂O₃-template, the particle size of α -Fe₂O₃ is similar and the morphology in both the samples is similar i.e. aligned forests. If this enhancement in magnetization α -Fe₂O₃@CNT was arising primarily due to the attributes such as nano-scaling of α -Fe₂O₃, the morphology (aligned forest), the effect would have persisted in the α -Fe₂O₃-template. It is to be noted that both the size effects and the morphology certainly have a role to play as far as weak ferromagnetism in α -Fe₂O₃ is concerned. [89, 90] However, the data presented in Figure 4.5 suggest that the significant

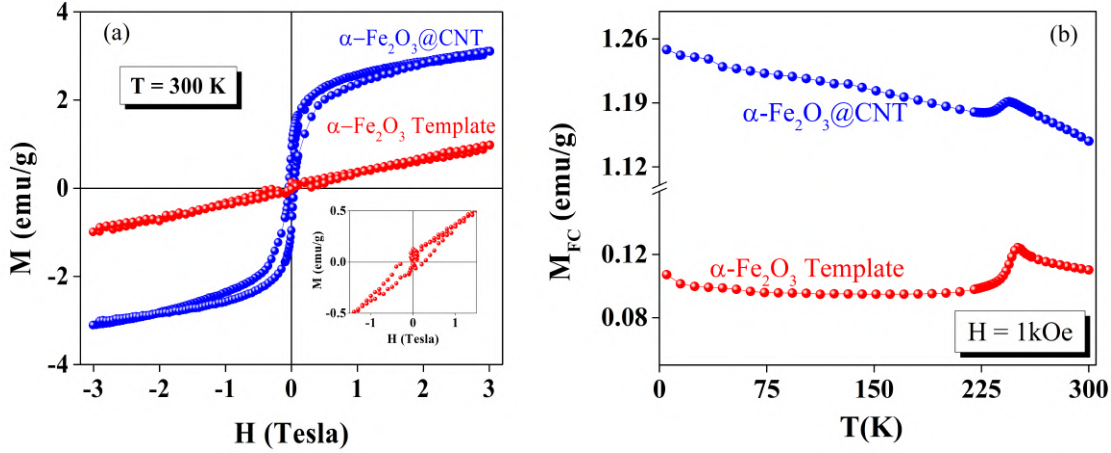


Figure 4.5: The main panel of (a) compares the M - H isotherms at 300K for α - Fe_2O_3 @CNT (blue dots) and α - Fe_2O_3 -template (red dots), depicting the enhancement in magnetization when α - Fe_2O_3 is encapsulated inside CNT. The inset of (a) shows the M - H isotherm for the template at lower field range. (b) compares the magnetization as a function of temperature for α - Fe_2O_3 @CNT (blue dots) and α - Fe_2O_3 -template (red dots) measured at $H = 1$ kOe following the FC protocol.

enhancement in magnetization is related to the encapsulation of α - Fe_2O_3 inside CNT and the resulting *interface* effects.

This order of magnitude enhancement in magnetization was observed at all H – 100 Oe, 1 kOe, and 10 kOe, for α - Fe_2O_3 @CNT (Figure 4.6(a-c)) as compared to the α - Fe_2O_3 -template (Figure 4.6(d-f)). For FC/ZFC recorded at different fields, we observe an interesting pattern. In conventional LRO or in complex magnetic systems, it is commonly observed that M_{FC} is greater than M_{ZFC} . [147, 148] However, in case of α - Fe_2O_3 @CNT and α - Fe_2O_3 -template, we observe the opposite M_{ZFC} is greater than M_{FC} , especially in the temperature region above T_M , as evident from Figure 4.6. This is not a commonly observed phenomenon, however, such behaviour has been reported earlier. [150, 151] (It is also observed that at higher fields ($H = 10$ kOe), the behaviour is different than what is observed at lower fields especially at low temperatures. We shall discuss this unusual behaviour at high fields in section 4.3.5.)

We believe that the unusual observation, M_{ZFC} greater than M_{FC} is a manifestation of the spin canting phenomenon in α - Fe_2O_3 . The spin canting in α - Fe_2O_3 starts from $T_M \sim 260\text{K}$, and persists right up to 950K, wherein a weak ferromagnetic to paramagnetic transition takes place. If the magnetic field is applied from below

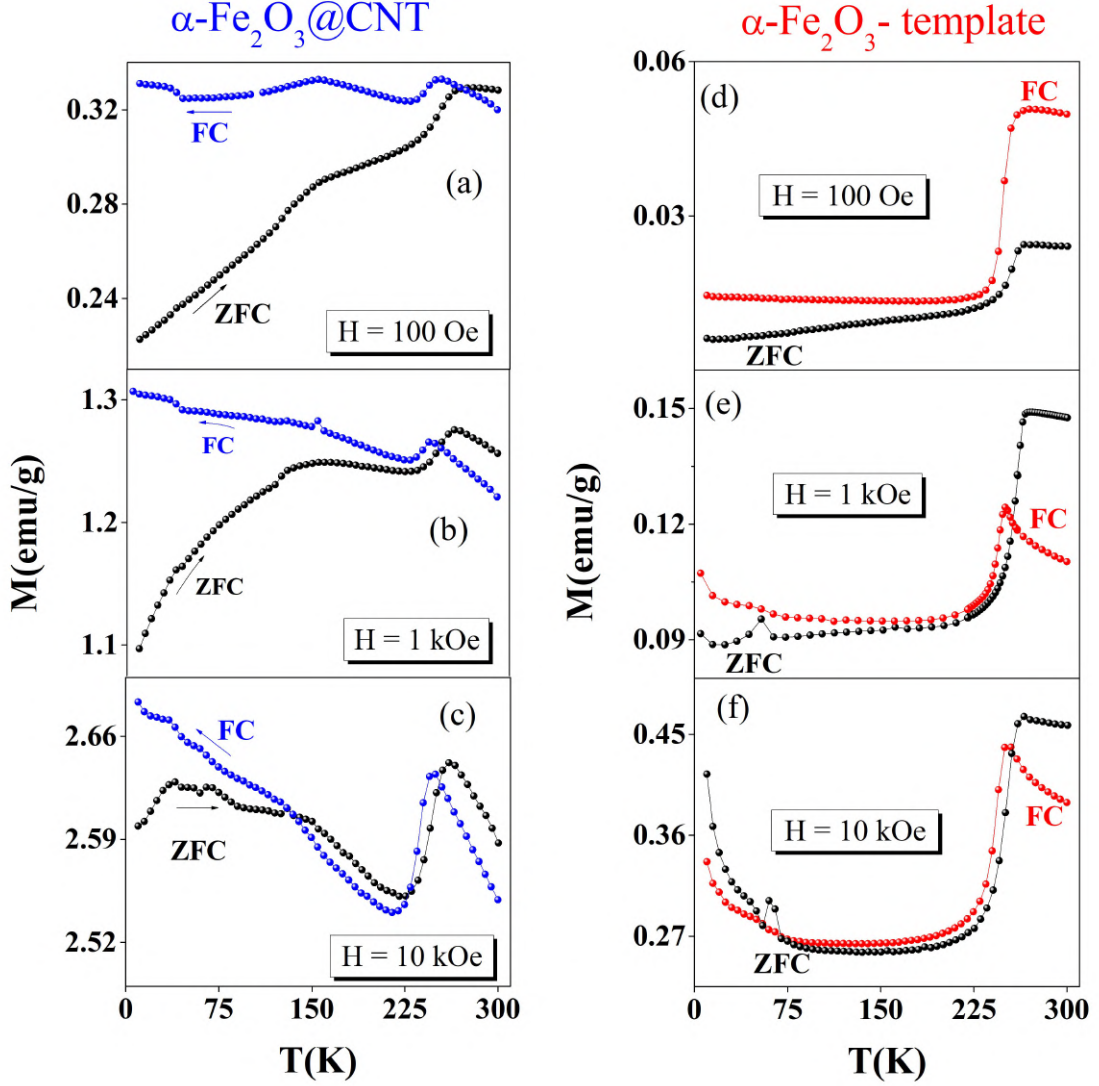


Figure 4.6: (a)-(c) shows M vs T in a typical FC (blue dots) and ZFC (black dots) for the sample $\alpha\text{-Fe}_2\text{O}_3\text{@CNT}$ measured at 100 Oe, 1 kOe and 10 kOe. (d)-(f) shows the same for the $\alpha\text{-Fe}_2\text{O}_3$ -template. At each measuring H , the magnitude of M is substantially larger for the sample $\alpha\text{-Fe}_2\text{O}_3$ as compared to what is observed for the $\alpha\text{-Fe}_2\text{O}_3$ -template.

T_M , before the onset of spontaneous canting, the direction of the net ferromagnetic moment associated with a canted AFM domain can be best modulated (w.r.t the direction of H). This leads to the observation of a larger M_{ZFC} . On the other hand,

in case of an FC measurement, when the magnetic field is applied from above the T_M , the spins are already spontaneously canted with a net ferromagnetic moment. Therefore, the contribution to the net magnetization is not entirely dictated by the magnetic field. This is due to the fact that it may not be energetically favourable for a small magnetic field to flip the direction of a weak ferromagnetic domain with net ferromagnetic moment pointing in unfavourable direction with respect to applied magnetic field.

It is also to be emphasized that all routine magnetic field driven process simultaneously exist as they do for any normal AFM under the influence of magnetic field. However, in case of α - Fe_2O_3 , the canting is spontaneous. Therefore, when the magnetization state is prepared by an *in-field* cooling (or heating) cycle, an ambiguity in the data (of the order of differences in FC/ZFC) is likely to exist as long as history effects are not wiped off by heating the sample above AFM to paramagnetic transition ($\sim 950\text{K}$). It is to be noted that heating the sample above T_N ($\sim 950\text{K}$) prior to another FC/ZFC cycle is practically not possible in case of α - Fe_2O_3 . Hence, for results presented in this work, the sample is heated in zero H from below its T_M prior to any M vs T in presence of H (either FC or ZFC). This protocol leads to more reproducible data on repeated temperature cycling in same H.

4.3.4 Remanence in α - Fe_2O_3 @CNT and α - Fe_2O_3 -template

We would like to recall that the manifestation of canting in α - Fe_2O_3 single crystal appears in the form of *time-stable* remanence with a functional form, which is evidently different from other physical mechanisms. [89] This effect was also found to be significantly tunable by nano-scaling. [90] This motivated us to perform similar measurements on α - Fe_2O_3 @CNT and compare the results with the bare α - Fe_2O_3 .

Interestingly, we find that the feature of *time-table* is also observed that when α - Fe_2O_3 is encapsulated inside CNT. Figure 4.7 shows remanence as a function of time for α - Fe_2O_3 @CNT at room temperature. The remanent state is prepared at $H = 100$ Oe using the ZFC protocol as stated in section 4.2.2

Considering the data presented in Figure 4.7, we observe that the magnetization value is ~ 0.46 emu/g prior to switching off the field. After the field is switched off, the magnetization value decays down ~ 0.32 emu/g retaining 69% of its *in-field* value as evident from Figure 4.7. However, a part of the remanence exhibits no decay with time, as shown in the inset of Figure 4.7. The magnitude of remanence is practically

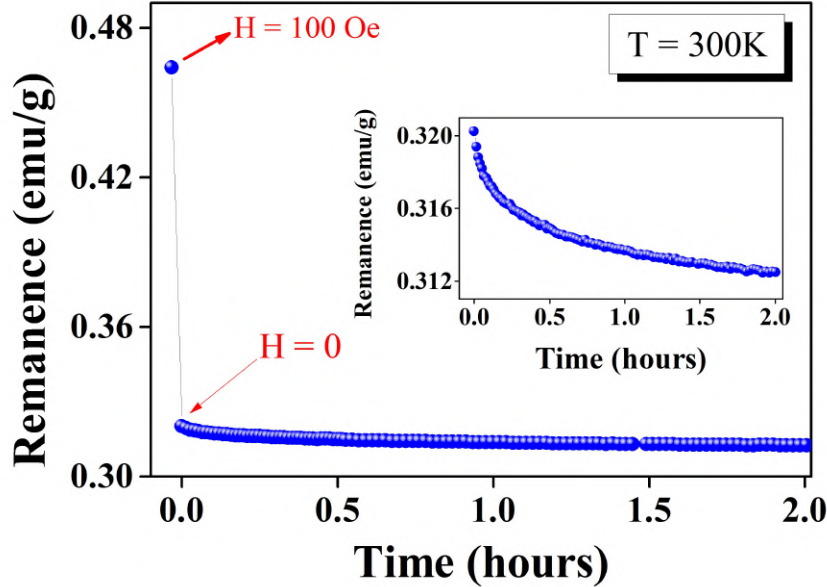


Figure 4.7: Remanence as a function of time for $\alpha\text{-Fe}_2\text{O}_3\text{@CNT}$. A single data point in the main panel is shown to depict the value of in-field magnetization ($H = 100$ Oe). The inset shows that the remanence is constant over a time period of two hours depicting time-stable nature of remanence.

constant with time displaying a change of less than $\sim 3\%$ over a time period of three hours. This part of the remanence (inset of Figure 4.7), which is a subject matter of investigation here, is fairly long lived in experimental time scale and can be termed as *time-stable* remanence.

To further investigate the role of CNT in $\alpha\text{-Fe}_2\text{O}_3\text{@CNT}$, we compare remanence versus time data at room temperature for $\alpha\text{-Fe}_2\text{O}_3\text{@CNT}$ and $\alpha\text{-Fe}_2\text{O}_3$ -template prepared at $H = 1$ kOe. We observe that the magnitude of remanence is significantly enhanced in case of $\alpha\text{-Fe}_2\text{O}_3\text{@CNT}$ as compared to $\alpha\text{-Fe}_2\text{O}_3$ -template as shown in Figure 4.8(a). This is a very intriguing and useful result in terms of practical applications. As shown in Figure 4.8(a), magnitude of remanence is at least an order of magnitude larger for $\alpha\text{-Fe}_2\text{O}_3\text{@CNT}$ (blue dots) than what is observed for the $\alpha\text{-Fe}_2\text{O}_3$ -template (red dots).

Figure 4.8(b) compares remanence as a function of time prepared at three different H – 100 Oe, 1 kOe, and 10 kOe, for $\alpha\text{-Fe}_2\text{O}_3\text{@CNT}$ depicting its stability

with time, and its counter - intuitive magnetic field dependence. We find that the remanence exhibits an unusual behaviour at different magnetic fields. The magnitude of remanence follows an increasing trend at lower fields up to a critical field, and thereafter exhibits a decreasing trend with increasing magnetic field. For instance, the magnitude of remanence at 100 Oe is ~ 0.3 emu/g which increases to ~ 0.6 emu/g at 1 kOe. However, the magnitude of remanence drops down to ~ 0.22 emu/g at 10 kOe. This type of behaviour is not expected for a regular ferromagnet

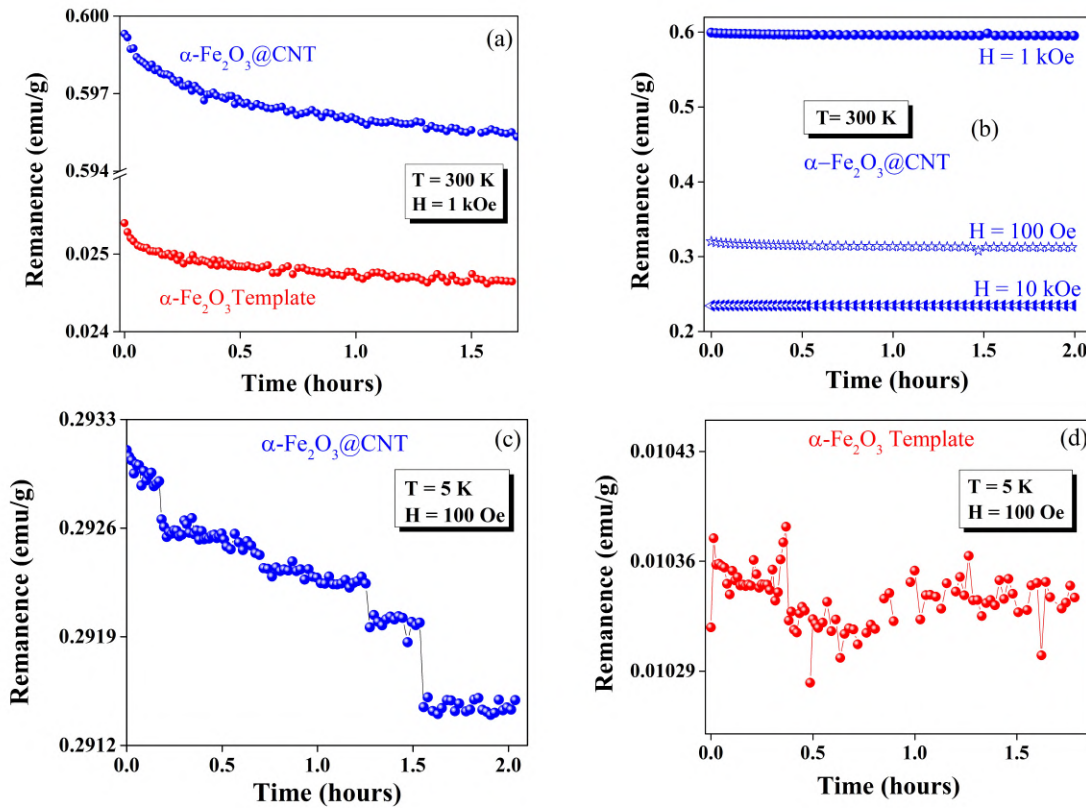


Figure 4.8: (a) Remanence as a function of time measured at 300K for $\alpha\text{-Fe}_2\text{O}_3\text{@CNT}$ (blue dots) and the $\alpha\text{-Fe}_2\text{O}_3$ -template (red dots). For both the samples, the remanence has been prepared by following the ZFC protocol mentioned in the text (b) shows remanence vs time for $\alpha\text{-Fe}_2\text{O}_3\text{@CNT}$ at 300K. Here, remanence is prepared at three different H , depicting its time-stable nature and its counter-intuitive magnetic field dependence. (c) and (d) show remanence vs time measured at 5K, for $\alpha\text{-Fe}_2\text{O}_3\text{@CNT}$ and the $\alpha\text{-Fe}_2\text{O}_3$ -template respectively. Here the remanence has been prepared following the FC protocol for both the samples.

or antiferromagnet. [73] The unique magnetic field dependence is attributed to WFM traits and has been observed for canted AFMs earlier. [89] It is to be emphasized that these features are not reflected in routine M-H isotherms and can be traced through remanence measurements.

Similar features are observed when the remanent state is prepared following a FC protocol at 100 Oe as shown in Figure 4.8(c) for α -Fe₂O₃@CNT. The magnitude of remanence observed is ~ 0.3 emu/g at 5K is substantially larger (Figure 4.8(c)) as compared to the α -Fe₂O₃-template which is ~ 0.01 emu/g (Figure 4.8(d)). In case of α -Fe₂O₃@CNT, occasional jumps in remanence are observed, albeit the change in magnitude is less than 0.5%. It is intriguing to note that the magnitude of remanence is larger, and exhibits more stability at 300K than at 5K, despite the fact that the thermal fluctuations should disrupt the remanence more at higher temperatures. The *time-stable* remanence at room temperature can be of great advantage for practical applications. We shall deal into the underlying reasons for the observation of enhanced time-stable remanence in subsequent sections.

4.3.5 Weak Ferromagnetism and *Time-Stable* Remanence

In recent studies, remanence was investigated in a number of canted AFMs. [89] These studies have enabled an understanding that canted AFMs leave some unique footmarks in remanence. As mentioned earlier, these features are not reflected in routine magnetization versus temperature, or M-H isotherms. [88,89] In this section, we discuss the intimate relation with weak ferromagnetism and *time-stable* remanence.

To delve into the reason for ultra slow magnetization dynamics responsible for *time-stable* remanence, we delve into the magnetic structure of α -Fe₂O₃. α -Fe₂O₃ exhibits both AFM and WFM states across T_M (~ 260 K). The spin configuration is shown in Figure 4.1 for pure AFM (Figure 4.1(a)) and the WFM state (Figure 4.1(b)). In pure AFM state, the spins are arranged along the c-axis. In WFM state, the spins are arranged in a specific sequence different from AFM state (Figure 4.1(b)), leading to a net ferromagnetic moment due to canting of the spins (Figure 4.1(c)). In case of WFM state, spontaneous canting of the type $\vec{D} \cdot (\vec{S}_i \times \vec{S}_j)$ is symmetry allowed and leads to a net ferromagnetic moment in an otherwise AFM.

In case of a regular AFM, when the magnetic field H is applied, the net in-field magnetization is dictated by the Zeeman energy, exchange energy and magnetocrystalline anisotropy. [61] However in case of WFM, an additional factor due to the

canted spins will also contribute. In the light of above scenario, we will now discuss the unusual results, the presence of a *time-stable* remanence with a counter intuitive H dependence and enhanced magnitude of magnetization and remanence in case α -Fe₂O₃@CNT.

When the remanent state is prepared following a FC or ZFC cycle, the net ferromagnetic moment in the system depends on the Zeeman energy as well as on the contribution of average net magnetization of WFM domains spontaneously canted in the direction of magnetic field. [89, 152] In case where the remanent state is prepared with magnetic field above a critical value, the Zeeman energy dominates. In this case, after switching off H, the remanence decays instantaneously. The magnetization relaxation is much faster in this case following a similar behaviour as what one observed for a regular AFM. Hence, at higher fields (above a critical value), the behaviour of the spins is primarily guided by the applied magnetic field and the effect of weak ferromagnetism is not dominant. [89, 152] This also explains the behaviour of the magnetization versus temperature data at higher fields shown in Figure 4.6. However, below the critical value of magnetic field, the magnetization dynamics is governed by the net ferromagnetic moment contribution from spontaneously canted spins and the Zeeman energy along with other routine terms. [89, 152] This leads to a peak like pattern in magnetic field dependence of *time-stable* remanence as we have observed in a number of canted AFM. [89] This also explains the peak-like behavior observed for α -Fe₂O₃@CNT (Figure 4.8(b)). [89, 152]

We shall now focus on the nature and existence of *time-stable* remanence in WFM. It has been experimentally observed that once a remanent state is set due to magnetic field applied in a particular direction, removing the magnetic field or reversing its direction in WFM region does not alter the magnitude or the direction of remanence. On removal of the magnetic field, the flipping of the WFM domain wall would have to be accompanied by flipping of the super exchange driven AFM lattice which is highly energetically unfavourable. [153] This due to the presence of a potential barrier between the two AFM states. [153] This explains the *time-stable* character of the remanence. Thus, the existence of *time-stable* remanence is intrinsic to WFMs arising from robust pinning mechanisms. Furthermore, it sheds light on the fact that at higher fields, the magnetization dynamics is driven by Zeeman energy and magnetocrystalline anisotropy when the high magnetic field is able to overcome the potential barrier. [89, 152]

Thus, the presence of this *time-stable* remanence is exclusively associated with the canting mechanism. This sheds light on the the ambiguity observed in the magnitude of magnetization on repeated cooling. [89] This also explains the importance of the exact sequence in which FC/ZFC runs are recorded. The above discussion holds true for both the type of samples presented in this chapter. Taking into account all these factors, an upper limit can be put to the ambiguity related with the magnitude of magnetization. This is $\sim 0.1 - 0.2$ emu/g in case of α -Fe₂O₃-template or bare α -Fe₂O₃ nano-particles reported earlier. [89,90]

From Figure 4.8(a), it is also evident that in both the samples, the magnetization dynamics is governed by similar physical process, as the data for α -Fe₂O₃ is a scaled version of the template. However, for the observation of about order of magnitude enhancement in the magnitude of magnetization as well as remanence in α -Fe₂O₃@CNT sample cannot be explained by the ambiguity related to heating / cooling protocols which is typically ~ 0.1 emu/g, estimated from the difference ($M_{FC} - M_{ZFC}$) from FC/ZFC cycles at any fixed magnetic field (Figure 4.8). Thus, the enhancement in magnetization and *time-stable* remanence observed in the α -Fe₂O₃ as compared to the α -Fe₂O₃-template is much larger which cannot explained by considering only history effects. Therefore, it can be concluded that the enhancement in magnitude of magnetization, and correspondingly remanence in α -Fe₂O₃ is not entirely due to nano-scaling (both contain nano-wires of α -Fe₂O₃), or morphology of α -Fe₂O₃ (which is quite similar in both samples (Figure 4.2(a) and 4.4(a-b))).

To further gain insights into the underlying reasons for enhancement in magnetization and remanence, we study the temperature variation of lattice parameters across T_M for both the samples.

4.3.6 Structural Correlation : *Interface Effects*

The results presented in earlier sections show that when DMI driven canted AFM α -Fe₂O₃ is encapsulated inside CNT, substantial enhancement in magnetic functionalities of the oxide encapsulate (α -Fe₂O₃) is observed. The enhanced functionalities are not observed when the sample α -Fe₂O₃@CNT is annealed to intentionally remove the CNT. These results indicate that the CNT is playing a major role leading to significant enhancement in magnetization and *time-stable* remanence. This section aims to gain a better understanding of the underlying reasons responsible for experimental observations of enhanced magnitude of magnetization and time-stable remanence

discussed in earlier sections.

The *time-stable* remanence for a number of symmetry allowed DMI driven canted AFMs has shown to exhibit an intimate correlation with the structural parameters. [89] Considering the case of MnCO_3 with lower T_N ($\sim 30\text{K}$) and $\alpha\text{-Fe}_2\text{O}_3$ with higher T_N ($\sim 950\text{K}$), it was observed that the ratio of the lattice parameters "c" and "a" exhibit a much rapid fall with decreasing temperature in case of MnCO_3 which has a relatively low T_N . MnCO_3 exhibits a more pronounced anomaly in the WFM region around the transition temperature than what is observed for $\alpha\text{-Fe}_2\text{O}_3$ which has a much higher T_N . [89] The magnitude of *time-stable* remanence is found to be larger for MnCO_3 (with lower T_N and more pronounced anomaly in lattice parameters) than $\alpha\text{-Fe}_2\text{O}_3$ (with higher T_N). [89] This trend indicates that the magnitude and stability of *time-stable* remanence are strongly correlated with the structural parameters. In addition, in case of $\alpha\text{-Fe}_2\text{O}_3$, this effect is found to be strongly dependent and tunable by size and morphology. [90]

In view of these observations, we investigated the temperature variation of lattice parameters for both $\alpha\text{-Fe}_2\text{O}_3\text{@CNT}$ and $\alpha\text{-Fe}_2\text{O}_3$ template. A study of the correlation between the lattice parameters can provide insights about the stress/strain in the system which can further explain substantial enhancement in magnitude of magnetization and remanence for $\alpha\text{-Fe}_2\text{O}_3\text{@CNT}$ as compared to $\alpha\text{-Fe}_2\text{O}_3$ -template. To derive the lattice parameters, we fit synchrotron XRD data of $\alpha\text{-Fe}_2\text{O}_3\text{@CNT}$ (Figure 4.2(c)) sample using a two-phase model in Rietveld Profile Refinement, corresponding to rhombohedral $\alpha\text{-Fe}_2\text{O}_3$ ($R\bar{3}c$; hex-setting), and the CNT ($\alpha\text{-Fe}_2\text{O}_3$). [49, 120] In case of the $\alpha\text{-Fe}_2\text{O}_3$ -template, all the peaks are identified with $\alpha\text{-Fe}_2\text{O}_3$. No signatures of graphite (CNT), or any other oxide of iron could be traced (Figure 4.4(c)). The lattice parameters have been derived from the Rietveld Profile fitting.

For both the samples, the lattice parameters "a" and "c" corresponding to $\alpha\text{-Fe}_2\text{O}_3$ phase as well as the respective volume of its unit cell are compared in Figure 4.9(a-c). As evident from Figure 4.9(a-b), the behaviour of lattice parameters "a" and "c", for the samples $\alpha\text{-Fe}_2\text{O}_3\text{@CNT}$ and $\alpha\text{-Fe}_2\text{O}_3$ -template, is similar in nature exhibiting a slight trend of expansion around the weak ferromagnetic region i.e. around 250K (T_M). A slight anomaly in the lattice parameters of $\alpha\text{-Fe}_2\text{O}_3$ around T_M is observed in both the samples. A slight expansion in lattice parameters "a" and "c" for $\alpha\text{-Fe}_2\text{O}_3$ phase around the Morin transition temperature T_M ($\sim 250\text{K}$) in the both the samples is observed.

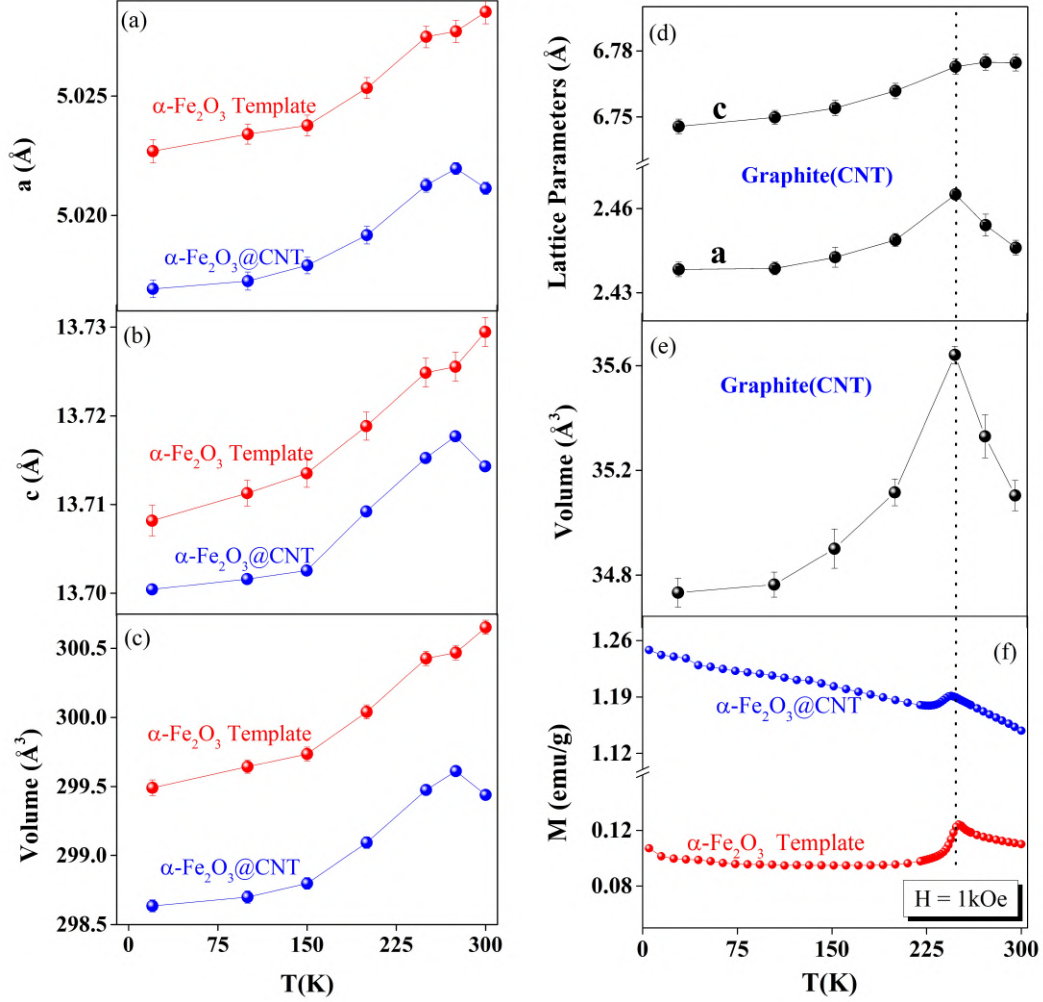


Figure 4.9: (a) and (b) compare the temperature variation of lattice parameters "a" and "c" corresponding to $\alpha\text{-Fe}_2\text{O}_3$ phase for $\alpha\text{-Fe}_2\text{O}_3$ @CNT (blue dots) and the $\alpha\text{-Fe}_2\text{O}_3$ -template (red dots). Here the lattice parameters have been derived considering two phase model discussed in text in $\alpha\text{-Fe}_2\text{O}_3$ @CNT. (c) Volume of the unit cell, exhibiting slight anomaly near $\sim 250\text{K}$. (d) Both the lattice parameters corresponding to CNT for the sample $\alpha\text{-Fe}_2\text{O}_3$ @CNT. Here, the lattice parameter "a" of CNT exhibit a clear anomaly at $\sim 250\text{K}$ around the Morin transition of the encapsulate. (e) Volume of the unit cell of CNT(corresponding to the graphitic phase) for the sample $\alpha\text{-Fe}_2\text{O}_3$ @CNT, exhibiting a pronounced anomaly at the Morin transition. This is also evident from the M vs T data presented in (f) for the bare particles of $\alpha\text{-Fe}_2\text{O}_3$ (red dots) and $\alpha\text{-Fe}_2\text{O}_3$ @CNT (blue dots). The vertical dotted line in (d) to (f) is a guide to eye.

However, significant compression effects are observed in the entire temperature range (20 - 300K) for both the lattice parameters "a" and "c" of α -Fe₂O₃@CNT (blue dots) as compared to α -Fe₂O₃-template (red dots). In this aspect, the data are similar to what has been observed for bare α -Fe₂O₃ nano-crystals in various morphologies, obtained using hydrothermal method. [90] A similar behaviour is observed for the volume of the unit cell corresponding to α -Fe₂O₃ phase in both the samples α -Fe₂O₃@CNT and α -Fe₂O₃-template as shown in Figure 4.9(c).

We now consider the graphitic phase (CNT) in the sample α -Fe₂O₃@CNT. We observe a very intriguing and interesting behaviour in the lattice parameters "a" and "c" of graphitic phase (CNT). It is surprising to observe a pronounced feature in the lattice parameter "a" of the graphitic phase (corresponding to CNT). This feature in CNT interestingly coincides with the Morin transition T_M , intrinsic to the oxide encapsulate (Figure 4.9(d)). A slight anomaly is also observed for the lattice parameter "c" corresponding to the CNT (Figure 4.9(d)) at the Morin transition temperature (T_M). The observation of anomaly in the graphitic phase at the magnetic transition of the oxide encapsulate hints towards the role of CNT. This anomaly is even more pronounced in the temperature variation of volume of the unit cell corresponding to the graphitic phase (CNT) as shown in Figure 4.9(e).

The pronounced anomaly in the lattice parameter "a" of the CNT around the magnetic transition of α -Fe₂O₃ (oxide encapsulate) provide promising evidence of the *interface* effects. The *interface* effect arising from the lattice mismatch between between rhombohedral α -Fe₂O₃ ($a = 5.038 \text{ \AA}$, $c = 13.772 \text{ \AA}$) and hexagonal CNT ($a = 2.47 \text{ \AA}$, $c = 6.79 \text{ \AA}$) appears to introduce strain effects in the system. These strain effects, in turn, could be to be responsible for the significant enhancement in the magnitude of the remanence, as experimentally observed (Figure 4.8(a)) in α -Fe₂O₃@CNT.

It is to be recalled that MnCO₃ is known to be a stronger WFM as compared to α -Fe₂O₃ due to its lower Néel transition temperature. [66] A larger T_N implies stronger AFM super exchange, which leads to a smaller spin canting in α -Fe₂O₃. [66] Thus, the weak ferromagnetic effect is relatively weak in bare α -Fe₂O₃ ($T_N \sim 950\text{K}$) as compared to MnCO₃ ($T_N \sim 30\text{K}$). Interestingly, it has been observed that the *time-stable* remanence also reflects this correlation. From the remanence data obtained on a number of canted AFM, on hematite and a number of DMI driven carbonates including MnCO₃, NiCO₃ and CoCO₃ (unpublished), it is consistently observed that

the magnitude of *time-stable* remanence bears an inverse correlation with the Néel temperature. [89] Thus, the magnitude of remanence is found to be much larger for MnCO_3 (~ 0.6 emu/g) with larger spin canting as compared to what is observed for $\alpha\text{-Fe}_2\text{O}_3$ (~ 0.05 emu/g) with smaller spin canting. This feature reflects the extent of spin canting through simple magnetization / remanence measurements in symmetry allowed canted AFM. [89,90]

From present set of data it is evident that the magnitude of *time-stable* remanence observed in $\alpha\text{-Fe}_2\text{O}_3\text{@CNT}$ at 300K (Figure 4.8(a)) is now on par with what has been observed for MnCO_3 below 30K. [89] Further, the anomaly observed in the lattice parameters near T_M in case of graphitic shells in $\alpha\text{-Fe}_2\text{O}_3\text{@CNT}$ (Figure 4.9(e)) is also more pronounced than what has been observed in the lattice parameters of pure MnCO_3 in its weak ferromagnetic phase. [89] Thus, we propose that encapsulation of $\alpha\text{-Fe}_2\text{O}_3$ within CNT leads to strain and *interface* effects, which, in turn, modulate the spin canting angle, Fe-O-Fe bond angle and bond lengths. [90]

The strain effects in $\alpha\text{-Fe}_2\text{O}_3$ in various morphologies and sizes are known to tune the Fe-O-Fe bond angle and bond lengths which, in turn, crucially affect the magnitude of *time-stable* remanence. [90] Hence, the data suggest that the weak ferromagnetic phase is modulated by the strain effects, as evident from volume compression (Figure 4.9(c)). This can considerably affect both the spin canting angle, and Fe-O-Fe bond lengths / bond angles associated with the AFM super exchange. [90] The enhancement in both the magnetization and the remanence is also consistent with these strain effects in the lattice parameters which are significantly larger for $\alpha\text{-Fe}_2\text{O}_3\text{@CNT}$ as compared to $\alpha\text{-Fe}_2\text{O}_3\text{-template}$. Especially with control experiment on the bare hematite, it appears that the observed enhancement in the magnitude of remanence is related to larger spin canting induced due to strain effects in the system.

In case of $\alpha\text{-Fe}_2\text{O}_3\text{@CNT}$, the experimental data are indicative that oxide/CNT *interface* effects enable larger spin canting and the associated spin orbit coupling which leads to the observed enhancement in the magnitude of remanence. This implies that the spin orbit coupling associated with the spin canting phenomenon intrinsic to the encapsulate is transmitted to the graphitic shells, particularly to its in-plane lattice parameter "a" (Figure 4.9(d)). In graphene-based systems, spin-orbit coupling is relatively weaker as compared to CNT owing to the curved surface of the CNT. [154,155] There have been reports on interfacial DMI on graphene/ferro-

magnetic metal based heterostructures. [156] Though microscopic measurements are needed to understand whether enhanced spin orbit coupling in $\alpha\text{-Fe}_2\text{O}_3\text{@CNT}$ plays a role, the present set of data hints towards this possibility.

The experimental data shown in Figure 4.9 suggest that the enhanced magnitude of magnetization and remanence is a manifestation of the *interface* effect arising from the interaction between the CNT and the oxide encapsulate. The *interface* effect produces strain in the system, which alter the WFM phase of the oxide encapsulate by modulating the spin canting angle. Though microscopic measurements [157–160] are certainly needed to confirm this, the data suggest that the between two functional materials – CNT and DMI driven canted AFM $\alpha\text{-Fe}_2\text{O}_3$ reveals its manifestation in the form of substantial enhancement in the magnitude of magnetization as well as remanence. The *interface* effect exists primarily because of the lattice mismatch between $\alpha\text{-Fe}_2\text{O}_3$ and the CNT. Furthermore, it is to be emphasized that it is non-trivial to gain information about the spin canting angle even through microscopic measurements. In this regard, the remanence measurements can prove to be a great asset to reveal the subtle magnetic features which are not evident in routine magnetization versus temperature and M-H isotherms. We reiterate that we have reasoned a plausible explanation to understand the mechanism arising at the of the oxide and the CNT, and microscopic measurements are certainly needed to confirm and gain a better insight about the interfacial effects.

4.3.7 Magnitude of Time-Stable Remanence at Room Temperature : Practical Implications

The *time-stable* remanence which arises exclusively from the weak ferromagnetic phase [89] has been enhanced by an order of magnitude by encapsulation of the weak ferromagnet – $\alpha\text{-Fe}_2\text{O}_3$ within the core cavity of the CNT. The experimental data discussed in previous section indicate that encapsulation of $\alpha\text{-Fe}_2\text{O}_3$ is the most efficient way to enhance the magnitude of *time-stable* remanence. Considering remanence as the capacity of magnetization retention, the two important aspects from applications point of view are: (i) magnitude of remanence, and (ii) the holding time.

We tabulate the magnetization (M) and *time-stable* remanence at 300K prepared using the ZFC protocol for the sample $\alpha\text{-Fe}_2\text{O}_3\text{@CNT}$ (Table 1). It is observed up to 70% of *in-field* magnetization is retained (in the form of remanence μ) after

Table 4.1: Numerical values of M and Remanence (μ) for the sample α -Fe₂O₃@CNT at room temperature to depict the magnetization retention. Both the values are quoted for three different magnetic fields.

Field (Oe)	T (K)	M (emu/g)	Remanence (μ) (emu/g)	Magnetization Retention (%) (μ /M)*100
100	300	0.46413	0.32024	69
1000	300	1.48752	0.59932	40
10000	300	2.5721	0.2344	9

the removal of magnetic field ~ 100 Oe and 40 % in case of magnetic field ~ 1000 Oe for the sample α -Fe₂O₃@CNT. Considering the application point of view, these values of magnetic field can easily be achieved by bar magnets. More importantly, these functional magnetic properties exist at room temperature where nano-spintronic devices are expected to work.

When the magnetic field is removed, the magnetization value decays with time to ~ 0.5 % in the measurement time span of two hours for α -Fe₂O₃@CNT, whereas it is ~ 5 % in case of the α -Fe₂O₃-template (Table 1, Figure 4.8). The remanence is stable, fairly long lived, and larger at 300K than at 5K. This also confirms that the magnetization dynamics observed in weak ferromagnetic region is different from what is observed in other magnetic systems including spin glasses and other nano-scale AFM. [73, 76]

Since this effect exists at room temperature, it can lead to promising technological implications. For instance, in routine FM/AFM exchange bias [161] systems, antiferromagnet can be replaced with a weak ferromagnet which can provide a new and a very robust magnetization pinning. This pinning would require rather low magnetic fields, and should also be tunable by stress. The encapsulation of weak ferromagnet inside CNT can be promising candidates for future nano-spintronic devices. The encapsulation of weak ferromagnetic oxides inside CNT can augments the functional properties of the oxide encapsulate and, in addition, the graphitic shells of the CNT provides protection of the oxide encapsulate. Novel nano-spintronic devices

can be envisaged exploiting the unique magnetic properties of the DMI driven WFM oxide encapsulate protected inside the graphitic shells of the CNT. Some preliminary experimental data depicting high magneto-resistance in $\alpha\text{-Fe}_2\text{O}_3\text{@CNT}$ have been included in Appendix C.

4.3.8 Magnetization and Remanence for $\text{FeO}_x\text{@CNT}$

In this section, we present magnetization (M) and corresponding remanence data for the sample $\text{FeO}_x\text{@CNT}$. This sample consists of two phases of iron oxides – weak ferromagnet $\alpha\text{-Fe}_2\text{O}_3$ and ferromagnet Fe_3O_4 , encapsulated inside CNT. Figure 4.10(a) shows magnetization as a function of temperature (T) following the FC protocol as specified in section 4.2. The data have been recorded while cooling the sample from 300K down to 5K in the presence of a magnetic field $H = 1$ kOe. The inset in Figure 4.10(a) shows the derivative of magnetization as a function of temperature. The derivative shows the presence of a subtle magnetic transition around 250K. This magnetic transition corresponds to the Morin transition (T_M) intrinsic to the $\alpha\text{-Fe}_2\text{O}_3$ present in the sample.

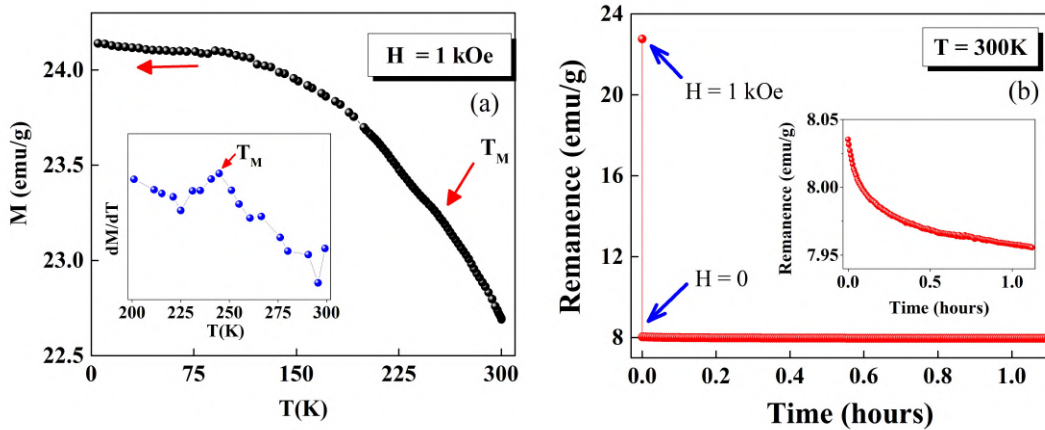


Figure 4.10: (a) Shows magnetization as a function of temperature for the sample Oxide@CNT . The sample exhibits Morin transition at $\sim 250\text{K}$ intrinsic to the encapsulate (hematite). The inset shows the derivative of magnetization as a function of temperature for 200-300K clearly showing the Morin transition at 250K. (b) Shows remanence as a function of time at room temperature depicting one data point for in-field ($H = 1$ kOe) magnetization. The inset depicts that the remanence is long-lived decaying over less than $\sim 1\%$ in a time period of more than one hour.

Figure 4.10(b) shows remanence as a function of time at 300K. The remanent state is prepared using the ZFC protocol (specified in section 4.2) at $H = 1$ kOe. It is observed that prior to switching off the magnetic field H , the magnetization value is ~ 23 emu/g as shown in the main panel of Figure 4.10(b). After switching off the magnetic field, the *in-field* magnetization decays instantaneously to ~ 8 emu/g, retaining 35% of the in-field magnetization value. It is to be noted that the remanence versus time does not exhibit the usual exponential decay which is generally observed in the case of a ferromagnet or ferromagnet encapsulated CNT. [19,61] It is to be emphasized that the magnitude of remanence decays to less than 1% over a time period of more than one hour. This indicates that the sample exhibits ultra slow magnetization relaxation phenomenon at room temperature.

It is to be noted that the magnitude of the *time-stable* remanence for α -Fe₂O₃@CNT at room temperature (prepared at $H = 1$ kOe) was observed to be ~ 0.5 emu/g, as shown in Figure 4.8(a). The results presented in Figure 4.10 indicate that the introduction of a ferromagnet in WFM encapsulated CNT can further enhance the magnitude of *time-stable* remanence, which is ~ 8 emu/g in this case (Figure 4.10(b)). A possible reason could be attributed to robust pinning mechanism occurring between the WFM (hematite) and ferromagnet (magnetite). [88] The *time-stable* character of remanence in WFM encapsulated CNT coupled with a ferromagnet can, thus, result in significantly long-lived remanence.

4.4 Summary

We have shown that encapsulation of a weak ferromagnet α -Fe₂O₃ inside CNT leads to a substantial enhancement in magnetization, and correspondingly a *time-stable* part of remanence which is exclusive to weak ferromagnetism. The appearance of *time-stable* remanence is intimately related to Dzyaloshinskii-Moriya Interaction driven spin canting phenomenon in weak ferromagnets such as hematite. Encapsulation of this oxide inside carbon nanotubes provides novel *interface* effects which reveal its manifestation in terms of significant enhancement in the magnitude of the *time-stable* remanence at the room temperature.

The strong anomalies observed in the lattice parameters of the CNT around the magnetic transition of the oxide encapsulate provide strong signatures of *interface* effects. The control experiments on bare α -Fe₂O₃-template bring into fore that the

weak ferromagnets such as $\alpha\text{-Fe}_2\text{O}_3\text{@CNT}$ are not as weak, as far as their remanence and stability with time is concerned, and encapsulation inside CNT leads to a substantial enhancement in these functionalities. Thus, encapsulation inside carbon nanotubes appears to be the most efficient way to manipulate spin canting and the associated weak ferromagnetism. It is to be emphasized that the method of encapsulation of this multi-functional oxide inside carbon nanotubes is cost effective, scalable, and provides ease of integration for direct patterning into spintronic devices.

We observed a manifestation of *interface* effects in the form of enhanced magnetization and *time-stable* remanence in this chapter. In the next chapter, we will probe the *interface* effects using Raman spectroscopy for the sample $\text{FeO}_x\text{@CNT}$, which contains both $\alpha\text{-Fe}_2\text{O}_3$ as well as Fe_3O_4 inside CNT. The morphology of the sample, the exact phase of the encapsulate, and the oxide particles adhering outside CNT play a crucial role.

Chapter 5

Interface-Effects in FeO_x @CNT using Raman Spectroscopy

5.1 Introduction

Among a variety of magnetic-oxides available, hematite ($\alpha\text{-Fe}_2\text{O}_3$) is one of the advantageous choices due to its abundance and benign nature. As discussed in chapter *four*, hematite ($\alpha\text{-Fe}_2\text{O}_3$) is a Dzyaloshinskii-Moriya Interaction (DMI) driven weak-ferromagnet (WFM) and possess both antiferromagnetic and weak ferromagnetic states. [66] Below its Néel temperature ($T_N \sim 950\text{K}$) the spins lie in the basal plane with a slight canting resulting in weak ferromagnetic phase. At Morin transition temperature ($T_M \sim 260\text{K}$), a spin reorientation transition occurs and the spins reorient along the c-axis of the unit cell resulting in antiferromagnetic phase. [66]

A recent studies have shown that the temperature dependent Raman spectra of $\alpha\text{-Fe}_2\text{O}_3$ reveal anomalies in the phonon modes in the vicinity of the Morin transition temperature T_M . [162] A peak-like behaviour was observed in the Raman shifts of the phonon modes around the Morin transition from weak-ferromagnetic to antiferromagnetic phase. [162] Further, the results presented in chapter *four* revealed the presence of anomalies in the lattice parameters of the $\alpha\text{-Fe}_2\text{O}_3$ encapsulate and the graphitic shells of the CNT around the Morin transition, suggesting the presence of *interface* effects. This prompted us to study the temperature dependent Raman spectra around the Morin transition when $\alpha\text{-Fe}_2\text{O}_3$ is encapsulated inside CNT. The goal of this chapter is to explore and gain insights about the novel *interface* effects through Raman spectroscopy.

In this chapter, we present results of temperature-dependent Raman studies on a hybrid sample – $\text{FeO}_x\text{@CNT}$. This sample consists of WFM hematite encapsulated inside CNT with a mixture of ferrimagnet – magnetite (Fe_3O_4). The results included in this chapter complement the studies presented in chapter *four*, hinting towards the presence of strong *interface* effects.

5.2 Results and Discussion

5.2.1 Characterization

The sample $\text{FeO}_x\text{@CNT}$ was prepared by annealing 10 mg Fe@CNT at 500 °C for 10 minutes under carbon dioxide atmosphere. The sample $\text{FeO}_x\text{@CNT}$ consists of two phases of iron oxides – $\alpha\text{-Fe}_2\text{O}_3$ and Fe_3O_4 encapsulated inside CNT. Figure 5.1(a-d) displays the FESEM micrographs, obtained for the sample $\text{FeO}_x\text{@CNT}$, depicting the morphology of the sample at different magnifications. The sample consists of aligned forest of oxide encapsulated inside CNT as evident from Figure 5.1(a-b). The forests are few 100 $\mu\text{-m}$ in length and typical diameter of the CNT is 30-40 nm. This sample

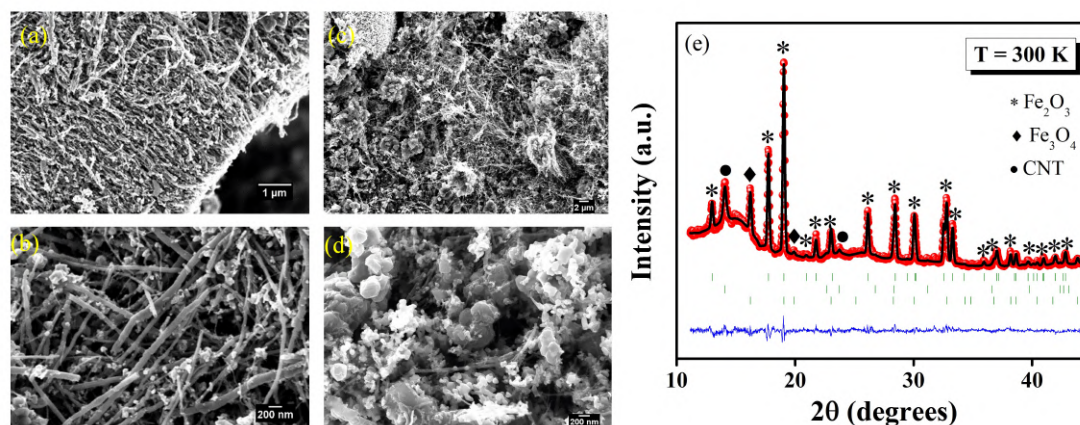


Figure 5.1: (a-d) Representative FESEM image depicting the morphology of the hybrid $\text{FeO}_x\text{@CNT}$. The sample consists of aligned forests (a-b) along with chunks of oxide nanoparticles (c-d). (e) Synchrotron XRD of the sample $\text{FeO}_x\text{@CNT}$ recorded at room temperature. The data (red dots) is fitted (black line) using three phase model using Rietveld Profile Refinement. The black dots show the peak reflections from CNT (graphite). The stars and diamonds indicate peak reflections from hematite and magnetite respectively.

also consisted of large chunks of oxide nanoparticles along with forests of FeO_x@CNT (Figure 5.1(c-d)).

Figure 5.1(e) shows the synchrotron XRD at room temperature. The synchrotron data (red dots) have been fitted (black line) using Rietveld Profile Refinement using three-phase model corresponding to rhombohedral α -Fe₂O₃ ($R\bar{3}c$; hex setting), cubic Fe₃O₄ ($Fd\bar{3}m$) and graphitic phase CNT ($P63mc$; graphite). [120] The black dot, stars, and diamonds in Figure 5.1(e) indicate the reflections corresponding to the graphitic (CNT) phase, hematite and magnetite respectively. The goodness-of-fit obtained was 1.73. The fractional percentage yielded from the synchrotron data are: hematite – 31%, magnetite – 29% , CNT – 40%.

In the following sections, we probe this sample using Raman spectroscopy to gain insights about the *interface* effects around the Morin transition.

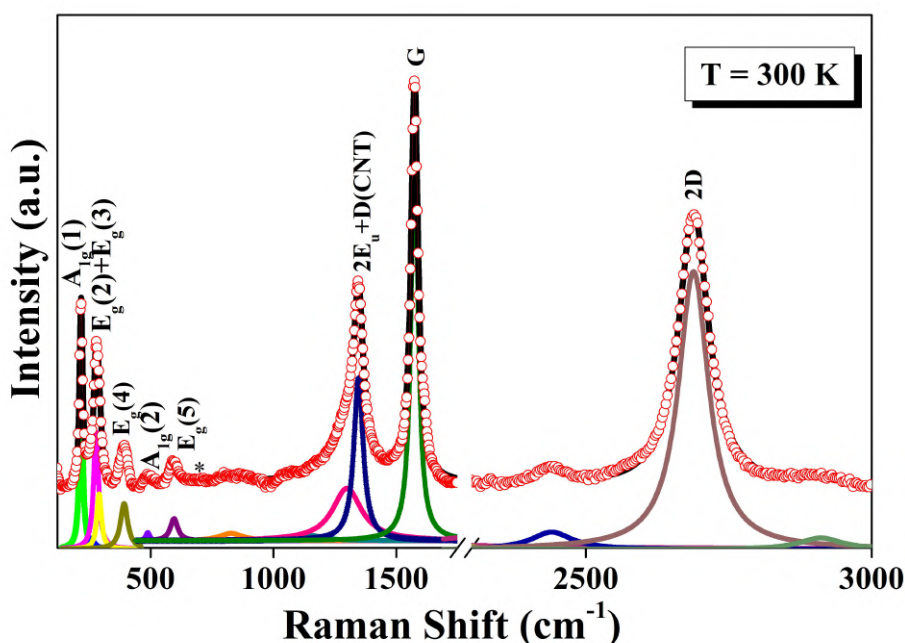


Figure 5.2: Representative Raman spectra obtained for the hybrid FeO_x@CNT at room temperature with Lorentzian fitting of the bands.

5.2.2 Temperature Evolution of Raman Spectra of FeO_x@CNT

Figure 5.2 shows a representative Raman spectra acquired for the hybrid sample FeO_x@CNT using green laser at room temperature. The spectra consists of bands corresponding to the magnetic oxide – hematite as well as the graphitic shells of the CNT. It is to be noted that even though the Rietveld analysis (bulk measurement) yielded $\sim 29\%$ of magnetite in the sample, the intensity of the band corresponding to magnetite at $\sim 670 \text{ cm}^{-1}$ was found to be feeble and could not be resolved. Since Raman spectroscopy is a statistical measurement, a probable reason for the un-resolvable peak corresponding to magnetite could be that the laser beam was hit on the forest containing hematite in major quantities. The FESEM images recorded in broad area showed big chunks of oxide particles, outside CNT (Figure 5.1 (c-d)). From present set of data, it was difficult to resolve whether the encapsulate primarily consisted of hematite. The Raman spectra recorded on this sample showed the modes corresponding to hematite as well as CNT.

5.2.2.1 Temperature Evolution of Raman Spectra of Hematite

Hematite belongs to the space group $R\bar{3}c$ with rhombohedral structure. The group theory predicts two classes of Raman-active vibrational modes: A_{1g} and E_g . [163–165] A typical Raman spectrum of bulk hematite exhibits seven phonon bands which includes two A_{1g} (~ 225 and 498 cm^{-1}) and five E_g bands ($\sim 247, 293, 299, 412$ and 613 cm^{-1}). [163, 164] The A_{1g} band at 225 cm^{-1} describes the movement of the iron ions along the c -axis, whereas the E_g mode at 412 cm^{-1} is assigned to the symmetric stretching of Fe-O bonds in the plane perpendicular to c -axis. [163, 166, 167] The mode at 827 cm^{-1} is identified as a magnon mode. In addition, an infrared active longitudinal optical (LO) E_u mode is sometimes observed at $\sim 660 \text{ cm}^{-1}$. This mode is forbidden in Raman scattering but is understood to arise from the presence of disorder in the hematite crystalline lattice. [167] A strong band which is assigned to an overtone of the E_u band, is observed at around 1320 cm^{-1} . [165, 168, 169]

Figure 5.3 shows the Raman spectra of the FeO_x@CNT in the frequency range $200 - 1500 \text{ cm}^{-1}$ consisting of all the Raman bands corresponding to hematite phase. Raman spectra at a few representative temperatures from 300K up to 198K across the Morin transition of hematite ($T_M \sim 250\text{K}$) are shown in Figure 5.3 for better clarity. The region of interest is around the magnetic transition temperature, Morin

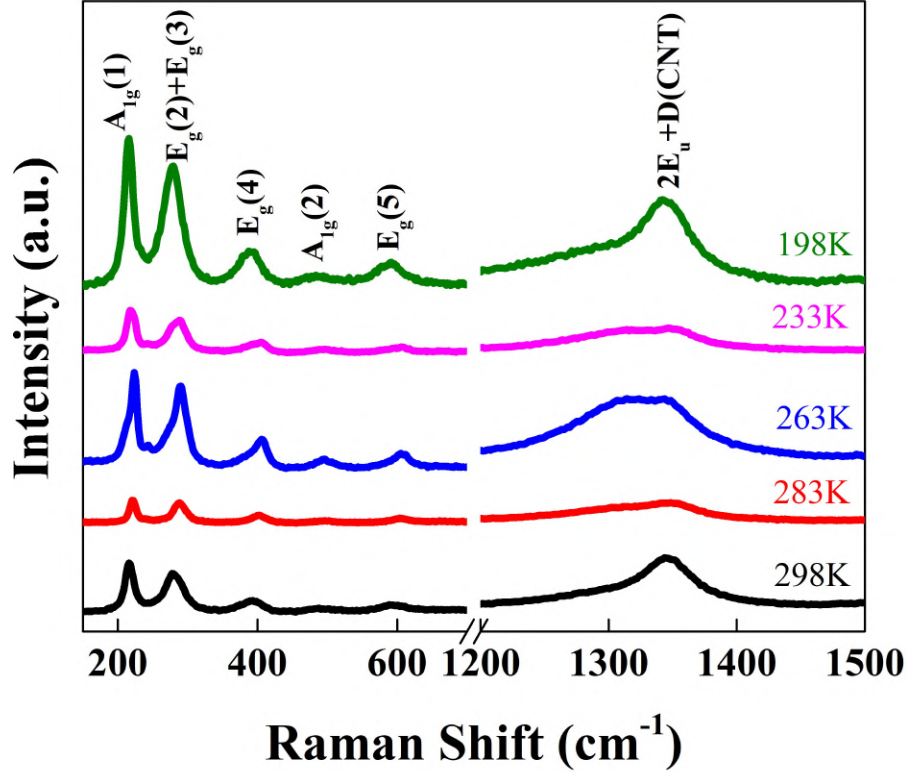


Figure 5.3: Raman spectra of the sample acquired at different temperatures across the Morin transition ($T_M \sim 250K$). For the sake of clarity, only five representative spectra are shown in the range $100 - 1500 \text{ cm}^{-1}$ consisting of all bands corresponding to oxide encapsulate.

transition ($T_M \sim 250K$), and the behaviour of the Raman bands is emphasized around the T_M throughout the text. The spectra exhibit all seven of the signature bands corresponding to hematite. The peaks observed at 216 and 488 cm^{-1} are assigned to the A_{1g} modes. [165, 168, 169] The bands observed at $243, 277, 289, 390, 596 \text{ cm}^{-1}$ are assigned to the E_g modes. [165, 168, 169] The bands obtained in the spectra are observed to be shifted towards lower wavenumber. The red-shift of the bands is expected due to reduction of the particle size and is consistent with the previous reports. [167] A weak magnon mode is also observed at $\sim 820 \text{ cm}^{-1}$. The $2E_u$ peak at around 1300 cm^{-1} can be observed as a shoulder of D-band band corresponding to CNT.

It is observed that the $2E_u$ peak is resolved at lower temperatures and the splitting

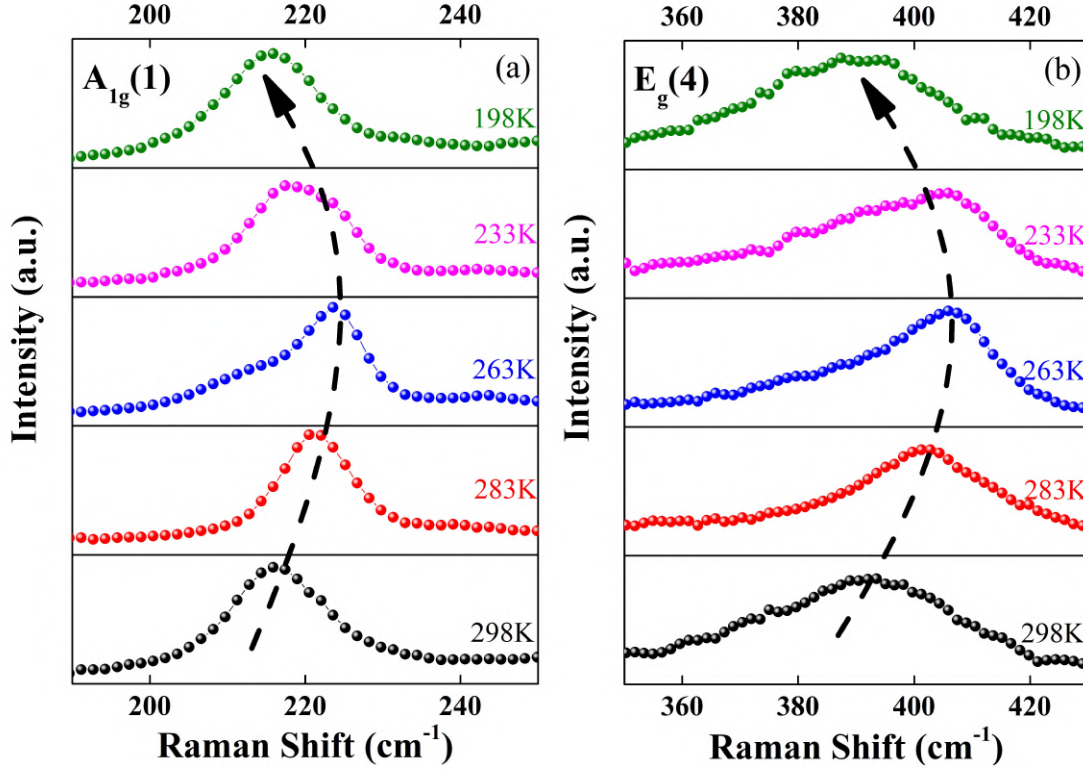


Figure 5.4: Shows the temperature evolution for (a) A_{1g} (216 cm^{-1}) mode, and (b) E_g (390 cm^{-1}) mode across the Morin transition.

of the two bands is clearly evident at 263K as shown in Figure 5.3. For the sake of clarity, we have shown Raman spectra recorded at temperatures below and above the magnetic transition temperature (T_M) to study the effect of magnetic ordering on the lattice vibration.

Figure 5.4 shows the temperature evolution of A_{1g} mode (vibration of Fe atoms along the c -axis) at 216 cm^{-1} and E_g mode (symmetric breathing mode of O atoms relative to Fe atoms) at 390 cm^{-1} across the magnetic Morin transition. It is observed that the phonon frequency exhibits an increasing trend up to 263K and thereafter follows a decreasing trend up to 198K. This anomalous behaviour is observed for the both the modes around the Morin transition (T_M). This anomalous behaviour observed for both the modes indicates that the phonon modes are affected at the onset of the magnetic transition. This type of behaviour is consistently observed for all the A_{1g} and E_g bands.

To understand the anomalous behavior of phonon modes, especially in the vicinity of the Morin transition temperature, we first consider the change in frequency of a phonon mode as a function of temperature: [170]

$$\begin{aligned}\omega(T) = & \omega_o + \Delta\omega_{latt}(T) + \Delta\omega_{anh}(T) + \Delta\omega_{e-ph}(T) \\ & + \Delta\omega_{s-ph}(T),\end{aligned}\tag{5.1}$$

where,

ω_o is the harmonic frequency of the phonon.

$\Delta\omega_{latt}(T)$ is the contribution to the phonon frequency due to the lattice expansion/contraction.

$\Delta\omega_{anh}(T)$ is the intrinsic anharmonic contribution.

$\Delta\omega_{e-ph}(T)$ is the effect of renormalization of the phonon frequency due to electron-phonon coupling.

$\Delta\omega_{s-ph}(T)$ is the contribution due to spin-phonon coupling caused by the modulation of the exchange integral by lattice vibrations.

The anharmonic contribution to the phonon frequency $\Delta\omega_{anh}(T)$ in equation 5.1 can be written as [170, 171]

$$\Delta\omega_{anh}(T) = -A \left(1 + \frac{2}{\frac{\hbar\omega_o}{e k_B T} - 1} \right).\tag{5.2}$$

Here C is anharmonic constant, k_B is the Boltzmann constant.

To explore the nature of the anomalous behaviour shown in Figure 5.4 observed for bands A_{1g} and E_g , we plot the temperature-dependence of peak positions and normalized Raman intensities for representative E_g and A_{1g} . Figure 5.5 shows the temperature-dependent behaviour of phonon frequencies and normalized intensities for A_{1g} and E_g . The phonon frequencies and intensities are extracted from the Lorentzian line fitting at different temperatures. According to equation 5.2, the phonon frequency of a particular mode should exhibit gradual hardening with decreasing temperature. A deviation from the model given in equation 2 had been used to identify the presence of spin-phonon coupling in magnetic systems in a specified temperature range. [162, 171] As evident from Figure 5.5(b) and 5.5(d), the phonon frequencies for A_{1g} and E_g deviate significantly from the anharmonic behaviour pre-

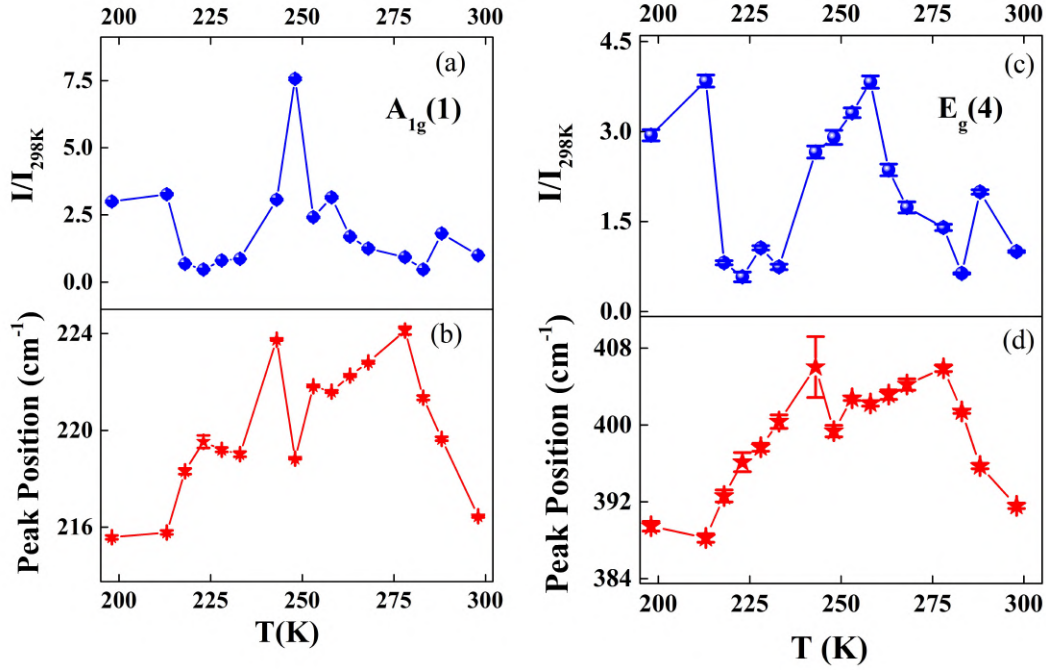


Figure 5.5: Shows the normalized intensity and phonon frequencies respectively as a function of temperature for (a-b) A_{1g} mode, and (c-d) E_g mode. The peak positions and intensities are extracted from the Lorentzian fitting. A shift of $\sim 10 \text{ cm}^{-1}$ is observed for A_{1g} mode and $\sim 18 \text{ cm}^{-1}$ for E_g mode around T_M .

dicted as per equation 5.2. The phonon frequencies exhibit an hardening up to $\sim 265\text{K}$, and thereafter exhibit an anomalous softening around the Morin transition temperature resulting in a broad hump like feature across the T_M . These data reveal the role of magnetic transition on the phonon modes.

In addition, the peak positions as a function of temperature for A_{1g} and E_g (Figure 5.5(b) and (d)) exhibit a dual Morin transition. A second Morin transition has been previously observed in hematite nano-particles in magnetization studies. [90,172,173] This is attributed to either a wide size distribution or due to a mixture of different morphologies. [89] In our case, it is difficult to rule out this possibility, since this samples consisted of forests $\text{FeO}_x@\text{CNT}$ along with chunks of oxide nanoparticles of different sizes. Although, this feature of dual Morin transition is not observed for magnetization versus temperature data (section 4.3.7), the temperature variation of Raman spectroscopy brings out this interesting feature.

The observation of anomalous behaviour of Raman intensity and the softening of

the phonon modes near the Morin transition temperature T_M indicate that the lattice vibrations are effectively altered due to the magnetic ordering. These anomalies of the Raman shift around the magnetic transition temperature support the existence of spin-phonon coupling. The anomalous phonon softening can be attributed to the spin-phonon coupling term $\Delta\omega_{s-ph}(T)$ in equation 5.1. The spin-phonon contribution can be written as: [174,175]

$$\Delta\omega_{s-ph}(T) = -\gamma\langle\vec{S}_i\cdot\vec{S}_j\rangle, \quad (5.3)$$

where γ is the spin-phonon coupling constant and $\langle\vec{S}_i\cdot\vec{S}_j\rangle$ is the spin correlation function. The spin-phonon behaviour is expected to be dependent on the spin-phonon coupling constant γ . Further, different phonon modes can be coupled with different spin-spin interactions due to complexities in the magnetic structure. [174,175] Thus, lattice vibrations perpendicular and parallel to any axis will exhibit different spin-phonon coupling behaviours. As evident from Figure 5.5, the E_g mode involving symmetric breathing mode of O atoms relative to Fe atoms at 390 cm^{-1} shows a relatively larger deviation from anharmonic behaviour ($\sim 18\text{ cm}^{-1}$) as compared to A_{1g} mode involving vibration of Fe atoms along the c-axis at 216 cm^{-1} ($\sim 14\text{ cm}^{-1}$).

The anomalies in the phonon frequencies around the magnetic transition and the deviation in the anharmonic behaviour (equation 5.2) suggest the presence of spin-phonon contributions (equation 5.3) in the system. A similar behaviour around Morin transition has been previously observed in the case of hematite nanoparticles. [162] It is interesting to note that a shift of $\sim 15\text{ cm}^{-1}$ is observed for E_g (390 cm^{-1}) mode, and $\sim 10\text{ cm}^{-1}$ for A_{1g} (216 cm^{-1}). It is worth mentioning that a shift of $\sim 25\text{ cm}^{-1}$ is obtained for the $2E_u$ band. The Raman shifts corresponding to hematite inside CNT are significantly larger than what is observed for bare hematite nanoparticles ($\sim 2\text{-}5\text{ cm}^{-1}$). [162]

The normalized Raman intensities are with respect to Raman intensity at room temperature. As evident from Figure 5.5(a) and 5.5(c), the intensity for both the modes exhibit an anomalous behaviour around T_M ($\sim 250\text{K}$). This behaviour is peculiar and intriguing because the Raman intensity is expected to increase with decreasing temperature due to the reduced phonon scattering at low temperatures. [176]

Hence, it can be concluded that the anomalies of the Raman shift around the magnetic transition temperature support the existence of spin-phonon coupling. A

significant enhancement in the Raman shift ($\sim 10 - 25 \text{ cm}^{-1}$) of the bands corresponding to hematite encapsulated inside CNT as compared to bare hematite nanoparticles ($\sim 6 - 10 \text{ cm}^{-1}$) [162] indicate that the graphitic shells certainly play a crucial role for the strong coupling between spin and phonon degrees of freedom. To further investigate the role of the CNT responsible for the significant enhancement of the Raman shift, we study the behaviour of bands corresponding to graphitic shells as a function of temperature in the next section.

5.2.2.2 Temperature Evolution of Raman Spectra of Carbon Nanotubes

A typical Raman spectra of multi-wall CNT is dominated by three prominent bands. Figure 5.6 shows the Raman spectra of the hybrid $\text{FeO}_x\text{@CNT}$ in the region $1200 - 3000 \text{ cm}^{-1}$ recorded at room temperature. A strong band at 1575 cm^{-1} is the most dominant band in CNT and is referred to as G-band. The G-band is due to the degenerate phonon mode with E_{2g} symmetry. This band is characteristic feature of graphitic layers corresponding to tangential or in-plane vibration of carbon atoms (Figure 5.6(b)). [59, 60] The band around 1340 cm^{-1} , known as the D-band, is assigned to the presence of disorder in graphitic materials. [60] A band present around 2690 cm^{-1} is an overtone or second harmonic of the D-mode. This band

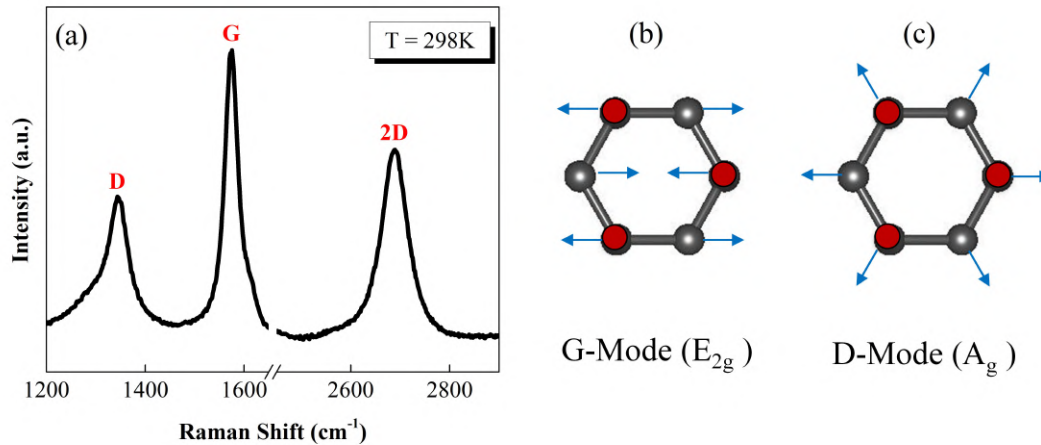


Figure 5.6: (a) Raman spectrum for typical multi-wall CNT in the range $1200-3000 \text{ cm}^{-1}$ recorded at room temperature. The Spectra shows the typical bands pertaining to CNT in the hybrid. (b and c) show the vibration of the carbon atoms for G-band and 2D-band respectively.

is referred to as G' or 2D band. This band belongs to A_{1g} symmetry and involves in-plane vibrational motion of carbon atoms towards and away from the centre of the hexagon ring (Figure 5.6(c)). [59, 60] This band is indicative of the interaction between different graphitic layers. [59, 60]

In view of the unusual magnetization dynamics at the interface of hematite and CNT (chapter *four*), and the anomalies with significant Raman shifts obtained for the hematite encapsulate (Figure 5.5), we investigate the temperature evolution of the Raman bands of the hybrid FeO_x@CNT pertaining to CNT. Figure 5.7 shows the temperature dependent variations of the dominant bands (D-, G-, and 2D-) of the CNT. Owing to the presence of a shoulder of 2E_u band of hematite in the vicinity of the D-band, we show the temperature variation shown for the D-band in Figure 5.7(a) extracted from the Lorentzian fitting. Figure 5.7(b) and 5.7(c) shows the temperature variation of G- and 2D- bands obtained from the raw data. It is observed that the phonon frequencies increases up to 263K; and thereafter start to shift towards lower wavenumbers up to 198K. This behaviour is consistently found in all the bands of the CNT (Figure 5.7).

Figure 5.8 shows the temperature evolution of peak positions of the the D-, G-, and 2D- bands of CNT respectively. It is interesting to note that the behaviour of the phonon modes with temperature shows a deviation from what is commonly observed and reported. [177, 178] The previous reports show that the phonon frequencies of CNT exhibit an monotonically increasing trend with decreasing temperature. [177–179] The origin of this shift is attributed shortening of the C-C distance as the temperature is lowered. [177, 179] However, Figure 5.8(a-c) depict clear anomalies

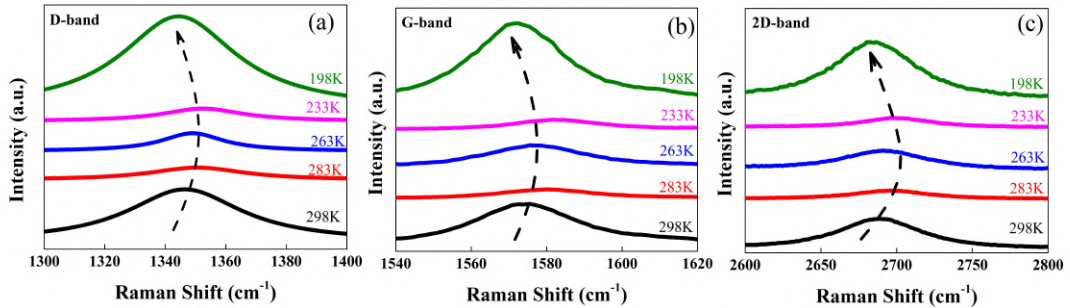


Figure 5.7: Temperature evolution of (a) D-band, (b) G-band, and (c) 2D-band across the magnetic transition of the encapsulate (hematite).

different from previous reports. [177, 178]

In addition, an important observation is that these anomalies occur around the magnetic transition ($T_M \sim 250\text{K}$) of the encapsulate. The Raman shifts observed in CNT bands are $\sim 10\text{-}15\text{ cm}^{-1}$ which cannot be solely explained by anharmonic behaviour of the bands. It is to be noted that a Raman shift as large as $\sim 10\text{-}15\text{ cm}^{-1}$ has not been observed in earlier reports (on pristine CNT). [177–179] The anomalous behaviour across the magnetic transition (T_M) is also reflected in the normalized intensity variation with temperature for the three bands as shown in Figure 5.8(d-f). The intensity of Raman bands exhibit an increasing behaviour on lowering the temperature. [176, 178] The normalized intensity for all the three bands exhibit clear deviations in the temperature region 230-280 K from the expected behaviour.

The results in Figure 5.7 and 5.8 cannot be explained by conventional anharmonic contribution to the phonon frequencies. The observed anomalies in the phonon fre-

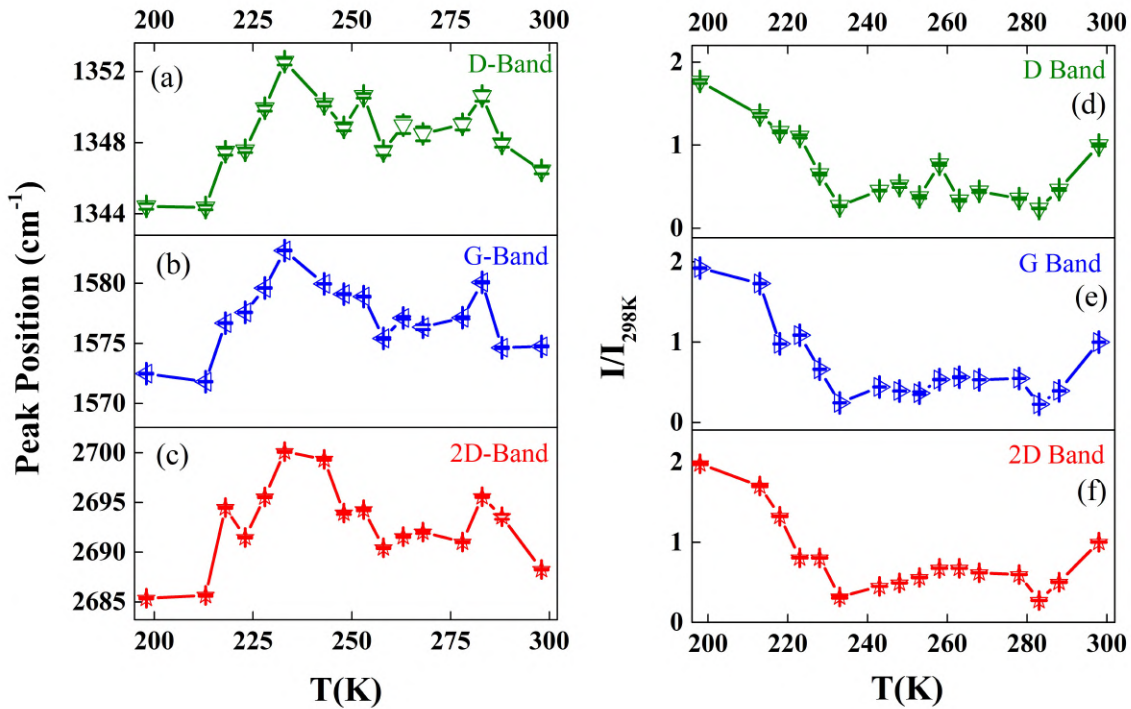


Figure 5.8: Phonon frequencies as a function of temperature for (a) D-band, (b) G-band, and (c) 2D-band. The peak positions are extracted from Lorentzian fitting of the Raman spectra. (d-f) show normalized intensity as a function of temperature for D-band, G-band, and 2D-band respectively.

quencies around the magnetic transition of the encapsulate ($T_M \sim 250\text{K}$). These results are intriguing and points towards *interface* effects between the CNT and the magnetic encapsulate.

5.2.2.3 Influence of Magnetic System's (Hematite) Environment on Carbon Nanotubes : *Interface* Effects

The anomalies observed in the Raman bands of graphitic shells with a remarkable shift in the phonon frequencies ($\sim 10 - 15 \text{ cm}^{-1}$) suggest that the contribution to the phonon frequencies are not purely inherent to thermal factors and anharmonicity (phonon-phonon coupling). [177–179] These significant shifts have not been observed earlier in pristine CNT. [177–179] Further, the Raman shifts observed for the encapsulate – hematite ($\sim 15 - 25 \text{ cm}^{-1}$) are surprising which are significantly larger than what has been observed for hematite bare nano-particles. [162]

This prompted us to study the correlation between the phonons of the oxide encapsulate (hematite) and the phonon modes of the CNT. A closer inspection of the temperature dependent Raman spectra reveals interesting spectral changes as a

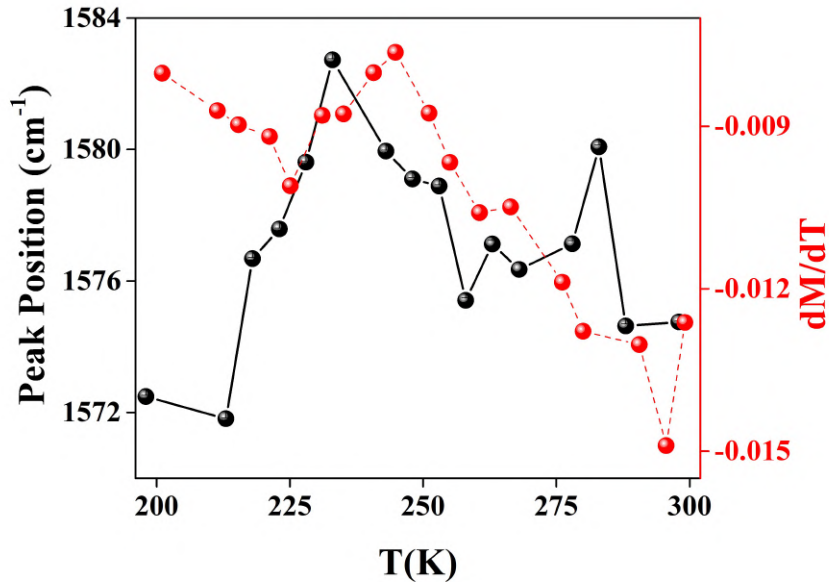


Figure 5.9: Temperature evolution of phonon frequencies of G-band (black dots) corresponding to CNT. The red dots denote the derivative of magnetization of encapsulate (hematite) as a function of temperature. The lattice vibrations of CNT band exhibit anomalies around the magnetic transition of the encapsulate.

function of temperature. Figure 5.9 shows the temperature evolution of G-band (black dots) as a function of temperature. These anomalies surprisingly coincide with the magnetic transition of encapsulate– hematite. For the sake of clarity, the derivate of the magnetization curve of the hybrid $\text{FeO}_x\text{@CNT}$ is shown in red dots(Figure 5.9). The G-band pertaining to CNT exhibit strong anomalies around the magnetic transition of the encapsulate. This anomalous behaviour is also observed for D- and 2D-bands as shown in Figure 5.8.

The results discussed in the previous section establishes the presence of the strong interaction of the spins and the phonons in the hematite system. The anomalous behaviour of the non-magnetic CNT bands around the magnetic transition temperature (T_M) appears to be a manifestation of strong *interface* effects. These *interface* effects are substantiated by a shift ($\sim 10 - 25 \text{ cm}^{-1}$) in the Raman phonon frequencies of hematite as well as the CNT across the magnetic transition. This is consistent with the unusual magnetization dynamics in presented in $\alpha\text{-Fe}_2\text{O}_3\text{@CNT}$ and the anomalies in the structural parameters of CNT around the magnetic transition of the encapsulate presented in chapter *four*

5.3 Summary

Temperature-dependent Raman spectroscopy measurements were conducted on magnetic-oxide encapsulated inside CNT ($\text{FeO}_x\text{@CNT}$). Anomalous behaviour in phonon frequencies corresponding to the encapsulate – hematite indicate the existence of spin-phonon coupling. Interestingly, pronounced anomalies are observed in phonon frequencies pertaining to CNT bands around the magnetic transition (T_M) of the encapsulate. These results reveal how the phonon behaviour of CNT is altered due to the presence of magnetic material in close proximity. Significant Raman shifts of $\sim 15 \text{ cm}^{-1}$ were observed for the phonon modes of the CNT, whereas, Raman shifts of $\sim 15 - 25 \text{ cm}^{-1}$ are observed for the encapsulate – hematite. These shifts are substantially large as compared to what is observed in bare nano-particles ($\sim 2 - 5 \text{ cm}^{-1}$). [162] The Raman shift observed for CNT $\sim 15 \text{ cm}^{-1}$ are much larger than what has been observed for pristine CNT, hence, signifying the strong influence of the magnetic encapsulate on graphitic shells of the CNT. These can be exploited in the design of spin-nanomechanical and nano-spintronic devices.

The results presented in this chapter provide signatures of novel *interface* effects.

Chapter 6

Oxides-filled CNT as Anode Materials in Lithium-ion Batteries

This chapter presents the applications of various transition metal oxides (TMOs) encapsulated inside CNT as potential anode materials for Li-ion batteries (LIBs). In the first part of this chapter, electrochemical performances of various oxides encapsulated inside CNT are discussed individually. The second section of this chapter discusses the significance of the CNT structures and their morphology in the overall electrochemical performance of LIB.

6.1 Introduction

Li-ion Batteries have become a pivotal part of the modern era in the field of energy storage devices and have emerged as the most promising candidate for rechargeable energy technologies. [92–95] Numerous efforts are being made to study and develop suitable electrode materials which are environment-friendly, exhibit better cycling stability, and higher capacity. [93, 102] We would like to recall that the commercial LIB employ graphite as the anode material which has a theoretical capacity of 372 mA h g^{-1} . [97] In this regard, efforts have been made to explore the alternatives to achieve higher capacity with better stability to meet the increasing demand of LIB. Transition metal oxides (TMOs), such as iron, cobalt, nickel, and copper oxides, etc., have attracted considerable attention as promising electrode materials due to their higher theoretical capacities, low cost, abundant resources and low toxicity. [98–101] Nano-structured TMOs, such as nano-rods, nano-flowers, nano-flakes, micro-spheres,

and several other morphologies have been explored as anode materials because of their large effective surface area which leads to improved performance. [113, 180–184] The lithium storage capacity of TMOs is ascribed to the reversible reaction between Li^+ ions and metal oxide which leads to the formation of metal nanoparticles in a Li_2O matrix. [113, 180–184] However, the practical applications of oxides are hampered due to the large volume changes – expansion and contraction of the active material during the conversion reaction during the cyclic process which eventually causes rapid capacity fading during long term cycling and destruction of the electrode during electrochemical cycling. [97] The low electrical conductivity of TMOs also demotes the performance of LIB, hence, limiting the practical realization of TMOs in commercial batteries.

To circumvent the problem of volumetric variation during charging/discharging processes, one effective strategy is to introduce carbonaceous materials to improve the structural stability and electrical conductivity. [97, 102–106] Electrochemical performance of composites of carbonaceous materials with oxides have been reported earlier. [97, 102–106, 134, 185, 186] Among various carbon materials, CNT possess excellent conductivity, chemical stability and structural flexibility. Due to this reason, CNT is widely explored for hybrid electrode materials. [55, 107–113]

In this regard, $\alpha\text{-Fe}_2\text{O}_3\text{@CNT}$ (hematite) and $\text{Fe}_3\text{O}_4\text{@CNT}$ encapsulated within the core cavity of the CNT has been explored earlier. [55, 106, 113] However, encapsulation of other oxides – nickel oxide and cobalt oxide inside CNT as anode materials for LIBs has not been explored. The theoretical capacity of nickel oxide ($\sim 750 \text{ mA h g}^{-1}$) and cobalt oxide ($\sim 950 \text{ mA h g}^{-1}$) is high, but their applications in LIB is hindered due to the drastic volume variation. [98–101] As mentioned above, encapsulation of these oxides inside CNT can provide the structural stability to these materials. Their exceptional mechanical properties can be utilized to buffer the volumetric strain in the electrode materials during charging/discharging processes. [55, 107–113] The high electrical conductivity of CNT can also add to the superior electrochemical performance.

Another important and necessary consideration in the market of energy storage in today's era is implementation of green chemistry while designing new hybrid electrode materials for LIB. It is also essential to consider the cost associated with producing storage devices, which is decided by the abundance of the materials and their synthesis process. LIB have attracted a lot of attention due to its versatility in a wide range of

applications. However, developing green and cheap electrode materials with higher capacity has been a great challenge in the field of energy storage devices. Thus, it is necessary to design green method to prepare high-performance electrode materials which are environmentally benign as well as cost-effective.

In this chapter, we present electrochemical performance of a variety of oxides – iron-oxide (entangled and aligned forests), nickel-oxide (entangled tubes), cobalt-oxide (aligned forests) encapsulated CNT in different morphologies for anode materials in LIB. The morphology of these samples have been controlled by innovative use of camphor, which an environment-friendly and green compound. In the first part of the chapter, lithium-ion storage performance of Oxides@CNT is discussed in detail. These materials deliver exceptional performance with superior cyclic stability and good rate capability. In the second part, a comparative study of performance of Oxides@CNT with that of the bare oxides (without CNT). These results bring into fore the significance of CNT structures for providing cyclic stability. In addition, the role of morphology, outside residual particles, and carbon nanotubes is discussed, which primarily affect the cycling performance of CNT as anode materials.

The samples tested for electrochemical performance ~ 10 mg were fabricated using two different types of cell – Swagelok-type and Coin cell. The method for cell fabrication has been discussed in detail in chapter *two*, section 2.3.1.

6.2 Iron-Oxide filled Carbon Nanotubes

6.2.1 Structural Characterization

The samples are scaled up by conducting multiple synthesis runs using identical synthetic parameters. Further to this, Fe@CNT was suitably annealed to form FeO_x @CNT as described in chapter *three*. The sample discussed was prepared by annealing 10 mg Fe@CNT at 300 °C for 10 minutes under carbon dioxide atmosphere. The oxide@CNT forms the same morphology of the parent Fe@CNT. The crystallographic structure and morphology of the *as-prepared* FeO_x @CNT samples were characterized using XRD, Raman, TGA and FESEM. Figure 6.1 shows the characterization for the sample FeO_x @CNT. Figure 6.1(a-d) displays the representative FESEM images obtained for FeO_x @CNT under different magnifications. The forest-like structures consist of filled CNT with length $\sim 20 \mu$ and diameter in the

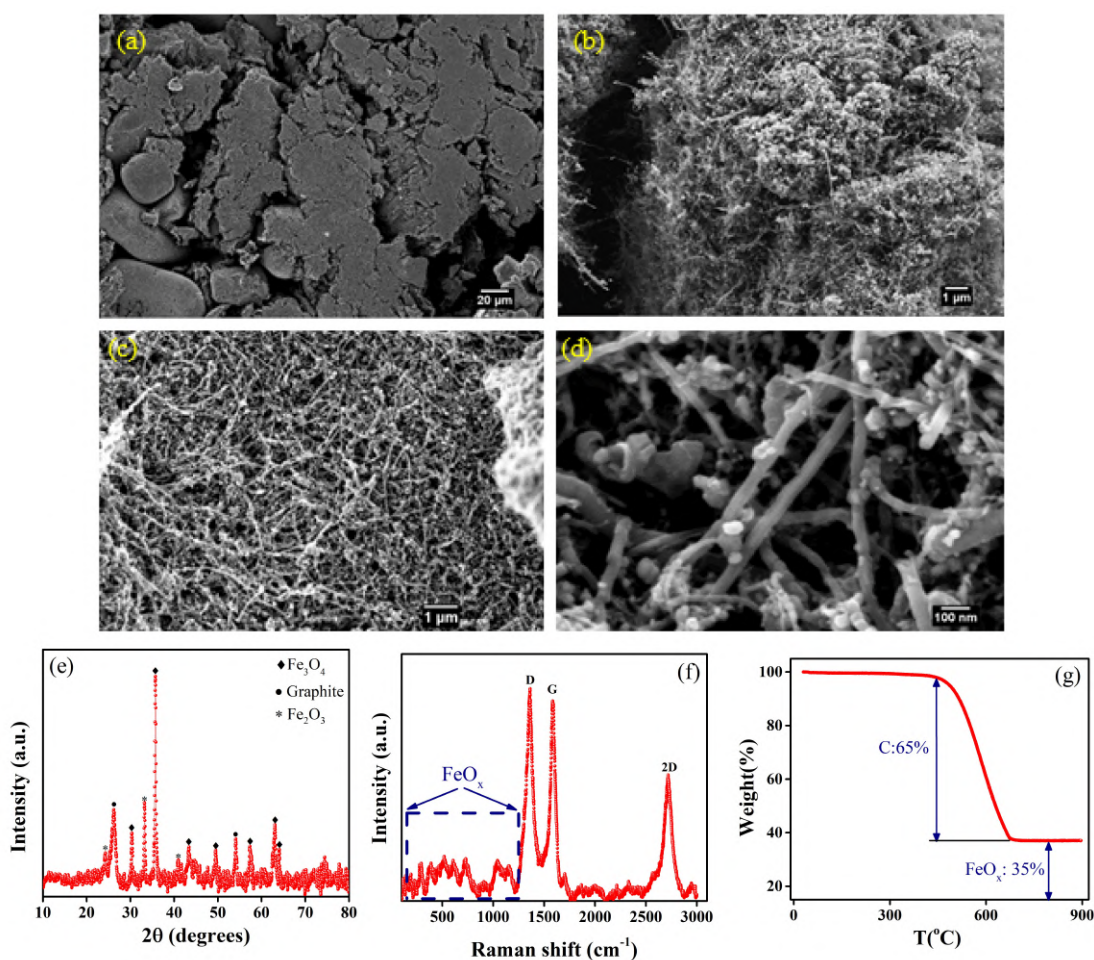


Figure 6.1: (a) - (d) Representative FESEM images of the sample $\text{FeO}_x\text{@CNT}$ at obtained different magnifications. Aligned forest-like structures with typical length of $\sim 100 \mu\text{m}$ are obtained. (e) shows the XRD pattern for the sample $\text{FeO}_x\text{@CNT}$. The XRD data consist of reflections corresponding to graphitic shells as well as iron oxide (magnetite and minor phase of hematite). (f) Raman spectrum of the sample recorded at room temperature depicting D-, G-, and 2D- bands corresponding to CNT. The bands enclosed within blue dotted square correspond to iron oxide. (g) displays TGA curve obtained in air from 30°C to 900°C at a heating rate of $15^\circ\text{C min}^{-1}$. The CNT and iron-oxide content is found to be $\sim 65\%$ and $\sim 35\%$ respectively.

range 20-40 nm. The $\text{FeO}_x\text{@CNT}$ consists of aligned tubes with iron-oxide nanoparticles encapsulated within the core cavity of the CNT. The iron-oxide nanoparticles are also observed to be anchored onto the outer surface of CNT, which in turn, can add to the capacity of the Li-ion batteries.

The crystallographic structure of the hybrid material was examined using XRD, shown in Figure 6.1(e). Figure 6.1(e) shows the XRD pattern of the sample. The diffraction peak reflecting to CNT is observed at around 26.3° corresponding to the (002) plane (ICSD code: 015840). Sharp diffraction peaks corresponding to Fe_3O_4 and minor phase $\sim 10\%$ of Fe_2O_3 are also observed.

The *as-prepared* $\text{FeO}_x\text{@CNT}$ was also characterized using Raman spectroscopy shown in Figure 6.1(f). Raman peaks corresponding to the carbon nanotubes were obtained at $\sim 1356\text{ cm}^{-1}$ (D band), $\sim 1578\text{ cm}^{-1}$ (G band), and $\sim 2715\text{ cm}^{-1}$ (2D or G' band), confirming the presence of CNT. [11] The increase in the number of defects on the CNT surfaces may also help enhance the diffusion of Li^+ ions. In addition, the bands contributing from Fe_3O_4 as well as Fe_2O_3 are also observed. [164]

TGA measurement in air was obtained from $30\text{ }^\circ\text{C}$ to $900\text{ }^\circ\text{C}$ at a heating rate of $15\text{ }^\circ\text{C min}^{-1}$ to identify the amount of carbon in $\text{FeO}_x\text{@CNT}$. The corresponding curve is shown in Figure 6.1(g). Significant weight loss is observed from 450° to $670\text{ }^\circ\text{C}$ which is attributed to the oxidation of the CNT. The carbon content was estimated to be around 65%, and the content of iron-oxide was estimated to be 35%. The amount of iron-oxide represents the percentage of the active material for the sample to be tested as anode material for LIB.

6.2.2 Electrochemical Performance

The electrochemical performance of the sample $\text{FeO}_x\text{@CNT}$ was evaluated in detail using cyclic voltammetry and cyclic stability. The reversibility and kinetics of lithium intercalation and de-intercalation is studied using cyclic voltammetry (CV) measurement. CV curves conducted at a scan rate of 0.1 mV s^{-1} in the voltage window $0.01 - 3.0\text{ V}$ are shown in Figure 6.2(a), for the first three cycles. In the first cycle, a well-defined reduction peak at 0.85 V corresponds to the conversion of Fe_3O_4 into metallic Fe and formation of solid electrolyte interphase (SEI) film. [55, 113, 187] The anodic peaks at 1.62 and 1.84 V represent the oxidation of Fe to Fe_3O_4 . The anodic peaks show no significant difference in subsequent cycles, indicating reversibility and capacity stability. The CV curves as evident from Figure 6.2 are found to be highly reproducible indicating good excellent reversibility of $\text{FeO}_x\text{@CNT}$ as an anode.

The overall electrochemical reaction of the cycle can be described as:

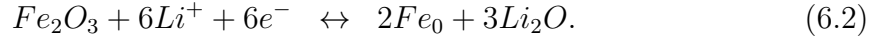
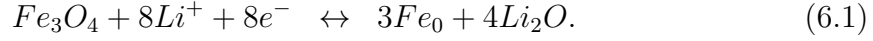


Figure 6.2(b) displays the voltage profiles for the discharging and charging at different cycles recorded at a current density 200 mA g^{-1} . The $FeO_x@CNT$ electrode exhibits a high initial discharge capacity of 955 mA h g^{-1} . The sample delivers an irreversible capacity of 385 mA h g^{-1} in the first cycle. This is attributed to the formation of SEI film due to decomposition of the electrolyte, which is a common phenomenon, well-known for transition metal-oxides. [55,105,134] In the second cycle, the capacity reduces to 570 mA h g^{-1} and in the subsequent cycles, the electrode retains high capacity values up to 100th cycle, indicative of excellent stability and reversibility of the electrode.

Figure 6.3(a) displays the cyclic performance of the sample $FeO_x@CNT$ at a current density of 200 mA g^{-1} for 100 cycles. The discharge capacity obtained in the first cycle is 950 mA h g^{-1} . Despite the capacity decay in the first cycle, the sample delivers a reasonable reversible capacity retaining a value of 570 mA h g^{-1} . It is to

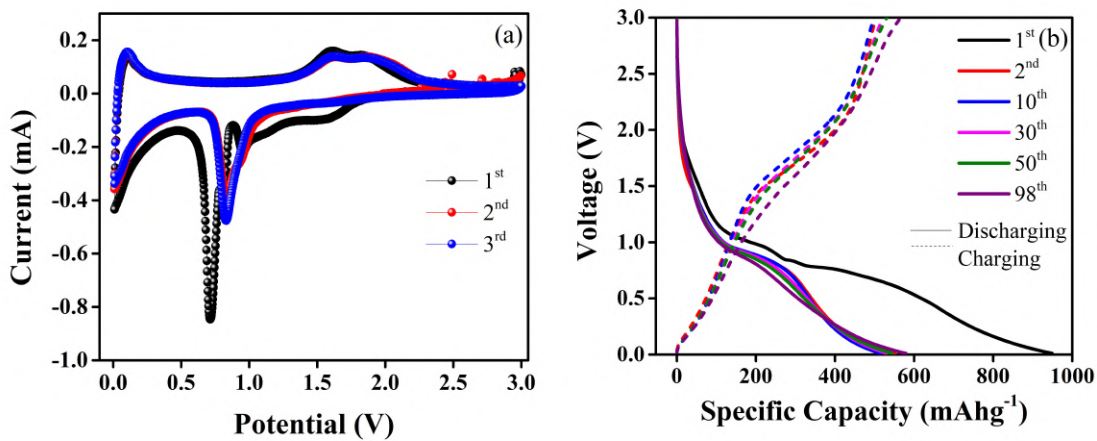


Figure 6.2: (a) Cyclic voltammetry (CV) curves of $FeO_x@CNT$ between 3.0 and 0.1 V at a scan rate of 0.1 mV s^{-1} . (b) Galvanostatic discharge/charge voltage profiles of $FeO_x@CNT$ at a current density of 200 mA g^{-1} .

be noted that the capacity exhibits an increases trend during cycling. This has been previously observed for metal oxide electrodes in long-term cycling. [14,188] Although no consensus has been reached in this regard, various possible reasons have been proposed, such as increase in the surface area of the electrode due to pulverization, increase in the conductivity owing to the formation of metallic nanoparticles, etc. [14] The calculated contribution of the incorporated iron-oxide nanoparticles based on a filling fraction of 35% is around 940 mA h g^{-1} . The obtained value for the reversible discharge capacity is on par with its theoretical capacity (926 mA h g^{-1}). The cycling performance of $\text{FeO}_x\text{@CNT}$ was also tested at higher rate as shown in Figure 6.3(b). The electrode exhibits reversible capacity $\sim 450 \text{ mA h g}^{-1}$ up to 600 cycles, even at high current densities 1 A g^{-1} . These data reveal that the carbon nanotube network supplies the structural support for volume variation of iron-oxide nanoparticles. These data indicate that the material $\text{FeO}_x\text{@CNT}$ exhibits a good capacity retention circumventing the bottleneck associated with fast capacity fading of bare transition metal oxides.

In addition to the cyclic performance, rate proficiency of the electrode material is also an important factor for high power applications. The rate performance for the sample is shown in Figure 6.3(c). As the current densities are increased to $0.1, 0.25, 0.5, 1, 1.5, 2 \text{ A g}^{-1}$, the discharge capacities observed are $515, 472, 447, 425, 410, 390 \text{ mA h g}^{-1}$ respectively. When the current density is switched to 0.5 A g^{-1} , the capacity of $\text{FeO}_x\text{@CNT}$ is restored to a stable capacity of 540 mA h g^{-1} . This rate performance can be attributed to the enhancement of lithium-ion diffusion capability

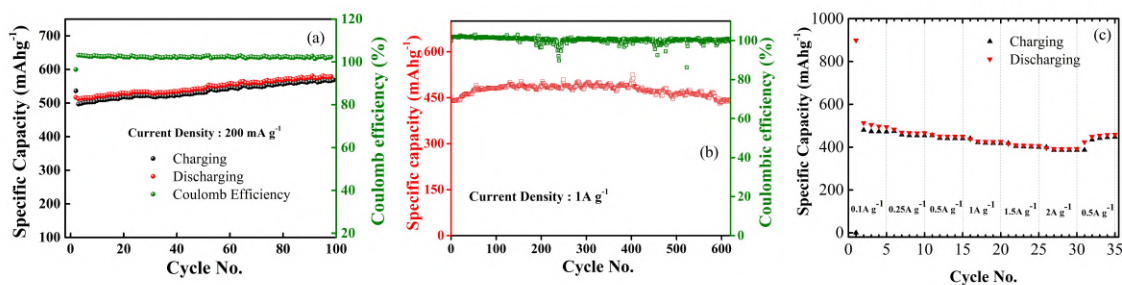


Figure 6.3: (a) shows discharge and charge capacities for $\text{FeO}_x\text{@CNT}$ as a function of number of cycles at current density of 200 mA g^{-1} . (b) shows cycling performance of $\text{FeO}_x\text{@CNT}$ at 1 A g^{-1} . (c) shows discharge and charge capacity of $\text{FeO}_x\text{@CNT}$ at different current densities.

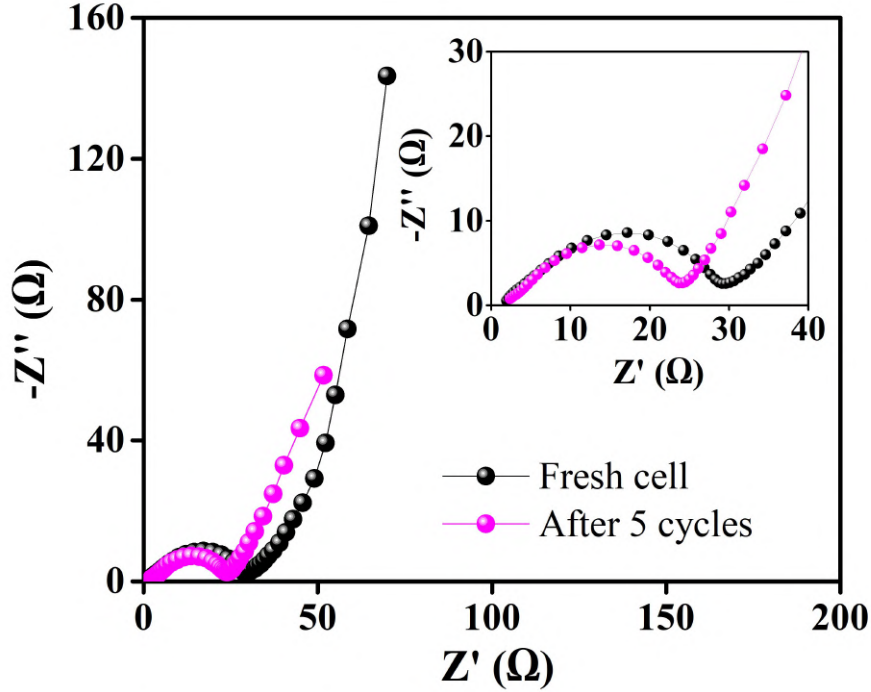


Figure 6.4: *Electrochemical impedance spectroscopy (EIS) spectra of the sample $\text{FeO}_x\text{@CNT}$ for fresh cell (black dots) and post five cycles (pink dots).*

and structural flexibility even at higher current density of 2 A g^{-1} .

Electrochemical impedance spectroscopy (EIS) measurement was performed in $\text{FeO}_x\text{@CNT}$ and the Nyquist plot obtained is shown in Figure 6.4. The large semicircle in the mid-frequency region corresponds to the charge transfer resistance (R_{ct}) and the straight line in the low-frequency region characterizes the Warburg impedance of the lithium-ion diffusion. [189] The diameter of the semicircle in the mid-frequency region is significantly smaller than previous reports on iron-oxide electrode materials. [55, 113, 188] The R_{ct} for $\text{FeO}_x\text{@CNT}$ is found to be $\sim 28 \Omega$. The lower R_{ct} could be due to increased electrical conductivity facilitated by the CNT network. The low ohmic resistance facilitates easy electron transfer during charging/discharging, resulting in enhanced electrochemical performance of the electrode material $\text{FeO}_x\text{@CNT}$.

6.3 Nickel-Oxide filled Carbon Nanotubes

6.3.1 Structural Characterization

Similar to the case of Fe@CNT, Ni@CNT was also scaled up by performing multiple synthesis runs under identical conditions. The parent Ni@CNT sample was then suitably annealed to prepare NiO@CNT, as discussed in chapter *three*. These samples are characterized using XRD, Raman, TGA, and FESEM. Representative FESEM images shown in Figure 6.5(a-d) for the sample NiO@CNT reveal that the pristine morphology of the parent sample (Ni@CNT) is retained after oxidation of the sample to NiO@CNT. The *as-prepared* NiO@CNT display *spaghetti*-like morphology with NiO nanoparticles encapsulated within the core cavity of the CNT. The *spaghetti*-like CNT with long curled structures can offer a higher surface area and more active sites for the intercalation of Li⁺ ions and may be preferable over the forest morphology. Figure 6.5(d) demonstrates magnified FESEM image depicting existence of NiO nanoparticles wrapped inside CNT.

The crystallographic structure of the hybrid material was examined using XRD, shown in Figure 6.5(e). Figure 6.5(e) shows the XRD pattern of the sample. The XRD pattern exhibits three diffraction peaks located at $2\theta = 37.2^\circ$, 43.2° , and 62.9° identified as (111), (200), and (220) planes, respectively. The diffraction peak corresponding to CNT is also observed at around 26.3° reflecting the (002) plane (ICSD code: 015840).

The *as-prepared* NiO@CNT was further characterized using Raman spectroscopy shown in Figure 6.5(f). Raman spectra (Figure 6.5(f)) display bands corresponding to CNT at about $\sim 1356\text{ cm}^{-1}$, $\sim 1568\text{ cm}^{-1}$, and $\sim 2717\text{ cm}^{-1}$, identified as D-, G-, and 2D-band respectively. [11] In addition, the peaks contributing from NiO are also observed which are in good agreement with the previous reports. [190] TGA measurement was performed in air from 30 °C to 900 °C at a heating rate of 15 °C min⁻¹ to determine the weight fraction of NiO and CNT. The corresponding curve is shown in Figure 6.5(g). The carbon content was found to be around 88%, and the content of NiO was estimated to be $\sim 12\%$.

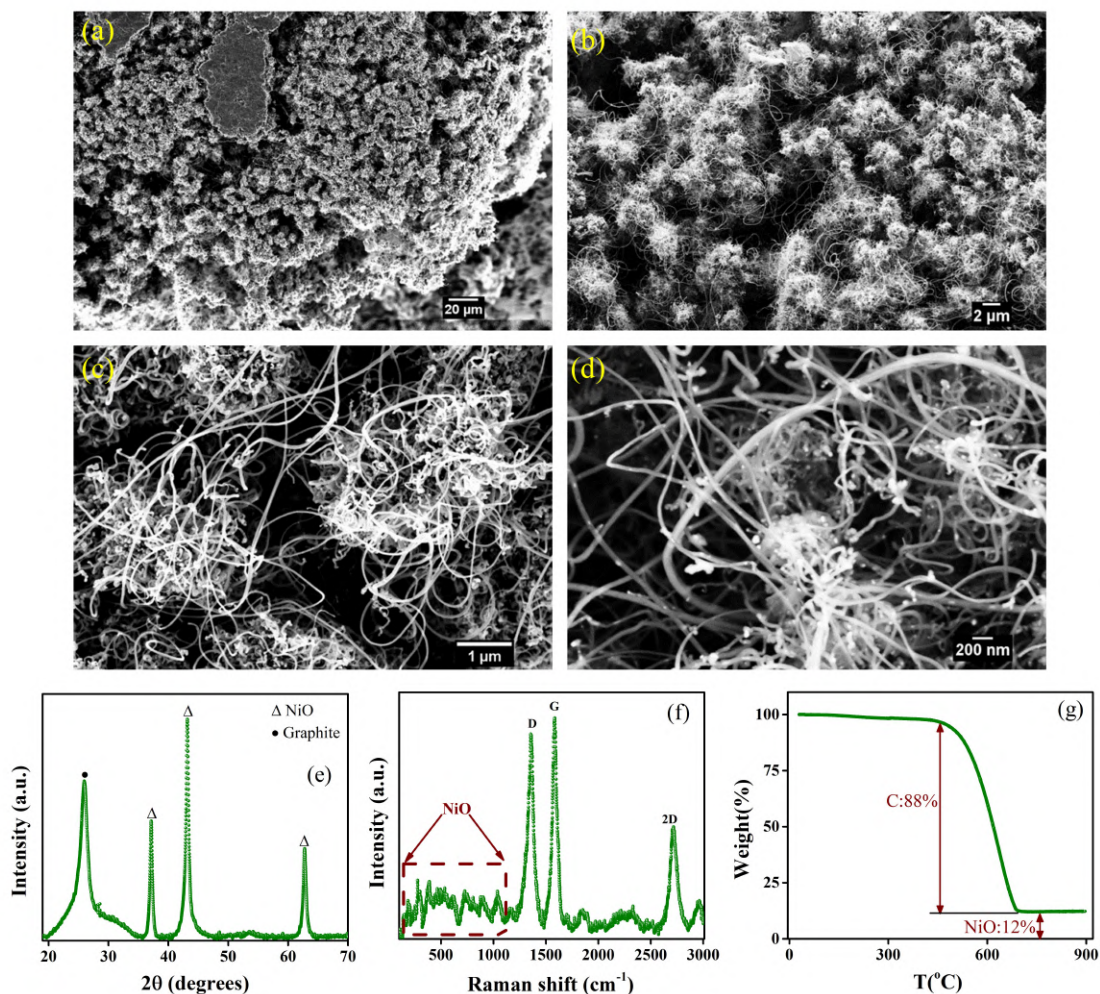


Figure 6.5: (a-d) Representative FESEM images of the sample NiO@CNT at different magnifications. Long entangled structures with NiO encapsulated within carbon nanotubes are obtained. (e) shows the XRD pattern with a well-defined peak at 26.3° corresponding to the graphitic shells and reflections confirming the presence of NiO are also obtained. (f) Raman spectrum of the sample NiO@CNT recorded at room temperature. (g) displays TGA curve obtained in air. The residual weight is found to be $\sim 12\%$ (nickel oxide), and the CNT content is $\sim 88\%$.

6.3.2 Electrochemical Performance

The electrochemical performance of the sample NiO@CNT is assessed by cyclic voltammetry (CV) curves within the voltage range 0.01 - 3.0 V at a scan rate of 0.1 mV s^{-1} (Figure 6.6(a)). A substantial difference is observed between the first and the

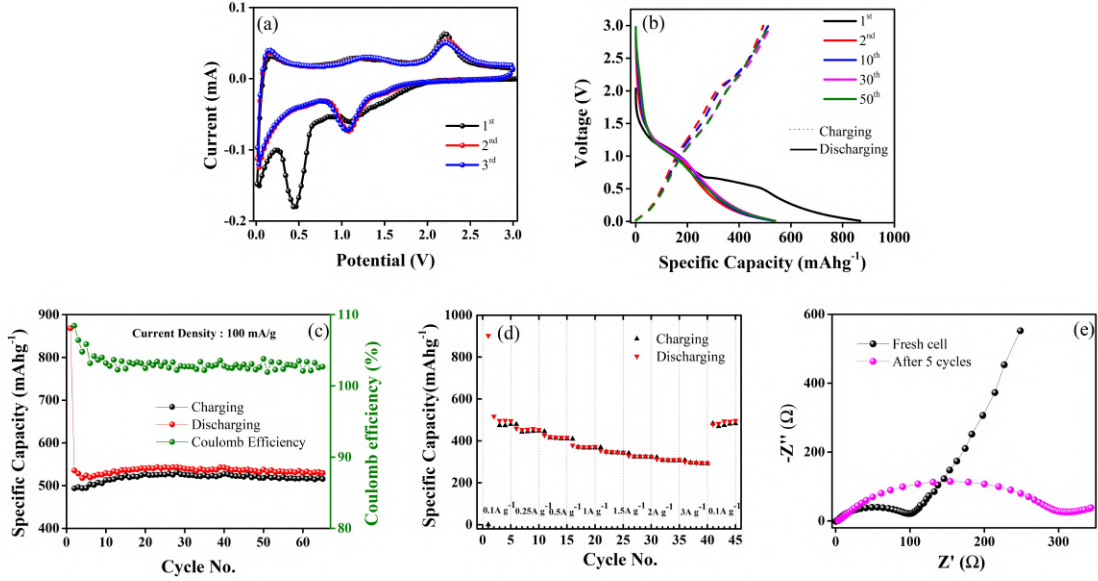


Figure 6.6: (a) Cyclic voltammetry (CV) curves of NiO@CNT between 3.0 and 0.1 V at a scan rate of 0.1 mV s^{-1} . (b) Galvanostatic discharge/charge voltage profiles of NiO@CNT at a current density of 100 mA g^{-1} . (c) Discharge and charge capacities as a function of cycle number at current density of 100 mA g^{-1} . (d) Discharge and charge capacity of NiO@CNT at different current densities. (e) Nyquist plot of ac impedance spectra of NiO@CNT for fresh cell (black dots) and after five cycles (pink dots).

subsequent cycles. In the first cycle, two peaks appear at approximately 0.45 V and 1 V in the cathodic scans. The peak located at 0.45 V originates due to the formation of SEI film resulting from the decomposition of the electrolyte. [134, 184, 191] The second peak at 1.08 V can be ascribed to the reduction of Ni^{2+} to Ni. [184] For the second and third cycles, the reduction peak is shifted to 1.05 V. In the anodic scans, peak at 1.16 V is associated with the partial decomposition of the SEI film. [134, 184, 191] The second peak at 2.21 V is attributed to the oxidation of Ni to Ni^{2+} . [134, 184, 191] The anodic peaks show no significant difference in subsequent cycles, indicating reversibility and capacity stability.

The overall electrochemical reaction of the cycle can be represented as:

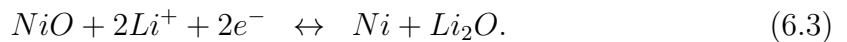


Figure 6.6(b) displays the discharging and charging voltage profiles of different

cycles at a current density 100 mA g^{-1} . The NiO@CNT electrode exhibits a high initial discharge capacity of 870 mA h g^{-1} . The sample delivers an irreversible capacity of 330 mA h g^{-1} in the first cycle attributed to the formation of SEI. [134,192] The charge / discharge curves in the subsequent cycles overlap from the second cycle, which indicates a good cyclic stability and electrochemical reversibility.

Figure 6.6(c) displays the cyclic performance of the sample NiO@CNT at a current density of 100 mA g^{-1} for 100 cycles. The discharge capacity obtained in the first cycle is 870 mA h g^{-1} . Despite the capacity decay in the first cycle, the sample delivers reversible capacity retaining a value of 540 mA h g^{-1} even after 100 cycles with a coulomb efficiency of 105%. Regardless of the low loading ratio (12% of the weight, Figure 6.5(f)) of NiO inside carbon nanotubes, the electrode displays performance on par with FeO_x@CNT. The discharge capacity contributed by NiO nanoparticles can be calculated as 1766 mA h g^{-1} . The obtained value for the reversible discharge capacity even surpasses the theoretical capacity of NiO (718 mA h g^{-1}). Thus, the sample NiO@CNT conjoins the advantages of both NiO and CNT, and hence, a superior anode material for LIB.

The rate capabilities of the sample NiO@CNT tested at various current densities are shown in Figure 6.6(d). The sample delivers an outstanding rate performance even at high current densities. When the current density is restored to 100 mA g^{-1} from 3 A g^{-1} , a stable capacity of 540 mA h g^{-1} is reached back. The exceptional rate performance can be attributed to the enhancement of lithium-ion diffusion and structural adaptability of CNT.

Figure 6.6(e) displays the EIS Nyquist plot of the sample NiO@CNT. The plot consists of a depressed semicircle in the medium-to-high frequencies and a straight line in the low frequency region. The diameter of the semicircle in the mid-frequency region is significantly smaller than previous reports on nickel-oxide electrode materials. [134,184] The charge transfer resistance $\sim 100 \Omega$ is improved as compared to bare NiO nanoparticles, due to the interface between NiO and CNT which in-turn is responsible for the enhanced electrochemical performance of the sample NiO@CNT. [134,189] It is to be noted that the increased value of resistance $\sim 300 \Omega$ post five cycles has also been observed earlier for bare NiO. [193]

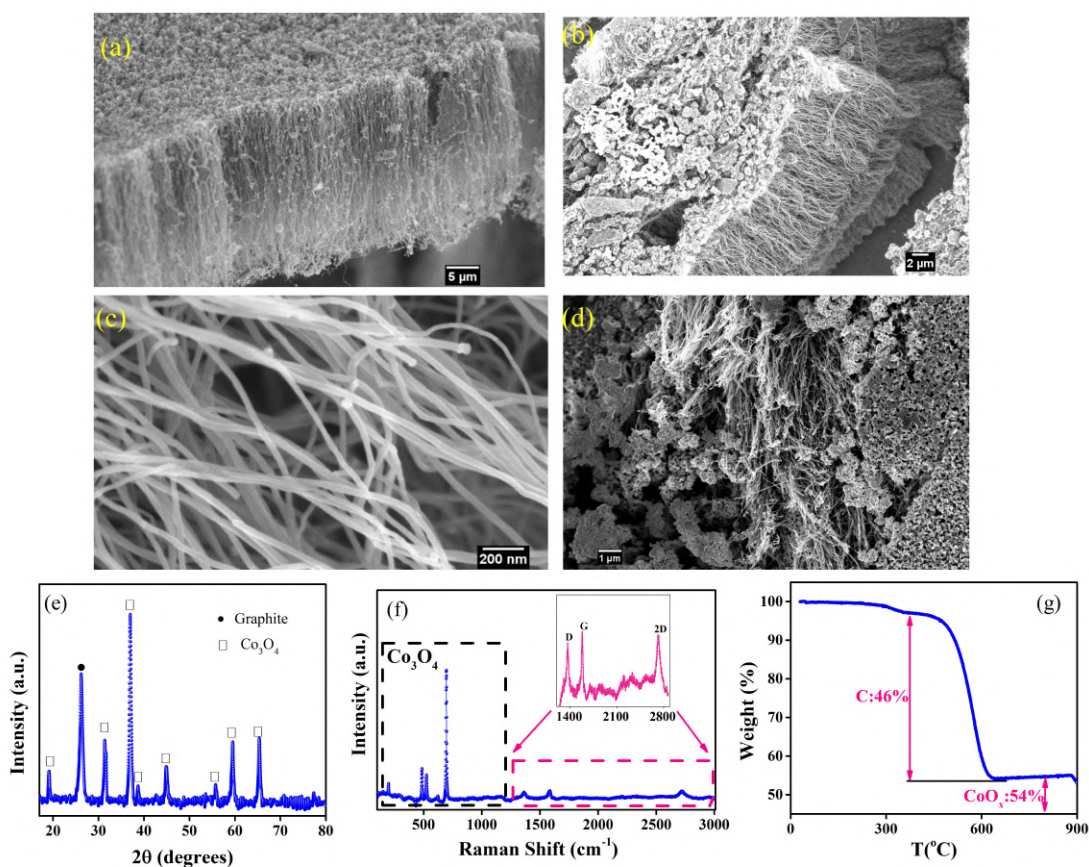


Figure 6.7: (a) displays large carpets of aligned $\text{Co}_3\text{O}_4@\text{CNT}$. The carpets are up to $\sim 100 \mu\text{m}$ in length consisting of aligned tubes filled with cobalt oxide. (b) - (d) are representative FESEM micrographs at higher magnifications. (e) Representative XRD pattern consisting of reflections obtained from the graphitic shells as well as Co_3O_4 . (f) shows the Raman spectrum recorded at room temperature. The enclosed area under black rectangle consists of band contributing from cobalt oxide. The inset shows the magnified enclosed within pink rectangle. Bands contributing from the graphitic shells are shown in the inset for better clarity. (g) shows TGA curve obtained under air and the residual weight of Co_3O_4 is $\sim 50\%$.

6.4 Cobalt-Oxide filled Carbon Nanotubes

6.4.1 Structural Characterization

The sample cobalt-oxide filled CNT ($\text{Co}_3\text{O}_4@\text{CNT}$) has been also been synthesized by annealing the parent sample cobalt-filled CNT under carbon dioxide atmosphere for ten minutes at $500 \text{ }^\circ\text{C}$ (Appendix B). The morphology of the parent

sample Co@CNT is retained post oxidation. Figure 6.7(a-b) shows broad area FE-SEM images, depicting the aligned bundles of nanotubes depicting the aligned forest morphology of the sample. This sample consists of many oxide particles outside the CNT.

The crystallographic structure of the sample Co_3O_4 @CNT is analyzed using XRD shown in Figure 6.7(e). The XRD peak at 26° can be indexed as (002) diffraction peak corresponding to graphite. Oxide peaks confirming the presence of Co_3O_4 are also observed (JCPDS No. : 00-042-1467). The Raman spectrum of the sample Co_3O_4 @CNT is shown in Figure 6.7(f). The Raman spectrum consists of bands characteristic to CNT and Co_3O_4 (dotted box). [11, 194] The inset of Figure 6.7(f) displays the characteristic D- and G- and 2D-bands corresponding to CNT. Figure 6.7(g) shows the TGA curve performed in air from 30°C to 900°C at a heating rate of $15^\circ\text{C min}^{-1}$. The carbon content is estimated to be $\sim 50\%$ and the Co_3O_4 was estimated to be $\sim 50\%$.

6.4.2 Electrochemical Performance

Figure 6.8(a) shows the CV curves for the sample Co_3O_4 @CNT. In the first cathodic sweep, the reduction peak observed at 0.85 V can be attributed to the formation of SEI film. [180, 195, 196] In addition, two reduction peaks are observed at 0.95 V and 1.16 V corresponding to the reduction processes, from Co_3O_4 to CoO and CoO to Co respectively. [196] The reduction of Co_3O_4 to Co is accompanied by the formation of Li_2O . In the anodic sweep, a broad hump at around 1.5 V and a sharp peak at ~ 2.07 V are observed which are associated with oxidation of Co to Co_3O_4 . [180, 195, 196] The overall reaction involved can be described as:

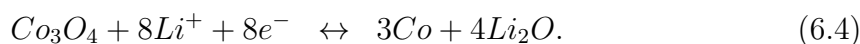


Figure 6.8(b) shows typical charge/discharge capacity voltage profiles for Co_3O_4 @CNT electrode for different cycles at a current density of 100 mA g^{-1} . The long potential plateau at 1.12 V is ascribed to the reduction of Co_3O_4 to an intermediate phase CoO and eventually metallic Co which is in good agreement with the typical characteristic capacity voltage profiles. [195, 196] The Co_3O_4 @CNT electrode delivers an initial discharge capacity of 890 mA h g^{-1} which decays to 600 mA h g^{-1} in the second cycle. The initial capacity fade can be attributed to the formation of SEI film and

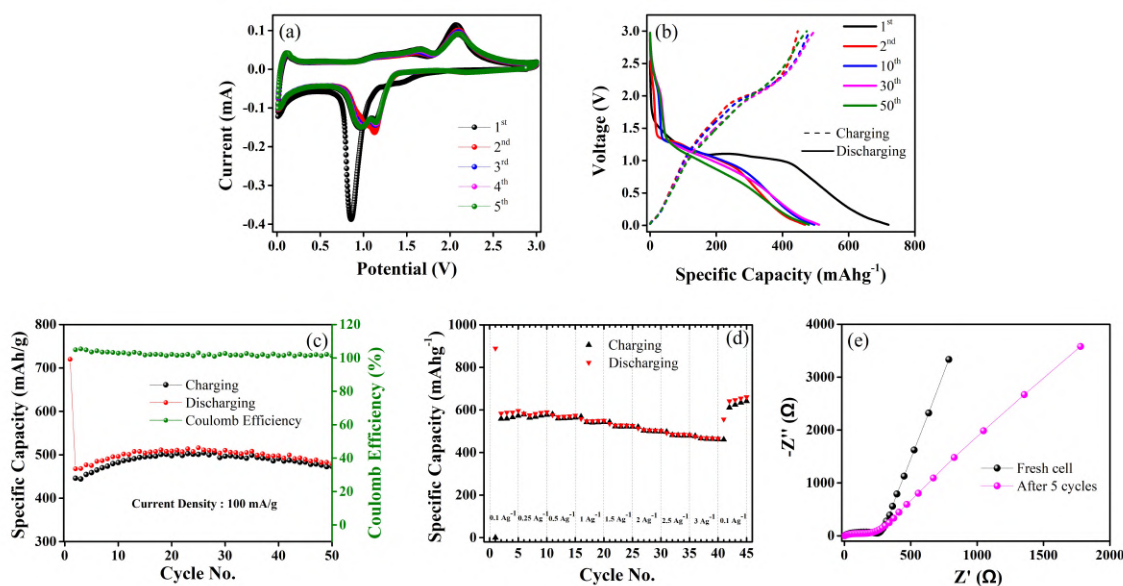


Figure 6.8: (a) CV curves of $\text{Co}_3\text{O}_4@\text{CNT}$ recorded at a scan rate of 0.1 mV s^{-1} between 3.0 and 0.01 V. (b) shows discharge-charge voltage profiles at current density of 100 mA g^{-1} for $\text{Co}_3\text{O}_4@\text{CNT}$. (c) Cycling performance of $\text{Co}_3\text{O}_4@\text{CNT}$ at 100 mA g^{-1} . (d) Rate capability at different current densities from 0.1 A g^{-1} to 2 A g^{-1} . (e) Electrochemical impedance spectroscopy of the sample fresh cell (black dots) and after five cycles (pink dots).

the irreversible reactions consistent with the previous reports. [180, 195, 196] In the subsequent cycles, the capacity retains a value of around 580 mA h g^{-1} for about 100 cycles. It is to be noted that despite a high percentage of active material (Co_3O_4) $\sim 50\%$ in the electrode, the anode delivers a value of 600 mA h g^{-1} . This could be due to the presence of a large number of oxide particles adhering outside the CNT. This can lead to the capacity fade as expected for bare oxide particles. Other factors include low filling efficiency and the aligned forest morphology which also affects the electrochemical performance. The significance of morphology is discussed in detail in the next section.

The charge-discharge capacity as a function of cycle number is shown in Figure 6.8(c). The initial discharge capacity delivered by the $\text{Co}_3\text{O}_4@\text{CNT}$ electrode is 893 mA h g^{-1} which drops to 448 mA h g^{-1} due to the formation of SEI film. [196] In the subsequent cycles, a reversible capacity of 440 mA h g^{-1} is maintained demonstrating good cyclic stability. The discharge-charge curves obtained at different current rates are shown in Figure 6.8(d). A slight decreasing trend is observed when the current

rate is increased from 100 mA g^{-1} to 3 A g^{-1} , and the capacity drops from 583 mA h g^{-1} to 463 mA h g^{-1} . This drop could be due to limited access of surface area at higher rates. When the current rate is restored to 100 mA g^{-1} , reversible capacity of 600 mA h g^{-1} is resumed. This shows the sample exhibits good rate performance.

Figure 6.8(e) shows the Nyquist plot of fresh cell and post five cycles for $\text{Co}_3\text{O}_4@\text{CNT}$. The R_{ct} obtained from the curve was $\sim 260 \Omega$ for fresh cell. After five cycles, the R_{ct} is $\sim 230 \Omega$ maintaining a low charge-transfer resistance post cycling. It is be noted that a higher value of charge-transfer resistance could be due to the presence of a large number of oxide particles outside CNT, which adversely affect the overall electrical conductivity.

6.5 Role of Morphology of CNT for LIB

In previous sections, we investigated various oxides in two different morphologies – aligned forests and entangled CNT. $\text{NiO}@\text{CNT}$ (section 6.3) consisting of long entangled tubes delivered higher cyclic capacity despite a low loading ratio of active material i.e. 12%. These interesting results were indicative that the morphology of CNT has a significant role to play which can affect the cyclic stability and overall electrochemical performance considerably.

The significance of the morphology of pristine CNT in the electrochemical performance of the LIB has been well-understood and studied. [197] The length, diameter of the CNT along with the defects can influence the performance of CNT-based anode materials significantly. To further delve into the effect of morphology, we studied and compared one sample $\text{Fe}_2\text{O}_3@\text{CNT}$ in different morphologies.

Figure 6.9 compares the cyclic performance of $\text{Fe}_2\text{O}_3@\text{CNT}$, prepared using coin-cell, at current density of 100 mA g^{-1} in two morphologies – entangled long tubes (Figure 6.9(a)) and aligned forests (Figure 6.9(b)). It is interesting to observe that the sample consisting of long entangled CNT exhibit an increasing trend as evident from Figure 6.9(a) in the plot of specific capacity as a function of cycle number. From an initial capacity of $\sim 400 \text{ mA h g}^{-1}$ in second cycle, it increases up to $\sim 700 \text{ mA h g}^{-1}$. This type of trend has been observed earlier for Fe_2O_3 , and was attributed to a number of factors such as decreased cell resistance, electrochemical milling leading to more Li^+ diffusion, re-activation of active material. [198]

In contrast, the sample with aligned forests shown in Figure 6.9(b) exhibits a

falling trend with capacity dropping from $\sim 700 \text{ mA h g}^{-1}$ to $\sim 450 \text{ mA h g}^{-1}$ in 100 cycles. This sample mimics the behaviour of bare nanoparticles exhibiting a fast capacity fade. [97] $\text{Fe}_2\text{O}_3@\text{CNT}$ in aligned forest morphology appears to follow a decreasing trend of capacity which is drastically different from what is observed for $\text{FeO}_x@\text{CNT}$ (section 6.2). This could be the forest morphology of the CNT, which appears to be non-conductive for intercalation of Li ion. Another plausible reason could be that the volume change case of Fe_2O_3 ($\sim 8\%$) in lithiation-delithiation is much more than what is expected for Fe_3O_4 ($\sim 4\%$). The excellent electrochemical performance for entangled morphology can be attributed to increase in the surface area. The long curled nanotubes can offer a higher surface area and more active sites for the intercalation of Li^+ ions. This explains the superior electrochemical observed for $\text{NiO}@\text{CNT}$ in section 6.3 and $\text{Fe}_2\text{O}_3@\text{CNT}$ (Figure 6.9(a)).

Further to this, the quality of CNT and the amount of residual particles as compared to the content of CNT appear to affect the electrochemical performance of the electrode materials crucially. The sample shown in Figure 6.9(c), prepared using Swagelok-type cell, follows a fast capacity fade as a function of number of cycles. This indicates that when the residual particles (adhering outside CNT) are more as compared to the content of CNT, the electrochemical performance as a function of cycle number is adversely affected. This behaviour similar to what is expected and observed in case of bare oxide nanoparticles indicating that the quality of CNT do play a significant role affecting the cyclic performance considerably.

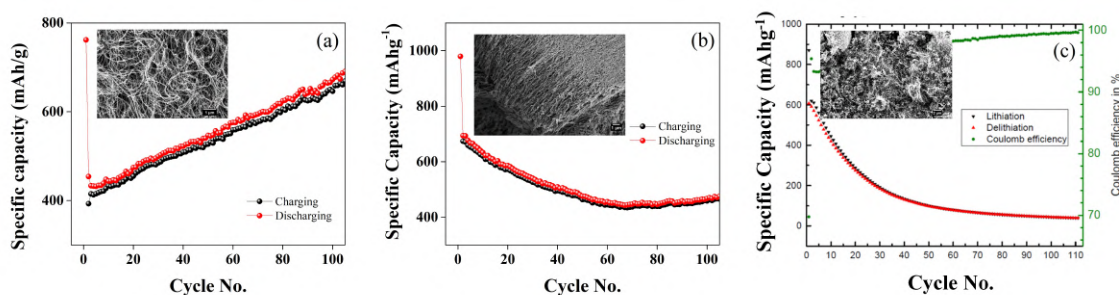


Figure 6.9: Cycling performance of $\text{Fe}_2\text{O}_3@\text{CNT}$ current density of 100 mA g^{-1} for (a) entangled morphology and (b) aligned forest-like morphology. (c) shows the cycling performance of $\text{Fe}_2\text{O}_3@\text{CNT}$ consisting of more outside particles and less amount of CNT.

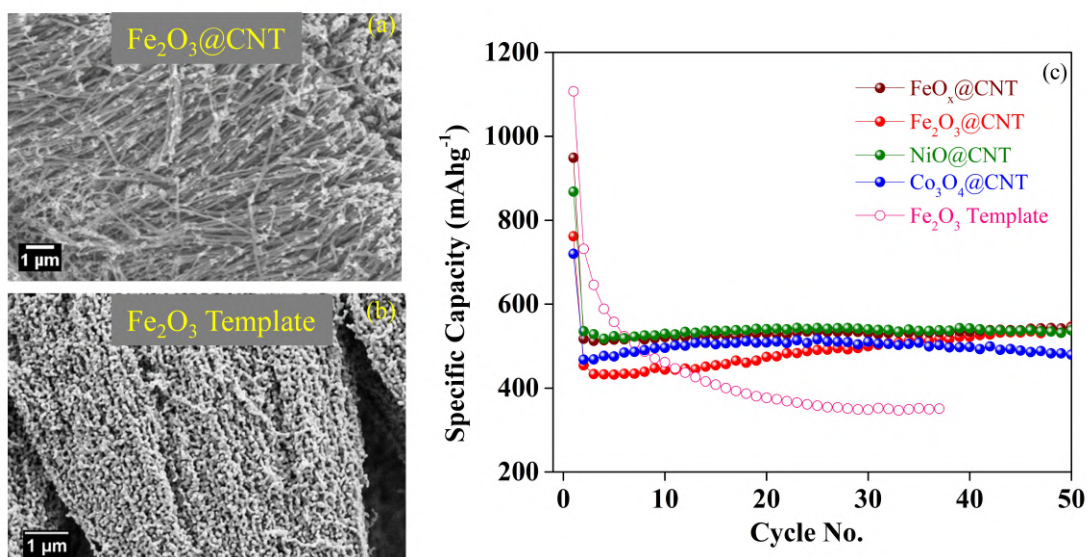


Figure 6.10: Representative FESEM image of (a) $\text{Fe}_2\text{O}_3@\text{CNT}$ and (b) Fe_2O_3 bare oxide template without CNT. Both the samples are in the form of aligned forests. The inset in (b) shows the overall morphology of the bare oxide template depicting aligned forests of bare oxide template. (c) shows the comparison of cycling performance of various Oxides@CNT with bare oxide template (no CNT). All the Oxides@CNT ($\text{NiO}@\text{CNT}$: green dots, $\text{Fe}_2\text{O}_3@\text{CNT}$: red dots, $\text{Co}_3\text{O}_4@\text{CNT}$: blue dots, $\text{FeO}_x@\text{CNT}$: wine dots) deliver a stable discharge capacity, whereas the performance of bare oxide template (pink open circles) exhibits a decaying trend after a few initial cycles.

6.6 Significance of Carbon Nanotubes

In order to study the impact of unique structure of carbon nanotubes structure on the performance of li-ion batteries, the electrochemical performance of a variety of oxides encapsulated inside CNT was compared with bare oxide template. The oxide@CNT was annealed at high temperatures ($900\text{ }^\circ\text{C}$) to burn the graphitic shells to form the bare oxide template in the same morphology as of the parent oxide@CNT. Figure 6.10(a) and 6.10(b) depicts the morphology of the parent oxide@CNT and bare oxide template (after annealing) respectively.

Figure 3.10(c) displays the cycling performance of bare oxide template (pink open circles) at a current density of 100 mA g^{-1} . The specific capacity of bare oxide template drops down from 1100 mA h g^{-1} at first cycle to 350 mA h g^{-1} after 35 cycles exhibiting a poor cycle capacity retention of $\sim 32\%$. The primary reason for

poor cyclability of the bare oxide materials as anode materials in Li-ion batteries is pulverization of the material. The oxide particles expand drastically during lithiation and delithiation. The drastic volume variation during cyclic process and low electrical conductivity lead to poor cycle life. [97]

In contrast, all oxides@CNT (Figure 6.10(c)) deliver excellent cycling performance exhibiting good cyclic stability and higher reversible capacities. The excellent stability and high capacity of oxides@CNT can be attributed to the introduction of carbon nanotubes structures which alleviate the volume changes in the oxide materials during cycling and increase the electrical conductivity of the oxide materials. [55,107,109,180] The CNT assembly buffers the strain of the oxide materials and improves the electrical conductivity, and hence, result in significantly improved cycling performance. The CNT structures also protect the electrode materials from pulverization, which in-turn offers long-term stability of the electrode materials.

Thus, it can be concluded that the CNT assembly provides cyclic stability to oxides improving the cyclic life of otherwise unstable oxides with poor cycle life. In addition, the morphology of the CNT plays a significant role deciding the cyclic stability of the CNT-based anode materials. Large amount of outside oxide particles can lead to fast capacity fade, affecting the cyclic performance of Oxides@CNT significantly.

It is imperative to mention the usage of cheap and non-toxic compound camphor to prepare these Oxides@CNT. A relatively simple and environment-friendly route to prepare different Oxides@CNT using benign compound camphor. It is to be emphasized that the use of camphor provides a way to obtain morphology of the desired form in addition to a better control over the filling efficiency of oxides inside CNT. The loading ratio and the dimensions (length and the diameter) of the CNT based oxides can be controlled by varying the amount of camphor during the synthesis as discussed extensively in chapter 3, section 3.4.3. Hence, morphologies such as aligned forests, entangled, etc. can be easily achieved by employing camphor. In light of green chemistry, this can be of a great advantage towards achieving sustainable battery technologies.

6.7 Summary

Various Oxides@CNT – Iron Oxide, Nickel Oxide, Cobalt Oxide prepared using an economic and environment-friendly approach via a scalable synthesis route were tested for anodes in LIB. These oxide/CNT hybrids in different morphologies deliver superior performance as anode materials for lithium-ion batteries, especially in terms of long-term stability. The high reversible capacity and durable long-term stability are investigated using CV, EIS, and charge-discharge tests. The carbon nanotubes shells offer not only conductive networks, but also protect the oxides from pulverization. The results also bring into fore the importance of morphology of carbon nanotubes for CNT-based anode materials. Sustainability of the as-prepared anode materials and scalability of the synthesis process render a promising route for future applications as high-performance anodes.

Chapter 7

Conclusions and Future Outlook

The primary goal of this thesis was to study the encapsulation of functional magnetic oxides inside Carbon Nanotubes (CNT). These oxides when encapsulated within the core cavity of the CNT give rise to emergent phenomenon at the interface of these multi-functional hybrids. We studied the effect of encapsulation of transition metal oxides (TMOs) inside CNT from both fundamental and application point of view. The thesis can be divided into three major sections. The first part of the thesis is devoted to the growth of the good quality metal- and metal-oxide filled CNT and their characterization. The second part of the thesis deals with the fundamental studies of a special class of oxides – antiferromagnet (AFM) encapsulated inside CNT. The final part of the thesis shows the application-related studies of various oxides encapsulated CNT.

Metal (iron, cobalt, or nickel) filled CNT with high filling efficiency and controlled morphology were obtained using a *single-zone* furnace with a modified synthesis chamber design. The metallocenes were pyrolyzed to synthesize the samples in a *single-zone* furnace instead of the routinely used *dual-zone* furnace. The respective metallocenes in all three cases were sublimated in the form of powder. This is a crucial factor to obtain metal filled CNT with high filling efficiency. While iron-filled CNT has been routinely produced using this technique, well-formed nickel-filled CNT or cobalt-filled CNT samples were reported for the first time. This was achieved by using *camphor* as a co-precursor in combination with nickelocene (or cobaltocene).

The *as-prepared* samples nickel- or cobalt-filled CNT exhibit some of the highest saturation magnetization values, at least an order of magnitude higher than that reported earlier. The results further elucidated on the reasons why nickel- or cobalt-

filled CNT are relatively challenging to obtain by pyrolyzing powder metallocene alone. The use of camphor as a co-precursor allowed us to obtain the samples in various morphologies by tuning the amount of camphor. Thus, by varying the amount of camphor, the samples could be tailored according to the needs of the application. A systematic variation of synthesis parameters was studied for all the samples which provided insights to obtain narrow length/diameter distribution with reduced residual particles adhering outside the filled CNT. These factors are pertinent for device-related applications. The metal-filled CNT were further annealed at suitable annealing conditions to obtain metal-oxide filled CNT.

We have extensively explored magnetic properties of α -Fe₂O₃ inside CNT. α -Fe₂O₃ is a Dzyaloshinskii–Moriya interaction driven weak ferromagnet (WFM) and a piezomagnet. The magnetization data obtained using SQUID magnetometry revealed exciting results, arising conclusively at the interface of two functional materials – graphitic shells of CNT and α -Fe₂O₃. We showed that encapsulation of α -Fe₂O₃ inside CNT leads to a substantial enhancement in magnetization and correspondingly in remanence that is *time-stable* in character. The appearance of *time-stable* remanence is intimately related to Dzyaloshinskii–Moriya interaction driven spin canting phenomenon in WFMs such as α -Fe₂O₃, and is exclusive to the weak ferromagnetic phase. Earlier studies have shown that the magnitude of *time-stable* remanence scales up with the extent of spin canting and exhibits an inverse correlation with the Néel temperature. α -Fe₂O₃ with its Néel temperature ~ 950 K possess weak spin canting, and hence, the magnitude of *time-stable* remanence is less in comparison with others WFMs with lower Néel temperature. We showed that encapsulation of a WFM α -Fe₂O₃ inside CNT appears to be the most efficient way to manipulate its weak ferromagnetic traits. Up to 70% of in-field magnetization was found to be retained in the form of remanence at room temperature. The existence weak ferromagnetism in α -Fe₂O₃ at room temperature, and with significant effects upon encapsulation inside CNT can open new avenues in the field of spintronic applications.

To delve into the reasons responsible for the enhanced magnetic functionalities in the encapsulate α -Fe₂O₃, synchrotron X-ray diffraction studies were performed. The lattice parameter of the CNT derived from the synchrotron X-ray diffraction exhibited a clear anomaly around the Morin transition of the encapsulate. The results suggested presence of novel *interface* effects.

Temperature-dependent Raman spectroscopy measurements were conducted on

magnetic oxide encapsulated inside CNT to explore the unusual *interface* effects. The results revealed how the phonon behavior of CNT is altered due to the presence of magnetic material in close proximity and exhibits pronounced anomalies around the magnetic transition of the encapsulate. These results provide experimental evidence for spin-phonon coupling. Significantly large Raman shifts of $\sim 15 \text{ cm}^{-1}$ were observed in the phonon modes of the CNT indicating the strong influence of the magnetic encapsulate. Raman shifts of $\sim 15\text{-}25 \text{ cm}^{-1}$ were observed for the magnetic-oxide encapsulate. These shifts were substantially enhanced in comparison to what is usually observed in case of bare nano-particles ($\sim 2\text{-}5 \text{ cm}^{-1}$). Overall, the influence of spin-phonon coupling unveiled itself in the form of significant enhancement in the Raman shifts. These experimental results can be exploited in the design of spin-nanomechanical and nano-spintronic devices.

Electrochemical performance of various transition metal oxides encapsulated inside CNT were tested as anode materials for lithium-ion batteries (LIB). TMOs@CNT ($\alpha\text{-Fe}_2\text{O}_3$, Fe_3O_4 , NiO, and Co_3O_4) delivered excellent performance in terms of cyclic stability and high reversible capacity. The introduction of CNT improves the electrochemical performance as compared to what is observed in bare oxides. The high reversible capacity and durable long-term stability were also investigated using cyclic voltammetry, electrochemical impedance spectroscopy, and charge-discharge tests. The oxides-filled CNT maintained outstanding cyclic life and stable high-reversible capacity even at higher current densities. The results also elucidate on the significance of morphologies and residual particles adhering outside CNT and filling fraction of the oxide encapsulate on the overall performance of these samples as anode materials in LIB.

This thesis explored *interface* effects in Oxide/CNT hybrids through SQUID magnetometry and synchrotron X-ray diffraction studies. To gain a further understanding, microscopic measurements such as X-ray magnetic circular dichroism and Neutron diffraction are needed. These studies can shed some light on the underlying mechanism which can be useful when integrating these samples for device-related spintronic applications. Novel nano-spintronic devices can be envisaged comprising of the multi-functional oxide encapsulated CNT. For example, I-V characteristics on a single filled CNT can be performed which can further underline the role of the magnetic encapsulate. It would be interesting to study these results which serve as a road map for utilization of Oxide/CNT hybrids in spintronic and nano-electronic devices.

This thesis focused on one compound of the family of Dzyaloshinskii-Moriya driven weak ferromagnets, i.e. α -Fe₂O₃. The encapsulation of other weak ferromagnets belonging to two different classes of weak ferromagnets – Dzyaloshinskii-Moriya driven such as orthoferrites, and weak ferromagnetism driven by single-ion anisotropy such as NiF₂, FeF₂, etc. can bring into fore interesting results which can be important for future spintronic applications.

Appendix A

Glossary of Battery-related Terms

- *Specific capacity* of a battery is defined as the amount of energy it can deliver in a single discharge for a given amount of mass of the active material (electrode). It is specified in amp-hours (Ah).
- *C-rate* of a battery specifies the rate at which the battery is charged or discharged. For instance, consider the case of a 500 mAh battery. At 1C, the battery will discharge 500 mA of current in one hour. At 0.5C, the battery will deliver 250 mA current for two hours, and at 2C, it will deliver 1000 mA for half an hour.
- *Cycle life* of a battery is the number of cycles up to which it can be charged and discharged under specific conditions before the capacity falls to a specific performance criterion (typically 80% of the rated capacity).
- *Coulomb efficiency* depicts the charge transfer efficiency in batteries. It is expressed as the ratio of the total charge extracted and the total input charge to the battery in a full cycle.

Appendix B

Cobalt- and Cobalt Oxide- filled Carbon Nanotubes

B.1 Cobalt-filled Carbon Nanotubes

B.1.1 Synthesis and Characterization

Cobalt-filled Carbon Nanotubes (Co@CNT) were synthesized using a single-zone furnace with modified synthesis chamber design as discussed in section 3.2. [58, 138] good quality Co@CNT involved using camphor as a co-precursor. No combination of synthesis parameters yielded Co@CNT without the use of camphor as a co-precursor. The optimized synthesis conditions for Co@CNT are: $T_{pyro} = 800$

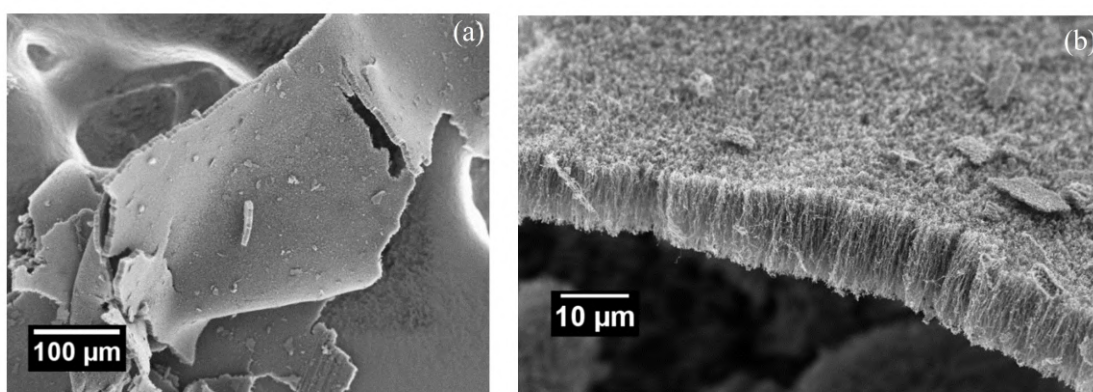


Figure B.1: (a) - (b) FESEM images of Co@CNT at different magnifications depicting large carpets of CNT which are $\sim \mu\text{-m}$ in length. [58, 138]

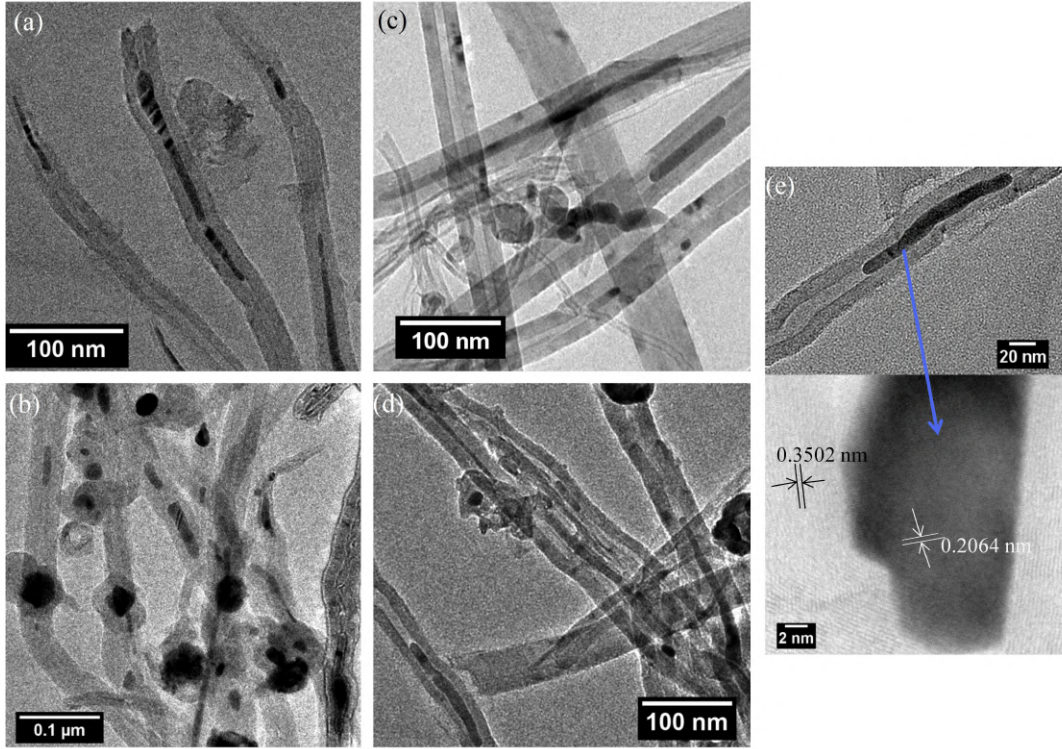


Figure B.2: (a)-(d) representative TEM micrographs for Co@CNT, showing the metal-filling in the form of nano-wire within the core cavity of CNT. (e) High-Resolution TEM micrographs of CNT filled with Co. The black and white arrows mark the lattice spacing of the graphitic shells and the encapsulated metal respectively.

$^{\circ}\text{C}$; $T_{sub} = 200^{\circ}\text{C}$; Amount of cobaltocene – 500 mg; Amount of camphor – 100 mg.

Figure B.1 shows FESEM images for the sample Co@CNT at different magnifications. The sample consists of large carpets of $\sim 100 \mu\text{-m}$ in length. TEM images recorded at different magnifications to indicate the filling efficiency are shown in Figure B.2(a-d). Figure B.2(e) shows the high-resolution TEM image depicting the well-formed graphitic shells and lattice fringes of the cobalt encapsulate.

Figure B.3(a) shows the representative powder XRD depicting reflections from graphite (CNT) and cobalt. Figure B.3(b) shows the Raman spectrum recorded at room temperature. The Raman spectrum consists of three dominant bands – D-, G-, and 2D- pertaining to CNT. The ratio of intensities of D- and G- band is ~ 0.6 .

The filling efficiency of sample Co@CNT was gauged by TGA and saturation magnetization (M_S). Figure B.3(c) shows the TGA curve obtained under air from 30

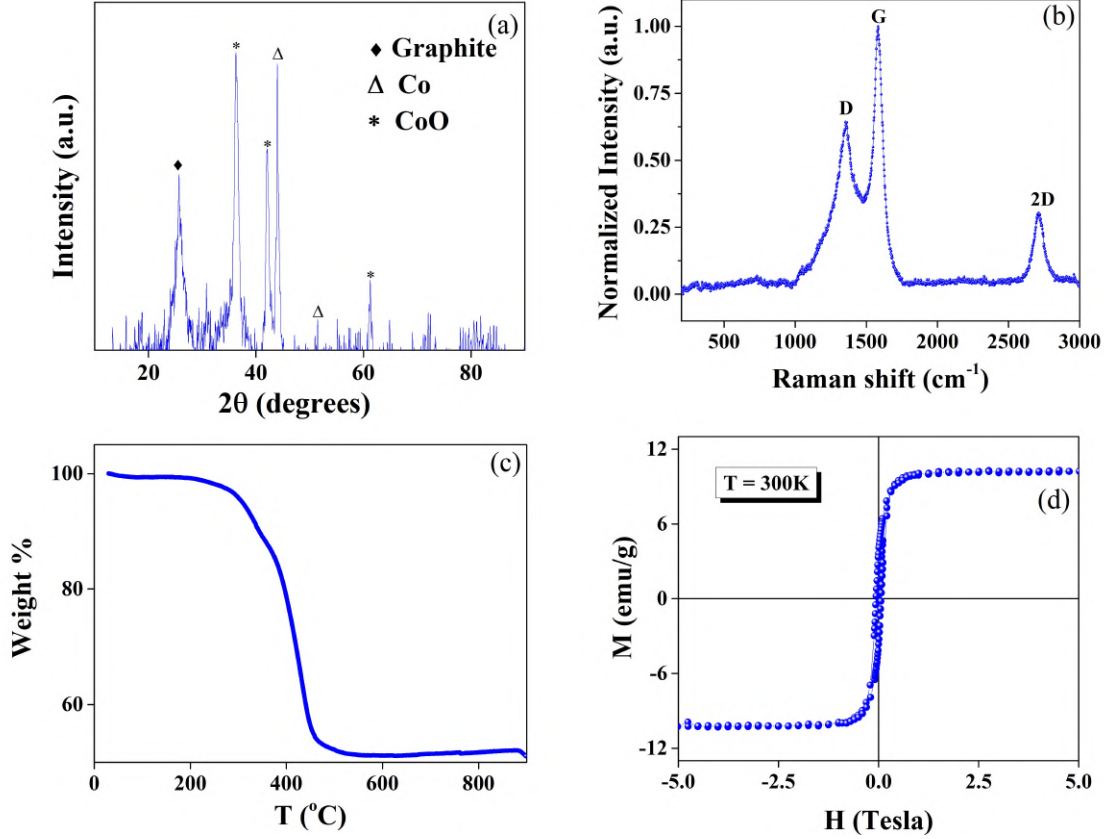


Figure B.3: (a) Representative powder XRD of Co@CNT. (b) Representative Raman spectrum at room temperature for Co@CNT depicting D-, G-, and 2D-band. (c) TGA curve obtained under air from 30 $^{\circ}\text{C}$ to 900 $^{\circ}\text{C}$. (d) M-H isotherm recorded at room temperature depicting $M_S \sim 12$ emu/g. [58, 138]

$^{\circ}\text{C}$ to 900 $^{\circ}\text{C}$. The residual weight is $\sim 30\%$ indicating a high-filling efficiency. The high-filling efficiency is also reflected from high M_S as evident from Figure B.3(d). It is to be noted that the observed value of M_S is much larger than what has been reported earlier for Co@CNT $\sim 0.1 - 0.5$ emu/g. [57]

B.1.2 Variations in morphology with the change of synthesis parameters

Figure B.4 shows the morphology of the Co@CNT in which all synthesis parameters are similar to the Co@CNT shown in Figure B.1 except the rate of argon-flow, which is lower in this case. Lowering the rate of argon-flow, we find that no CNT are

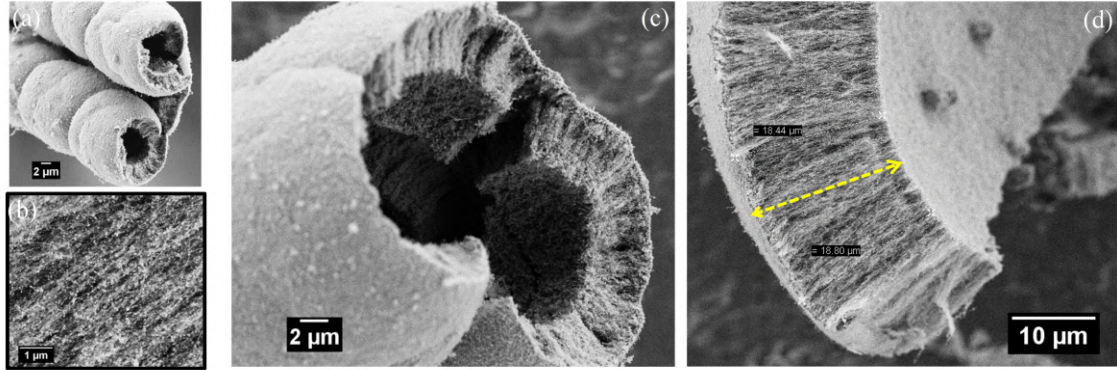


Figure B.4: Representative FESEM micrographs of Co@CNT formed at T_{pyro} : 800 °C and T_{sub} : 200 °C. (a) Displays fairly large rolled-over self-organized structures obtained from variable temperature zone. The catalytic particle density is larger, as evident from (b). Images (c) and (d) indicate that Co@CNT obtained from the variable temperature zone exhibit a wider distribution in length of the CNT (3-20 μ -m) in these rolled-over structures.

deposited in the pyrolysis zone. However, self-organized structures of Co@CNT are found with significant yield in variable temperature zone. [58]

Figure B.4 displays aligned forests of Co@CNT with a tendency to roll over. These tubular structures are fairly large, extending up to few 100 μ -m in length. The length of the CNT, in different rolled-over structures obtained from T_{var} zone ranges from \sim 3 to 20 μ -m as evident from Figure B.4(c-d). This again confirms the CNT deposition in the varying temperature region which leads to significant variations in the length of the CNT.

The overall data on Co@CNT suggest that manipulating the ratio of the amount of camphor and cobaltocene as a synthesis parameter, it is easier to form self-organized structures of Co@CNT. The M-H isotherms recorded on samples synthesized in different batches depict the M_S values in the range of 5-40 emu/g. Various combinations of all four synthesis parameters can be further tuned to obtain desired morphology and filling efficiency.

B.2 Cobalt-Oxide filled Carbon Nanotubes

The sample Co@CNT is converted into respective cobalt-oxide@CNT by annealing the sample under carbon dioxide atmosphere at 500 °C for ten minutes. The oxide

thus formed is Co_3O_4 , and the sample retains the morphology of the parent sample – Co@CNT . Figure B.5(a) - B.5(b) shows the FESEM image of and representative XRD of $\text{Co}_3\text{O}_4\text{@CNT}$.

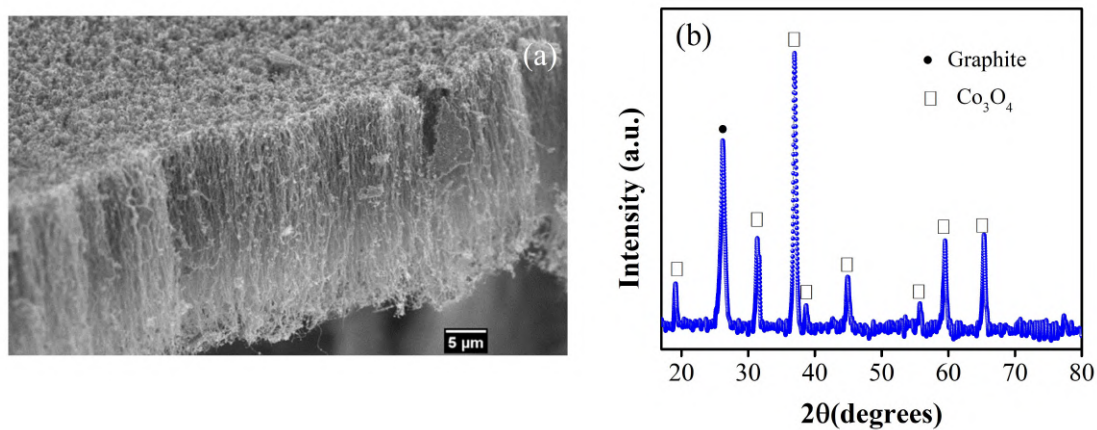


Figure B.5: Representative (a) FESEM image and (b) powder XRD of $\text{Co}_3\text{O}_4\text{@CNT}$.

Appendix C

Magnetoresistance on Iron-Oxide filled Carbon Nanotubes

The strain effects in the lattice parameters of CNT as depicted in Figure 4.8 indicate that the magnetic state of the insulating encapsulate influences the graphitic shells of the CNT. This prompted us to perform temperature variation of resistance in a pressed pellet of $\alpha\text{-Fe}_2\text{O}_3\text{@CNT}$ which is about 7 mm in diameter and 3 mm in

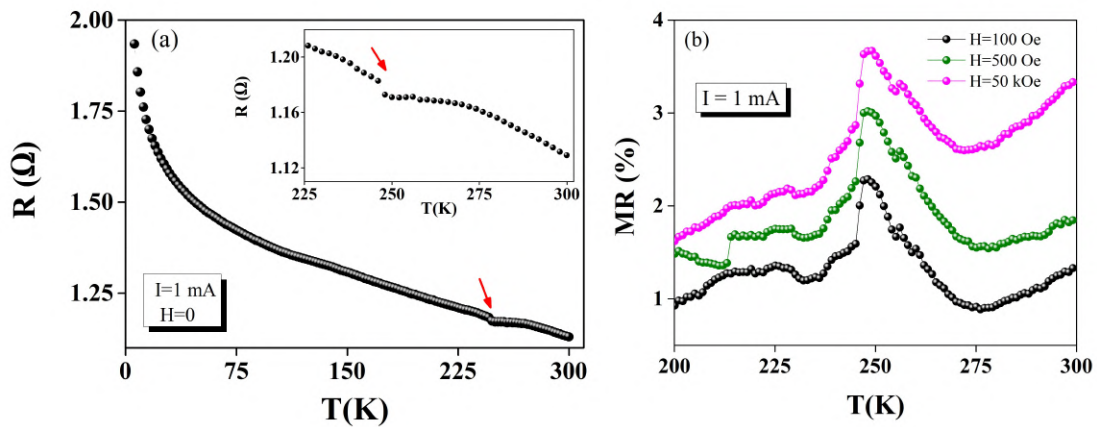


Figure C.1: (a) shows resistance vs temperature in zero magnetic field conducted on a pressed pellet of $\alpha\text{-Fe}_2\text{O}_3\text{@CNT}$. An anomaly around the Morin transition of insulating encapsulate is observed. This matches with the anomaly seen in the lattice parameters of the graphitic shells of CNT. (b) shows magnetoresistance as a function of temperature in three different magnetic field, $H = 100$ Oe, 500 Oe and 50 kOe. The MR shows a peak like effect around the Morin transition of the encapsulate.

thickness. The results of four probe electrical transport measurements in zero field are shown in Figure B.

The resistance (R) is measured as a function of temperature (T) in the temperature range from 5K to 300K, the data has been recorded in heating cycle. It is to be emphasized that the system comprises of CNT that contains a nano-scale insulator within its core cavity. Thus, the electrical conduction is primarily through the graphitic shells of CNT. However, the temperature variation of resistance exhibits an activated type of transport with a clear anomaly near the Morin Transition (marked by red arrow in Figure B(a)). The functional form of conduction is different above the anomaly as evident from Figure B(a). The region around the Morin transition in a narrow temperature range is shown in the inset of Figure B(a).

We also recorded resistance as a function of temperature in presence of magnetic field. From these data, temperature variation of magnetoresistance (MR) is derived, which is presented in Figure B(b). Here MR is defined as $[R(H)-R(0)] / R(0)$. This MR is substantial near the room temperature. These results need further measurements and investigation to comment on the mechanisms resulting in substantial magnetoresistance. The anomaly around the Morin transition confirms the novel interface effects in CNT/Iron-Oxide hybrid. More importantly, this substantial magnetoresistance at room temperature can have promising technological implications and can be envisaged in the design of novel spintronic devices.

Bibliography

- [1] T.V. Hughes and C.R. Chambers. Manufacture of 0 n filaments, US Patent No.:405480 June 1889.
- [2] L.V. Radushkevich and V. M. Lukyanovich. On the carbon structure formed during thermal decomposition of carbon monoxide in the presence of iron. *Journal of Physical Chemistry of Russia*, 26:88, 1952.
- [3] A.Oberlin, M. Endo, and T. Koyama. High resolution electron microscope observations of graphitized carbon fibers. *Carbon*, 14:133, 1976.
- [4] A. Oberun and M. Endo. Filamentous growth of carbon through benzene decomposition. *Journal of Crystal Growth*, 32:335, 1976.
- [5] H.W. Kroto, J.R. Heath, S.C. O'Brien, et al. C60: buckminsterfullerene. *Nature*, 318:162, 1985.
- [6] S. Iijima. Helical microtubules of graphitic carbon. *Nature*, 354:56, 1991.
- [7] S. Iijima. Helical microtubules of graphitic carbon, JP2687794B2 Dec 1997.
- [8] S. Iijima and T. Ichihashi. Single-shell carbon nanotubes of 1-nm diameter. *Nature*, 363:603, 1993.
- [9] D.S. Bethune, C.H. Kiang, M.S. de Vries, et al. Cobalt-catalysed growth of carbon nanotubes with single-atomic-layer walls. *Nature*, 363:605, 1993.
- [10] U. Weissker, S. Hampel, A. Leonhardt, et al. Carbon nanotubes filled with ferromagnetic materials. *Materials*, 3:4387, 2010.
- [11] R. Saito, G. Dresselhaus, and M.S. Dresselhaus. *Physical Properties of Carbon Nanotubes*. London: Imperial College Press, 1998.

- [12] L. Liu, C. S. Jayanthi, and M. Tang. Controllable reversibility of an sp^2 to sp^3 transition of a single wall nanotube under the manipulation of an AFM tip: A nanoscale electromechanical switch. *Physical Review Letters*, 84(21):4950, 2000.
- [13] X. Liang, J. Xia, G. Dong, et al. Carbon nanotube thin film transistors for flat panel display application. *Topics in Current Chemistry*, 374(6):80, 2016.
- [14] J. Luo, J. Liu, Z. Zeng, et al. Three-dimensional graphene foam supported Fe_3O_4 lithium battery anodes with long cycle life and high rate capability. *Nano Letters*, 13:6136, 2013.
- [15] J.E. Fischer and A.T. Johnson. Electronic properties of carbon nanotubes. *Current Opinion in Solid State and Materials Science*, 4(1):28, 1999.
- [16] I.V. Zaporotskova, N.P. Boroznina, Y.N. Parkhomenko, et al. Carbon nanotubes: Sensor properties. a review. *Modern Electronic Materials*, 2(4):95 – 105, 2016.
- [17] A. Bianco, K. Kostarelos, and M. Prato. Applications of carbon nanotubes in drug delivery. *Current Opinion in Chemistry and Biology*, 9:674, 2005.
- [18] Y. Wang and J.T.W. Yeow. A review of carbon nanotubes-based gas sensors. *Journal of Sensors*, 2009:493904, 2009.
- [19] A. Bajpai, Z. Aslam, S. Hampel, et al. A carbon-nanotube based nano-furnace for in-situ restructuring of a magnetoelectric oxide. *Carbon*, 114:291–300, 2017.
- [20] B.I. Yakobson and P. Avouris. Mechanical properties of carbon nanotubes. *Topics in Applied Physics*, 80:287, 2001.
- [21] T. Filleter, R. Bernal, S. Li, et al. Ultrahigh strength and stiffness in cross-linked hierarchical carbon nanotube bundles. *Advanced Materials*, 23(25):2855, 2011.
- [22] J. Hone. Phonons and thermal properties of carbon nanotubes. *Topics in Applied Physics*, 80:273, 2001.
- [23] J. Hone, M.C. Llaguno, M.J. Biercuk, et al. Thermal properties of carbon nanotubes and nanotube-based materials. *Applied Physics A*, 74(3):339, 2002.

Bibliography

- [24] M. Martin-Gallego, R. Verdejo, M. Khayet, et al. Thermal conductivity of carbon nanotubes and graphene in epoxy nanofluids and nanocomposites. *Nanoscale Research Letters*, 6:610, 2011.
- [25] Z. Han and A. Fina. Thermal conductivity of carbon nanotubes and their polymer nanocomposites: A review. *Progress in Polymer Science*, 36(7):914, 2011.
- [26] M. Kumar. Chemical vapor deposition of carbon nanotubes: a review on growth mechanism and mass production. *Journal of Nanoscience and Nanotechnology*, 10(6):6, 2010.
- [27] A. Eftekhari, P. Jafarkhani, and F. Moztarzadeh. High-yield synthesis of carbon nanotubes using a water-soluble catalyst support in catalytic chemical vapor deposition. *Carbon*, 44(7):1343, 2006.
- [28] L.S. Ying, M.A.bin Mohd Salleh, H.b.M. Yusoff, et al. Continuous production of carbon nanotubes – a review. *Journal of Industrial and Engineering Chemistry*, 17(3):367, 2011.
- [29] P.G. Collins. Nanotubes for electronics. *Scientific American*, 283(6):67, 2000.
- [30] A. Eatemadi, H. Daraee, H. Karimkhanloo, et al. Carbon nanotubes: properties, synthesis, purification, and medical applications. *Nanoscale Research Letters*, 9(1):1, 2014.
- [31] T. Guo, P. Nikolaev, A. Thess, et al. Catalytic growth of single-walled nanotubes by laser vaporization. *Chemical Physics Letters*, 243(1-2):49, 1995.
- [32] A. Thess, R. Lee, P. Nikolaev, et al. Crystalline ropes of metallic carbon nanotubes. *Science*, 273:483, 1996.
- [33] R. Sen, A. Govindaraj, and C.N.R. Rao. Carbon nanotubes by the metallocene route. *Chemical Physics Letters*, 267(3-4):276, 1997.
- [34] C.N.R. Rao, R. Sen, B.C. Satishkumar, et al. Large aligned-nanotube bundles from ferrocene pyrolysis. *Chemical Communications*, 15:1525, 1998.

- [35] L.M. Dyagileva, V.P. Mar'in, E.I. Tsyganova, et al. Reactivity of the first transition row metallocenes in thermal decomposition reaction. *Journal of Organometallic Chemistry*, 175:63, 1979.
- [36] L.A. Torres-G'omez, G. Barreiro-Rodr'iquez, and F. M'endez-Ru'iz. Vapour pressures and enthalpies of sublimation of ferrocene, cobaltocene and nickelocene. *Thermochimica Acta*, 124:179, 1988.
- [37] P. Mahanandia, P.N. Vishwakarma, K.K. Nanda, et al. Synthesis of multi-wall carbon nanotubes by simple pyrolysis. *Solid State Communications*, 145:143, 2008.
- [38] X. Yang, Y. Li, H. Yu, et al. Enhanced catalytic activity of carbon nanotubes for the oxidation of cyclohexane by filling with Fe, Ni, and FeNi alloy nanowires. *Australian Journal of Chemistry*, 69(6), 2015.
- [39] H. Terrones, F. López-Urías, E. Muñoz-Sandoval, et al. Magnetism in fe-based and carbon nanostructures: theory and applications. *Solid state Sciences*, 8:303, 2006.
- [40] S. Hampel, A. Leonhardt, D. Selbmann, et al. Growth and characterization of filled carbon nanotubes with ferromagnetic properties. *Carbon*, 44:2316, 2006.
- [41] R. Andrews, D. Jacques, A.M. Rao, et al. Continuous production of aligned carbon nanotubes: a step closer to commercial realization. *Chemical Physics Letters*, 303:467, 1999.
- [42] R. Kamalakaran, M. Terrones, T. Seeger, et al. Synthesis of thick and crystalline nanotube arrays by spray pyrolysis. *Applied Physics Letters*, 77:3385, 2000.
- [43] X. Zhang, A. Cao, B. Wei, et al. Rapid growth of well-aligned carbon nanotube arrays. *Chemical Physics Letters*, 362:285, 2002.
- [44] S.S. Meysami, A. Kóos, M. Dutta, et al. Aerosol-assisted chemical vapour deposition synthesis of multi-wall carbon nanotubes: Iii towards upscaling. *Carbon*, 88:148, 2015.
- [45] R. Kumari, A. Singh, B.S. Yadav, et al. Filled-carbon nanotubes: 1 d nanomagnets possessing uniaxial magnetization axis and reversal magnetization switching. *Carbon*, 119:464, 2017.

- [46] A. Leonhardt, M. Ritschel, D. Elefant, et al. Enhanced magnetism in ferromagnetic-filled carbon nanotubes produced by pyrolysis of ferrocene. *Journal of Applied Physics*, 98:074315, 2005.
- [47] A. Leonhardt, S. Hampel, C. Muller, et al. Synthesis, properties, and applications of ferromagnetic-filled carbon nanotubes. *Chemical Vapour Deposition*, 12:380, 2006.
- [48] F.C. Dillon, A. Bajpai, A. Koós, et al. Tuning the magnetic properties of iron filled carbon nanotubes. *Carbon*, 5:3674, 2012.
- [49] T. Peci and M. Baxendale. Length and α -fe content control of self-organised ferromagnetic nanowires encapsulated by multiwalled carbon nanotubes by low flow-rate cvd. *Carbon*, 98:519, 2016.
- [50] G.V. Grechnev, V.A. Desnenko, A.V. Fedorchenko, et al. Structure and magnetic properties of multi-walled carbon nanotubes modified with iron. *Low Temperature Physics*, 36(12), 2010.
- [51] R. Bhatia and V. Prasad. Synthesis of multiwall carbon nanotubes by chemical vapor deposition of ferrocene alone. *Solid State Communications*, 150:311, 2010.
- [52] S. Park, M. Vosguerichian, and Z. Bao. A review of fabrication and applications of carbon nanotube film-based flexible electronics. *Nanoscale*, 5:1727, 2013.
- [53] M.P. Anantram and F. Leonard. Physics of carbon nanotube electronic devices. *Reports on Progress in Physics*, 69:507, 2006.
- [54] E.A. Laird, F. Kuemmeth, G.A. Steele, et al. Quantum transport in carbon nanotubes. *Review of Modern Physics*, 87:703, 2015.
- [55] N. Yan, X. Zhou, Y. Li, et al. Fe₂O₃ nanoparticles wrapped in multi-walled carbon nanotubes with enhanced lithium storage capability. *Scientific Reports*, 3:3392, 2013.
- [56] R. Klingeler and R.B. Sim. *Carbon Nanotubes for Biomedical Applications*. Springer, 2011.
- [57] U. Ritter, P. Scharff, G.E. Grechnev, et al. Structure and magnetic properties of multi-walled carbon nanotubes modified with cobalt. *Carbon*, 49:4443, 2011.

- [58] A. Kapoor, N. Singh, A. B. Dey, et al. 3d transition metals and oxides within carbon nanotubes by copyrolysis of metallocene & camphor: High filling efficiency and self-organized structures. *Carbon*, 132:733, 2018.
- [59] A.C. Ferrari and D.M. Basko. Raman spectroscopy as a versatile tool for studying the properties of graphene. *Nature Nanotechnology*, 8:235, 2018.
- [60] M.S. Dresselhaus, A. Jorio, and R. Saito. Characterizing graphene, graphite, and carbon nanotubes by raman spectroscopy. *Annual Review of Condensed Matter Physics*, 1:89, 2010.
- [61] S. Blundell. *Magnetism in Condensed Matter*. Oxford Univ. Press, 2001.
- [62] J.M.D. Coey. *Magnetism and Magnetic Materials*. Cambridge Univ. Press, 2009.
- [63] E. Bousquet. <https://abinit14.sciencesconf.org/data/program/lecture>, 2014.
- [64] R.S. Tebble and D.J. Craik. *Magnetic Materials*. Wiley, New York, 1996.
- [65] S. Jain, A. O. Adeyeye, and C. B. Boothroyd. Electronic properties of half metallic Fe₃O₄ films. *Journal of Applied Physics*, 97:093713, 2005.
- [66] E. Dzyaloshinskii. Thermodynamical theory of weak ferromagnetism in antiferromagnetic substances. *Journal of Experimental and Theoretical Physics*, 32:1259, 1957.
- [67] L. Néel. Magnetic properties of ferrites; ferrimagnetism and antiferromagnetism. *Annales de Physique*, 12:99, 1948.
- [68] Y. Li. Domain walls in antiferromagnets and the weak ferromagnetism of α -Fe₂O₃. *Physical Review*, 101:1450, 1956.
- [69] T. Moriya. Anisotropic superexchange interaction and weak ferromagnetism. *Physical Review*, 120:91, 1960.
- [70] S.K. Banerjee and J.P. Mellema. A new method for the determination of paleointensity from the a.r.m. properties of rocks. *Earth and Planetary Science Letters*, 23(2):177, 1974.

- [71] S. Skorobogatov. Data remanence in flash memory devices. In *Proceedings of the 7th International Conference on Cryptographic Hardware and Embedded Systems*, CHES'05, page 339. Springer-Verlag, 2005.
- [72] S. Bhatti, R. Sbiaa, A. Hirohata, et al. Spintronics based random access memory: a review. *Materials Today*, 20(9):530 – 548, 2017.
- [73] M.J. Benitez, O. Petracic, H. Tuysuz, et al. Spin glasses: Experimental facts, theoretical concepts, and open questions. *Physical Review B*, 83:134424, 2011.
- [74] F. Donati, S. Rusponi, S. Stepanow, et al. Magnetic remanence in single atoms. *Science*, 352(6283):318, 2016.
- [75] L. Lundgren, P. Svedlindh, P. Nordblad, et al. Dynamics of the relaxation-time spectrum in a cumn spin-glass. *Physical Review Letters*, 51:911, 1983.
- [76] M. Suzuki, I.S. Suzuki, and M. Matsuura. Memory and aging effect in hierarchical spin orderings of the stage-2 CoCl_2 graphite intercalation compound. *Physical Review B*, 73:184414, 2006.
- [77] C.N.R. Rao. Transition metal oxides. *Annual Review of Physical Chemistry*, 40:291, 1989.
- [78] S.D. Bader. Opportunities in nanomagnetism. *Review of Modern Physics*, 78:1, 2006.
- [79] S. Coh, W. Gannett, A. Zettl, et al. Surface atom motion to move iron nanocrystals through constrictions in carbon nanotubes under the action of an electric current. *Physical Review Letters*, 110:185901, 2013.
- [80] K. Svensson, H. Olin, and E. Olsson. Nanopipettes for metal transport. *Physical Review Letters*, 93:145901, 2004.
- [81] M. Loeffler, U. Weissker, T. Muhl, et al. Current induced mass transport in filled multiwalled carbon nanotubes. *Advanced Materials*, 23:541, 2011.
- [82] J. Rockenberger, E.C. Scher, and A.P. Alivisatos. A new nonhydrolytic single-precursor approach to surfactant-capped nanocrystals of transition metal oxides. *Journal of American Chemical Society*, 121(49):11595, 1999.

- [83] T. Nguyen and M.de F. Montemor. Metal oxide and hydroxide-based aqueous supercapacitors: From charge storage mechanisms and functional electrode engineering to need-tailored devices. *Advanced Science*, 6(9):1801797., 2019.
- [84] J.D. Aiken and R.G. Finke. A review of modern transition-metal nanoclusters: their synthesis, characterization, and applications in catalysis. *Journal of Molecular Catalysis A: Chemical*, 145(1):1 – 44, 1999.
- [85] P.M. Ajayan, O. Stephan, Ph. Redlich, et al. Carbon nanotubes as removable templates for metal oxide nanocomposites and nanostructures. *Nature*, 375:564, 1995.
- [86] D. Halley, N. Najjari, H. Majjad, et al. Size induced enhanced magnetoelectric effect and multiferroicity in chromium oxide nanoclusters. *Nature Communications*, 5:3167, 2014.
- [87] V. Baltz, A. Manchon, M. Tsoi, et al. Antiferromagnetic spintronics. *Review of Modern Physics*, 90:015005, 2018.
- [88] A. Bajpai, R. Klingeler, N. Wizen, et al. Unusual field dependence of remanent magnetization in granular CrO_2 : The possible relevance of piezomagnetism. *Journal of Physics Condensed Matter*, 22(9):096005, 2010.
- [89] N. Pattanayak, A. Bhattacharyya, A.K. Nigam, et al. Quasistatic remanence in dzyaloshinskii-moriya interaction driven weak ferromagnets and piezomagnets. *Physical Review B*, 96:104422, 2017.
- [90] N. Pattanayak, A. Bhattacharyya, S. Chakravarty, et al. Weak ferromagnetism and time-stable remanence in hematite: effect of shape, size and morphology. *Journal of Physics: Condensed Matter*, 31:365802, 2019.
- [91] J. Hong, A. Stroppa, J. Iniguez, et al. Spin-phonon coupling effects in transition-metal perovskites: A DFT + U and hybrid-functional study. *Physical Review B*, 85:054417, 2012.
- [92] J. B. Goodenough and K.S. Park. The Li-ion rechargeable battery: A perspective. *Journal of the American Chemical Society*, 135:1167, 2013.

- [93] J. F. Peters, M. Baumann, B. Zimmermann, et al. The environmental impact of Li-ion batteries and the role of key parameters – a review. *Renewable and Sustainable Energy Reviews*, 67:491, 2017.
- [94] V. Aravindan, Y. S. Lee, and S. Madhavi. Research progress on negative electrodes for practical li-ion batteries: Beyond carbonaceous anodes. *Advanced Energy Materials*, 5:1402225, 2015.
- [95] S. Hameer and J. L. van Niekerk. A review of large-scale electrical energy storage. *International Journal of Energy Resources*, 39:1179, 2015.
- [96] D. Linden and T.R. Reddy. *Handbook Of Batteries 3rd Edition*. McGraw Hill, 2002.
- [97] L. Ji, Z. Lin, M. Alcoutlabi, et al. Recent developments in nanostructured anode materials for rechargeable lithium-ion batteries. *Energy Environmental Sciences*, 4:2682, 2011.
- [98] J. Zhang and A.Yu. Nanostructured transition metal oxides as advanced anodes for lithium-ion batteries. *Science Bulletin*, 60:823, 2015.
- [99] C. Tian, F. Lin, and M. M. Doeff. Electrochemical characteristics of layered transition metal oxide cathode materials for lithium ion batteries: Surface, bulk behavior, and thermal properties. *Accounts of Chemical Research*, 51:89, 2018.
- [100] K. Cao, T. Jin, L. Yanga, et al. Recent progress in conversion reaction metal oxide anodes for li-ion batteries. *Materials Chemistry Frontiers*, 1:2213, 2017.
- [101] M. Zheng, H. Tang, L. Li, et al. Hierarchically nanostructured transition metal oxides for lithium-ion batteries. *Advanced Sciences*, 5:1700592, 2018.
- [102] N. J. Song and C. Ma. A green synthesis of Mn_3O_4 /graphene nanocomposite as anode material for lithium-ion batteries. *International Journal of Electrochemical Sciences*, 13:452, 2018.
- [103] Y. Wang, Z. Wang, X. Yub, et al. Hierarchically structured carbon nanomaterials for electrochemical energy storage applications. *Journal of Material Research*, 33:1058, 2018.

- [104] Z.S. Wua, G. Zhoua, L.C Yina, et al. Graphene/metaloxide composite electrode materials for energy storage. *Nano Energy*, 1:107, 2012.
- [105] Y. Zhao, L. P. Wang, M. T. Sougrati, et al. A review on design strategies for carbon based metal oxides and sulfides nanocomposites for high performance Li and Na ion battery anodes. *Advanced Energy Materials*, 7:1601424, 2017.
- [106] T. Jiang, F. Bu, X. Feng, et al. Porous Fe₂O₃ nanoframeworks encapsulated within three-dimensional graphene as high-performance flexible anode for lithium-ion battery. *ACS Nano*, 11:5140, 2017.
- [107] H. Zhou, L. Zhang, D. Zhang, et al. A universal synthetic route to carbon nanotube/transition metal oxide nano-composites for lithium ion batteries and electrochemical capacitors. *Scientific Reports*, 6:37752, 2016.
- [108] W. D. Zhang, B. Xu, and L. C. Jiang. Functional hybrid materials based on carbon nanotubes and metal oxides. *Journal of Material Chemistry*, 20:6383, 2010.
- [109] Z. Cao and B. Wei. A facile route to metal oxides/single-walled carbon nanotube macrofilm nanocomposites for energy storage. *Frontiers in Materials*, 2:40, 2015.
- [110] A. Ottmann, M. Scholz, M. Haft, et al. Electrochemical magnetization switching and energy storage in manganese oxide filled carbon nanotubes. *Scientific Reports*, 7:13625, 2017.
- [111] D. Puthusseri, V. Aravindan, S. Madhavi, et al. 3d interconnected porous graphene sheets loaded with cobalt oxide nanoparticles for lithium-ion battery anodes. *Energy Technology*, 4:816, 2016.
- [112] X. Tang, M. Liang, Y. Zhang, et al. Ultrafine ternary metal oxide particles with carbon nanotubes: a metal-organic-framework-based approach and superior lithium-storage performance. *Dalton Transactions*, 48:4413, 2019.
- [113] Y. Liu, N. Wu, Z. Wang, et al. Fe₃O₄ nanoparticles encapsulated in multi-walled carbon nanotubes possess superior lithium storage capability. *New Journal of Chemistry*, 41:6241, 2017.

- [114] C.W. Oatley, W.C. Nixon, and R.F.W. Pease. Scanning electron microscopy. *Advances in Electronics and Electronic Physics*, 21:181, 1965.
- [115] B. Fultz and J. Howe. *Transmission Electron Microscopy and Diffractometry of Materials*. Springer, 2007.
- [116] C. Hammond. *The Basics of Crystallography and Diffraction*. Oxford Univ. Press, 2015.
- [117] H.P. Klug and L.E. Alexander. *X-Ray Diffraction Procedures: For Polycrystalline and Amorphous Materials*. John Wiley and Sons 2nd Edition, 1974.
- [118] T. Uruga. *Synchrotron-Radiation Sources, X-ray Optics and Beamlines*. Springer, 2017.
- [119] S. Mobilio, F. Boscherini, and C. Meneghini. *Synchrotron Radiation Basics, Methods and Applications*. Springer-Verlag Berlin Heidelberg, 2015.
- [120] R.A. Young. *The Rietveld Method*. International Union of Crystallography Oxford University Press, 1993.
- [121] P.S. Goh, A.F. Ismail, and B.C. Ng. Chapter 2 - raman spectroscopy. In *Membrane Characterization*, pages 31 – 46. Elsevier, 2017.
- [122] M. Kumar and Y. Ando. Single-wall and multi-wall carbon nanotubes from camphor—a botanical hydrocarbon. *Diamond and Related Materials*, 12:1845, 2003.
- [123] A. Cantarero. Raman scattering applied to materials science. *Procedia Materials Science*, 9:113 – 122, 2015.
- [124] N.S. Mueller, S. Heeg, M.Pe. Alvarez, et al. Evaluating arbitrary strain configurations and doping in graphene with raman spectroscopy. *2D Materials*, 5(1):015016, 2017.
- [125] R.S. Das and Y.K. Agrawal. Raman spectroscopy: Recent advancements, techniques and applications. *Vibrational Spectroscopy*, 57(2):163 – 176, 2011.
- [126] J. Clarke and A. I. Braginski. *The SQUID handbook*. Wiley-Vch, 2004.

- [127] <https://ncmn.unl.edu/thinfilm/mpms-squid>.
- [128] C. Lecoeur, B. Daffos, R. Lin, et al. Self-standing electrochemical double layer capacitors for operation in severe temperature conditions. *Mater Renew Sustain Energy*, 2013.
- [129] A. Bahadur, S. Iqbal, M. Shoaib, et al. Mesoporous hollow rods of magnetite used for the electrochemical study of specially designed graphene-Fe₃O₄-polyaniline nanocomposite as a high-performance anode exhibited superior reversible current capacity for lithium-ion battery. *Dalton Transactions*, 2018.
- [130] <https://www.gamry.com/application-notes/battery-research/electrochemical-capacitors-cyclic-charge-discharge-and-stacks>.
- [131] A.J. Bard and L.R. Faulkner. *Electrochemical Methods: Fundamentals and Applications*. Wiley, 2000-12-18.
- [132] <https://www.zimmerpeacocktech.com/knowledge-base/faq/cyclic-voltammetry>.
- [133] J. Jiang, X. Bing, X. Zhao, et al. Data-based fractional differential models for non-linear dynamic modeling of a lithium-ion battery. *Energy*, 135, 2017.
- [134] Y. Xu, S. Hou, G. Yang, et al. Nio/cnts derived from metal-organic frameworks as superior anode material for lithium-ion batteries. *Journal of Solid State Electrochemistry*, 22:785, 2018.
- [135] M. Sharon, W.K. Hsu, H.W. Kroto, et al. Camphor-based carbon nanotubes as an anode in lithium secondary batteries. *Journal of Power Sources*, 104:148, 2002.
- [136] L. Brissonneau, R. Sahnoun, C. Mijoule, et al. Investigation of nickelocene decomposition during chemical vapor deposition of nickel. *Journal of Electrochemical Society*, 147(4):1443, 2000.
- [137] J. Kang and S. Rhee. Metalorganic chemical vapor deposition of nickel films from Ni(C₅H₅)₂/H₂. *Journal of Material Research*, 15(8):1828, 2000.

- [138] N.K. Singh. Synthesis of cobalt and cobalt oxide filled carbon nanotubes. Master's thesis, Indian Institute of Science Education and Research, <http://localhost:8080/xmlui/handle/123456789/770>, 2017.
- [139] A.P. Balan, S. Radhakrishnan, C.F. Woellner, et al. Exfoliation of a non-van der waals material from iron ore hematite. *Nature Nanotechnology*, 13:602, 2018.
- [140] U.K. Roßler, A.N. Bogdanov, and C.P. Pfleiderer. Spontaneous skyrmion ground states in magnetic metals. *Nature*, 442:797, 2006.
- [141] G. Beutier, S.P. Collins, O.V. Dimitrova, et al. Band filling control of the dzyaloshinskii-moriya interaction in weakly ferromagnetic insulators. *Physical Review Letters*, 119:167201, 2017.
- [142] O. Gomonay, V. Baltz, A. Brataas, et al. Antiferromagnetic spin textures and dynamics. *Nature Physics*, 14:213, 2018.
- [143] T. Kikuchi, T. Koretsune, R. Arita, et al. Dzyaloshinskii-moriya interaction as a consequence of a doppler shift due to spin-orbit-induced intrinsic spin current. *Physical Review Letters*, 116:247201, 2016.
- [144] L.M. Sandratskii. Insight into the dzyaloshinskii-moriya interaction through first-principles study of chiral magnetic structures. *Physical Review B*, 96:024450, 2017.
- [145] A. Bajpai, S. Gorantla, M. Löffler, et al. The filling of carbon nanotubes with magnetoelectric Cr_2O_3 . *Carbon*, 50(4):1706 – 1709, 2012.
- [146] J.P. Cleuziou, W. Wernsdorfer, T. Ondarcuhu, et al. Electrical detection of individual magnetic nanoparticles encapsulated in carbon nanotubes. *ACS Nano*, 5:2348, 2011.
- [147] P.A. Joy, P.S. Anil Kumar, and S.K. Date. The relationship between field-cooled and zero-field-cooled susceptibilities of some ordered magnetic systems. *Journal of Physics: Condensed Matter*, 10:11049, 1998.
- [148] S. Mitra, S. Das, S. Basu, et al. Shape- and field-dependent morin transitions in structured $\alpha\text{-Fe}_2\text{O}_3$. *Journal of Magnetism and Magnetic Materials*, 321:2925, 2009.

- [149] N. Amin and S. Arajs. Morin temperature of annealed submicronic α -Fe₂O₃ particles. *Physical Review B*, 35(10):4810, 1987.
- [150] D.J. Dunlop. Transition warming and cooling remanences in magnetite. *Journal of Geophysical Research*, 112:B11103, 2007.
- [151] B.C. Zhao, Y.Q. Ma, W.H. Song, et al. Magnetization steps in the phase separated manganite La_{0.275}Pr_{0.35}Ca_{0.375}MnO₃. *Physics Letters A*, 354:472, 2006.
- [152] A. Kapoor, A.B.Dey, C. Garg, et al. Enhanced magnetism & time - stable remanence at the interface of hematite and carbon nanotubes. *Nanotechnology*, page 385706, 2019.
- [153] V.P. Andratskiā and A.S. Borovik-Romanov. Piezomagnetic effect in α -Fe₂O₃. *Journal of Experimental and Theoretical Physics*, 24:687, 1967.
- [154] F. Kuemmeth, S. Ilani, D. C. Ralph, et al. Coupling of spin and orbital motion of electrons in carbon nanotubes. *Nature Letters*, 452:448, 2008.
- [155] J. Jeong and H. Lee. Curvature-enhanced spin-orbit coupling in a carbon nanotube. *Physical Review B*, 80:075409, 2009.
- [156] H. Yang, G. Chen, A.A.C. Cotta, et al. Significant dzyaloshinskii-moriya interaction at graphene-ferromagnet interfaces due to rashba-effect. *Nature Materials*, 17:605, 2018.
- [157] V.E. Dmitrienko, E.N. Ovchinnikova, S.P. Collins, et al. Measuring the dzyaloshinskii–moriya interaction in a weak ferromagnet. *Nature Physics*, 10:202, 2014.
- [158] A. Kleibert, A. Balan, R Yanes, et al. Direct observation of enhanced magnetism in individual size - and shape-selected 3d transition metal nanoparticles. *Physical Review B*, 95:195404, 2017.
- [159] J. Zemen, Z. Gercsi, and K.G. Sandeman. Piezomagnetism as a counterpart of the magnetovolume effect in magnetically frustrated mn-based antiperovskite nitrides. *Physical Review B*, 96:024451, 2017.

- [160] A. Michels, D. Mettus, D. Honecker, et al. Effect of dzyaloshinski-moriya interaction on elastic small-angle neutron scattering. *Physical Review B*, 94:054424, 2016.
- [161] W.H. Mieklejohn and C.P. Bean. New magnetic anisotropy. *Physical Review B*, 105:904, 1957.
- [162] N. Pattanayak, J. Kumar, P.P. Patra, et al. Dielectric and raman spectroscopy in hematite crystallites across the morin transition. *arXiv:1904.07299v1*, 2019.
- [163] I.R. Beattie and T.R. Gilson. The single-crystal raman spectra of nearly opaque materials. iron(iii) oxide and chromium(iii) oxide. *Journal of Chemical Society A*, pages 980–986, 1970.
- [164] D.. A. de Faria, S. Venâncio Silva, and M.T. de Oliveira. Raman microspectroscopy of some iron oxides and oxyhydroxides. *Journal of Raman Spectroscopy*, 28:873, 1997.
- [165] D. Bersani, P.P. Lottici1, and A. Montenero. Micro-raman investigation of iron oxide films and powders produced by sol–gel syntheses. *Journal of Raman Spectroscopy*, 30:355, 1999.
- [166] S.. S. Porto and R.S. Krishnan. Raman effect of corundum. *Journal of Chemical Physics*, 47:1009, 1967.
- [167] I.V. Chernyshova, M.F. Hochella Jr, et al. Size-dependent structural transformations of hematite nanoparticles. 1. phase transition. *Physical Chemistry Chemical Physics*, 9:1736–1750, 2007.
- [168] K.F. McCarty. Inelastic light scattering in α -Fe₂O₃: Phonon vs magnon scattering. *Solid State Communications*, 68(8):799 – 802, 1988.
- [169] M.J. Massey, U. Baier, R. Merlin, et al. Effects of pressure and isotopic substitution on the raman spectrum of α -Fe₂O₃: Identification of two-magnon scattering. *Physical Review B*, 41:7822–7827, 1990.
- [170] E. Granado, A. García, J. A. Sanjurjo, et al. Magnetic ordering effects in the raman spectra of La_{1-x}Mn_{1-x}O₃. *Physical Review B*, 60:11879–11882, 1999.

- [171] M. Balkanski, R.F. Wallis, and E. Haro. Anharmonic effects in light scattering due to optical phonons in silicon. *Physical Review B*, 28:1928–1934, 1983.
- [172] J. Ma and K. Chen. Dual morin transitions during the oriented attachment process. *Europhysics Letters*, 108(3), 2014.
- [173] J. Wang, V. Aguilar, L. Li, et al. Strong shape-dependence of morin transition in α -Fe₂O₃ single-crystalline nanostructures. *Nano Research*, 8(6):1906, 2015.
- [174] D.J. Lockwood and M.G. Cottam. The spin-phonon interaction in FeF₂ and MnF₂ studied by raman spectroscopy. *Journal of Applied Physics*, 64:5876, 1988.
- [175] E. Aytan, B. Debnath, F. Kargar, et al. Spin-phonon coupling in antiferromagnetic nickel oxide. *Applied Physics Letters*, 111:252402, 2017.
- [176] P.B. Allen and V. Perebeinos. Self-trapped exciton and franck-condon spectra predicted in LaMnO₃. *Physical Review Letters*, 83:4828–4831, 1999.
- [177] P.V. Huong, R. Cavagnat, P.M. Ajayan, et al. Temperature-dependent vibrational spectra of carbon nanotubes. *Physical Review B*, 51:10048–10051, 1995.
- [178] M.R. Joya, J.D. Gonzalez, and J. Barba-Ortega. Anharmonicity study of semiconductors and metallic nanotubes by inelastic spectroscopy. *Fullerenes, Nanotubes and Carbon Nanostructures*, 23(6):566–571, 2015.
- [179] H.N. Liu, X. Cong, M.L. Lin, et al. The intrinsic temperature-dependent raman spectra of graphite in the temperature range from 4k to 1000k. *Carbon*, 152:451–458, 2019.
- [180] D. Zhang, A. Qian, J. Chen, et al. Electrochemical performances of nano-Co₃O₄ with different morphologies as anode materials for Li-ion batteries. *Ionics*, 18:591, 2011.
- [181] L. Fan, W. Zhang, S. Zhu, et al. Enhanced lithium storage capability in Li-ion batteries using porous 3D Co₃O₄ nanofiber anodes. *Industrial and Engineering Chemistry Research*, 56:2046, 2017.
- [182] M. V. Reddy, T. Yu, C. H. Sow, et al. α -Fe₂O₃ nanoflakes as an anode material for li-ion batteries. *Advanced Functional Materials*, 17:2792, 2007.

- [183] Q. Li, G. Huang, D. Yin, et al. Synthesis of porous NiO nanorods as high-performance anode materials for lithium-ion batteries. *Particle and Particle Systems Characterization*, 33:764, 2016.
- [184] Y. Pang, J. Zhang, D. Chen, et al. 3D hierarchical porous nio nanoflowers as an advanced anode material with remarkable lithium storage performance. *Royal Society of Chemistry Advances*, 6:30395, 2016.
- [185] Z. Yang, J. Shen, and L. A. Archer. An in situ method of creating metal oxide-carbon composites and their application as anode materials for lithium-ion batteries. *Journal of Material Chemistry*, 21:11092, 2011.
- [186] G. Wang, Y. Meng, L. Wang, et al. Yolk-shell Co_3O_4 -CoO/carbon composites for lithium-ion batteries with enhanced electrochemical properties. *International Journal of Electrochemical Sciences*, 12:2618, 2017.
- [187] X. Wang, X. Liu, G. Wang, et al. One-dimensional hybrid nanocomposite of highdensity monodispersed α - Fe_2O_3 nanoparticles and carbon nanotubes for high-capacity storage of lithium and sodium. *Material Chemistry A*, 4:18532, 2016.
- [188] Y. Huang, Z. Xu, J. Mai, et al. Revisiting the origin of cycling enhanced capacity of Fe_3O_4 based nanostructured electrode for lithium ion batteries. *Nano Energy*, 41:426, 2017.
- [189] T.Q. Chen, L.K. Pan, X.J. Liu, et al. A comparative study on electrochemical performances of the electrodes with different nanocarbon conductive additives for lithium ion batteries. *Material Chemical Physics*, 142:345, 2013.
- [190] N. Mironova-Ulmane, A. Kuzmin, I. Sildos, et al. Polarisation dependent raman study of single-crystal nickel oxide. *Central European Journal of Physics*, 9(4):1096, 2011.
- [191] W. Cao, A. Hu, X. Chen, et al. Nio hollow microspheres interconnected by carbon nanotubes as an anode for lithium ion batteries. *Electrochimica Acta*, 213:75, 2016.

-
- [192] J. Cheng, B. Wang, C. M. Park, et al. Cnt@Fe₃O₄@c coaxial nanocables: One-pot, additive-free synthesis and remarkable lithium storage behavior. *Chemical European Journal*, 19:9866, 2013.
- [193] A. Khalil, B.S. Lalia, and R. Hashaikah. Nickel oxide nanocrystals as a lithium-ion battery anode: structure-performance relationship. *Journal of Materials Science*, 51(14):6624, 2016.
- [194] V.G. Hadjiev, M.N. Iliev, and I.V. Vergilov. The Raman spectra of Co₃O₄. *Journal of Physics C: Solid State Physics*, 21:199, 1988.
- [195] F. Wang, Q. Hana, Z. Yi, et al. Synthesis and performances of carbon fiber@Co₃O₄ based on metal organic frameworks as anode materials for structural lithium-ion battery. *Journal of Electroanalytical Chemistry*, 807:196, 2017.
- [196] C. Yan, G. Chen, X. Zhou, et al. Template-based engineering of carbon-doped Co₃O₄ hollow nanofibers as anode materials for lithium-ion batteries. *Advanced Functional Materials*, 26:1428, 2016.
- [197] Z. Xiong, Y. S. Yun, and H. J. Jin. Applications of carbon nanotubes for lithium ion battery anodes. *Materials*, 6:1138, 2013.
- [198] M.F. Hassan, Z. Guo, Z. Chen, et al. α -Fe₂O₃ as an anode material with capacity rise and high rate capability for lithium-ion batteries. *Materials Research Bulletin*, 46:858, 2011.
